The structural characterisation of porous media for use as model reservoir rocks, adsorbents and catalysts

Evbuomwan, Irene

Award date:
2009

Awarding institution:
University of Bath

The Structural Characterisation of Porous Media for use as model Reservoir Rocks, Adsorbents and Catalysts

Irene Osagie Evbuomwan

A thesis submitted for the degree of Doctor of Philosophy

University of Bath

Department of Chemical Engineering

July 2009

Table of Contents

Chapter 2: Pore Characterisation and Distribution Analysis

Chapter 3: Porous Media Synthesis/Characterisation

Chapter 4: Transport Properties

Dedication

I dedicate this thesis to Engr. & Mrs Bless Osagie Evbuomwan, my parents, with love and admiration. God bless you!

Acknowledgements

I would like to express profound gratitude to my supervisor Dr Sean Rigby for his assistance and guidance throughout the course of this research.

I will also like to thank Dr Karen Edler for performing the SAXS experiments, and for kindly allowing the use of her lab for synthesis. Acknowledgement is also given to all the technical staff and my colleagues in the department of Chemical Engineering University of Bath for their technical support, and especially to Fernando Acosta for running water vapour experiment 4. I also wish to thank the staff at Johnson Matthey for running the mercury porosimetry characterisation of the F127 and P123 templated silicas and the integrated nitrogen sorption and mercury porosimetry experiments. I will also like to thank Prof. R. Richardson, of the Department of Physics, University of Bristol, U.K. for the SAXS characterisation of the surfactant templated materials, and Taghi Miri, of the Centre for Formulation Engineering, Department of Chemical Engineering, School of Engineering, University of Birmingham, U.K. for running the X-ray Images of pellets containing entrapped mercury.

I am also grateful to the Department of Chemical Engineering, University of Bath for financial support.

I would like to thank God for making this possible. I am also grateful to my parents and sisters Efe, Eki, Noma and Kaka for all their love and support; and to Greg for standing by me, I could not have done this without you. You guys mean the world to me. Huge thanks also to all my friends and family, especially Tanko, Zama, Sabah and Benhilda my Bath crew of 2009! we did it!

Abstract

The concept of creating heterogeneous structures by nanocasting techniques from a combination of several homogeneous surfactant templated structures to model reservoir rock properties has not been approached prior to this research project, and will be used to test and provide better understanding of gas adsorption theories such as the pore blocking phenomenon (Seaton, 1991). Porous media with controlled pore sizes and geometry can be used to mimic a variety of reservoir rock structures, as it can be engineered to consist of a network of elements which, individually, could have either regular or irregular converging and diverging portions. The restrictions in these elements are called throats, and the bulges pores. Catalysts developed from a range of Nanotechnology applications could be used in down-hole catalytic upgrading of heavy oil. They could also be used as catalyst supports or to analyse the coking performance of catalysts. These studies will highlight the pore structure effects associated with capillary trapping mechanisms in rocks, and potentially allow the manipulation of transport rates of fluids within the pore structure of catalysts.

Mercury-injection capillary pressure is typically favoured for geological applications such as inferring the size and sorting of pore throats. The difference between mercury injection and withdrawal curves will be used to provide information on recovery efficiency, and also to investigate pore level heterogeneity. Mercury porosimetry studies are carried out to provide a better understanding of the retraction curve and the mechanisms controlling the extrusion process and subsequently the entrapment of the non-wetting phase. The use of model porous media with controlled pore size and surface chemistry allows these two effects to be de-convolved and studied separately. The nanotechnology techniques employed mean that uncertainty regarding exact pore geometry is alleviated because tight control of pore geometry is possible. Trapping of oil and gas on a microscopic scale in a petroleum reservoir rock is affected by the geometric and topologic properties of the pores, by the properties of the fluids and by properties related to fluid-rock interaction such as wettability. Several distinct mechanisms of trapping may occur during displacement of one fluid by another in a porous media, however in strongly water-wet rocks with large aspect ratios, trapping in individual pores caused by associated restricting throats (may be/is) the most important mechanism of trapping. The results of the proposed research will be both relevant to the

oil and gas as well as the solid mineral sector for application as catalyst or catalyst supports. By providing a better understanding of the relationship between reservoir rock pore space geometry and surface chemistry on the residual oil levels, a more accurate assessment of the potential of a particular reservoir could be generated.

The analysis of gas adsorption/desorption isotherms is widely used for the characterization of porous materials with regard to their surface area, pore size, pore size distribution and porosity, which is important for optimizing their use in many practical applications. Although nitrogen adsorption at liquid nitrogen temperature is considered to be the standard procedure, recent studies clearly reveal that the use of additional probe molecules (e.g. argon, butane, carbon dioxide, water, hydrogen, and hydrocarbons e.g. cyclohexane and ethane) allows not only to check for consistency, but also leads to a more comprehensive and accurate micro/mesopore size analysis of many adsorbents. Furthermore, significant progress has been achieved during recent years with regard to the understanding of the adsorption mechanism of fluids in materials with highly ordered pore structures (e.g., M41S materials, SBA-15). This has led to major improvements in the pore size analysis of nanoporous materials. However, there are still many open questions concerning the phase and sorption behaviour of fluids in more complex pore systems, such as materials of a heterogeneous nature/differing pore structures, which are of interest for practical applications in catalysis, separation, and adsorption. In order to address some of these open questions, we have performed systematic adsorption experiments on novel nanoporous materials with well defined pore structure synthesised within this research and also on commercial porous silicas. The results of this study and experiments allow understanding and separating in detail the influence of phenomena such as, pore blocking, advanced condensation and delayed condensation on adsorption hysteresis and consequently the shape of the adsorption isotherms. The consequences of these results for an accurate and comprehensive pore size analysis of nanomaterials consisting of more complex nanoporous pore networks are also investigated.

Published Work

Nanocasting of Novel, Designer-Structured Catalyst Supports. Chemical Engineering Science 2004, Volume 59, 5113-5120.

Using Nano-Cast Model Porous Media and Integrated Gas Sorption to Improve Fundamental Understanding and Data Interpretation in Mercury Porosimetry
Particle & Particle Systems Characterisation (2006) Volume 23, 82-93

Experimental and Modelling Studies of the Kinetics of Mercury Retraction during Porosimetry in the Transport and the Quasi-Equilibrium Regimes.Chemical Engineering Science 2008, Volume 63, 5771-5788.

Pore Blocking Phenomena Using Gas Adsorption Kinetics
For Submission to J. Phys. Chem. B

Nomenclature

Å	Angstroms
A	Area (m^2)
A_i	Area occupied by gas in layer i
a	Particle size (m)
C	BET constant
D_k	Knudsen diffusivity, $m^2 s^{-1}$
D_a	Diffusion coefficient of phase a, $m^2 s^{-1}$
D_e	Effective diffusivity, $m^2 s^{-1}$
D	Fractal dimension
D	Diffusivity Constant
d	Fractal dimension
E_i	Energy of adsorption
f	Percolation factor
g	Grams
I(q)	Scattering Intensity
k	Mass transfer coefficient (Linear Driving Force Model)
K	Constant of proportionality
K	Constant of proportionality for the Kelvin Equation
K *(Darcy's Law)*	Darcy's law constant
l	Distance
L	Avogadro constant
l	Pore length, m
m	Dry mass of adsorbent
mg	Miligrams
na	Amount of Gas Adsorbed
n^a	Amount of gas adsorbed
n_m	Molecular capacity
ΔP	Pressure difference applied
P_0	Saturation Pressure of Gas at T
P/P^0	Relative Pressure
P	Applied pressure, bar
P^0	Saturation pressure, bar

Pa	Pascal
R	Molar gas constant, 8.314 J mol^{-1} K^{-1}
R	Radius, m
r_c	Radius of curvature of the cavity
R_t	Throat radius, m
Tc	Critical Temperature
T	Absolute Temperature
t_a	Thickness of the adsorbate film
t	Time, s
t_m	t-layer thickness, m
V	Volume of Adsorbed Gas at Equilibrium Pressure
V_m	Volume of Gas in a Monolayer
W	Pore Width
ε	Voidage fraction
γ	Gyromagnetic ratio, rad T^{-1} s^{-1}
γ	Surface Tension
λ	Surface layer thickness, m
ρ	Density of liquid, kg m^{-3}
σ	Molecular cross-sectional area, nm^2
θ	Solid-liquid contact angle
I	X-ray intensity, arbitrary units
l	Pore length, m
R_t	Throat radius, m
μ	Viscosity
ρ	Density of the adsorbate
α	Percolation analysis
β^0	Compressibility
σ	Average area occupied by each adsorbed molecule
ρ	Density of the adsorbate
λ	Wavelength of the radiation
θ_{ray}	Scattering angle
ξ	Characteristic length of the structure producing scattering
ΔH	Activation energy

Abbreviations

ASAP	Accelerated Surface Area Porosimeter
API	American Petroleum Index
BET	Brunauer Emmett and Teller Theory
BJH `	Barrett Joyner and Halenda Method
BRIJ 56_t	Polyoxyethylene-10-cethyl-ether Templated Material
BRIJ 57_t	Polyoxyethylene-10-steryl-ether Templated Material
BVI	Bound Volume Index
$CTAB_t$	Cetyltrimethylammonium Bromide Templated Material
C – C	Carbon – Carbon
CH_3	Methyl groups
CPG	Controlled Pore Glass
cmc	Critical Micelle Concentration
cc `	Cubic Centimetre
Expt.	Experiment
FHH	Frenkel-Halsey-Hill Theory
$F127_t$	Pluronic F127 ($EO_{106}PO_{70}EO_{106}$) Templated Material
FCC	Fluid Catalytic Cracking
GCMC	Grand Canonical Monte Carlo
HK	Hovarth Kawazoe
HT	Hydrogen Transfer
HCL	Hydrochloric Acid
hr	Hours
IUPAC	International Union of Pure and Applied Chemistry
IGA	Intelligent Gravimetric Analyser
IFT	Interfacial Tension
K	Kelvin
LDF	Linear Driving Force Model
MFDT	Mean-Field Density Theory
MRI	Magnetic Resonance Images
MC	Monte Carlo
MD	Molecular Dynamics

min	Minutes
ml	Millilitres
NLDFT	Nonlocal Density Functional Theory
N_2	Nitrogen
NMR	Nuclear Magnetic Resonance
Nwp	Non-wetting Phase
N	Newton
PSD	Pore Size Distribution
PDD	Pore Diameter Distribution
$P123_t$	Pluronic P123 ($EO_{20}PO_{70}EO_{20}$) Templated Material
PS	Polystyrene Beads
PFG	Pulse Field Gradient
Pa	Pascal
psi	Pounds per Square-inch
rpm	Revolutions per Minute
SEM	Scanning Electron Microscopy
SANS	Small Angle Neutron Scattering
SAXS	Small Angle X-ray Scattering
ST	Surface Tension
s	Seconds
TEM	Transmission Electron Microscopy
TMOS	Tetramethlyorthosilcate
TEOS	Tetraethlyorthosilcate
Kpa	Kilo-Pascal
mD	Mili-Darcy
^oC	Degree Centigrade
nm	Nanometer
mbar	Millibar
MPa	Mega-Pascal

List of Figures

List of Equations

List of Tables

Chapter 1: Literature Review

1.1 - Introduction

The World's growing need for energy obtained in economically, socially and environmentally responsible ways has further fuelled the need for improved oil recovery techniques. The 20th century saw the use of hydrocarbons dominate the process industries and arguably it still does. Only 1.08 trillion barrels of petroleum reserves are left on the planet (World Oil Journal, 2005), and with only one new barrel discovered for every four used. Over 31.03 billion barrels are consumed annually worldwide which is continually increasing, and there is less than 25.4 years left of reserves (World Oil Journal, 2006). Hence the world's petroleum reserves are finite. It is also increasingly likely that most of the 'giant' fields have already been discovered and that future finds are likely to be smaller and more complex than previously discovered reservoir fields. Because they are rapaciously being consumed, their costs are rising. As a result, drastic measures have to be taken to find more oil from existing oil reservoirs (Enhanced Oil Recovery), to avoid wastage and to increase recovery efficiency by lowering the hydrocarbon irreducible saturation.

Therefore, as the era of easy oil is said to be over, we are now faced with more complex reservoirs e.g. heavy oil and oil sands. The Athabasca Tar Sands in Canada is the largest oil reserve in the world. Heavy oil will be needed if we are to obtain a smooth transition from the 'Oil Age' to other energy technologies. Although alternative forms of energy may grow rapidly, the World is going to need a lot more hydrocarbons to keep up with the rapidly growing demand and development needs. Hence new technologies and techniques, targeted to the exploration of complex oil reservoir systems are receiving great attention, and rightfully should, as they are essential in sustaining global energy supply. In addition the rocketing price of oil means that those unconventional sources such as heavy oil and oil sands are now more economical to extract and sell. As emerging economies like India and China continue to grow, the need for more affordable energy will be essential to improving the quality of livelihoods globally. Oil recovery efficiency is heavily influenced by the structure of the void space oil occupies within the reservoir rocks. Hence, characterisation of porous materials, such as

nanoporous materials of heterogeneous nature which mimic reservoir rock structure, can be used to study the relationship between pore structure, pore size distribution, and ultimately permeability and fluid transport mechanisms in porous media. Effective pore structure characterisation could eventually improve the prediction of the Bound Volume Index (BVI) parameter for oil reservoir rocks. This parameter characterises the irreducible fluid saturation level, and is used to quantify the economic potential of an oil reservoir as well as in reservoir modelling of enhanced oil recovery. This project attempts to determine the relationship between the structure of a porous medium, such as a reservoir rock, and the quantity of non-wetting fluid such as oil, that becomes entrapped within the void space. As there are still gaps surrounding effective means of predicting the BVI of reservoirs, any improvements in this prediction could save plenty of money and time. The particular experimental processes employed within this research for the study of the transport phenomena in porous media and the entrapment of the non-wetting phase (as a model for oil entrapment) include a combination of gas adsorption, mercury intrusion and extrusion and microscopy techniques. Experimental studies on model reservoir rocks could reveal additional information towards achieving a better interpretation of the mechanisms of entrapment that could lead to more accurate predictions of the BVI.

So, as target fields are getting smaller, it is particularly important that exploration and appraisal wells are sited more accurately and with greater chance of success. Increasing the efficiency of the exploration process is more important than ever before in terms of saving energy, time, labour and technical costs, and is crucial in meeting the enormous energy demands of the world. This could be improved greatly by better reservoir characterisation and pre-exploration analysis which include the passage of one or more fluids through a porous sample. This is the basis for which this research has been carried out. This chapter contains a general introduction to petroleum reservoirs, methods of oil recovery, and the factors influencing oil recovery efficiency with particular emphasis on ways of improving oil recovery (EOR techniques), as well petroleum catalysis which looks briefly into the use of catalysts as enhancers in the hydrocarbon refining process. Finally, the nature of work undertaken within this research, in an attempt to improve the understanding of the role of pore structure on transport phenomena, for example, through a more accurate interpretation of pore

structure analysis techniques is detailed along with a general description of each of the chapters of the thesis.

1.2 - General Background to Petroleum Reservoirs

Today, exploration for oil begins with geologists seeking out likely areas, and then pinpointing the most suitable site at which to drill an exploration. Potential oil bearing areas are then found wherever sedimentary basins exist. Porous sedimentary rock structures might have encouraged oil to collect in pockets in combination with formations of overlaying dense impervious cap rock layers. The expense of drilling a well and the high risk of failure in finding oil, make oil exploration including surveying, one of the costliest stages of the oil industry. Detailed characterisation and field analysis may delay 'first oil' to be produced from the field by several years, and may add to the initial investment required, but the overall profitability of the reservoir may be improved by the time the decision is made to drill. Subsequently more accurate information about the reservoir and its hydrocarbon fluid can be obtained and then the capacity/size and properties of the formation and the fluid are determined. In other to make concrete recommendations concerning the manner in which a hydrocarbon fluid should be explored, the production engineer needs to have a sound grasp of the principles governing the movement of oil, gas, and water from the formation to the well head. Only with such understanding can the engineer correctly apply the available engineering techniques and decide on the precise specifications of production equipment to be used in any particular well.

Once drilling has reached a reservoir with economic potential, the reservoirs internal pressure provides the natural drive to lift the structure's oil to the surface, in effect forcing the oil through the rock pores to the well and then up to the surface, usually through a process of displacement. However, the level of reservoir permeability, i.e. the ability of oil to move through the reservoir rock, can prove a major problem when it prevents sufficient oil flow. Hence a reservoir with higher oil content may not necessarily be of higher economic potential if it possesses a lower rate of accessibility or connectivity factor. Advances in structural characterisation techniques such as in-situ and laboratory scale measures seek to effectively estimate the fluid transport

behavioural pattern of a pore system. The permeability factors and other mechanisms that could deter fluid flow such as pore blockages due to pore size distribution and also condensation of hydrocarbon vapours within the pore structure can be better understood to improve recovery efficiency. The physical geology of a reservoir rock is discussed in more detail further on. This includes basic rock classifications and the geological processes that directly relate to the formation of petroleum; and petroleum geology, which explains the origin and characteristics of petroleum reservoirs. The reservoir geology controls the producibility of a formation, i.e. the relationship between the fluid flow and the applied pressure. Hence, a detailed understanding of the geological processes undergone by the petroleum reservoir is vital to oil recovery. The depositional environment, structure and digenesis (conversion of loose sediment into a rock) of a field provide invaluable information, towards describing and quantifying geologically controlled reservoir parameters.

Reservoirs are generally layers of rocks along with which animal and plant matter were laid down as sediments on the surface of the earth million of years ago. These layers could have been sand dunes, beaches, deserts, or coral reefs, which were buried and compressed deep in the Earth to depths of three to even thirty thousand feet as a result of geological shifts. Variables such as geological time scales, pressure (due to burial and depth) and temperature (due to geothermal gradient related to depth) resulted in the conversion of the organic material into petroleum reservoir fluids, and the mud, sand and silt into rock. The pores between the rock components, e.g. the sand grains in sandstone will be filled with water, prior to migration, and then displaced by the migrating hydrocarbon which gradually fills up the reservoir. These reservoir fluids (oil and gas) which are fossil fuels trapped within the rocks, can be found in both offshore and onshore locations. A rock that contains organic material that converted into petroleum reservoir fluids is referred to as a ‘source rock’. Petroleum fluids can migrate within a porous media, and hence the rocks from which it is produced are usually not the ones (source rocks) from which it was formed (Dandekar, 2006). The reservoir rocks that hold petroleum are mostly sandstone and limestone (also called carbonates including dolomites). Most reservoirs in the Gulf of Mexico and the North Sea are contained in a sandstone depositional environment, while many of the giant fields of the Middle East are found in carbonate rocks (McCaslin, 1989).

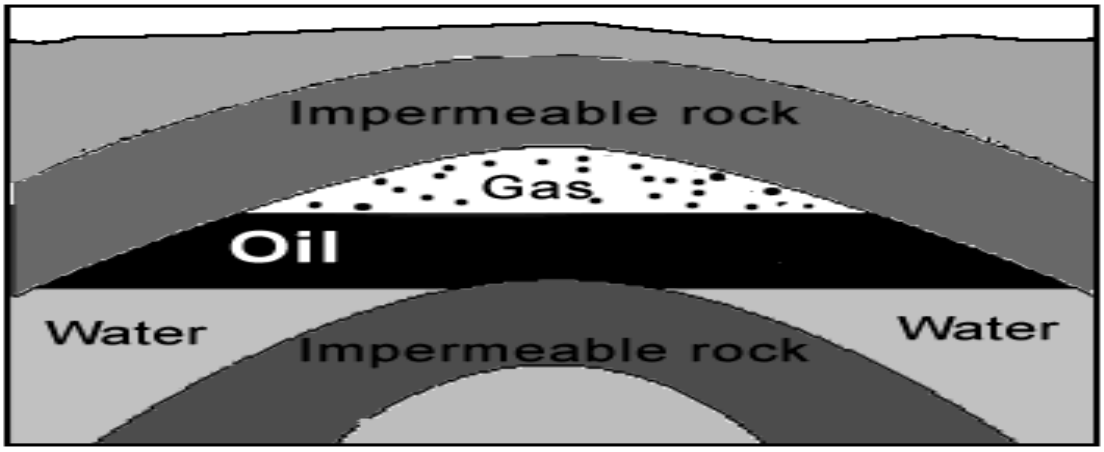

Figure 1.1: Schematic of an idealised petroleum reservoir.

In a typical oil field gaseous hydrocarbons, which are the lightest, occupy the highest part of the reservoir; this part of the field is called the 'gas cap'. The part just beneath is the 'oil zone' occupied by liquid hydrocarbon. Further down, the pores of the reservoir rock contain only water and this area is called the 'aquifer'. Most petroleum reservoirs contains at least two fluid phases, either gas and water or oil and water. Having said that, some might contain all three phases, that is, gas, oil, and water. In principle they are supposed to be separated by gravity segregation but parameters such as rock/fluid properties and solubility, restrict complete gravitational segregation as shown in Figure 1.1. For an effective reservoir, the pores need to be interconnected to allow migration and also flow towards the borehole once a well is drilled into the structure. The pore space is referred to as the 'porosity', and in oil field terms the permeability measures the ability of a rock to allow fluid flow through the pore system. A reservoir rock of good porosity but with a too low permeability to allow fluid flow is termed, tight'.

1.2.1 - Rocks

A rock is a naturally occurring solid composed of a naturally occurring element or compound with a definite composition and structure (Giuliano, 1981). There are three major classifications of the Earth's rock, based on the origin of the rock the structure and depositional environments, which have been researched extensively by researchers (such as Giuliano, 1981; Chilingar, 1967) and they are defined below:

- Igneous Rocks: Derived from the Latin word 'ignis', meaning fire. These rocks were once magma, which subsequently cooled and solidified. Igneous rocks could be either extrusive or intrusive where the magma flows over the earth's surface to cool and form into a rock, or cool and harden while beneath the earth surface respectively. Cores of mountain ranges are typically composed of igneous rocks, most usually granite.
- Sedimentary Rocks: The term sedimentary also comes from the Latin word 'sedimentum' meaning settling. These rocks are composed primarily of particles that have been broken off of pre-existing rocks, and are transported by water, wind or air to a depositional area. Following the deposition, lithification occurs and hence a sedimentary rock is formed.
- Metamorphic Rocks: Derived from two Greek words 'meta' and 'morphe' meaning 'change' and 'form' respectively. These rocks have changed their form because of pressure, temperature and accompanying chemical reactions. For example soft coal can change to hard coal and then graphite under high temperatures and pressures. Common metamorphic rocks include marble and slate.

Understanding sedimentary rocks is particularly important since most oil and gas producing rocks are sedimentary in origin. Since with a few exceptions, reservoir rocks are mainly sediments and could either be of clastic or carbonate composition. Clastic rocks are composed of silicates, usually sandstones, while carbonate rocks are composed of biogenetically derived detritus such as coral or shell fragments. The two common types of reservoir rocks (sandstones and carbonates) are classified in more detail below. The nature of the rocks affects the quality of the reservoir and its interaction with the fluids, which flow through them. Based on the aforementioned, the significance of reservoir rock and fluid properties in the exploration and production of reservoirs is clearly evident. Therefore, a detailed knowledge of reservoir rock topology and its effect on fluid transport properties is the backbone to success in all exploration and production related activities such as reservoir engineering.

1.2.2 - Sandstone Rocks

Sandstone reservoirs are by far the most widespread, accounting for 80 % of all reservoirs and 60 % of oil reserves. Sandstone reservoirs are formed after the sand grains have been transported over large distances and have deposited in particular environments of deposition. The main component of sandstone reservoirs, also known as siliclastic reservoirs, is quartz (SiO_2). This is a fairly stable mineral, which is not easily altered by changes in pressure, temperature, or acidity of pore fluids.

1.2.3 - Carbonate Rocks

Carbonate rocks consists chiefly carbonate minerals such as limestones ($CaCO_3$) and/or dolomites ($CaCO_3$, $MgCO_3$), and is usually found in situ (place of formation). Carbonate rocks are susceptible to alteration by the processes of digenesis, and carbon minerals are fairly unstable. A common type is shaly carbonates, but marls, which contain between 35 to 65 % shale, are not reservoirs due to the small proportion of shale binding the grain together, which considerably decreases permeability. Carbonate reservoirs tend to have more complex pore systems than sandstones because they are exposed to more intricate depositional environments and post depositional processes. Carbonate rocks are results of the lithification of the organic debris, such as the hard fragments of coral reefs or algae or less commonly by direct precipitation of the carbonates from seawater. The classification of carbonate rocks puts into place the proper behaviour of each of the elements that have an effect on the particular system. These elements determine the general behaviour of the carbonate rocks. Limestones are composed of more than 50 % carbonate minerals of which 50 % or more consists of calcite and or aragonite. Clay particles or organic matter causes the grey colour. The origin, occurrence, classification and the physical and chemical aspects of carbonate rocks are reported in much detail by Chilingar *et al.* (1967). The authors show that the core analysis of some carbonate rocks is complicated by the presence of fractures and solution cavities. A good example is the Fullerton clearfork dolomite limestone reservoir in the Permian Basin, where 82 % of the core samples were reported to have permeabilities of less than 1 mD. If 1 mD was used as the minimum productivity permeability as opposed to the actual value of 0.1 mD, which accounts for discrepancies

in estimating the ultimate recovery, the results would then be 70 % in error. Such complicated porous structures should be analysed by 'whole' or large core analysis (where the whole core is analysed instead of small plugs). There are three constituents of carbonate rocks according to the classification of (Chilingar *et al.*, 1967), namely 'allochems', 'microcrystalline ooze' or carbonate mud and 'sparry calcite cement'. The texture of the matrix defines the minute pore structure that links the visible porosity as well as the hidden porosity in some rock types. The minute and not readily visible pore spaces may add 25 % or more to the pore space. The types of textures available include: 'compact crystalline, 'chalky' and 'granular'. The types of porosity in carbonate rocks may be classified into three sections on the basis of pore size, namely 'cavernous' (> 2 mm), 'very coarse' (1-2 mm) and 'coarse' (0.5-1 mm). A test is required to determine the extent of interconnection between the pores, and the pore throat. Geometry defines the size of the pore throats and its effectiveness, and is a crucial factor to hydrocarbon-producing potential.

1.3 - Oil recovery

The oil production process involves sweeping the reservoir between injection wells and production wells, and the amount recoverable is determined by a number of factors. However, the knowledge of fluid flow is paramount to understanding oil recovery. These factors include the permeability of the rocks, the strength of the natural drives required to push oil flow to the well (includes the gas present, and pressure from adjacent water or gravity), and the viscosity of the oil. Accordingly a number of reservoir characteristics have strong influence on recovery as well as the effect of the nature of fluids present and the injected fluids (fluid-fluid interactions). When the reservoir rocks are tight, such as shaly carbonates, oil generally cannot flow through, but when they are permeable such as in sandstones, oil flows freely. Reservoir geology confirms an impermeable barrier opposing the flow of fluids is not desirable; however it is trickier to detect e.g. a formation such as shale/sandstone or carbonate formations can exhibit sedimentations of permeable materials and close-packed materials creating interlocking masses that make fluid circulation difficult. There are subsequently three types of recoveries, 'primary' and 'secondary' and 'tertiary' as discussed below.

1.3.1 - Primary Recovery

In primary recovery, hydrocarbons are recovered through wells drilled through the surface of the reservoir into the oil zone, and as the initial pressure in the fluids occupying the pore space of the reservoir is very often higher than the hydrostatic pressure, such that, by opening a well, the pressure at its bottom is reduced, thus driving the reservoir fluids towards the well. If the natural pressure drop obtained in the well is too small, then it becomes hard to force oil to the surface. The presence of gaseous fuels, natural gas or water and gravity are the main suppliers of the needed pressure. Usually about 20 % of the oil in a reservoir is extracted by using primary recovery methods

1.3.2 - Secondary Recovery

After primary recovery the pressure in the whole reservoir drops progressively as the fluids are recovered. Pressure drops in the gas zone and aquifer causes gas and water to flow into the oil zone and thus flows with the oil towards the producing well. The amount of gas and water in the extracted fluids could become too much, and hence uneconomical, or the pressure in the reservoir could become insufficient for substantial production. In order to produce more oil, the pressure in the reservoir must be maintained by injecting another fluid, which also helps to push forward the oil contained in the reservoir towards the producing wells and this act is termed ‘secondary recovery’. Secondary oil recovery employs various techniques to aid the oil recovery process from pressure depleted reservoirs. Pumps are generally used to bring the oil to the surface. However other techniques of increasing the reservoirs pressure such as water injection, natural gas re-injection, air injection and carbon dioxide injection are also employed. The combination of primary and secondary recovery generally recovers between 25 % - 35 % of the reservoir’s oil.

1.3.3 - Tertiary Recovery

Production is no longer cost effective when an injected fluid makes up a large proportion of the extracted fluids, and as a result alternative more sophisticated techniques are adopted to increase the recovery of the desired fluid (hydrocarbons). This act is termed 'tertiary recovery' and includes all attempts made to recover remaining oil, either by increasing the displacement efficiency or by increasing the sweep efficiency. Oil viscosity is usually reduced in order to improve oil production in tertiary oil recovery. For example thermally Enhanced Oil Recovery methods (TEOR) are considered tertiary, as the oil is heated to make it less viscous and hence easier to extract. Steam injection is the most common form of TEOR. Tertiary recovery techniques allow an extra 5 - 15 % of the reservoir's oil to be recovered.

1.4 - Factors Influencing Recovery

This section reviews the various factors influencing oil recovery, which includes porosity, permeability, electrical properties of reservoir rocks, interfacial and surface tension, wettability and the effects of heterogeneity. This will provide additional information towards better understanding the oil recovery process and hence provide insights into means of improving oil recovery.

1.4.1 - Porosity

Reservoirs that hold petroleum fluids are mostly sandstones and limestones that appear to be solid but often not so solid (also known as porous solids). Porous solids are such materials generally characterised by parameters such as the overall average voidage fraction (porosity), pore size distribution (probability density function), specific surface area and pore connectivity (mean pore co-ordination number) (Rigby *et al.*, 2003). Sandstones started out as individual sand particles of varying grain sizes, which were buried during the depositional process, and hence resulted in spaces between the particles. These tiny spaces or pores (typically up to 300 μm) in petroleum reservoir rocks are the ones in which petroleum reservoir fluids are present, much like a sponge

holding water (Dandekar, 2006). This particular storage capacity of reservoir rocks is called porosity. Porosity is defined as a ratio of the pore volume (void space) in a reservoir rock to the total volume (bulk volume) and it is often expressed as a percentage. The void space is the summation or combined volume of all the pore spaces in a given reservoir rock. Porosity is donated by ϕ and expressed by the following relationship:

$$\phi = \text{Pore volume/Total or bulk volume} \quad \textbf{(1.1)}$$

1.4.1.1 - Types of Porosities

The fact that reservoir rocks were formed as a result of the deposition of sediments, gives rise to different types of voids or pores. Some of these voids that developed, were interconnected with other void spaces and as a result form a network, while some were connected with other void spaces but with a dead-end or cul-de-sac; and some pores became completely isolated or closed from other void spaces because of cementation (Dandekar, 2006). Figure 1.2 shows a typical schematic representation of a porous material. The first category of pores are those totally isolated from their neighbours, as in region (a), are described as closed pores. These pores influence macroscopic properties such as bulk density, mechanical strength and thermal conductivity, but are inactive in processes such as fluid flow and adsorption of gases. However, pores which have a continuous channel of communication with the external surface of the body, like (b) (c) (d) (e) and (f), are described as open pores. Some may be open only at one end like (b) and (f); they are then described as blind pores. Others may be open at two ends (through pores), like around (e). Pores may also be classified according to their shape. They may be cylindrical (either open (c) or blind (f)), ink-bottle shaped (b), funnel shaped (d) or slit-shaped. Roughness is similar to porosity; this is normally found at the external surface, represented around (g) (Sing *et al.*, 1985). Based on these types of pores, the total or absolute porosity of a reservoir rock comprises of effective and ineffective porosity (Dandekar, 2006).

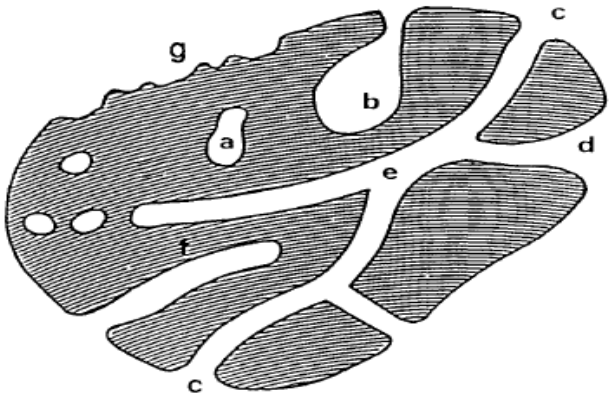

Figure 1.2: Schematic cross section of a porous solid (Rouquerol *et al.*, 1999)

'Effective porosity' is mathematically expressed by the following expression:

$$\phi = \frac{C}{B} \qquad \textbf{(1. 2)}$$

Where;
C = Vol. of interconnected pores + Vol. of dead-end pores
B = Total or bulk volume

The effective porosity value is the quantitative value desired and it's used in almost all calculations because it represents the pore occupied by mobile fluids. The effective porosity of rocks varies between less than 1 % to over 40 %. The closed or isolated or completely disconnected pores are ineffective in producing any petroleum reservoir fluids due to their isolation. It is often stated that the porosity is:

- Low if ϕ < 5 %.
- Mediocre if 5 % < ϕ < 10 %.
- Average if 10 % < ϕ < 20 %
- Good if 20 % < ϕ < 30 %
- Excellent if ϕ > 30 %

1.4.2 - Permeability

Merely locating a reservoir rock with high porosity is not sufficient as the fluids contained in the pore spaces would require a pathway to flow to the surface. This particular property of the reservoir rock that measures its specific flow capacity is termed 'permeability' and is denoted k^p, for the purpose of this research. Several parameters of pore geometry are needed for estimating permeability which is a key parameter for the characterisation of reservoir sandstones. The detailed study of pore space properties of sedimentary rocks is a prerequisite for the exploitation of hydrocarbon reservoirs. Permeability is the most influential parameters in determining the production capabilities of a reservoir rock, and it allows reservoir fluids contained in pore spaces of reservoir rocks to flow so that they can be produced or brought to the surface of a well. In contrast to porosity which is a static property of a reservoir rock, permeability is a flow property, hence dynamic in nature, and can therefore only be characterised by performing flow experiments on reservoir rocks. There are two types of permeability measurements which includes 'absolute permeability' and 'relative permeability'. The former is the permeability measure of a rock which is 100 % saturated with a given fluid provided no chemical reaction occurs between the rock and the flowing fluid and latter is the permeability measure of the same rock filled with two or more fluids. The permeability of a rock is often connected to the interconnectivity of the pore structure, including open, closed and dead end pores. Absolute permeability can be measured using the 'Darcy's Law' which originated from his investigations on flow of water through sand filters for water purification for the city of Dijon in France.

Darcy's Law: $$Q = K_{(Darcy'sLaw)} A \frac{(h_1 - h_2)}{L} \quad \textbf{(1. 3)}$$

The investigations showed that the same principle can be applied to the flow of a fluid through a core plug, and if $K_{(Darcy's\ Law)}$ is expressed as a ratio of k^p/μ, where μ is the viscosity of a given fluid and k^p is the permeability of the porous medium, it can be extended to other fluids to give:

$$Q = \frac{k^p A \Delta P}{\mu L} \quad \textbf{(1. 4)}$$

Where

Q = Flow rate in m^3/s

k^p= Absolute permeability in m^2 (which can be converted to a field unit (mD or Darcy)

A = Cross sectional area in m^2

$\Delta P = P_1 - P_2$ is the pressure drop in N/m^2 of flow

μ = Fluid viscosity in $Nsec/m^2$. High vs. good permeability is favourable for recovery

L = Length the pressure drop is taking place over (m)

1.4.3 - The Relationship between Porosity and Permeability

Permeability depends on the continuity of pore space whereas porosity basically signifies the availability of a pore space, and as such there is no direct relationship between the two. It is also therefore possible to have a very high porosity without having any permeability and similarly a low porosity rock may have a high permeability, as in the case of a micro-fractured carbonate where most of the relatively unimpeded flow takes place through the micro-fracture. At the extreme, when porosity is zero, permeability is zero and when porosity is 100 % (e.g., a pipe) permeability is infinite. In general the quality of a hydrocarbon-bearing formation is judged according to its permeability and commonly falls within the range 0.1 to 1000 mD. Formations having permeabilities greater than 1 mD are considered very good and those less than 1 mD typically found in chalk formations are considered poor and referred to as tight formations. Such classifications could be considered relative to a certain extent, as so called tight formations (too tight for economically attractive commercial production) are producing reservoir fluids such as those in the Danish North Sea area.

1.4.4 - Electrical Properties of Reservoir Rocks

Due to the electrical properties of reservoir formation water, electrical well log techniques have become an important tool in the determination of water saturation vs. depth and hence a reliable resource for in-situ hydrocarbon evaluation. Reservoir rocks are comprised of solid grains and void spaces that are occupied by fluids of interest in petroleum technology. The solid particles that make up the reservoir rocks, with the exception of certain clay minerals, are non-conductors. The most significant electrical property of a reservoir rock is the electrical resistivity, which is generally dependent on the geometry of the pore space and the fluids that occupy the pore space, normally gas, oil, and water. Both gas and oil are non-conductors, whilst water can be a conductive fluid if it contains dissolved salts such as NaCl, $MgCl_2$, and KCL normally found in reservoir water. Electrical current is conducted in water by movement of ions termed 'electrolytic conduction'. This factor suggests electrical resistivity generally decreases with increasing porosity and increases with increasing hydrocarbon saturation. As such the resistivity of reservoir rocks saturated with fluids such as gas oil and water can serve as a measure of fluid saturation making it a valuable tool also for evaluating the producibility of a formation.

1.4.5 - Interfacial and Surface Tension

In petroleum engineering literature, interfacial and surface tension are often used interchangeably, and refer to the measure of free energy of a fluid interface. As mentioned earlier up to three fluid phases (gas, oil and water) may coexist, however they are immiscible at the relevant reservoir conditions. These immiscible fluid phases are separated by a well-defined interface when they come in contact, into gas - oil, gas - water, and oil - water pairs. The term 'surface tension' (ST) normally refers to the gas - liquid surface forces, simply because this interface is the liquid surface. However in describing the liquid - liquid interfacial forces in the case of two immiscible liquids the term 'interfacial tension' (IFT) is used, but regardless of the term used, the physical forces that cause the boundary or interface are the same. Interfacial tension is thus an important fluid - fluid interaction parameter that affects the trapping of oil in reservoirs through capillary pressure. Although interfacial tension or surface tension is entirely a

fluid or interface related property and not a petroleum reservoir rock property it significantly influences other important rock properties such as wettability, capillary pressure, and relative permeabilities, all of which in turn affect the production potential of a reservoir rock.

Reservoir conditions include a variety of high pressures and temperatures, which have an effect on the IFT and ST. It is therefore important to understand how IFT and ST variation with temperature influences the transport of fluids in a reservoir and hence the impact of interfacial forces on oil recovery. Surface tension has been shown to decrease with an increase in pressure and temperature. Katz (1995) reported a decline in ST values with an increase in temperature on a number of pure hydrocarbon components. Dandekar (2006) showed a similar trend of declining ST values with increasing temperature for both reservoir brine and a flashed North Sea crude oil. The effect of pressure on ST was also somewhat similar. When considering the gas-liquid ST at high pressures, in most cases, the high-pressure vapour over the surface of the liquid would result in a low ST by bringing a fairly large number of gaseous molecules within reach of the surface. The attractions of these molecules to the surface molecules of the liquid would neutralize, to some extent, and the inward attraction of the surface molecules would diminish the ST. The high pressure of the gas above the liquid is some what analogous to placing a second liquid of rather small attraction for the first, in place of gas. In other words, the high pressure gas phase tends to develop miscibility toward the companion liquid phase thereby reducing ST as pressure increases.

1.4.6 - Wettability

When two immiscible fluids contact a solid surface, one of them tends to spread or adhere to it more than the other. This tendency of surfaces to be preferentially wet by one fluid phase is termed ‘wettability’. The wettability factor of a reservoir rock is a measure of the affinity of its surface to water and or oil. A preferentially water wet reservoir is required for optimum oil recovery, although often reservoir rocks have intermediate wettability (Dandekar, 2006). For example, in a system comprising of oil, water (brine), and rock (sandstone or carbonate), one of the two phases has a tendency to preferentially wet the rock. In addition to the combinations of surface forces that exist

between the fluids, another important force is the force active at the interface between the liquids and the solids. This interactive force is very important in reservoir engineering simply because the petroleum reservoir fluids are continually in contact with the solid (reservoir rock) within a formation until they are produced on the surface.

The wettability of a reservoir rock is a key parameter that affects the petrophysical property of a reservoir rock, such as the distribution saturation and fluid flow in porous media. Also, such surface properties affect the quantity of oil displaced by water, and how the displacement proceeds, because they determine fluid distribution in the pores. This is why it is very important to use test samples that possess the same surface properties as the real reservoir rock in modelling studies. The knowledge of reservoir wettability is essential in determining reservoir rock properties (such as the distribution of gas, oil, and water within reservoir rocks), capillary pressure and relative permeability characteristics, and consequently the production of hydrocarbons (Dandekar, 2006).

Predicting reservoir wettability and its effect on fluid distribution and hydrocarbon recovery remains one of the major challenges in reservoir evaluation and engineering. Hence, an improved analysis of core wettability and or techniques for altering reservoir wettability will enhance oil recovery. Wettability is affected by several factors such as rock surface roughness, rock mineralogy, and the history of the reservoir. Wettability effects are studied by measuring the dynamic contact angles, and the interfacial tension of the mixture. Flow of fluids is generally governed by rock - fluid and fluid - fluid (IFT) interactions of the system. Wettability is generally considered to be one of the principal parameters influencing the distribution, saturation and flow of fluids in porous media. Reservoir rock wettability has long been approached by overall or indirect methods such as capillary pressure or relative permeability curves, contact angle measurements, and fluid displacement techniques.

Wettability has a significant effect on the redistribution of fluids in the pore space as pressures in the oil and water phases alter. At several scales wettability influences capillary pressure - saturation and resistivity - saturation relationships as it controls the distribution of fluids in the pore space. It is experimentally intensive to determine the wettability of reservoir core plug samples. In preferentially water-wet rocks, the brine

occupies the small pores and forms a continuous film on the grain surfaces throughout the desaturation process. In contrast, in an oil-wet rock, brine tends to be located in the centre of the larger pores, with an oil film contacting the grain surfaces. An extensive review of the effects of wettability on petrophysical properties can be found in Cuiec (1990). Sometimes the entire surface of rock has the same wettability, which may be more or less preferential to one of the fluids. More often wettability is considered as heterogeneous, with some parts preferentially water wet and others preferentially oil wet.

1.4.7 - The effects of Heterogeneity

Reservoir rocks are very often highly heterogeneous, with layers of different permeabilities. In some cases reservoirs are 'homogeneously heterogeneous' i.e. may contain a network of high permeability fractures surrounding matrix blocks of low permeability. Reservoir heterogeneities can have very important effects on the displacement of oil by another fluid. For example flow velocity may be greater in a more permeable layer, and in some cases the displacing fluid may reach the producing well through a pathway of high permeability while a large amount of oil remains trapped within a region of lower permeability. A severe extent of heterogeneity in permeabilities is an unfavourable factor for injection/recovery.

1.5 – Enhanced Oil Recovery (EOR)

In this section I will discuss/expand on Enhanced Oil Recovery techniques (EOR) and introduce the relevance of the work undertaken within research to its applications. Due to the rate of diminishing reserves as well as the difficulties and high cost of energy production, researchers are continually seeking ways to improve oil recovery. Enhanced oil recovery (EOR) is a modern approach and is also called 'improved oil recovery', it represents techniques employed for the purpose of increasing the amount of oil that can be extracted from an oil field. Enhanced oil recovery is faced by the question of what leads to non-total recovery. The factors involved in understanding and successfully applying EOR techniques, range from the effect of fluid - solid, and fluid - fluid interactions, and the effects of rock heterogeneity. EOR techniques include the

commonly used gas injection, as well as thermal and chemical injection, where polymers are injected to increase the effectiveness of waterfloods, or the use of surfactants such as Rhamnolipids to help lower the capillary pressure that often prevents oil droplets from moving through a reservoir. This technique can be viewed as a method of altering the wettability of a reservoir rock. Surfactants are wetting agents that lower the surface tension of a liquid, allowing easier spreading, within a reservoir to favour the displacement of oil. It is also similar to other secondary methods of recovery where the reservoir is flushed down with brine to displace oil.

Water flooding is commonly used as an enhanced method of recovery sometimes with "improved water", and thus an understanding of the phenomenon occurring during fluid injection into a porous medium containing reservoir fluids (brine and crude oil) is thus extremely important. Previous researchers have long shown that oil recovery during water flooding depends on numerous parameters, among which pore geometry, fluid distribution, saturation, saturation history, and oil/water viscosity ratio are all inclusive (Anderson, 1987). Following this development, it has become common practise to carry out laboratory experiments of oil displacement by water, using reservoir rocks and reservoir fluids whilst still respecting the initial saturation, temperature and pressure conditions of the reservoir prior to recovery.

For analysing the way in which enhanced oil recovery methods operate two separate aspects of oil recovery efficiency are generally distinguished: the displacement efficiency of oil at the pore scale (for example by using alkaline or surfactant flooding to reduce the interfacial tension or change the rock wettability), and the sweep efficiency at the macroscopic scale (for example by using polymer flooding to increase the water viscosity or by using in-situ combustion or steam drive to decrease the oil viscosity).

Some EOR methods will act mainly on one of these aspects of oil recovery efficiency while other methods act on both. For example in-situ combustion acts on the sweep efficiency at the macroscopic scale by decreasing the oil viscosity and also acts on the displacement efficiency at the pore scale since essentially no residual oil remains behind the combustion front.

Targeted EOR methods have been introduced for dealing with heavy oil reservoirs, due to the extremely viscous nature and complexities involved in exploring such reservoirs. The Improved Oil Recovery (IOR) Research Group at the University of Bath invented the Toe-to-Heel Air Injection (THAI™) technique, which is an advanced EOR process (see Figure 1.3). The technique uses a system where air is injected into the oil deposit down a vertical well and is ignited. The heat generated in the reservoir reduces the viscosity of the heavy oil, allowing it to drain into a second horizontal well from where it rises to the surface (Greaves and Turta, 1997). The work of Greaves and Xia (2006) reported investigations of the down-hole upgrading of virgin Athabasca Tar Sand bitumen in a series of 3-D experiments using (THAI™) and on the details of the first field pilot plant of the (THAI™) process at the Christina Lake, Alberta Canada in 2006. The main area for application of THAI™ is heavy oil and bitumen which is rather complex to deal with, but constitute a large percentage of the largest oil reserves in the world. An even more efficient technique called the CAPRI™ process, which adopts the use of a catalyst add-on process in the reservoir underground following the THAI™ process, has also been invented. In the CAPRI™ technique, thermally cracked oil produced by THAI drains into the horizontal producer well, first passing through the layer of catalyst, like a radial inflow reactor. Thus, THAI™ and CAPRI™ can achieve very significant upgrading (conversion of the heavy oil, transforming it almost into light oil). THAI™/CAPRI™ achieve in-situ upgrading virtually for free, compared to the cost of surface upgrading techniques (approximately £100's millions). The layer of catalyst to be used in CAPRI™ will have to be designed to exacting specifications in terms of pore size and selectivity, in order to achieve the desired performance.

Effective analysis of the transport mechanisms within the pore structure of the reservoir rocks will improve the interpretation of displacement rates and thus help decide the most suitable EOR technique to be applied, and the conditions for optimum recovery. The success of EOR techniques therefore depend heavily on an accurate determination of the influence of pore structure information on fluid transport properties, for example oil recovery parameters such as the irreducible fluid saturation which are fed into EOR modelling of reservoirs.

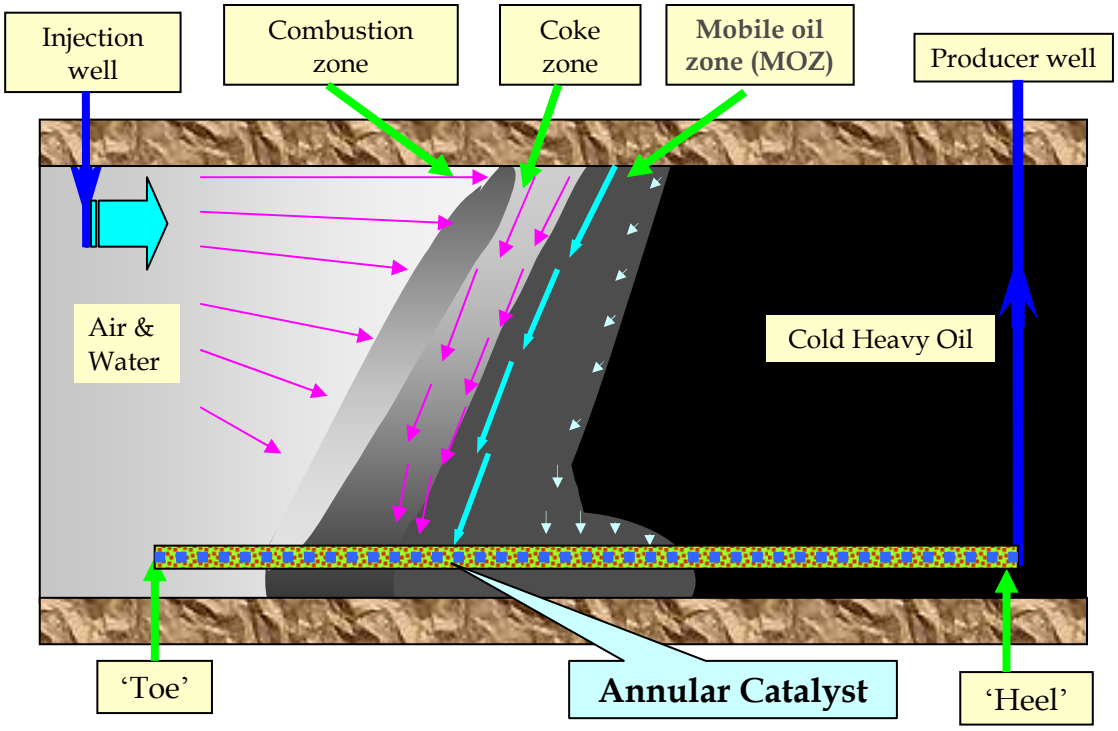

Figure 1.3: Schematic of THAI™ process courtesy Professor M. Greaves, University of Bath.

1.6 - Petroleum Catalysis

In a process known as catalysis, a relatively small amount of foreign material, called a catalyst, augments the rate of a chemical reaction without being consumed in the reaction; hence a catalyst makes a reaction happen. A catalyst can make a reaction go faster and in a more selective manner. Because of its ability to speed up some reactions and not others, a catalyst enables a chemical process to work more efficiently and often with less waste. Understanding the structure and chemistry of the catalyst surface is essential, because that's where the reaction takes place, and because the reaction takes place on the surface, these materials can work efficiently in small amounts.

In addition to catalytic cracking processes long involved in petroleum refining, catalysis is also being employed in down-hole catalytic upgrading techniques (EOR) such as in CAPRI™ (previously discussed) in an attempt to improve recovery efficiency and product quality of the so called unconventional oil sources such as heavy oil and tar sands. Catalysis is thus becoming increasingly vital to oil recovery/production processes. Cracking is the term used in petroleum refining, to describe the process of breaking

down complex organic molecules such as heavy hydrocarbons into simpler molecules (e.g. light hydrocarbons) by breaking the carbon - carbon bonds in the precursors. The rate of cracking and the end products are strongly dependent on the temperature and presence of any catalysts.

This section also presents a general overview of the catalytic processes involved in petroleum technology that are of relevance to the fluid transport studies of porous media proposed to be carried out within this research.

1.6.1 - Petroleum Refining

A petroleum refinery is capable of performing 4 main functions;

a. Separation of crude oil into fractions based on their boiling points e.g. distillation.
b. Conversion of materials within the fractions to saleable products or intermediates.
c. Treatment of fractions or products to meet environmental restrictions e.g. low sulphur gasoline or fuel oil.
d. Blending of converted and treated fractions as well as additives to achieve desired final product specifications.

Conversion and treatment units contain catalysts that speed up the reaction and also provide alternate reaction pathways to a variety of other products that would otherwise be unobtainable. A catalyst can convert one molecule to a different molecule or treat a molecule usually by adding another molecule, to make a “better” frequently environmentally “better” molecule. In most cases of catalyst applications, active sites are situated on or near the surface of a high-surface-area support which spreads out the active sites such that interaction of the sites with incoming molecules is facilitated. The pore structure controls molecular movement to active sites where desired reactions can occur. To achieve optimum control of molecular movement, catalysts are designed to contain pore sizes appropriate to the reactions catalysed, allowing sufficient pore space for molecules to fit in and access active sites, be adsorbed onto, react and subsequently be desorbed. The greater the surface area of a catalyst the better its performance as this

means more molecules can interact with it. The surface area of a catalyst can be measured using the BET technique which measures the amount of gas that adsorbs onto the surface. The sensitivity of a reaction to higher temperatures can also be measured by a quantity called the 'activation energy'; high activation energy means increased effect of temperature. A vast majority of petroleum catalysts contain oxygen, silicon or aluminium. They are usually used as silica SiO_2 and alumina Al_2O_3, typically as the porous high surface area catalysts support. Silica itself is rarely used alone in petroleum catalysts, but, in combination with alumina, it forms the solid acid used as the principal active entity in cracking and hydrocracking. To form the composite catalysts, chemists rely on inorganic chemistry to form alumina/silica sols and gels which control the structure of the highly porous, high surface area support or finished catalyst, which is similar to the technique employed within this research for the synthesis of model porous materials.

1.6.2 - Catalytic Cracking

Also known as Fluid Catalytic Cracking (FCC), it is one of the premier conversion process found in the refinery, nearly 20% of all distilled crude oil is processed in catalytic cracking units, containing tons of catalyst which are dispensed when spent and replaced with fresh ones regularly (Magee and Dolbear, 1998). Eugene Houdry invented catalytic cracking in the 1920s, when he discovered that acid treated natural clays catalysed the conversion of hydrocarbon molecules to smaller ones by lowering the molecular weight of the fraction (Magee and Dolbear, 1998). The active sites of cracking catalysts are solid acids (formed by interactions of silica and alumina), and they initiate the reactions that result in cracking and other side reactions that follow. Catalytic cracking is an endothermic process and as a result the heat required to drive the process comes from the combustion of coke formed in the process. Coke is a necessary product of cracking and leads to 'coking' of the catalyst. A solid black material that is rich in carbon and low in hydrogen forms on the surface and in the pores of the catalyst (coke), blocking active sites and deactivating the catalyst. This coke can be burnt off the catalyst to restore its activity.

Catalytic crackers are run today to maximise olefin yields and gasoline, while minimising coke yield. There are two main kinds of reactions in catalytic reactions namely primary and secondary reactions as discussed by Magee and Dolbear (1998). Primary reactions are those that happen first, while secondary reactions are those in which some primary products undergo further reaction. Cracking is the actual breaking of C - C bonds by reducing the molecular size of the feed molecules to yield paraffin and an olefin. Common primary reactions include:

- Paraffins cracked to give olefins and smaller paraffins
- Olefins cracked to give smaller olefins

Important secondary reactions occur rapidly and include:

- Isomerisation of olefins to iso-olefins. Isomerisation of an ion is the rearrangement of one or more CH_3 groups on a carbon chain to yield a more stable isomerised product and is highly favoured and quite rapid
- Hydrogen transfer between naphthenes and olefins, forming aromatics and paraffins thereby increasing the molecular weight distribution of products; this also leads through aromatic condensation reactions to form coke.

Hydrogen transfer (HT) is a basic reaction that occurs between olefins and paraffins or cycloparaffins (i.e. naphthenes) and yields paraffins and aromatics as products. Since naphthenes are contained in most cracking feeds, all that is needed is an olefin from the primary reactions to initiate a HT. For example, butylene can react with cyclohexane to form butane and benzene. This reaction has used up a valuable light olefin (butylene) to make a light gas and an aromatic whose use in gasoline is now carefully regulated and not particularly desirable. These HT reactions occur readily in Type Y zeolites (synthesised in Na form) catalysts. This is mainly because the two reactants are closely confined in the zeolite structure and this closeness favours the exchange of hydrogen molecules between the two.

The effect of pore size distribution is important to various applications in industry, and a good example is the use of catalysts for refining purposes, say in the desulphurization of

heavy oils containing asphaltenes (fairly large molecules containing metals such as nickel which could damage catalysts) can be achieved easily by restricting access only to smaller harmless molecules through pore size control. Pore size distribution is also relevant in terms of size, location and variation of active sites in relation to the size of reacting molecules. The modification of pore structures of porous materials could be used to achieve desired pore size distribution which could be used to control hydrogen transfer reactions. Lower levels of hydrogen transfer results in lower gasoline yields, as well as low coke yields and high olefin yields from carbon molecules. Undesirable reactions could occur in catalytic cracking and eventually lead to pore-blockages, which could result in slower reaction rates and reduced diffusivity. The effect of pore blockages in pore structure can also be investigated by the use of the synthesised catalyst models designed to possess pore shielding barriers.

1.6.3 - Hydrocracking Catalyst

Hydrocracking is the process of converting gas oils into gasoline, diesel, and jet fuel. It is similar to fluid catalytic cracking but is especially useful for aromatic gas. It operates with an atmosphere of high pressure hydrogen and it consumes large amounts of hydrogen making it an expensive process to run. Hydrocracking produces clean high-quality products that are low in sulphur, olefins and aromatics, and as such the products meet or exceed today's difficult environmental regulations.

Hydrocracking processes are extremely beneficial because the volume of product is 10 - 20 % larger than the volume of feed (Magee and Dolbear, 1998), because, by adding hydrogen to crack large molecules to smaller ones, the liquid density is reduced and thus the volume is increased. Hydrocracking reactions include:

- Addition of hydrogen (H_2) to aromatic centres to convert them to paraffinic structures as they tend to form coke.
- Addition of H_2 to olefin double bonds to convert olefins to paraffins.
- Acid-catalysed cracking of parafins and paraffinic side chains on aromatics into smaller pieces.

- Acid-catalysed isomerisation of parafins and isoparaffins.
- Formation of coke on the surface of catalysts.
- Removal of coke by addition of hydrogen.

The combination of reactions 1 and 3 gives hydrocracking its power, and makes it possible to convert higher boiling aromatic materials without coking. FCC cannot make this kind of conversion as it does not include the addition of hydrogen; it rejects carbon molecules instead, which is essentially the main difference between both processes.

Hydrocracking catalysts are generally solid particles ranging from extrudates to pellets, and their sizes and shapes depend on the balance of effects depending on both the flow of liquids and molecules in confined spaces. Catalyst supports must be strong enough to support the mass of catalyst loaded above, and the spaces between the particles must be sufficiently large to allow free flow of the feed and product liquids downward through the catalyst bed without excessive pressure drop. The inter-particle spaces are roughly the same as the space taken by the particles, and as such the particles must be large enough to allow the needed flow. A balance must be met, as on the other hand, molecules must diffuse through the pores of a catalyst particle to reach active sites with the particle. If the particles are too large only the outer layer of catalyst gets used. One technique used to balance this factor, is to use pore structure manipulation by making grooved cylinders with cross sections similar to cloverleaf pattern. This gives inter-particle volumes big enough to fit large particles, but grooves reduce the distance from the surface to the centre (Magee and Dolbear, 1998).

1.6.4 - Hydrotreating Catalyst

Hydrotreating generally refers to a wide collection of processes (performed as treatment) used in the refinery and in many petrochemical operations. Hydrotreating to remove sulphur is called ‘hydrodesulphurisation’, and to remove hydrogen is hydrogenation. Other names are used as well, relating to what is being treated e.g. gas oil, residuals, naphtha etc. Hydrotreating is used to clean up streams and can be done either to protect the catalysts in other processes or to make more valuable products. For example,

hydrocracker feeds are hydrotreated to remove nitrogen which is a poison for the acid catalysts. Fluid catalytic cracking feeds can also be treated to remove sulphur and nitrogen to increase the hydrogen to carbon ratio for improved cracking reactivity, as well as residual oils to make low sulphur fuel oils.

1.7 - Scope of Work

The work proposed to be undertaken within this research is centred on the nanocasting of silica around hexagonal or cylindrical surfactant structures in order to create mesoporous materials to act as models for reservoir rocks. As reservoir rocks are chemically and geometrically heterogeneous, understanding fluid transport processes occurring in them is difficult. These types of models will allow for the study of the effect of one type of heterogeneity at one time and hence reduce complications. This work reports on various nanosynthesis techniques based on surfactant templating for creating ordered mesoporous materials following the development of synthesis routes for producing designer-structured porous materials such as the MCM-41 type materials. The synthesis techniques of such materials had already been investigated intensively by several researchers in the chemical industry (Kresge *et al.*, 1992; Beck *et al.*, 1991, 1992; Bhatia *et al.*, 2001). Due to their controlled pore size distributions, these ordered mesoporous materials also have significant potential as catalyst supports and also offer the possibility of precision manipulation of transport rates within pore structures.

Several researchers in the field of nanosynthesis have identified a gap in the range of stable ordered mesoporous materials available (Feng *et al.*, 2000). Most of the early synthesis work in literature has produced materials of relatively small pore sizes, smaller than those required for the passage of large molecules in catalytic processes, and also shown less success in creating heterogeneous samples. In order to expand upon the range of highly ordered and/or controlled pore size materials a variety of different synthesis methods have been developed. Silica sources have been polymerised around a range of different templates such as organic liquid crystals (Kresge *et al.*, 1992) and triblock copolymers (Zhao *et al.*, 1998). More recent work has moved onto the synthesis of bi-modal and hierarchical materials. Van der Voort *et al.* (2002) carried out with some success an approach of filling larger mesopores with microporous materials.

In contrast, the work described here, will be exploring options of synthesizing ordered mesoporous materials of much bigger pores (~10 nm and above) and more complex nature than previously reported, in order to model structural complexity in rocks. This research also involves a different approach of coating particles in order to create dual-structured particles with two well defined regions and porosity, hence possessing two different ranges of pore sizes and/or geometries. The new coating technique adopted, creates bimodal mesoporous silica pellets where one type of template was used to synthesis the pellet core zone and a different type for the outer surrounding shell zone. Surfactants such as:

- Cetyltrimethylammonium bromide (CTAB)
- Polyoxyethylene-10-steryl-ether (Brij 57)
- Polyoxyethylene-10-cethyl-ether (Brij 56) with hydrophobic/hydrophilic regions
- The well investigated tri block co-polymers: Pluronic F127 ($EO_{106}PO_{70}EO_{106}$), and Pluronic P123 ($EO_{20}PO_{70}EO_{20}$)

were used to create homogeneous structures (core materials) as well as the heterogeneous bi-modal structures of silica in the mesoporous range. The resulting highly ordered porous silica structures have undergone a series of modification in the method of synthesis, which have led to varying structures, pore sizes, and surface chemistries. These designer structured materials could improve the understanding of the effect of desorption hysteresis in gas adsorption, and the pore blocking effect can be investigated in more detail than previously done, as such model materials will help eliminate some variables for a more independent study of such pore mechanisms. The characterisation of the synthesised model porous solids by N_2 adsorption, and SEM techniques in order to validate the structure, surface chemistry and transport properties of the synthesised materials is also within the scope of this research. Pore structure information such as surface area measurements, pore bodies and pore neck sizes, and other general sorption characteristics can then be used to confirm the existence of precisely engineered diffusion barriers in these engineered materials. Their diffusion coefficients will also be assessed using gas adsorption techniques. Investigations into the occurrence of gas adsorption hysteresis in ordered mesoporous materials will also be carried out, and it is hoped that the level of pore connections will be high enough for the

designed core materials, and hence result in little or no structural hysteresis (based on pore connections). However as most mesoporous adsorbents are reported to possess complex networks of different sizes, and in addition the condensation/evaporation process is unlikely to occur independently in each pore, some hysteresis will be expected. A more apparent hysteresis is expected for the bimodal samples, as the homogeneity of the structures is compromised by the addition of a distinctive region of varying pore sizes. Another set of highly ordered porous materials made from the same tri-block co-polymers, and hence with similar pore sizes but different silica source were also synthesised. This will make it possible to investigate the effect of differing surface chemistry (which leads to a different product affinity for fluids), on the adsorptive properties of the designed materials. An attempt is also made to produce larger pore sized silica solids with pore sizes more similar to real reservoir rocks, by templating on polystyrene beads (PS) of ~ 100μm.

Ultimately, these synthesised silica materials mimic the pore structure of real reservoir rocks and hence could serve as artificial model rocks for the purpose of this study. Obviously pore interconnections within such porous materials would heavily influence transport properties. As the pore structure of such materials could potentially be manipulated, hence the term designer structures, this will provide additional information towards a better understanding of the mechanisms that affect the transport of non-wetting fluids and potentially lead to oil entrapment. The synthesized materials were built of silica, and hence possess the same chemical component as sandstone reservoir rocks, ensuring a direct comparison with these materials could be made in terms of surface chemistries and wettability effects. Sandstones are the most common type of reservoir rocks, and its main component is quartz (SiO_2), which is a fairly stable mineral, which is not easily altered by changes in pressure, temperature, or acidity of pore fluids, and thus makes it a safer and more straight-forward choice to replicate sandstone reservoir rock through nanocasting techniques. The entrapment of oil in strongly water wet reservoirs by analogy is similar to the displacement by air and subsequent entrapment of mercury as a non-wetting fluid following porosimetry analysis on the silica synthesized materials. This entrapment factor therefore translates to the BVI, which quantifies the irreducible hydrocarbon saturation. The fundamentals of how non-wetting fluids behave is consistent, and hence validates the use of the mercury analogy

to model oil displacement by brine. Therefore mercury intrusion and extrusion can stipulate the transport mechanism of hydrocarbons in reservoir rocks.

The concept of creating heterogeneous structures by nanocasting techniques from a combination of several homogeneous surfactant templated structures to model reservoir rock properties has not been approached prior to this research project, and will be used to test and provide better understanding of the transport properties that govern the entrapment of non-wetting fluids. Real sandstones have geometric and chemical heterogeneity because of the existing strong van der Waals forces, and hence could be quite complicated to model. As a result the steps towards better understanding the transport behaviour and the entrapment of non-wetting fluids in porous media adopted within this research begins by developing a simpler model of controlled geometry and chemistry to test out the already existing theories of gas uptake/diffusivity and entrapment prior to progressing to more complex models. The nanocasting techniques employed within this research are therefore used to create materials of uniform chemistry and simple geometry and then a progression to a type of heterogeneous solid of two differing regions of controlled geometry but same surface chemistry (bi-modals) will be used as model reservoir rocks. Future work could look at more complex combinations/geometries. The nanocasting technique employed within this research could also be applied to synthesize structured mesoporous and macroporous materials using a carbon source, which will enable similar comparisons to be made to carbonate reservoir rocks.

The technique of mercury porosimetry is carried out within this research to investigate how mercury injection, withdrawal and entrapment are affected by the pore structure and connectivity, and in particular, the mechanisms controlling non-wetting phase entrapment during pressure reduction. The porosimetric study of the silica materials will provide invaluable addition towards researching and implementing successful EOR techniques on sandstone reservoirs. Technologists are continually dealing with issues surrounding characterising porous solids effectively and predicting transport properties of reservoir samples. Previous studies have looked at ways of improving pore characterization techniques by using 3D computer simulations such as the simulation studies of self-diffusion of point-like and finite-size tracers in stochastically

reconstructed Vycor porous glasses (Kainourgiakis *et al.*, 1999) or even experimental studies of macroporous cut glass micromodels (Wardlaw and McKellar, 1981).

The work presented in this thesis thus takes an approach that addresses some of the problems and cases of inaccurate pore structure representation by models that fail to account for certain behavioural patterns of fluid transport in such porous media. This report aims to show that the effective structural characterisation and analysis of these materials can improve the understanding of the behaviour of several porous media, in relation to invasion, retraction and recovery processes. It uses a combination of pore probing techniques to infer the pore structure of test samples which consist of synthesized well ordered porous materials and commercial catalysts supports before modelling their transport properties. Comparisons to analysis methods of transport behaviours for more complex models will be taken into consideration in the future-work. The ultimate goal of this research is to address issues surrounding ineffective porous media characterization by better understanding characterization techniques using simple non-complex systems which are well understood in terms of pore structure parameters to develop a more realistic model, which can be used to better infer the pore structure of porous materials. It hopes to achieve this through running mercury porosimetry studies of model systems that are purer, and more controlled than real reservoir rocks and by studying gas adsorption kinetics in controlled materials (to investigate existing adsorption theories) as well as the designer structured bi-modal materials to investigate the effects of diffusion barriers on transport properties of condensable vapours. The use of mercury intrusion and extrusion data within this research to investigate fluid transport in porous silica materials serves two purposes, firstly its relevance in terms of application and data interpretation to the petroleum industry as a pore characterization technique and secondly as a model capable of mimicking the process of oil - brine displacement in reservoirs and the subsequent entrapment of the non-wetting phase (irreducible fluid saturation). Integrating the results of gas adsorption and the use of the air and mercury analogy through mercury porosimetry studies will lead to more accurate modelling of fluid displacement and entrapment parameters as well as the factors controlling capillary condensation within the pores of the reservoir rocks during fluid injection in EOR processes such as water flooding.

The synthesised model porous materials also have significant potential as catalyst supports, and could therefore also be used as models for understanding fluid transport and reaction mechanisms in catalysts pellets used in petroleum catalytic processes. Catalytic cracking processes are usually accompanied by side reactions leading to carbonaceous deposits on the catalyst (coke) leading to deactivation through pore blockages within the pore structure. Investigations into the effects of coke deposition on the activity and selectivity of catalysts in different reactions is important to modelling transport properties and reaction rates in catalytic processes, and can be achieved through understanding of how catalysts operate and how their pore structure changes with coking and its subsequent effects on the behaviour/fluid transport rates in chemical reactions and separation processes. Down-hole catalytic upgrading techniques using gasification and thermal cracking techniques such as THAI^{TM}/CAPRI which are aimed at improving oil recovery also employ the use of catalyst supports for cracking of large hydrocarbons, or separation of reactants and products or bi-products. So therefore these models developed within this research are also applicable in investigating the transport rates of molecules in and out of the catalysts beds for the above applications. Fluid transport phenomena in porous media is a controlling factor in the oil recovery process, as well as in the use of catalysts for separation and in heterogeneous catalytic processes involved in petroleum refining and EOR processes. They all involve the displacement of one fluid by another, which is affected by the properties of the porous media such as interconnectivity or the solid - fluid interaction forces such as wettability. A better understanding of fluid displacement within such porous materials obtainable through a better understanding of pore probing techniques could improve upon the information derived from relative permeability tests (which are used to measure the conductivity of a fluid), and hence could lead to catalyst designs that achieve a more effective separation/upgrading process. Gas adsorption analysis within such porous media undertaken within this research also offer an alternative technique of observing the displacement of condensed vapour by gas during the desorption process and as such could provide additional understanding of the related mechanisms in heterogeneous catalytic processes. Gas is also generated in reservoirs through upgrading processes, or injection through EOR techniques in addition to the already existing gas originally in the reservoir, hence gas transport phenomena is an intrinsic part of hydrocarbon recovery processes. Such additional information could also improve the understanding of some of the most common catalyst related issues such as coking and flow problems

and lead to better/more effective catalysts and catalyst supports designs. The bimodal synthesised materials could also be used to investigate the application of different environments for pore-structure-sensitive reactions in different parts of a catalyst pellet. Gas permeation studies on these engineered materials are also used to assess the variation in transport properties through gas diffusivity measures with pore structure and surface chemistry. A comparative study of the materials with same geometry but differing surface chemistry could also be used to assess the effect of wettability on transport rates.

Catalyst development and effective characterisation is crucial to the advancement of advanced EOR processes such as THAI^{TM}/CAPRI^{TM}. Studies within this research aim to provide a better understanding of the mechanisms occurring within mesoporous materials of diverse functionalities for use in such processes. Effective porous media characterisation of the catalyst bed would be of relevance to both the assessment of fluid flow parameters and the effects of active sites with regards to the conversion reaction processes. The synthesised materials are also perfect models for such catalysts supports and hence a more improved understanding of the effect of pore topology on catalyst performance through the cause of this research could be the beginning of the steps to improve the efficiency of processes to achieve desired products, as well as to provide insights into the mechanisms occurring within the pore structure of a catalyst during chemical reactions that eventually lead to coking (pore blockages). Down-hole catalytic upgrading techniques have the potential to increase AP1 by 8 degrees thereby producing higher quality hydrocarbons (light oil). To achieve equivalent oil conversion in a surface upgrading plant would cost £100's millions. The technique of down-hole cracking is an effective means of EOR and recovers around 70 – 80 % of original oil thereby reducing BVI which translates to huge economic benefits.

1.8 - Description of Thesis Chapters

The overall description of this project including its significance can therefore be divided into seven main chapters. The first chapter is the introduction chapter, which discusses the literature review leading to this research, and the implications of research subject to both catalysis and oil recovery

The second chapter discusses the adsorption theory and its application in porous media characterisation including the assessment of pore size distribution (PSD) analysis. It also consists of a description of adsorption forces, methods of adsorption isotherm measurements as well as a description of the various types of isotherms observed in gas adsorption. The region of irreversibility in the gas adsorption isotherm known as hysteresis is also discussed along with the causes/theories in literature explaining this phenomenon.

Thirdly, is the synthesis chapter which includes a review of a range of nanosynthesis techniques for creating silica based structured porous media of both homogeneous and heterogeneous nature which then serve as models for reservoir rocks. This chapter is structured to contain both the methodology of synthesis and the characterization of the silica pellets.

The fourth chapter involves the use of gas permeation data to characterise the transport properties of mainly the synthesised materials and also the commercial C10 silica pellets with a more heterogeneous structure in comparison to the core materials synthesised. The results of gas permeation for the molecules adsorbed onto the porous media can be very useful for gas field's three phase (water/oil/gas) systems. This chapter also investigates the adsorption mechanisms that may exist pertaining to varying adsorbate - adsorbant combinations and the effects of surface chemistries, roughness, initial saturation levels and test sample preparation techniques relating to pre-depositional state. Mass transfer coefficients are measured for the range of test materials and a diffusivity factor is obtained. The transport properties of the different bulk materials is estimated, and also investigated at each stage of the adsorption step (defined by pressure increases) with particular emphasis on the region of capillary condensation and any reflections of the pore blocking phenomenon.

The fifth chapter includes an assessment of various adsorption phenomena including advanced and delayed adsorption as well as the effect of the heat of adsorption and the net enthalpy which may lead to misinterpretation of adsorption analysis results if not well accounted for. A better understanding of these phenomena will lead to more accurate estimates of pore measurements. This section also discusses the concept of 'fractals' which is a measure of the surface roughness of a porous material, which may offer a method by which complex porous materials may be characterised.

The sixth chapter explores mercury porosimetry as a technique for characterising pore structure, and introduces it as especially useful in studying intrusion, retraction processes and the entrapment of the non-wetting phase (nwp) when used alongside nitrogen adsorption in a technique known as 'The Integrated Nitrogen Adsorption and Mercury Porosimetry' which provides additional information to that obtained when both techniques are used separately. The integrated nitrogen sorption and mercury porosimetry experiments will be used to determine the mechanism(s) of the entrapment of the nwp within the amorphous porous solids. This chapter also includes the mercury porosimetry studies of commercial porous solids and the synthesised materials; examining the causes of non-wetting phase entrapment and the mechanical stability of the synthesised materials at the high pressures exerted during testing. In a mercury experiment, a plot of the decrease of mercury in the capillary in relation to the pressure produces a porosimetric curve, which indicates how large a volume penetrated into the pores of the sample at a given time. These curves are useful in interpreting pore geometry and give information which is valuable in assessing multiphase fluid behaviour in oil and gas systems and especially in a strongly water wet system. The trapping of oil or gas is controlled mainly by capillary forces and as aforementioned a direct analogy with the air-mercury system is possible. After making the appropriate corrections for wettability, these results can be related to the oil and brine system in real reservoirs. A significant feature of mercury porosimetry curves is the occurrence of hysteresis between the intrusion and extrusion branches. In addition, entrapment is observed, i.e., mercury remains contained in the porous network after extrusion. These phenomena are investigated, as a detailed understanding is essential in obtaining a more accurate mesopore size analysis. From the results of these experiments, it is envisaged that the relationship between various structural parameters, such as pore connectivity, and the nwp entrapment can be assessed. The intrusion and extrusion curve patterns are

analysed to assess the flow regime and controlling factors in the retraction curve, and entrapment patterns for mesoporous silica pellets.

The seventh chapter summarises the main conclusions and future recommendations of this research.

Chapter 2: Pore Characterisation and Distribution Analysis

2.1 – Introduction

The quantitative evaluation of the pore structure of porous solids is a crucial aspect of the processes involved in the design and application of these materials as models for adsorption and catalysis. It is also of major interest in industrial processes such as oil recovery. The transport and reaction properties of porous solids are determined by both their pore morphology and the connectivity of the pore network. The use of gas adsorption to probe porous media is the key technique for obtaining pore size and pore structure information. This has long been recognized in such diverse fields as catalysis, soil science and building technology, and hence will be the focus of the pore distribution analysis reviewed within this work. A key issue is to understand how the geometric and interfacial confinement of the pore structure affects numerous phenomena such as the effective diffusivity of molecules, reaction kinetics and the adsorption and capillary condensation. The main areas of interest in understanding porous structures are porosity (pore volume divided by total sample volume), average pore size, pore to throat size ratio, pore shape structural correlation within the solid, and the pore network and connectivity. All these features indicate the need for a more accurate statistical analysis of the pore structure of porous media.

This section discusses the theoretical aspects of adsorption and it consists of a description of adsorption forces, methods of adsorption isotherm measurements as well as a description of the various types of isotherms observed in gas adsorption. According to Sing *et al.* (1985), gas adsorption appears to be the most suitable pore characterisation technique as it provides information both of the pore size distribution as well as the surface characteristics of the materials.

2.2 - Theory of Adsorption

Adsorption occurs whenever a solid surface is immersed in or exposed to liquid or gas. Adsorption can be defined as the enrichment of a material, or increase in density of the fluid in the vicinity of an interface (Rouquerol *et al.*, 1999). Adsorption techniques are used to characterize the surface properties and texture of particles such as powders, pigments and porous materials like clays and membranes. Gas adsorption has become one of the most widely used techniques for determining the surface area and pore size distribution of porous materials. Nitrogen adsorption analysis is adopted for the characterisation of a range of microporous to mesoporous materials synthesized during the course of this research. It is hoped that this will provide the necessary key descriptors, to enable the use of these materials as model porous media with known void space, geometry and relatively chemically homogeneous surfaces for the study of the behaviour of non-wetting phases in porous media.

Chappuis (1881) and Kayser (1881) made the first attempts to relate the amount of gas adsorbed to the pressure required, and they introduced the term adsorption, and then followed by the terms isotherm and isothermal curve, which were applied to the results of adsorption measurements made at constant temperature (Masel, 1996). The development of the BJH and BET methods of obtaining pore size distributions and surface area respectively marks a major advancement in the characterization of porous solids. These techniques are applied within this research, as well as the Horvath Kawazoe method which is a more suited analysis for the existence of micropores within the mesoporous structure of test samples or purely microporous samples. Brunauer *et al.* (1938) published the BET theory, which is now established as a standard technique for determining the surface area of a wide range of porous materials. They used low temperature adsorption of nitrogen to determine the surface area of an iron synthetic ammonia catalyst. The resulting isotherms for N_2 and a number of gases measured at temperatures near or at their boiling points were s-shaped, with certain differing features. They recognized that gas adsorption was not always restricted to monolayer coverage and hence adopted an empirical approach to ascertain the stage at which multilayer adsorption starts. Brunauer *et al.* (1938) characterized the completion of the monolayer by the beginning of the middle nearly linear section of the adsorption isotherm prior to

the point labelled B (capillary condensation region) in Figure 2.1, thus point C is the beginning of multilayer adsorption.

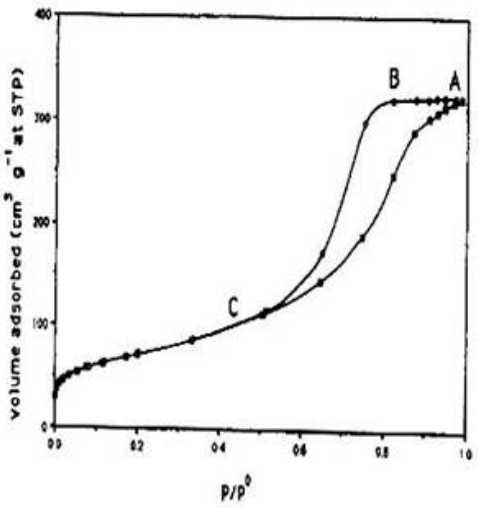

Figure 2.1: Shows a typical isotherm for a mesoporous material used to explain hysteresis in the capillary condensation region (Rouquerol *et al*., 1999)

Figure 2.1 shows that the "cut off point" for the formation of hysteresis loops occurs at a relative pressure (P/P^0) of approximately 0.4, this is due to the fact that the limit of stability of the nitrogen is exceeded past this point, and hence the system will become thermodynamically unstable (Rouquerol *et al.*, 1999).The surface area was then calculated from the amount adsorbed at point B assuming that the completed monolayer was in a closed- packed state.

In adsorption one of these phases must be a solid and the other a fluid. The process may be accompanied by absorption, which is the penetration of the fluid into the solid phase, and followed by its retraction. Adsorption (penetration) and desorption (retraction), are used to indicate the direction from which the equilibrium states have been approached. Adsorption hysteresis arises, when the amount adsorbed is not brought to the same level by desorption after adsorption at a given equilibrium pressure or bulk concentration. The relationship that exists at constant temperature, between the amounts adsorbed and the equilibrium pressure, or the concentration, is popularly known as the adsorption isotherm.

Two types of adsorption have been identified: namely physisorption which is physical adsorption in which the van der Waals interactions are involved and chemisorption which is chemical adsorption, where the adsorbed molecules are attached by chemical bonding. Langmuir (1916) concluded that equations derived for plane surfaces were not applicable to adsorption by highly porous adsorbents such as charcoal. This led Dubinin *et al.* (1960), to put forward additional evidence to show that the mechanism of physisorption in very narrow pores is not the same as that in wider pores. By experimenting on a wide range of activated carbons, Dubinin *et al.* (1960) identified three groups of pores of different width: micropores, transitional pores (also known as mesopores), and macropores. IUPAC now defines microporous, mesoporous and macroporous regions as shown in Table 2.1 (Gregg and Sing, 1982).

Table 2.1: Classification of pores according to their width

Classification	**Pore Width**
Micropores	Less than 2 nm
Mesopores	Between 2 and 50 nm
Macropores	More than 50 nm

The amount of gas adsorbed by a solid is dependent on the equilibrium pressure, the temperature and the nature of the adsorbate - adsorbent interaction. For a given gas adsorbed onto a particular solid at a constant temperature:

$$\frac{n^a}{m^s} = f(p)_T \qquad \textbf{(2. 1)}$$

Where n^a = Amount of gas adsorbed

m^s = The mass of a solid

p = Equilibrium pressure

T = temperature

if the gas is below its critical temperature, it is possible to rewrite Equation 2.1 as Equation 2.2.

$$\frac{n^a}{m^s} = f\left(\frac{p}{p^0}\right)_T \qquad \textbf{(2. 2)}$$

Where, the standard pressure p^0 is equal to the saturation pressure of the adsorptive at temperature *T*. Both Equations (2.1) and (2.2) represent the relationship between the amount adsorbed by a unit mass of solid and the equilibrium pressure (or relative pressure), at a known temperature.

2.3 - Methods for Measuring Uptake

The available methods of measuring the amount of gas absorbed can be divided into two groups.

1. Those that depend on the amount of gas removed from the phase are called volumetric methods.
2. Those, which measure the uptake of gas by adsorbent for example, direct determination of increase in mass, are called gravimetric methods.

In practice, static or dynamic techniques may be used to determine the amount of gas adsorbed. In the static volumetric technique, a known quantity of pure gas is usually admitted into a confined volume containing the adsorbent, maintained at constant temperature. As adsorption takes place, the pressure in the confined volume falls until equilibrium is established. The amount of gas adsorbed at the equilibrium pressure is given as the difference between the amount of gas admitted and the amount of gas required to fill the space around the adsorbent, that is, the dead space at the equilibrium pressure. The adsorption isotherm is usually constructed point after point by the admission to the adsorbent of successive charges of gas with the aid of a volumetric

dosing technique and application of the gas laws. The volume of dead space must be known accurately, and it is obtained either by pre-calibration of the confined volume and subtracting the volume of the adsorbent (calculated from its density), or by the admission of a gas which is adsorbed to a negligible extent.

2.4 - Types of Adsorption Isotherms

Adsorption isotherms measured on a range of gas - solid systems have a variety of forms, and the majority of them can be grouped into one of six types according to the IUPAC classification 1985 with the majority resulting from physisorption. Figure 2.2 shows the six types of isotherms, which only hold for the adsorption of a single component gas within its condensable range, and are very useful for the study of porous materials (Rouquerol *et al.*, 1999).

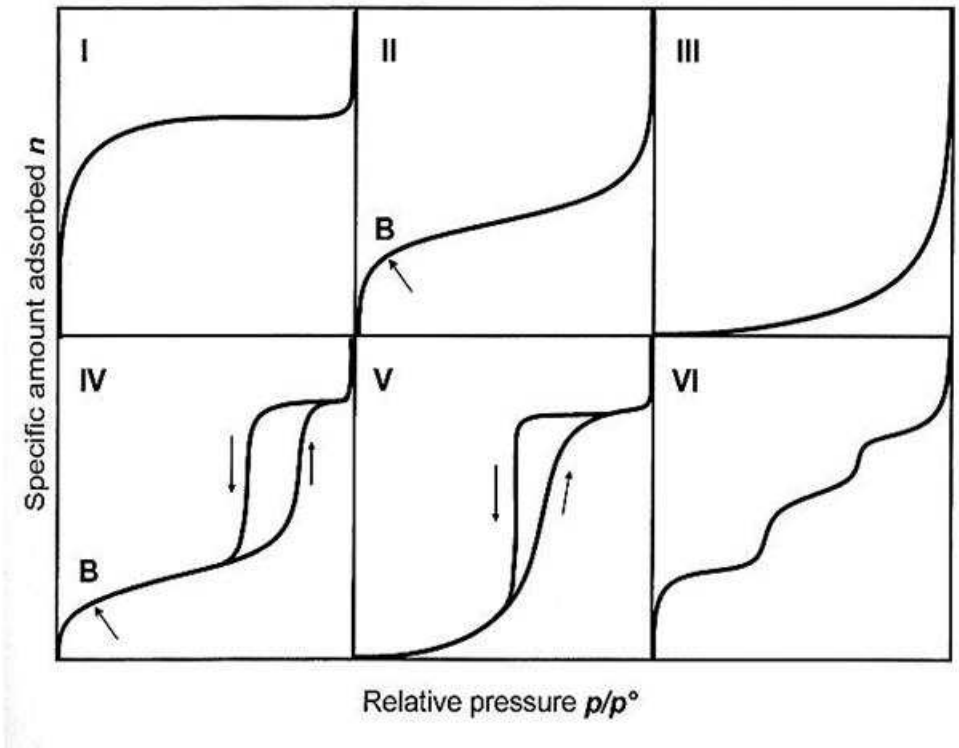

Figure 2.2: The six main types of isotherms, according to the IUPAC classification by Rouquerol *et al.* (1999)

2.4.1 - Type 1

This isotherm is characterised by its concave shape to the relative pressure (P/P^0) axis. The curve rises sharply at low relative pressures until it reaches a plateau after which the amount of fluid adsorbed by a unit mass of solid (n^a/m^s) approaches a limiting value as P/P^0 goes to 1. Strong adsorbate – adsorbent interactions occur in micropores of molecular dimensions, hence a decrease in pore width below 2 nm will lead to an increase in adsorption energy as well as a decrease in the relative pressure at which micropore filling occurs. According to Rouquerol *et al.* (1999), the narrow range of relative pressure necessary to attain the plateau in Type 1, signifies the existence of a limited range of pore size. The appearance of a nearly horizontal plateau is an indication of a very small horizontal pore surface area in terms of pore width and this is typical of microporous solids.

2.4.2 - Type II

The Type II isotherm is also concave to the P/P^0 axis initially, then almost linear and finally convex to the P/P^0 axis. The Type II isotherm is an indication of the formation of an adsorbed layer, whose thickness increases progressively with increasing relative pressure as P/P^0 approaches 1. If the knee of the isotherm is sharp, the point labelled B in Figure 2.1 signifies the completion of a monolayer and the onset of multilayer adsorption. This point yields an estimate of the amount of adsorbate required to cover the unit mass of solid surface to a monolayer capacity. Complete reversibility of the sorption isotherm must be met for normal monolayer- multilayer adsorption on an open and stable adsorbent. The Type II isotherm is associated with non-porous and macroporous adsorbents which permits monolayer – multi-layer adsorption at high values of relative pressure (P/P^0).

2.4.3 - Type III

This is convex to the relative pressure axis, over the whole range, and as such, has no knee. According to Rouquerol *et al.* (1999), this is characteristic of weak adsorbent - adsorbate interactions, and more so, true Type III isotherms are not common.

2.4.4 - Type IV

This isotherm exhibits a similar concave shape to the P/P^0 axis as Type II but differs in that it levels off at high relative pressures. The main characteristic of this isotherm is its incomplete reversibility. This forms what is known as a hysteresis loop which varies from one system to another. Hysteresis loops in Type IV isotherms are associated with capillary condensation, which governs the filling and emptying of pores. The standard IUPAC classification identifies four types of hysteresis loops namely H1, H2, H3 and H4.

2.4.4.1 - Types of Type IV Isotherms

de Boer (1968) classified hysteresis curves into five types of loops, A, B and E being the most representative. A loop of Type A is delimited by two very steep (almost vertical) and nearly parallel sorption boundary curves. In Type B loops (H3), the ascending and descending boundary curves are sloping and usually the desorption branch also includes a steep region at which the remaining condensate comes out almost suddenly out of the pores as a consequence of the so-called tensile strength effect (Everett, 1967). Type B loops can be linked to slit-shaped pores with the ascending boundary curve of the isotherm following a trajectory similar to that obtained with non-porous adsorbents, and without converging to any limiting adsorption value. The E Type loops show a sloping adsorption branch as capillary condensation takes place, and in contrast to this pattern the desorption branch depicts a nearly vertical zone where vapour percolation takes place, thus leading to a sudden condensate emptying of the porous structure. The E Type loop has been traditionally ascribed to a collection of inkbottle type pores, however this may well be an oversimplification since network effects that usually occur in a wide variety of adsorbents, can produce the same result

(Sing *et al.*, 1985). According to Broekhoff and van Dongen (1970) diverse pore shapes or pore arrangements (random vs. non-random) may lead to the same type of hysteresis loop. For instance the A Type loop could be a result of either condensation in independent capillaries within a narrow size distribution or by globular solids made of spherical particles of about the same diameter. The more widely accepted IUPAC classification of Type IV isotherm; includes four categories denoted H1 (former Type A), H2 (former Type E), H3 (former Type B), and H4 as shown in Figure 2.3. These were reviewed by Seaton (1991) and they proposed that for the H1 isotherm the formation of the hysteresis loop is governed by delayed condensation of nitrogen in the pores, whereas the H2 isotherm is dependent on network percolation effects. The H3 and H4 are less common, and the reversibility depends on the adsorptive and operational temperature and parameters. A substantial amount of evidence is now available to suggest that condensation of gasses in cylindrical pores does not always occur clearly in accordance with the Kelvin equation, and that delayed meniscus formation is the cause of these anomalies and a significant contributor to the formation of H3 Type hysteresis loops (Foster, 1932).

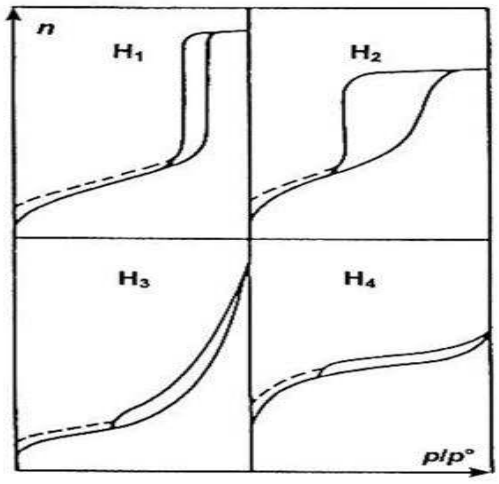

Figure 2.3: The Types of Type IV isotherms by Rouquerol *et al.* (1999)

2.4.5 - Type V

The Type V isotherm is convex to the P/P^0 axis in a similar manner to the Type III, and is also formed due to weak adsorbent – adsorbate interactions. The main characteristic difference is that the Type V isotherm exhibits a hysteresis loop which is due to the mechanism of pore filling and emptying by capillary condensation.

2.4.6 - Type VI

This has been more recently observed, and is termed the stepped isotherm. This is obtained from a layer by layer adsorption on a highly uniform surface.

2.5 - Assessment of Mesoporosity

This section discusses the use of adsorption measurements for the characterisation of mesoporous solids. The properties of mesoporous adsorption as well as the critical evaluation of the mathematical models that are used to interpret the analysis of mesoporous samples, is key in understanding how accurate and reliable the data obtained is.

In the case of mesopores, the Kelvin equation (Equation 2.3) provides a useful model for the transformation of adsorption data into a PSD (Rouquerol *et al.*, 1999; Bhatia *et al.*, 2001). This model is usually employed, but is limited to diameters greater than 2 nm, because below this size the liquid cannot be considered a fluid with bulk properties due to forces exerted by the pore wall. Theoretical calculations suggest that the properties of fluids in microporous structures are highly sensitive to the size of the pores (Rouquerol *et al.*, 1999). The established methods for the determination of the pore sizes are based on the Kelvin model or its variance such as the Barrett Joyner and Halenda (BJH) method (Barrett *et al.*, 1951) or other approaches that consider the fluid-solid interactions such as the Horvath Kawazoe (HK) method (Horvath Kawazoe, 1983). The BJH method is undoubtedly the most widely accepted method for the analysis of nitrogen adsorption/desorption PSD (Rouquerol *et al.*, 1999).

The Accelerated Surface Area Porosimeter (ASAP) cannot control pressure for P/P^0 > ~0.98, and hence the nitrogen adsorption technique cannot be used for characterising macropores (> 50 nm). The derived Kelvin equation is:

$$\frac{p}{p^0} = \exp\left[\frac{-2\gamma v_1}{RTr_c}\right] \qquad (\mathbf{2.3})$$

where, p^0 = Saturated vapour Pressure at given temperature T

γ = Liquid vapour surface tension

v_1 = Liquid molar volume

R = Universal Gas constant

r_c = Radius of curvature

Most methods of assessment are based on the application of the Kelvin equation and the concept of capillary condensation. Most computational analysis of adsorption data starts from the assumption that the pores are rigid and of well-defined shape, either regular cylinders or parallel sided slits. However, there are relatively few real adsorbents which conform to either (Rouquerol *et al.*, 1991). The underlying principles of mesopore filling are not fully understood and especially the significance of the validity of the lower limit of the Kelvin equation. However for Type IV isotherms, which are often obtained for mesoporous silicas, at relatively low pressures say P/P^0 < 0.3 a monolayer surface coverage occurs, and at higher pressures the adsorption in mesopores leads to multilayer formation, until condensation occurs leading to a sharp increase in the uptake curve. As the mesopores are filled, the adsorption continues on the external surface. The isotherms are usually reversible for pores smaller than a critical size and exhibit a sharp inflection at medium pore filling factors ranging from relative pressures of ~ 0.25 – 0.5 depending on the pore size of the material.

Nitrogen adsorption has been accepted as a standard method for mesopore size analysis and the Kelvin equation is generally applied to its sorption data to interpret pore structure information. The range of materials synthesised within this research are therefore modelled as an assembly of cylindrical mesopores, in which all of the pores have an identical radius (r_p). Rouquerol *et al.* (1999) applied the Kelvin equation

(Equation 2.3) to the following diagrammatical model as described in Figure 2.4. The radius r_p in the ideal and simplified situation of strict thermodynamic reversibility will be expected to have a vertical riser effect of pore filling in accordance with the above derived Kelvin equation (Rouquerol *et al.*, 1999).

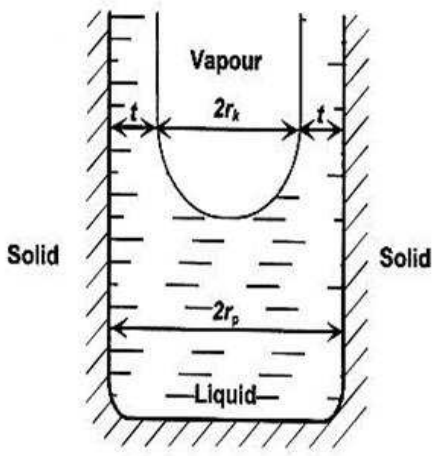

Figure 2.4: The relationship between the Kelvin radius and the pore radius (r_p) in a cylindrical mesopore (Rouquerol *et al.*, 1999).

The work of Lastoskie *et al.* (1993) reports that the Kelvin equation (Equation 2.3) probably underestimates pore size, and that its reliability may not extend below a pore size of ~ 7.5 nm, (10 nm has also be quoted in Rouquerol *et al.* (1999)). For a cylindrical pore shape, it seems reasonable to assume that the condensate has a meniscus of hemi-spherical form and radius r_k, however as some physisorption has already occurred on the mesopore walls, it is evident that r_k and r_p are not equal. If the thickness of the adsorbed multilayer is t, and has a finite contact angle, which is assumed to be zero, the radius of the cylindrical pore is simply:

$$r_p = r_k \cos\theta + t \qquad \textbf{(2. 4)}$$

and then

$$r_p = r_k + t \qquad \textbf{(2. 5)}$$

The initial intraparticle condensation is reversible, but as the advancing menisci meet the narrow openings between the particles, they are then randomly filled. The third stage involves the filling of the larger voids within the particles. In the initial stage of condensation a saddle shaped meniscus is developed, and the application of the Kelvin equation requires the designation of two radii of curvature of opposite sign, one being the concave radius and the other being convex. This results in a modification as follows:

$$\ln \frac{p}{p^0} = \frac{\gamma V_1}{RT}\left[\frac{1}{r_1} - \frac{1}{r_2}\right] \qquad (\mathbf{2.6})$$

Where r_1 is the concave radius and r_2 is the convex radius which is directly related to the particle radius. The second stages of capillary condensation and the third are evidently dependent on both the particle size and the degree of packing and the connectivity of the pores (Rouquerol *et al.*, 1999). The theory on pore filling for slit shaped pores is defined as a build up effect as shown in Figure 2.5, the micropores filling can be seen up until the 2 nm region where an inaccessible region is present, followed by a primary and secondary filling stage, past this point the 2nm range meniscus, and multilayer condensation play an important role in the pore filling effect.

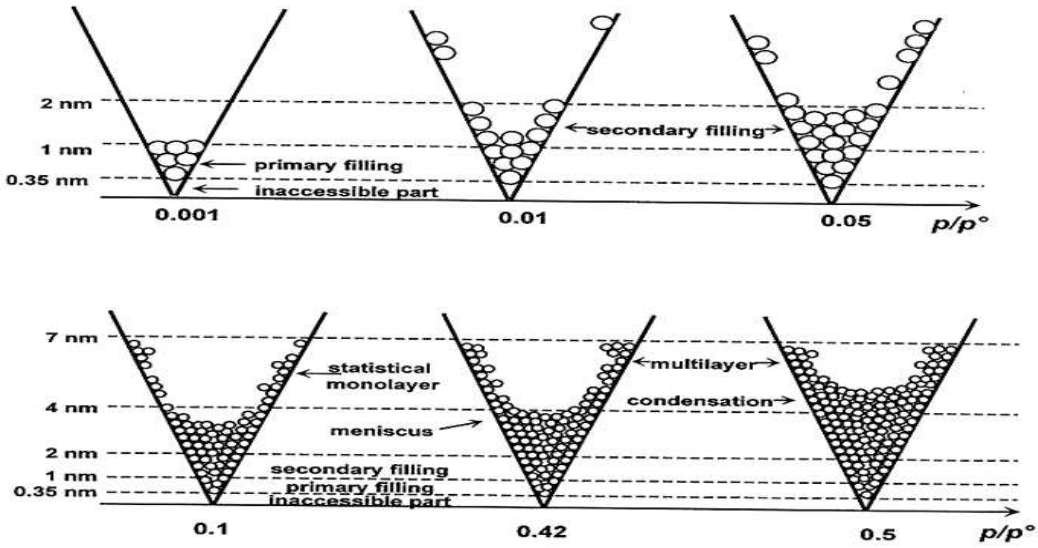

Figure 2.5: Main steps in the successive filling of micropores and mesopores during adsorption. The pressure scale gives order of magnitude for the case of N_2 at 77 K. The scale is twice as large in the upper row (Rouquerol *et al.*, 1999).

2.6 - Assessment of Microporosity

This research involves mainly mesoporous regions but for one surfactant templated silica type material synthesised within this research (CTAB core). The Kelvin equation tends to break down for the mesopores below 10 nm, and under these circumstances, methods such as the HK analysis should be adopted, because they give a more accurate representation. The two most common empirical analysis methods for micropores include the Dubinin-Radushkevich equation and the Horvath Kawazoe. The Dubinin-Radushkevich method is based on the theory that the isotherm is reversible, meaning there is no low pressure hysteresis. A straight line fit should be possible over a given range of P/P^0. A non linear relationship is usually a sign of significant adsorption in wider pores. It should be noted that however, even mesoporous solids may exhibit to a certain extent some linearity. The HK method however is a novel method for determining the micropore size distribution and was originally used in 1983 to analyze nitrogen adsorption on molecular sieve carbons with slit shaped pores, and has been modified to account for cylindrical shaped pores as in the case of silica mesopores (Saito and Foley, 1991). The HK method is based on the general idea that the relative pressure required for the filling of micropores of a given shape and size, is directly related to the adsorbent - adsorbate interaction energy. It is assumed that the entropy contribution to the free energy of adsorption is negligible compared to the large change in internal energy, which is directly related to depth of the potential energy available.

Although the target within this research is to synthesise mesopores, however micropores may result. It is also arguable that for mesopores below 10 nm theories based on the Kelvin equation could break down. The HK method will also be employed, in addition to the BJH method as a check measure for pore structure information. The filling of micro-pores (width $\leq$ 2 nm) tends to take place in two main phases, the primary (pre-capillary condensation range of a physical adsorption isotherm) and the secondary micro-pore filling. The primary phase is the region where the pore is only a few molecular diameters wide and pore filling occurs at very low relative pressures. The primary micropore filling process is associated with enhanced adsorbent - adsorbate interactions and always involves some distortion of the sub-monolayer isotherm. It occurs when the pore is only a few molecular diameters wide, and at very low relative pressures. Whereas the secondary phase, is where the wider micropores are filled by a

process that may extend into the multi-layer region at a higher range of relative pressure. Rouquerol *et al.* (1999) explained six main points that help in understanding the differences in the primary and the secondary micropore filling:

1. The adsorbent solid structure.
2. The surface composition.
3. The pore width and shape.
4. The polarities of the interacting centres and their ability to be polarized.
5. The adsorptive molecular size and shape.
6. The operational temperature, for thermodynamic reasons.

The micro pore filling capacity also depends heavily on the available pore volume and the packing of particles within the pores. Figure 2.6 shows how these factors affect the filling and the packing density of particles.

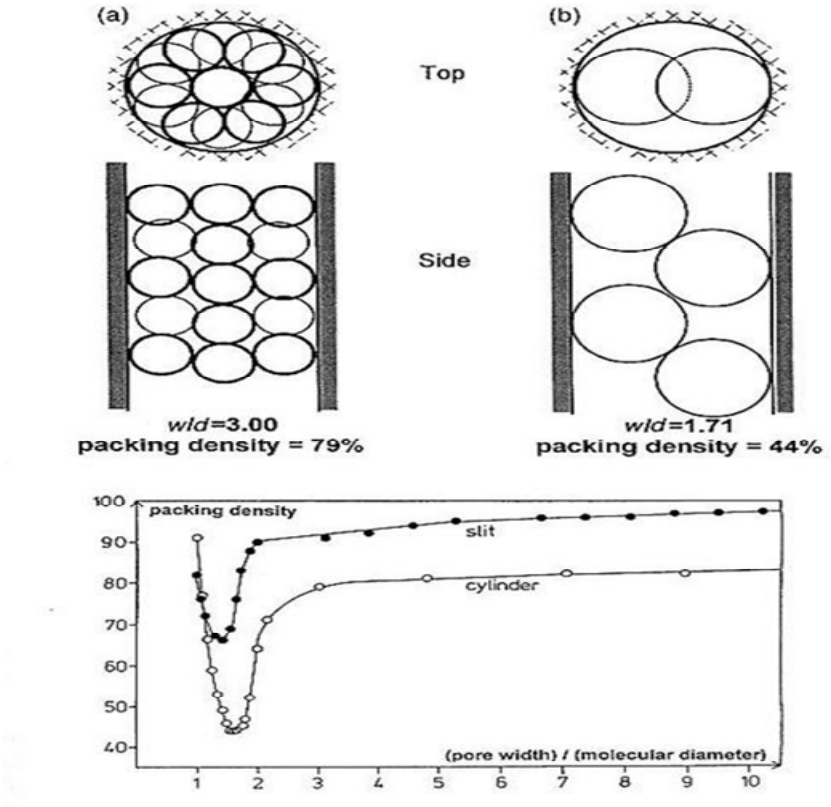

Figure 2.6: Diagram of how pore diameter and particle width can affect condensation (Rouquerol *et al.*, 1999)

2.7 – Characterisation

Conventionally nitrogen is the most widely adopted gas for adsorption characterisation, and often provides the input data for the analysis models for determining pore structure information. The range of mesoporous silica materials synthesised within this research, were characterised using nitrogen gas adsorption technique run on the Micrometrics ASAP. Capillary condensation (pore filling) is used to determine the pore size distribution, while multi-layer adsorption is used to determine the surface area. The cross sectional area per adsorbed molecule of N_2 was assumed to be 0.162 nm^2 (Brunauer *et al.*, 1938). During the nitrogen adsorption experiment, an adsorbed film of nitrogen begins to form on the walls of the pore, and as the pressure increases, the thickness of the film increases. This process continues until the condensation pressure is reached. At this point the pore begins to fill with a liquid like condensed phase which results in a steep increase in the adsorption isotherm. The condensation pressure is related to the pore size by the Kelvin equation (Equation 2.3). At pressures above the condensation pressure, adsorption increases gradually with pressure due to the condensed phase.

In theory it has been proposed, that condensation only occurs in pores above a critical pore size W_k which is ~ 2 nm. For pores smaller than W_k, the first order transition ceases to exists, causing the pores to fill up rapidly but continuously, with nitrogen, at a 'filling pressure'. In the past, due to thermodynamic reasons, pore size distributions were usually determined from desorption isotherms. However, Lowell and Shields (1984) made an exception for the case of 'bottle neck' pores exhibiting hysteresis, by using an adsorption isotherm to obtain PSD, in order to avoid underestimation. The narrow necks in the 'bottle neck' pores were reported to control the desorption process, and hence may lead to underestimation.

2.8 - Methods of Determining Pore Size Distribution

The Barrett *et al.* (1951) (BJH) method remains the most popular proposed method for mesopore size analysis, and the application of the BJH method involves the following assumptions:

1. Rigid cylindrical shaped pores.
2. The Kelvin equation applies.
3. The validity of the correction for multilayer adsorption.
4. Hemispherical meniscus with zero contact angle (assuming dead-end pores).

The algorithm used on the Micrometrics ASAP 2010 for the characterisation of the materials synthesised with this work is an implementation of the (BJH) method for pore volume and area distribution calculations, and it also assumes total pore space is filled at the top of adsorption isotherm. For adsorption data, the relative pressure and volume adsorbed data point pairs collected during an analysis were arranged in the reverse order to which the points were collected during analysis, to ensure that the data used is strictly in decreasing numerical value. Each data pair represents an interval boundary (or desorption step boundary) for intervals I = 1 to I = N - 1 where N = total number of relative pressure and volume pairs. All calculations were performed based on the desorption model, for both desorption and adsorption data.

Generally, the desorption branch of an isotherm is used to relate the amount of adsorbate lost in a desorption step to the average size of pores emptied in the step. A pore loses its condensed liquid adsorbate at a particular relative pressure related to the pore radius by the Kelvin equation, after which a layer of adsorbate remains on the wall of the pore. The thickness of the layer is calculated for a particular relative pressure from the thickness equation. The thickness decreases with decreasing pressure, so that the measured quantity of gas desorbed in a step is composed of a quantity equivalent to the liquid cores evaporated in that step plus the quantity desorbed from the pore walls of pores whose cores have been evaporated in that and in previous steps combined together.

As a check to the validity of the mesopore size analysis, the stated assumptions should be met, and in addition if the isotherm is of Type IV, H1, the desorption branch should

be adopted, and if the isotherm is of Type IV, H2, the adsorption branch is likely to provide more reliable overall estimate of the pore size distribution (Rouquerol *et al.*, 1999). The Barrett, Joyner and Halenda (BJH) technique takes a volumetric balance over an elemental volume of a pore, such that:

$$pore\ radius = r_c + t_a \quad \textbf{(2. 7)}$$

or

$$pore\ radius = r_h + t_a \quad \textbf{(2. 8)}$$

where

r_c is radius at which condensation occurs, assuming a cylindrical meniscus.

r_h is radius at which condensation occurs, within assuming a hemispherical meniscus.

t_a is thickness of the adsorbate film (varies with condensation or evaporation).

2.9 - Determining Surface Area

A key element in the characterisation of porous media is the determination of the surface area. Accurate measurement of the surface area of porous solids presented a significant problem in early studies of adsorption. If the physical adsorption capacity were limited to a close packed monolayer, the determination of the saturation limit from an experimental isotherm, with a molecule of known size, would be straightforward and hence lead to the specific surface area. However, this is not so as chemisorption sites are usually widely spaced such that the saturation limit bears no obvious relationship to specific surface area, and physisorption generally involves multilayer adsorption. In multilayer adsorption, molecular layering commences at pressures well below that required for completion of the monolayer which leads to uncertainties as to how to extract the monolayer capacity from the experimental isotherm. Brunauer *et al.* (1938), solved this problem, by developing a simple model isotherm (BET), which accounted for multilayer adsorption, and was used to extract the monolayer capacity and hence the

specific surface area. The BET method remains the most widely used technique for the measurement of specific surface area, and it is based on the following assumptions.

1. Each molecule in the first adsorbed layer is considered to provide one 'site' for the second and subsequent layers.
2. The molecules in the second and subsequent layers, which are in contact with other adsorbate molecules rather than the surface of the adsorbent are considered to behave essentially as the saturated liquid, while the equilibrium constant for the first layer of molecules in contact with the surface of the adsorbent is different. Hence, for the second and all higher layers, the energy of adsorption has the same value as the liquefaction energy $E_{L,}$ of the adsorptive (i.e. $E_2 = E_i = E_L$).
3. There is a uniform array of surface sites, with no lateral interactions between the adsorbed molecules. (since E_i is not dependent on the surface of the i^{th} layer.
4. The multi-layer has infinite thickness at $P/P^0 = 1$ (i = ∞).

For a given adsorbate, when the rate of condensation during the adsorption process, is equal to the rate of evaporation during the desorption process, an equilibrium pressure is achieved at a given temperature, *T*. Hence it is assumed that at equilibrium pressure *p*, the fractions of the covered surface remain constant, and the rate of condensation on the bare surface and the rate of evaporation from the first layer can be equated. The resulting equation is:

$$a_i p \theta_{i-1} = b_i \theta_i \exp\left(\frac{-E_i}{RT}\right) \qquad \textbf{(2. 9)}$$

where θ_{i-1} and θ_i are the fractions of surface covered by the *i-1* and *i* layers respectively, while a_i and b_i are adsorption and desorption constants, and E_i is a positive value, representing the energy of adsorption for the layer termed *i*. Based on the assumption that the multilayer has an infinite thickness at $P/P^0 = 1$, the amounts adsorbed in all layers were summed up and simplified to produce the BET equation:

$$\frac{\frac{P}{P^0}}{n\left(1-\frac{p}{p^0}\right)} = \frac{1}{n_m C} + \frac{1}{n_m C} + \frac{C-1}{n_m C}\frac{P}{P^0} \quad \textbf{(2. 10)}$$

n_m = Monolayer Capacity

C (BET) = Empirical constant

The BET constant is assumed, to be exponentially related to E_1 by the simplified equation:

$$C \sim \exp\left(\frac{E_1 - E_L}{RT}\right) \quad \textbf{(2. 11)}$$

$E_1 - E_L$ = The net molar energy of adsorption

C (BET) indicates the strength of the adsorbent and adsorbate interactions, with C (BET) < 20 and C (BET) > 100 representing low and high interaction strength respectively. The range of linearity of the BET plot is generally restricted to $P/P^0 \leq 0.4$. The linear transformed BET equation provides the basis for the plot of experimental isotherm data (Rouquerol *et al.*, 1999). The value of n_m and C can be derived from the plot of $[P/n\ (P^0\text{-}P)]$ versus P/P^0, with emphasis on the best linear fit. The BET surface area can be determined from the monolayer capacity by the stated equation.

$$(BET)_{AREA} = n_m L \sigma \quad \textbf{(2. 12)}$$

where L = Avogadro constant

σ = Average area occupied by each adsorbed molecule

The surface area was determined for particles analysed by Nitrogen adsorption at 77 K $\sigma\ (N_2) = 0.162$ nm^2 (Brunauer *et al.*, 1938).

2.10 – Capillary Condensation and Hysteresis in Gas Adsorption

A number of different methods have been proposed for the analysis of gas adsorption data, however even to date the debate surrounding the cause and existence of the hysteresis loops (region of irreversibility in the adsorption isotherm) exists, with several explanations being put forward. Hysteresis loops which appear in the multilayer range of physisorption isotherms are generally associated with capillary condensation, and are common for most mesoporous adsorbents.

As the adsorption process begins, the pressure is increased to attain monolayer adsorption, and then a transition occurs to multi-layer adsorption on the pore walls. The amount of adsorbate increases with the increase in pressure, until the condensation pressure is reached. This causes the smaller pores to become completely filled with liquid sorbate, because the saturation vapour pressure in a small pore is reduced, in accordance with the Kelvin equation (Equation 2.3), by the effect of surface tension (Sing and Gregg, 1967). The resulting first order transition which gives rise to pore filling with the liquid phase is termed capillary condensation. The onset of capillary condensation generally coincides with a point of inflection in the equilibrium isotherm, which is seen in a Type IV isotherm. In the region of capillary condensation, the isotherm generally exhibits a 'hysteresis loop', so that the apparent equilibrium pressures observed in adsorption are different from those of desorption, and there are several plausible explanations for this effect. According to the laws of thermodynamics, the amount adsorbed is controlled by the chemical potential of the adsorptive, and hence two branches of a loop cannot satisfy the requirement of thermodynamic reversibility.

The appearance of reproducible and stable hysteresis in the history of gas adsorption isotherms also implies the existence of certain well defined metastable states (Saam and Cole, 1975). As a result, Saam and Cole (1975) suggested a theory to explain the formation of hysteresis loops in cylindrical pore distributions. Their theory was based

on the regimes of stability in a multi-layer film as well as metastability and even instability. Their work defined the two opposing effects that contribute to the range of stability in a multi-layer film. The first effect is the long range adsorption forces, which were reported to stabilize the formed multi-layer film. The second effect is that of the capillary forces, which tends to cause the condensation of the liquid as the relative pressure increases. During evaporation, the liquid condensate requires a lower relative pressure in order to vaporize, and the resident film thickness is different to that of the critical condensation multi-layer film thickness, which represents the range of the multi-layer film, and is the cause of hysteresis.

Foster (1932) suggested that during adsorption, multi-layers build up on the capillary walls but a complete meniscus is formed only after saturation has been attained, at which all pores are filled. An appropriate multilayer isotherm analogous to the BET equation (though not valid within this range) will therefore govern the relationship between the pressure and the adsorbed phase concentration along the adsorption branch of the isotherm. Once the saturation limit of capillaries of a certain size has been reached, desorption will occur for a curved meniscus and the equilibrium pressure will be governed by the Kelvin equation. During the desorption process, the adsorptive vaporises from a liquid filled pore when the applied pressure is below the condensation pressure for that pore size, and when the pore has access to the vapour phase. According to the above theory, the adsorbed film formed during adsorption is in a metastable state, and the true equilibrium state is being represented by the capillary condensed liquid. The apparent stability of the multi-layer film depends on the absence of nuclei to allow condensation to the bulk fluid.

Seaton (1991) also proposed a theory based on a model of a porous network of varied pore diameters with connected ends, diagrammatically represented in Figure 2.7, of how pore connectivity affects the adsorption and desorption isotherm of mesoporous materials of a random pore network. Nitrogen adsorption analysis was employed to show how the formation of hysteresis loops can be explained by the networking effects of varying pore sizes.

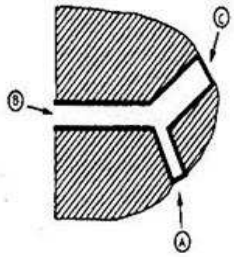

Figure 2.7: A simplified porous network with three different pore diameter sizes, going from smallest (a) to largest (c), Seaton (1991) (With kind permission of Elsevier).

Following capillary condensation effects, coupled with the effect of multi-layer adsorption, nitrogen enters the pores, and as pressure is increased nitrogen condenses in the pores in the order A, B and C i.e. increasing pore size as shown in Figure 2.7. In principle the reverse should occur for vaporisation, but due to the fact that only pore B is in contact with the vapour phase, the nitrogen in pore C remains as a metastable liquid below its condensation pressure. The nitrogen in channel C only vaporizes after that in channel B due to pore blocking effect; and this is then followed by the vaporization in pore A. According to Seaton (1991) this effect gives rise to the 'hysteresis loop' as shown in Figure 2.1. The kink at point B is where the percolation threshold for the sample is met. It was suggested by Seaton and co workers, that a percolation cluster of pores, which are below their condensation pressures, is formed, and the metastable liquid nitrogen in these pores vaporises. As the pressure drops further, f (percolation factor) increases and the nitrogen in the rest of the pores vaporizes. Broadbent and Hammersley (1957) best described the percolation theory and explained, that the square lattice can be considered to consist of a number of bonds that can either be occupied (denoted by a line) or unoccupied. The value f (which is the fraction of occupied bonds) represents the number of occupied bonds divided by the total number of bonds. The authors defined a percolation threshold as the value of f where there are enough occupied bonds to span the length of the lattice. Seaton (1991) used this analogy to further investigate the percolation theory, and their resulting representation is shown in Figure 2.8, where the percolation threshold for the lattice is 0.5.

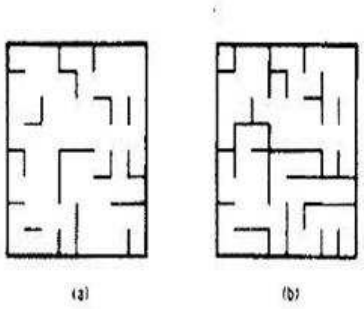

Figure 2.8: Percolation in a 2D lattice (a) f = 0.25, (b) f = 0.5 (percolation threshold), Seaton (1991) (With kind permission of Elsevier).

Mesoporous samples were characterized in terms of their pore size distributions, obtained by analyzing the nitrogen adsorption isotherm data using methods based on the Kelvin equation such as the BJH method. The connectivity factor of the pores is a very important aspect of the pore structure as it provides valuable information relating to the tortousity and porosity factor. As a result, Seaton (1991) and in subsequent work in (1992) and (1994) developed an analysis which uses the region of hysteresis between the adsorption and desorption branch, to probe the connectivity of the pore network. The data inputs into the analysis are the PSD obtained from the adsorption isotherm.

2.10.1 - Ink-bottle (Pore Blocking Effect) Theory

Most of the older theories of adsorption hysteresis made explicit use of the Kelvin equation. Zsigmondy (1911) was the first to suggest that the phenomenon was due to a difference in the contact angles of the condensing and evaporating liquid. This explanation may account for some of the effects produced by the presence of surface impurities, but in its original form cannot explain the reproducibility of the majority of recorded loops. Another early theory which has attracted a great deal of attention is the ink-bottle theory which was originally put forward by Kraemer (1931) and subsequently developed by Mcbain (1935). It is based on the principle that the rate of evaporation of a liquid in a relatively large pore is likely to be retarded if there is only one narrow exit. This led Brunauer (1945) to conclude that the liquid in the pore cannot be in true

equilibrium with its vapour during the desorption process and therefore it is the adsorption branch of the loop which represents thermodynamic reversibility.

The pore blocking effect, usually explains the phenomenon of capillary hysteresis in pores of varying cross section and pore networks. Ravikovitch *et al.* (2002) used experimental studies of the capillary condensation of N_2 at 77.4 K to present a new classification of the physical mechanisms of adsorption hysteresis in ink-bottle type pores. The analysis of the hysteresis loops and scanning desorption isotherm on spherical pores of ~ 15 nm revealed three mechanisms of evaporation: evaporation from blocked cavities controlled by the size of connecting pores (classical ink-bottle or pore blocking effect); spontaneous evaporation caused by cavitation of the stretched metastable liquid; and finally that of near equilibrium evaporation in the region of hysteresis from unblocked cavities that have access to the vapour phase. The authors quantitatively describe capillary hysteresis as being more pronounced in the ink-bottle type pores, following preliminary work by researchers such as Kraemer (1931) and Mc-Bain and Cohan (1938). The process of pore filling during capillary condensation occurs after the formation of a liquid film on the cavity wall, and thus is controlled by the radius of curvature of the cavity, r_c. The pressure of condensation is given by the Kelvin–Laplace equation (equation 2.1). During desorption, evaporation occurs after the formation of a hemispherical meniscus in the pore neck and thus is controlled by the radius of the neck r_n. The pressure for evaporation is also represented in a similar manner to condensation with r_c being replaced by r_n. The concept of pore blocking in ink-bottle type pores was successfully employed to describe the H2 hysteresis loops (Everett, 1967; Ravikovitch *et al.*, 2002), indicating exclusive dependence on the pore neck diameter. Pore blocking was reported to only take effect when the neck diameter is greater than a certain characteristic size of (~ 4 nm for nitrogen) (Ravikovitch *et al.*, 2002). The authors proposed a 'cavitation theory which states that for this critical 4 nm pore neck size and above pore blocking will take effect and for anything below there will be no pore blocking effects. The silica materials templated within this research; P123, Brij 76, Brij 56, F127 and CTAB, have average pore body sizes of ~ 8, 10, < 4, 4 and < 4 nm respectively, and therefore, the above theory will be tested/applied in their characterisation.

Gelb *et al.* (1996) further examined the adsorption hysteresis using mathematical techniques, such as Monte Carlo simulations as well as the use of molecular dynamic

simulations. The authors argued that the pore blocking effect, and the network connectivity factor have little to do with the shape of a given hysteresis loop. This is an area of scientific debate as previous work by Seaton (1991) argues the reverse.

In the classical description of adsorption in ink-bottle type pores, by Broekhoff and de Boer (1968), it was assumed that the evaporation is controlled by the size of the pore necks. The authors assumed that there is no means of establishing an equilibrium path of desorption in the case of spheriodal cavities. Ravikovitch *et al.* (2001) have shown that in highly ordered materials with sufficiently small cage like pores (~ 3 - 6 nm in diameter) the reversible capillary condensation steps corresponds to the equilibrium transition, as calculated by the 'Nonlocal Density Functional Theory' (NLDFT) for spherical pores. The validity of this interpretation has been confirmed by the fact that the pore diameters predicted by NLDFT matched the pore sizes obtained from geometrical models of these theories. Figure 2.9 shows a representation of the inkbottle type pores of spherical cavities, modelled by Ravikovitch *et al.* (2002). For sufficiently narrow pores, the free energy barrier for nucleation is relatively low while the fluctuations are strong, and hence leads to the regime of reversible capillary condensation and evaporation (Ravikovitch *et al.*, 2002).

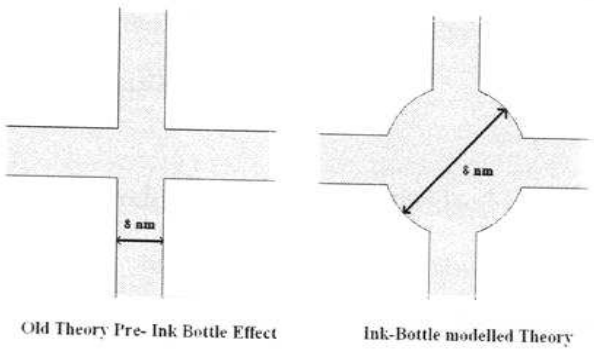

Figure 2.9: Schematic representation of ink-bottle type pores (Ravikovitch *et al.*, 2002) (With kind permission of the American Chemical Society).

Figure 2.10 shows the three different mechanisms of evaporation in ink-bottle type pores; cavitation, pore blocking and equilibrium respectively which have been reported by Ravikovitch *et al.* (2002) as possible scenarios in support of the confirmation of pore blocking effects. Wider spherical pores could also exhibit near equilibrium evaporation (Ravikovitch *et al.,* 2002). In the blocked cavities larger than ~ 6 nm in Figure 2.10, the barrier for the liquid - vapour nucleation (bubble formation) is very high, and hence desorption does not occur until either the liquid evaporates from the neighbouring pores, which block access to the vapour phase, or spontaneous cavitation of the metastable liquid trapped in the cavity occurs. The equilibrium evaporation however can only occur when the cavity has direct contact with the vapour phase, so that the liquid - gas interface can be formed, and thus the cavity is effectively unblocked. This can happen when the cavity possesses either a short neck or a wide window opening (Ravikovitch *et al.*, 2002).

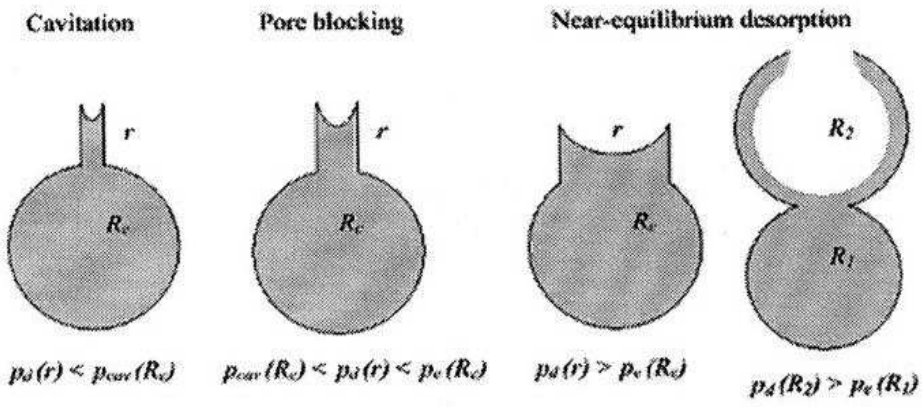

Figure 2.10: Three different mechanisms of evaporation in ink-bottle type pores (Ravikovitch *et al.*, 2002) (With kind permission of the American Chemical Society).

For experimental studies of the hysteresis phenomenon within this research, two model test materials are presented. Initially the first model, for ordered mesoporous materials is explored, based on nanosynthesis techniques similar to that of MCM-41 type materials, with controlled pore size and geometry. As most mesoporous adsorbents are reported to have complex network of different sizes, the second model thus reflects a more heterogeneous sample leading to a variety of pore structure configurations attained

by synthesising bi-modal materials with regions of differing pore sizes. This will enable direct investigations of the shielding effect of a distinctive region of varying pore diameter coated around another pore structure and hence test the validity of the interconnectivity theory of Seaton (1991). In the first model, uniform porosity is a target. Hence synthesised materials are therefore expected to be highly ordered and of uniform geometry, thereby limiting the formation of hysteresis loops based on the pore blocking effects and the network interconnectivity theory. There are also the so-called single pore theories of hysteresis, as the condensation and condensate evaporation process is unlikely to occur independently in each pore. There are also several other mechanisms which could lead to a percolation threshold (where pore blockage occurs), and thus the hysteresis loops cannot be completely removed. Therefore as it is not particularly clear whether hysteresis of the adsorption arises solely as a consequence of fluid behaviour in a single pore or whether the role of the pore network is a dominant factor, this investigation will be a useful addition.

Chapter 3: Porous Media Synthesis/Characterisation

3.1 - Introduction

The development of homogeneous and composite materials by the synthesis of an open framework of inorganic material such as silica and carbonate, with precisely engineered and controlled pore sizes is of great importance in many areas of modern science and technology, and especially in the catalyst and petroleum industry. The work described here aims to develop highly structured catalyst pellets, as well as designer structured catalyst pellets of multiple regions. Based on nanocasting techniques employing the use of standard surfactants with hydrophobic and hydrophilic regions as well as the tri block co-polymers, homogenous ordered pore structures (cores) in the microporous and mesoporous range can be created. The composite materials can also be designed to possess multiple but well-defined regiospecific pore geometries, as later shown within this research. By using one type of pore template for the pellet core zone and another for the surrounding shell region, bimodal structures (dual-structured) can be created. These materials have the potential to offer distinctively engineered diffusion barriers to the outside of the structured pellets and will be subject to investigation within this research. It is worthy to note that such complex designs in heterogeneous materials could also be employed in the technique of adding precisely engineered diffusion barriers to the outside of structured catalyst supports, or providing different environments for pore structure sensitive reactions in different parts of a catalyst pellet. Porous silica structures in the macroporous size range of ~100 nm and above were also synthesized, by templating on polystyrene beads (PS).

The pore structures of the synthesized materials will later be characterized using nitrogen sorption, butane and cyclohexane sorption, as well as the integrated nitrogen sorption and mercury porosimetry technique. Emphasis is being placed on the adsorption characteristics of the materials, their pore size distributions and on investigating the effects of pore shape and pore size as well as pore structure stability. The data arising from the series of experiments will then be analysed using the BET equations for surface area measurements, and the conventional BJH method for

obtaining the PSD as well as the HK technique suitable for the existence of micropores. This chapter is structured to contain both the methodology of synthesis and the characterisation of the silica pellets. This has been combined to serve as a quality assurance measure for the material synthesis, and experimental analysis. Although all the solid materials to be synthesized within this research will be made from silica, reference will also be made to techniques of synthesizing carbonates. (Note also that the terms silica(s) and silicates are interchangeably used in this thesis.

3.2 - Review of Nanocasting Techniques

Mesoporous materials can be synthesized by employing a removable template around which the inorganic material can form. Such templates include surfactant micelles, colloidal particles, organic molecules, or ions. In the early 1990s, Mobil scientists (Kresge *et al.*, 1992; Beck *et al.*, 1991, 1992), as well as some Japanese researchers (Inagaki *et al.*, 1993; Yanagisawa *et al*., 1990) as seen in (Bhatia *et al.*, 2001), were among the first researchers to report the first synthesis of novel periodic mesostructured materials following the conventional single (amine) molecule templated micropores known as zeolites (molecular sieves).

Kresge *et al.* (1992) described the method of synthesizing ordered mesoporous molecular sieves via liquid crystalline template mechanisms, which led to the formation of the now commonly used MCM-41, which consists of silicate walls between ordered pore spaces. These Mobil scientists created the M41 class of templated materials by first forming a micellar solution, and then carrying out a sol-gel reaction to form silica (or another desired oxide) in the solution surrounding the micelle (thus using the micelle phase as a template) (Kresge *et al.*, 1992). These structure directing agents are subsequently removed by calcination, solvent extraction, or ozonation, leaving a porous material with a pore space that replicates to some extent the original template. The conventional method of template removal is calcination at high temperature close to silica sintering temperature, ~ 600 ^{o}C which is being employed in this work. Since templates of diverse size and shape are obtainable, templating offers the prospect of producing porous materials with structures designed to specifications. The usual synthesis procedure begins with forming a dilute solution of surfactant with spherical

micelles, and on the addition of a silica source or another oxide, a liquid crystal phase is formed and polymerization of the silica occurs. The nature of the liquid crystal phase depends on the concentrations involved, the temperature of formation and the chemical nature of the surfactant and silica source. The addition of a silica source to a dilute surfactant solution s reported to causes a phase separation into a dilute surfactant phase and a surfactant-rich (liquid crystal) phase, where the latter can adopt different liquid crystal structures including hexagonal phases which are observed for low surfactant/silica ratios (0.6) and lamellar phases are found for higher surfactant/silica ratios (1.3) (Kresge *et al.*, 1992). Pore sizes of MCM-41 type materials can be varied according to the alkyl chain lengths of surfactant molecules in the range 2-5 nm.

Newer methods have been developed to tune much larger mesopores with relatively narrow pore size distributions. For example, pore size enlargement can be obtained by swelling surfactant aggregates with certain organic molecules, alcohols (Feng *et al.*, 2000) and aromatic hydrocarbons (Beck *et al.*, 1991). In an attempt to obtain larger pore-sizes, Zhao *et al.* (1998) reported the syntheses of well-ordered hexagonal mesoporous silica structures (SBA-15) with tunable large uniform pore sizes (up to ~300 Å) which were obtained by the use of amphiphilic block copolymers as organic structure-directing agents.

There are various categories of M41 silica mesophases, which includes the thermally stable MCM-41 having a hexagonal structure with unidimensional pore structure, the MCM-48 displaying a cubic structure with a three dimensional pore system, the MCM-50 with a lamellar pore structure, and the molecular organic octomer, which is a surfactant-silica composite species (Bhatia *et al.*, 2001). Inagaki *et al.* (1993) also synthesized mesoporous silica materials designated as FSM-16 from a layered form of sodium silicate and CTA surfactant cation via an ion-exchange process followed by hydrothermal treatment. This silica based mesophase of FSM-16 is structurally similar to the MCM-41, but with slightly differing adsorption properties and surface chemistry as shown by Vartuli *et al.* (1994), and Ishikawa *et al.* (1996) respectively.

It is interesting to note, that different choices of inorganic precursor, organic template, reaction conditions and synthetic pathways have resulted in a variety of mesoporous structures, with many having structures similar to the MCM-41 type materials (Huo *et*

al., 1994; Ryoo *et al.*, 1999; and Beck *et al.*, 1996). An extension to Mobil's self-organized surfactant procedure has resulted in several different silica mesophases by the use of different types of modified surfactant templates. Neutral surfactants, such as primary amines and poly (ethylene oxides), have been used to synthesize a series of disordered mesoporous silicate structures called HMS, through hydrogen-bonded interactions (Tanev *et al.*, 1995, 1996). Acid treated surfactant assemblies were also used to prepare mesoporous silicas termed SBA-n (where n=1-3,8,11,12, 14-16) structures using cationic surfactant and halogen acids through balanced columbic, hydrogen-bonding and Van Der Waals interactions (Zhao *et al.*, 1999; Huo *et al.*, 1994). Ryoo *et al.* (1996) synthesized hydrothermally stable mesoporous silicates called KIT-1, with disordered interconnected pore channels, by including the addition of ethylenediaminetetraacetic acid to a high pH synthesis gel.

The use of self organizing oil-water-surfactant mixed phase systems as a structure directing agent for reaction media in material synthesis has shown that the phase behaviour and compositions of these systems can be varied extensively, indicating markedly different inorganic structures and architectures can be fabricated. Whereas Kresge *et al.* (1992) showed that water-oil hexagonal and cubic phases can direct the formulation of mesoporous silicas, limited amounts of water were used in bicontinuous micro-emulsions to give rise to reticulated frameworks of amorphous silica and of calcium phosphate (Watzke *et al.*, 1994; Walsh *et al.*, 1994)). In the latter case, the macroporous architecture consists of interlinked micrometer sized crystals indicating that the length scales of the original micro-emulsion network and inorganic 'replica' are incommensurate. This suggests that the phase separation and a secondary mode of self-organisation can facilitate the construction of the microskeletal inorganic material (Walsh *et al.*, 1994). They employed the use oil-water-surfactant microemulsions supersaturated with calcium bicarbonate, to form thin cellular frameworks of either mesoporous or macroporous aragonite samples. They synthesized hollow porous shells of crystalline calcium carbonate (aragonite) that resemble the marine algae cocospheres.

More recent work has shown that mesoporous silicas themselves can be used as templates for carbonate materials (Jun *et al.*, 2000). The syntheses of more complex bi-modal and hierarchical materials have also been reported, such as the approach of synthesising bi-modal materials based on filling larger mesopores with microporous

materials (van der Voort *et al.*, 2002). Velev *et al.* (1997) also successfully synthesized organized silica flakes of very low density by a method of varying the size of the microspheres used to produce pore sizes ranging from 150 nm to 1μm. Later on Sen *et al.* (2003) reported a similar synthesis technique for a hierarchical structure using synthetic latex spheres to produce 3D interconnected macroporosity, block copolymer to produce mesoporosity and individual polymer templating to produce microporosity.

These materials have been shown to possess well-defined tailored cylindrical, hexagonal or cubic micropores, mesopores and even macropores with a simple geometry. The above progress led to the work carried out within this research, where individual surfactant templates including the triblock copolymers are used as structure-directing agents, to synthesise ordered microporous and mesoporous materials, as well as dual-structured materials involving a different approach of coating particles.

3.3 - The Applications of Ordered Mesoporous Materials

The discovery of periodic mesoporous MCM-41 and similar porous solids has attracted significant attention for various fundamental purposes related to the pore structure, as well as in its application as molecular sieves.

These highly structured solids can also be used as models in the validation of theories in areas such as gas sorption. The properties of the ordered mesoporous materials of type MCM-41 that have been synthesised, makes them conducive for a variety of applications, which include adsorption, catalysts and supports, molecular hosts, molecular sieves and as models for investigating fluid flow. These materials have significant potential as catalyst supports in fine chemistry due to their controlled pore size and a relatively narrow pore size distribution and they could also be used in the production of special polymer materials (Weckhuysen *et al.*, 2000).

Heterogenizing the synthetic procedures in fine chemical production forms the basis of achieving the goals of green, sustainable production processes and end of pipe waste reduction. These mesoporous materials can be used to develop heterogeneous catalysts and catalyst supports to meet strict legislation governing the disposal of hazardous

waste. The quest for a greener environment can benefit from the prospects of a viable alternative such as heterogeneous catalysis which offers the advantages of simple separation by the use of an engineered adsorbent, that can easily be recovered, reused, and eliminates the use of hazardous chemicals. As opposed to the use of traditional stoichiometric, and conventional homogeneous catalytic processes which are more expensive.

Catalyst support materials with controlled pore size and geometry also offer the possibility of the precision control of the rates of transport processes taking place within the pore structure. For example, the precise control of reaction rates is important in auto-thermal reaction systems, where the thermal requirements of an endothermic reaction (e.g. steam reforming) are coupled to an exothermic reaction (e.g. oxidation). The requisite matching of the rates may be achieved by introducing a diffusive barrier into a catalyst support. The particular catalyst activity required can be obtained by specially engineered diffusion barrier to produce the required mass transport rates.

The use of mesoporous materials in separation and adsorption processes, offers additional advantages as they posses large pore volumes with a structural diversity that can be exploited for the purpose of selective adsorption for a variety of gasses and liquids. The surface hydroxyl groups in the pore walls can be replaced by trimethylsilyl groups to produce a more hydrophobic material that will substantially reduce the sorption capacity of polar molecules (Bhatia *et al.*, 2001), and also reduces reactivity with molecules with higher affinity for silanols to produce desired effects. The grafting of thiol functionalised tris- (methoxy/propoxy)-mercaptopropylsilane on MCM-41 has been reported as a technique for recovering heavy metal ions from wastewater, which is another great advancement in industrial pollution control process (Bhatia *et al.*, 2001). These materials also have potential use as a molecular host in the area of quantum structures in confined environments. Due to its mesoporous structure, it is thus considered as a suitable material for the loading and encapsulation of various metals and metal oxides and nanowires (Orzin, 1992; Moller *et al.*, 1998).

Highly ordered porous solids can also be used as model porous materials for detailed experimental studies of the behaviour of non-wetting fluids within porous media. They could be designed to mimic the structure of a reservoir rock and thus can be used to

better the prediction of the pore bound volume index as well to investigate the adsorption properties of porous materials.

Techniques similar to that adopted by van der Voort *et al.* (2002) in producing a new templated ordered structure with combined micro- and mesopores and internal silica nanocapsules could be applied as innovative catalyst supports, which should allow heterogenization of catalytic processes (such as upgrading of petroleum products), by increasing the efficiency and selectivity. It is arguable however, whether silica nanocapsules could be used to heterogenise most catalytic processes, since problems such as leaching of catalytic active components from the particles might occur, or there might be transport limitations. The authors created the silica materials with a very broad range and distinctively different characteristics by changing the synthesis parameters (surfactant/TEOS ratio, synthesis temperatures and time) in a controlled way.

3.4 - Synthesis and Formation of MCM-41

According to the originally proposed mechanism of synthesis of MCM-41 by the Mobil scientists, (Kresge *et al.*, 1992; Beck *et al.*, 1991), the pathways of formation have been diagrammatically represented by Vartuli *et al.* (1998), as seen in Figure 3.1.

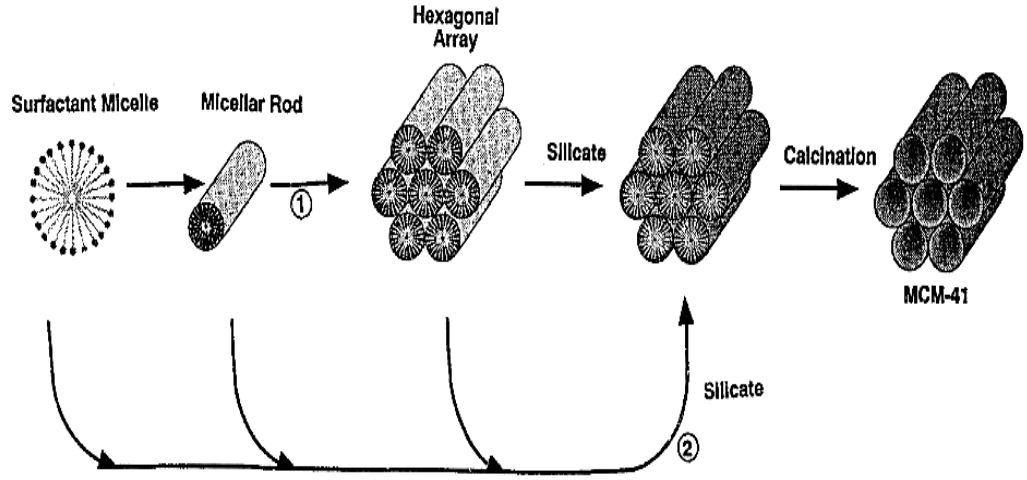

Figure 3.1: Proposed mechanism of synthesis by Vartuli *et al.* (1998) **(**with kind permission of Springer Science and Business Media).

For these M41S materials, having structures like the hexagonal (MCM-41), cubic (MCM-48), and lameller (MCM-50), which display liquid crystal phases strongly suggests the proposed mechanisms. The first pathway proposes that the presence of liquid crystal mesophase prior to the addition of reagents causes the formation of the MCM-41 material. The first step in the formation process is the pre-existence of the surfactant aggregates which, form rod-like micelles, followed by the migration and polymerization of silicate anions. The second step is that the self-assembly of the liquid crystal-like structures as a result of the mutual interactions between the silicate anion and the surfactant cations in the solution i.e. the silicate species generated in the reaction mixture influences the ordering of surfactant micelles to the desired liquid crystal phase. This was suggested by Chen *et al.* (1993), when they identified silica aggregates in the synthesis mixture using ^{14}N NMR spectroscopy. In addition, the fact that the different structures can be formed through variations in the silica concentration at constant surfactant concentration is a support for the latter mechanism (Vartuli *et al.*, 1998). Davis and Burkett (1995) proposed a similar mechanism which is represented by path way (2) (see Figure 3.2) where depending on the reaction temperature, the formation of MCM-41 occurs via disordered or lamellar structure.

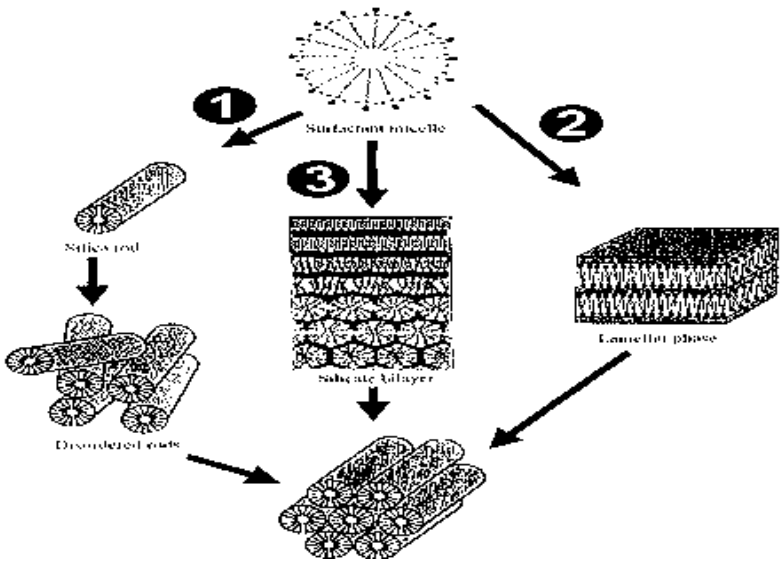

Figure 3.2: Bhatia *et al.* (2001), presents a figure of proposed mechanistic pathways of formation presented by (1) Stacking of silicate surfactant rods via the formation of an initial (2) lamellar intermediate and (3) silicate bilayer (Vartuli *et al.*, 1998) **(**with kind permission of Springer Science and Business Media).

3.5 - Surfactants

Surfactants are also known as amphipathic compounds, meaning that they would prefer to be in neither water nor organic phases. They are comprised of a hydrophilic portion, usually a long alkyl chain, attached to hydrophilic or water solubility enhancing functional groups (the hydrophobic PO and the hydrophilic EO molecular units). As a result when in solution they locate at the phase boundary between the organic and water phases, or if there is no more room there, they will congregate together and form micelles. The concentration at which surfactants begin to form micelles is known as the critical micelle concentration (cmc). Equilibrium is reached between the surfactant monomer, surface monolayers and micelle in an aqueous medium. Due to the limited solubility of surfactants in water, aggregates are formed in which the hydrophobic or hydrophilic sections of the surfactant are stuck together. The micelle may be represented as a globular cylindrical cluster of individual surfactant molecules in equilibrium with its monomers. Planar, bilayers, or small unilamellar vesicles are also formed depending on the reverse orientation.

The tri-block co-polymers are some of the most widely used surfactant micelle species for nanocasting, and it has now been well established that block copolymer of the type $(EO)_x(PO)_y(EO)_x$ behave in many ways like a normal hydrocarbon based surfactant. These compounds are surface active, and form micelles and liquid crystalline phases. In comparison to normal surfactants these compounds have the peculiarity that their cmc and their surface activity depend more on temperature than for the classic ionic surfactants. The use of these tri-block co-polymers have been extensively researched by Wanka *et al.* (1994), and they found that for high tri-block co-polymer concentrations the systems form liquid crystalline phases. This is a result of the effective volume of the systems being much larger than the real volume; hence the liquid crystal formation can occur in concentration regions where it is normally not expected for hydrocarbon surfactant. It was shown that the gelation process that is observed in some moderately concentrated block copolymer solutions, with increasing temperature is actually due to the formation of a cubic phase. With further increasing concentrations transition to hexagonal and to lamellar phases are observed.

The two tri-block co-polymers proposed for the course of this research, include the Pluronic F127 ($EO_{106}PO_{70}EO_{106}$), and the Pluronic P123 ($EO_{20}PO_{70}EO_{20}$). The phase diagram for the block co-polymers explains the formation of the coated hexagonal templated silica (CHTS) and the coated cubic templated silica (CCTS) for P123 and F127 respectively and is shown in Figure 3.3.

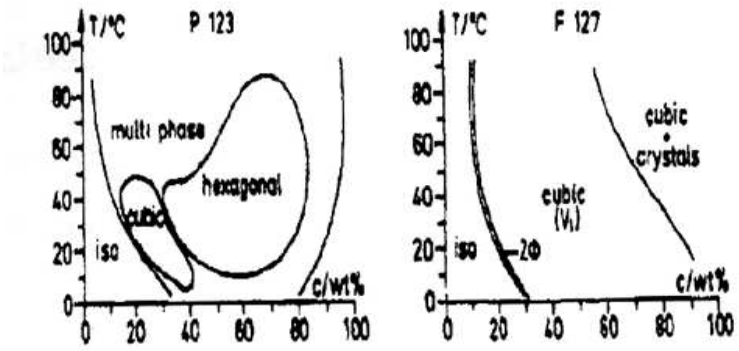

Figure 3.3: The phase diagram for block copolymers (Wanka *et al.*, 1994) (With kind permission of the American Chemical Society).

3.6 - Experimental Synthesis Method Section

The first method of synthesis is a standard technique; according to Attard *et al.* (1995), which creates pore structures depending on the surfactant chain length in the range 4-10 nm. In addition a coating technique is employed to create bimodal materials by employing one surfactant for the core and another for the shell. The second method of synthesis adopts the same steps as in the first method of synthesis except that the aim here is to design similar structures to the cores synthesised in the first method but with different surface chemistries for the purpose of investigating the effect of surface properties on uptake measurements and the entrapment of non-wetting fluids. The third method is adopted from Feng *et al.* (2000), and here the effect of the addition of alcohol (such as pentanol and butanol, for creating pore sizes larger than those of method 1 and 2) during the templating process using tri-block copolymers (F127, and P123) is

investigated. The fourth method of synthesis involves creating polystyrene latex spheres (PS) from styrene polymerisation, and then compacting spheres into a structural framework, for silica casting to create much larger silica solids ~ 500 nm.

3.6.1 - First Method Description

Initially core particles were prepared using a range of surfactants including Brij 56 (Polyoxyethylene-10-cethyl-ether), Brij 76 (Polyoxyethylene-10-steryl-ether), CTAB (Cetyltrimethylammonium bromide) and the triblock copolymer surfactants Pluronic F127 and, P123. Tetramethlyorthosilcate (TMOS) was selected as the ceramic starting material, for ease and accuracy of analysis as its hydrolysis and condensation behaviour under a range of temperature has been investigated extensively by McKenzie (1988). The cores were prepared by mixing each surfactant with 0.5 M HCL such that the resulting solution had a ratio of surfactant to water of 50 wt%. TMOS was added to dissolve the surfactant prior to the addition of the 0.5 M HCL solution, such that the final amount of TMOS was not more than 0.25 M equivalent with respect to the water. After mixing, a gentle vacuum was used to remove the methanol produced by TMOS hydrolysis. The masses of surfactant and acid solutions used were equal in order to produce a 50 wt% solution of surfactant, after removal of the methanol, which falls in the desired region of the surfactant liquid crystalline phase diagram (see Figure 3.3). For F127, a 50 wt% solution in water should place it in a cubic phase, while a 50 wt% P123 solution should be in the hexagonal part of the phase diagram (Wanka *et al.*, 1994). The phases in which the produced lattice structures are formed holds over a broad region, and hence it is unlikely to synthesize structures of varied phases at the chosen concentrations. After methanol removal a viscous solution remained in the bottom of the vial. The vial was sealed and heated at 45 °C for 5-7 days. Upon removal from the oven the now formed material was dried slowly for several days to prevent are changes due to a sudden change in conditions. It was found that the pellets cracked due to rapid solvent evaporation. The resulting surfactant-silica composite was a hard and glassy material, which was later broken into smaller pieces. Some of these pieces of material were kept aside uncalcined, to be used as cores in the making of the bi-modal structures while some were calcined at 600 °C and reserved for characterisation. The core samples kept aside for coating were left uncalcined so that the still surfactant-filled pores will

prevent the coating layer from entering the pores within the core. The cores were then coated using a similar high surfactant concentration solution. The P123 templated cores were coated in a solution containing F127, whilst the F127 cores were coated in P123 templated material. Other surfactant templates were used, and the resulting silica solids and their combinations are given below in Table 2.1.

Table 3.1: Showing the combinations of composite materials synthesized

COATS	CORES			
	P123	F127	CTAB	Brij 76
P123	N/A	✓	✓	✓
F127	✓	N/A	✓	✓
CTAB	✓	×	N/A	✓
Brij 76	✓	✓	✓	N/A
Brij 56	✓		✓	✓

The solutions for the coats were prepared in the same manner as the cores. After methanol extraction, the core particles were dipped into the viscous solution, and then removed to a clean vial. The vial containing the core-shell particles were sealed and heated at 45 °C for 2 days, and dried slowly after removal from the oven. The composite particles were calcined in air at 600 °C for 4 hours to remove the surfactant and open up the pores.

3.6.1.1 - Summary of Steps in First Synthesis Method

Chemical used:

- Silica Source : TMOS (Tetramethylorthosilicate)
- Surfactants

1. Pluronic F127 (a triblock copolymer ($EO_{106}PO_{70}EO_{106}$))
2. Pluronic P123 (a triblock copolymer ($EO_{20}PO_{70}EO_{20}$))
3. Brij 56 (Polyoxyethylene-10-cethyl-ether)
4. Brij 76 (Polyoxyethylene-10-steryl-ether)

5. CTAB (Cetyltrimethylammonium bromide)

Steps:

1. Add 1.39 g of surfactant to a small medium sized glass vial.
2. Dissolve the surfactant in 2.50 g of tetramethlyorthosilicate.
3. Heat to approximately 40 ^{O}C in other to dissolve the surfactant into the TMOS solution. Care should be taken to prevent the polymerisation of the TMOS/ surfactant solution due to excessive heat.
4. The dissolved mixture will be a clear solution, which is then allowed to cool.
5. Add 1.39 g of 0.5 M HCL; note this results in an exothermic reaction.
6. Water driven suction pump is then used to evacuate the methanol vapour. Sufficient pressure is required to suck the methanol, however care should be taken to ensure the entire solution is not lost.
7. Place the solution in an oven at 45 ^{o}C for 5-7 days to ensure the mixture is treated sensitively at low temperature.
8. Break up any large pieces and keep some pieces uncalcined, so that when the particles are coated the pores don't fill up with the dip coating solution.
9. The surfactant remaining is then removed from the filled pores by calcining (burning out). This is carried out in a specialized oven at 600 ^{o}C for three hours and then allowed to cool gradually overnight, since surfactant calcining temperature is ~ 600 ^{o}C. The calcined samples are later used for the analysis of the internal structure.

Bimodal porosity particles: The inner particles are synthesized using the same method of nanocasting, and the coats were prepared in a similar technique but this time the solution was a little bit running like the texture of cold honey. The core particles (not calcined) were then dipped in the coating solution so that all of the particles were covered in the coat and allowed to dry.

3.6.2 - Second Method of Synthesis

This method is a slight modification of the first method of synthesis, and it is aimed at exploring the effects of surface chemistry on the transport and uptake properties of model porous media. The tri-block copolymers are used to synthesis a more hydrophobic material in comparison to the ones from the first method. The silica source is adjusted to include an extra methyl chain on the surface of the newly created mesoporous silica solids, as opposed to the hydroxyl groups on the surface of the materials previously synthesized. For the purpose of this research, the samples from the first method and the second method will be referred to as hydrophilic and hydrophobic samples respectively. Solvent extraction is used for surfactant template removal in these materials, because of the delicate nature of the surface chemistry, as burning off the methyl chains will defeat the purpose.

3.6.2.1 - Summary of Steps in the Second Synthesis Method

1. Add 1.39 g of surfactant to a small medium sized glass vial.
2. Add 2.25 g of tetramethlyorthosilicate to the surfactant.
3. Then add 0.293 g of methlytetraorthosilicate to dissolve the surfactant.
4. Heat to approximately 40 ^{O}C in order to dissolve the surfactant into the TMOS solution. Care should be taken to prevent the polymerisation of the TMOS/ surfactant solution due to excessive heat.
5. The dissolved mixture will be a clear solution, which is then allowed to cool.
6. Add 1.39 g of 0.5 M HCL; note this results in an exothermic reaction.
7. Water driven suction pump is then used to evacuate the methanol vapour. Sufficient pressure is required to suck the methanol, however care should be taken to ensure the entire solution is not lost.
8. Place the solution in an oven at 45 ^{o}C for 5-7 days to ensure the mixture is treated sensitively at low temperature.
9. Break up any large pieces and keep some pieces uncalcined, so that when the particles are coated the pores do not fill up with the dip coating solution.
10. The surfactant remaining is then removed from the filled pores by means of soxhlet extraction. This process is explained below, and it is a way of extracting the surfactant by dissolving them in a solvent that is applicable. For

the tri-block copolymers F127 and P123, ethanol was used at its boiling temperature, of approximately 80 ^{o}C for 3 hours and allowed to dry gradually overnight. The extracted samples are later used for the analysis of the internal structure, some samples are collected prior to calcining, to be coated in the hydrophilic samples, to analyse the structure of the combination, and to investigate the existence of diffusional barriers.

3.6.3 - Alternative Techniques for Larger Pores

The method of silica casting over surfactant micelles adopted from Attard *et al.* (1995) has been applied successfully to tri-block copolymers resulting in pore sizes of the range 4 - 9 nm. Since the development of such materials, one goal in structural control has been to increase the size of pores, enough to permit the penetration of larger molecules into the porous media. As a result this research will employ an adapted method in an attempt to synthesise porous solids with pore sizes in the range 0.1 - 10 μm, which should be sufficient to permit the penetration of larger guest molecules.

The materials created by Kresge *et al.* (1992) had regular arrays of uniform channels with dimensions that vary from 16 - 100 Å which were determined by the choice of surfactant auxiliary chemicals and reaction conditions. However the work of Vandreuil *et al.* (2001) has confirmed the limitations of the use of surfactant micelle species like the ones being used in this experiment, to produce porous materials with maximum pore size of 30 nm. Various techniques have been proposed in the quest for ordered porous materials with larger pore sizes. However emulsions of non-miscible liquids that provide such an opportunity, lead to pores that are irregularly spaced and broadly distributed. Davies *et al.* (1997) synthesized porous materials by mineralising bacteria threads, and this produced materials with oriented and elongated pores of micrometer size, but lacked highly ordered and uniform pores of arbitrary size and shape. Feng *et al.* (2000) observed that by using pre-formed liquid crystals as templates in ternary systems, it is possible to synthesize highly stable hexagonal mesoporous silica from triblock copolymers, and attain a high degree of control over the pore sizes. The addition of a co-surfactant, acts as a special kind of swelling agent to allow an additional level of

control. This technique has been covered in the course of the research, and more detail can be found in section 3.6.5.

The potential applications of these materials can be extended greatly, if they can be made with a large range of pore sizes, to permit penetration by larger molecules. It is also within the scope of this research to synthesise macroporous materials for their study and characterisation in order to improve the understanding of the effect of pore structure variations in reservoir rocks on fluid transport and the irreducible fluid saturation in oil recovery. As a result, an investigation into templating porous materials at the macroscale, (> 50 nm), is therefore carried out in the third and fourth methods, by the use of co-surfactants for a pre-swelling effect, and also by adopting latex polymer spheres for templating instead of surfactants. Several researchers including Holland *et al.* (1998), produced highly ordered arrays of macropores connected by macro-windows using monodispersed polystyrene (PS) beads of 200 - 800 nm average diameter as templates. The beads were gathered together in a close packed arrangement using either centrifugation or filtration, using vacuum suction through a filter paper. The solid is later calcined to free the polymer from the oxide (silica, titania, or zirconia), and the array of macropores has been proven to be regular enough to confer photon trap properties to the solid (Wijnhoven *et al.*, 1998; Megens *et al.*, 1997). Holland *et al.* (1999) produced detailed documentation on latex sphere templating of highly ordered three dimensional macroporous structures from crystalline inorganic oxides, phosphates and hybrid composites. The polystyrene spheres were first synthesized, and these spheres are later packed to form close-packed arrays upon centrifugation, and the precursor permeates the voids between the spheres, which later condenses into a hard inorganic framework upon drying.

The work of Velev *et al.* (1997) reported the synthesis of organized silica flakes of very low density by varying the size of the microspheres used to produce pore sizes in the macroporous range (ranging from 150 nm to 1μm). They filtered PS latex microspheres (size range 200 - 1000 nm) in an attempt to increase their volume fraction in the vicinity of a flat wall, through a smooth narrow pore membrane. The microspheres were later soaked in hexadecyltrimethly ammonium bromide to induce polymerisation, and the excess HTAB was removed by washing with deionised water. A silica solution was then

added to mineralise the cavities, and once it had gelled inside the colloidal crystal layer, the excess was removed and the composite was allowed to dry under vacuum. Finally the polymerised silica was removed by calcinations at 450 ^{o}C for 4 hours. Vandreuil *et al.* (2001) contributed to the method of synthesizing macrostructured silica from PS beads, by reporting a simpler and faster technique designated as Sedimentation-Aggregation, which does not involve any pre-ordered arrangement of the latex beads. The nearly monodispersed latex beads made of PS in the range 200 - 800 nm are polymerised at 70 ^{o}C for 28 hours in degassed water in the presence of potassium persulphate as an initiator, and divinylbenzene as a cross linking agent. The resulting beads of ~400 nm are obtained by filtration, and washed with methanol and dried under vacuum at 60 ^{o}C for 24 hours. The porous silica was obtained from a mixture of TEOS and ethanol in a beaker containing the PS beads, and after 20 min of stirring at room temperature, the beads were evenly dispersed in the liquid phase, and the magnetic stirrer was removed to allow sedimentation of the PS beads for 10 min. The excess TEOS and ethanol could be removed either by evaporation under vacuum or by a slight suction. The materials are then calcined at 900 ^{o}C for 4 hours, which is above the silica sintering temperature of 700 ^{o}C and is shown to retain its macropore structure as calcinations at 900 ^{o}C only affects the smallest pores (> 40 nm).

An attempt will be made at creating a macroporous 'two layer' structure similar to the bimodal structured material which will be created in the mesoporous range discussed earlier on. This development could also be used to test gas adsorption theories such as the effect of pore blocking, and the critical pore to throat size ratio, or the extent of pore size variations necessary for the entrapment of a non-wetting fluid.

3.6.4 - The Use of Co-surfactants

The main aim for the introduction of co-surfactant into the nanocasting technique is to control the pore size. An increase in the carbon chain length of the co-surfactant leads to a significant expansion in the mesopore size. Feng *et al.* (2000) experimented with different co-surfactants at the same weight concentration for each component in the initial mixture. They found that the pronounced increase in pore size is due to an increased hydrophobic volume of co-surfactant molecules, which acts as a special

swelling agent to enable a higher degree of control to pore sizes. Co-surfactants were used to create a large single hexagonal phase domain for the surfactant, which makes it possible to achieve the hexagonal mesophases with much less surfactant than in the binary (F127/water, or P123/water) system. The F127/cosurfactant/water ternary system can have concentration of as low as 20 wt% surfactant, whereas the range for the binary system is in the range 65 - 80 wt. %. The P123/co-surfactant/water ternary system exhibits a much smaller hexagonal phase domain with regards to the co-surfactant /surfactant ratio, as there is a small range of applicability for the desired cylindrical pores. In the ternary system, the hexagonal phase is only achievable at low co-surfactant/surfactant mass ratios (below ~ 0.3) as opposed to 65 - 80 % in the binary system. Both butanol and pentanol were used as co-surfactants, which both gave similarly ordered hexagonal mesoporous silica, however pentanol produces larger pores. The largest pore size achieved by Feng *et al.* (2000) is 148 Å at a ratio of 0.72 Pentanol/F127. Because of the large phase domain that exists for hexagonal structures, the F127-butanol-water system of hexagonal phase has been successfully synthesized by Feng *et al.* (2000), with co-surfactant/surfactant ratios ranging from 0 to ~ 0.8. Feng *et al.* (2000) showed that by templating with liquid crystals from tertiary systems it is possible to synthesize highly stable hexagonal mesoporous silica with a high degree of control on pore sizes. They observed a birefringent H1 phase immediately upon complete mixing of all components, and the fluid mixture usually turns rigid within a few hours. The resulting nitrogen adsorption-desorption isotherms were in agreement with results of previous researchers such as Rouquerol *et al.* (1999), who characterized the binary system of surfactant and water. They showed the expected type IV adsorption isotherm behaviour with a type H1 hysteresis loop.

In conclusion, the above synthesis technique has been shown to produce highly stable mesoporous silica from F127 and P123 ternary systems, whose pore sizes can be controlled by co-surfactant/surfactant mass ratios, and hydrothermal treatment prior to calcinations. This will be experimented upon to see the highest pore sizes attainable for an ordered structure either in the higher mesoporous or macroporous range. Attempts will also be made towards creating a large mesoporous or macroporous ‘two layer’ structure similar to the bimodal structured material produced in the mesoporous range earlier on in the course of research.

3.6.5 - Third Method of Synthesis

The objective of the third method of synthesis is to synthesize mesoporous media with larger pore sizes, by a method of templating of liquid crystals in block Copolymer- Co-surfactant-Water systems which has been reported to offer a higher degree of pore size control. Previous techniques of templating periodic mesoporous materials have only used a few surfactants in the surfactant/water binary system which have resulted in pore sizes that are limited by surfactant lengths and the restricted range of compositions (Attard *et al.*, 1995; Kresge *et al.*, 1992; Huo *et al.*, 1994). More specifically, triblock co-polymers such as F127 and P123 used in the first method of synthesis generally give rise to pore sizes of approximately 4 and 7 - 9 nm respectively (Feng *et al.*, 2000). However they are additionally required in the third method of synthesis to synthesise highly ordered mesoporous silica samples of much greater pore sizes, hence the addition of the co-surfactant to investigate the above possibility. The materials resulting from the third method of synthesis are produced by templating, using the tri-block copolymers as used in the previous method over several combinations of surfactant to co-surfactant ratios (typically alcohols such as pentanol and butanol). The combinations of mesoporous and microporous structures resulting from the second method of synthesis are shown in Table 3.2.

Table 3.2: Combination of samples from second method of synthesis

1	P123 + 0.18 g Butanol	5	F127 + 0.4865 g Butanol
2	P123 + 0.21 g Butanol	6	F127 + 0.973 g Butanol
3	P123 + 0.349 g Butanol	7	F127 + 1 g Pentanol
4	P123 + 1g Pentanol	8	F127 + 0.5004 g Pentanol

3.6.5.1 - Summary of Steps in Third Synthesis Method

Chosen co-surfactants: Pentanol and Butanol

1. Add 1.39 g of surfactant to a small medium sized glass vial.
2. Dissolve the surfactant in 2.50 g of tetramethlyorthosilicate.
3. Add the required co-surfactant amount to the mixture of surfactant and TMOS

4. Heat to approximately 40 ^{O}C in order to dissolve the surfactant into the TMOS solution. Care should be taken to prevent the polymerisation of the TMOS/ surfactant solution due to excessive heat.
5. The dissolved mixture will be a clear solution, which is then allowed to cool.
6. Add 1.39 g of 0.5 M HCL; note this results in an exothermic reaction.
7. Water driven suction pump is then used to evacuate the methanol vapour. Sufficient pressure is required to suck the methanol, however care should be taken to ensure the entire solution is not lost.
8. Place the solution in an oven at 45 ^{o}C for 5-7 days to ensure the mixture is treated sensitively at low temperature.
9. Break up any large pieces and keep some pieces uncalcined, so that when the particles are coated the pores don't fill up with the dip coating solution.
10. The surfactant remaining is then removed from the filled pores by calcining (burning out). This is carried out in a specialized oven at 600 ^{o}C for three hours and then allowed to cool gradually overnight, since surfactant calcining temperature is ~ 600 ^{o}C. The calcined samples are later used for the analysis of the internal structure.

The technique being adopted in this section is similar to that employed by Feng *et al.* (2000) but under strongly acidic conditions. The synthesis method of Feng *et al.* (2000) involved mixing an aqueous dilute HCL solution with TMOS to produce a homogenous mixture of colloidal silica on evacuation of the resulting methanol from TMOS hydrolysis, and then the homogeneous mixture of the colloidal silica, surfactant Pluronic F127 or P123, and pentanol was then placed on a centrifuge to remove bubbles. Since the above method of synthesis is typically performed at room temperature, and under weakly acidic conditions, a much higher concentration of unreacted silanol groups in silica-surfactant-co-surfactant mesophases is recorded in comparison to those prepared under strongly basic or acidic conditions. As a result, a large shrinkage in the spacing occurred during calcinations of the mesophases prepared by direct liquid crystal templating (Feng *et al.*, 2000). Feng *et al.*, (2000) also suggests the hydrothermal treatment of composite nanostructures at 100 ^{o}C for 24 hours before calcination in order to promote further cross-linking of the inorganic framework, which could be employed in future attempts.

3.6.6 - Fourth Method of Synthesis:

Structured materials synthesis has long been explored; however one goal in structural control has been to increase the size of pores to permit the penetration of larger molecules into the porous media. The fourth method of synthesis is therefore adopted, in quest for macroporous structured materials with pore sizes in the range 0.1 - 10 μm. The method of latex sphere templating of highly ordered three dimensional macroporous structures from crystalline inorganic oxides is being adopted within this research according to a standard recipe in the Edler Group, of the Dept. of Chemistry, University of Bath. This should create model porous media of ~ 70 nm which is in a pore size range directly applicable to reservoir characterization. The resulting macroporous silica solids could also be used to create bimodal structures to further investigate the effect of macroscopic heterogeneities in pore structures, and also to re-visit the effect of pore blocking over a wide range of pore to throat size ratio. This method involves the synthesis of polystyrene spheres with a narrow size distribution from an emulsion process using dicotyl sulfosuccinate as the emulsifier and then compacted and used as a template for the synthesis of macroporous solids. These spheres are packed to form close-packed arrays upon centrifugation, and the precursor (TMOS) permeates the voids between the spheres, which later condense into a hard inorganic framework upon drying.

3.6.6.1 - Summary of Steps of Polystyrene Latex Spheres Synthesis

Materials: $NaHCO_3$, Dioctyl Sulfosuccinate Na, Styrene, $K_2S_2O_8$,

1. Purify 65.5 g of Styrene monomer using a silica column, to remove the inhibitor that encourages polymerization.
2. Mix 0.22 g of $NaHCO_3$, 2.05 g of dioctyl sulfosuccinate Na with 171.5 g of water in a 500 ml flask, and dissolve.
3. Add the purified styrene to the mixture and shake to make emulsion.
4. Preheat the emulsion in an oil bath to 70 ^oC.
5. Preheat 15 g of water (second water) in the bath to 70 ^oC.
6. Dissolve 0.225 g $K_2S_2O_8$ in the second water, and then add to bottle with other reactants. Close bottle tightly using Teflon tape to prevent O_2 access.

7. React in an oil bath at 70 ^{o}C whilst stirring at 200 rpm with a bar for 24 hours.
8. The resulting milky solution should be transferred into dialysis tubing.
9. Dialyse solution against water for 3 days with several changes of water per day, in order to get rid of excess surfactant and unreacted waste.
10. Filter through glass wool to remove coagulant.

All the water in the synthetic steps was deionised and the styrene was purified through a column made from glass wool. The flask containing the solution of $NaHCO_3$ and dioctyl sulfosuccinate was put on a plate with an electric motor driving a glass-stirring rod, until the contents had dissolved into the water.The purified styrene was added to the solution, resulting in a milky emulsion. The first water solution was heated to 70 ^{o}C and the solution from the second water already heated to 70 ^{o}C too was then mixed together in the 500ml flask resulting in a milky solution. The temperature was kept at 70 ^{o}C while the solution was stirred and heated in an oil bath for 24 hours. Dialysis is employed after the synthesis process to purify the solution containing formed spheres and to rid of any unwanted by-products by using semi-permeable dialysis tubing created from a natural source of cellulose that allows the passage of particles of molecular weight up to 14000 g/mol. It was filled with the solution, and then covered in water; the osmotic pressure drives the separation, to remove the surfactant and the remaining un-reacted materials. Efficient dialysis relies upon appropriate selection of the dialysis tubing and several washes with distilled water.

3.6.7 - Increasing the Size Polystyrene Beads

The size of the synthesized spheres, determine the pore sizes of the resulting silica solids, and following the initial synthesis stage, in an attempt to increase the size of the polystyrene beads, 1 ml of styrene is added to 20 ml of the polystyrene beads in solution. This is then allowed to stir for 12 hours, and then heated for approximately 5 hours to allow the polymerization of styrene. The spheres were initially formed from polymerised styrene, so are hydrophobic, and are suspended in water/their own liquor. Styrene itself is hydrophobic, and as such it separates from the water if it is not stirred. When mixing the added styrene with the polymerised styrene spheres suspended in their

liquor, the styrene will prefer to be inside the spheres than in the water, as the stirring goes on. So the styrene goes into the spheres and the spheres swell because you have "dissolved" the polystyrene chains in styrene. Then after the stirring step, the solution is heated at 70 ^{o}C overnight, to polymerise the new styrene inside the spheres, making them solid.

3.6.8 - Synthesis of Macroporous Solids

The resulting latex spheres were left suspended in their mother liquor, until they were needed for use as structure directing agents. For the synthesis of macroporous solids, the latex spheres or polystyrene beads (PS) were compacted, using a centrifuge at 10000 rpm for a few hours, until close packed spheres were gathered at the bottom, and a clear solution (water) at the top. The water was tipped off, and the spheres were allowed to air dry. The diameter of the spheres was estimated using scanning electron microscopy (SEM) to be within the range 0.1 - 0.3 μm, which should produce pore sizes well above 100 nm. Holland *et al.* (1999) used a similar technique of PS synthesis, under varied conditions, and they produced spheres with diameters ranging from 0.4 – 0.697 μm (421 nm – 697 nm) with stir rates of 245 - 360 rpm resulting in latex particle templated materials of micron scale pore sizes, which are equivalent to the size of the PS beads synthesized.

Macroporous silica solids were then prepared by placing millimetre-sized chunks of dried latex spheres in a Buchner funnel attached to a vacuum suction, and wetting with approximately 1ml of butanol prior to adding the silica. The butanol is added to adjust the viscosity of the solid packed spheres and to make them more hydrophobic towards the alkoxides and to ensure that all the spaces between the latex particles are filled with silica walls. TMOS is used again as a source of silica and the process of wetting the particles is done multiple times. About 10 ml of solution was used per 0.25 g of dried spheres. The coated spheres were then allowed to air dry gradually over several days. The Polystyrene spheres were removed from the inorganic framework by calcining at 600 ^{o}C for 3 hours, to expose the walls between the silica walls.

Macroporous calcium carbonate solids could also be synthesized by the crystallization of calcium carbonate on latex particles which serve as templates. The $CaCl_2$ solution is used to re-wet the dried latex pellets in the same manner as done with the silica particles. The wetted pellet is then placed in the sealed container next to a dish containing 1.5 g $(NH_4)_2CO_3$ to allow crystallization by the diffusion of CO_2 into the $CaCl_2$ around the latex particle. This is repeated several times, (re-wetting the latex particle with $CaCl_2$ solution) and then putting the pellet back into the sealed container with $(NH_4)_2CO_3$ in order to fill all the spaces between the latex particles with $CaCo_3$. An attempt has been made towards synthesising calcium carbonate solids with some success, however due to time limitations it could not be pursued further.

3.6.9 - Soxhlet Extraction

As an alternative to calcinations at 600 ^oC, to attain milder conditions, in order to maintain delicate surface chemistry during template removal, soxhlet extraction method is adopted to remove the PS templates. A funnel containing a filter paper carrier, in which the sample sits, is placed over the extracting solvent in a round bottom flask and sealed. A condenser is placed over this arrangement, and sealed together. The solvent is heated so that it evaporates, through the sample, and condenses back onto the sample contained in a cylindrical paper filter. The solution eventually drips through to the flask after collecting on the side of the funnel, extracting the surfactant (in the case of the Hydrophobic P123 and F127 templated solids) or the polystyrene spheres, (in the case of macroporous materials synthesized from PS), to open up the pores.

3.7 - Characterisation

3.7.1 - Nitrogen Adsorption

Nitrogen adsorption is used to characterize the structures of all the materials synthesized within this research, and it is also used to identify the effects of the various pore size modifications techniques. Nitrogen adsorption experiment is also used to characterize the P123 (hydrophobic) to investigate the effect of the difference in surface chemistries between the hydrophilic materials synthesized under the first method of synthesis and the hydrophobic silica surfactant templated materials synthesized by the second method of synthesis. These materials possess a lesser affinity for water than the materials synthesized in the first method, due to the extra methyl group (CH_3 bond) that exists in the structure, as opposed to the hydroxyl bonds in the latter.

The nitrogen adsorption experiments at 77 K were performed using a Micrometric Accelerated Surface area and porosimetry (ASAP) 2010, which is a volumetric adsorption apparatus. Volumetric gas adsorption (manometry) is based on the measurement of the pressure of the adsorptive gas at constant temperature before and after the adsorption by a given mass of adsorbent. Therefore in the ASAP, the amount adsorbed is evaluated from the change of pressure. The sample to be analysed is placed in a round bottom tube, and a glass rod is placed gently into the sample tube, to reduce the free space volume and then sealed. The weight of the tube and the glass rod is recorded, and hence the sample initial weight is known. The first stage of the analysis is to degas the sample, to drive off any physisorbed water on the sample, without changing the sample morphology. The sample tube is then loaded into the degassing port, and a heating mantle is attached and heated under vacuum at a 170 ^{o}C overnight. It is essential to degas the sample effectively, as any liquid present on the sample will hinder the adsorption of nitrogen molecules into the sample, and hence provide inaccurate results. The ASAP 2010 has a facility to ensure that the sample has reached vacuum. Once this check has been completed, the degassed sample is then allowed to cool off. The sample tube and its contents are then reweighed to obtain the sample dry weight, which is then entered into the analysis data, prior to the analysis, in order to calculate the volume adsorbed per gram of sample. The sample tube is placed in liquid nitrogen at 77 K prior to the adsorption measurements. A piece of foam is used to cover the liquid nitrogen

tanks to prevent evaporation of the liquid nitrogen. A leak test, and a free space analysis is set up to occur during the analysis, and an equilibration time of 45 s was allowed for each adsorption point.

The full adsorption/desorption isotherms obtained were analysed using the previously discussed, well-known BJH method to obtain the pore diameter distributions (PDD). The film thickness for multilayer adsorption was accounted for by using the well-known Harkins and Jura equation. In the Kelvin equation, the adsorbate property factor was taken as 9.53×10^{-10} m and it was assumed that the fraction of pores open at both ends was 0.0 for both adsorption and desorption. It was therefore assumed that capillary condensation commenced at the closed end of a pore to form a hemispherical meniscus and the process of evaporation also commenced at a hemispherical meniscus.

3.7.2 - Scanning Electron Microscopy and Transmission Electron Microscopy.

The shapes and sizes of the Polystyrene beads (PS) used as templates for porous media synthesis were obtained using both scanning electron microscopy and transmission electron microscopy, since in order to synthesise ordered mesoporous materials, it is essential to have synthesised uniform polystyrene spheres. The form of packing resulting from compaction taken by these spheres is, in itself, interesting, as the resulting templated material is expected to conform to even the littlest detail of the consolidated structure. Micrographs of the silica solids were also obtained by using both SEM and TEM to show the finished product when the PS is removed by calcining.

3.7.2.1 - Scanning Electron Microscopy (SEM)

An extension of magnification by several orders of magnitude up to about 100,000 is obtained with the SEM. SEM gives an extension to light microscopy, and the added advantage of much better depth of focus, and its image has an inherent three-dimensional (3D) appearance, which gives realism to surfaces with a rough or porous

structure. The sample preparation is usually simple and quick, and it accepts macroscopic-sized specimen.

3.7.2.2 - Transmission Electron Microscopy (TEM)

The TEM gives a higher resolution in comparison to the SEM, and the operation is more complicated. The sample is prepared by diluting in water, as high density sample will lead to extremely difficult interpretation of the electron micrographs. Here the electron beam is transmitted through the sample, and commercial instruments are routinely used at final magnifications of millions of times since the sizes of the spheres are generally larger in Figure 2.20, 2.21 and 2.22, than in reality (for example a primary magnification of 500,000 x followed by optical enlargement up to 10 x) to produce micrographs with detail of at least atomic dimensions.

3.8 - Results and Discussions

The results section consists of results from the N_2 adsorption experiments for all test samples, as well as the SEM/TEM images. The adsorption isotherms for F127, P123 and CTAB along with those of the corresponding composite materials are shown and discussed in detail, and a theory is proposed. By the use of different templates and through modification to these standard templates, a range of varying pore structure combinations are achieved and analysed to establish any trends and to further support any theories proposed. Tables 3.4 to 3.8 contain the results summary of the pore structure parameters obtained for all the synthesised materials reviewed within this research. The general collection of isotherms, BET plots and pore size distribution curves for the work done here, can be found in Appendix B.

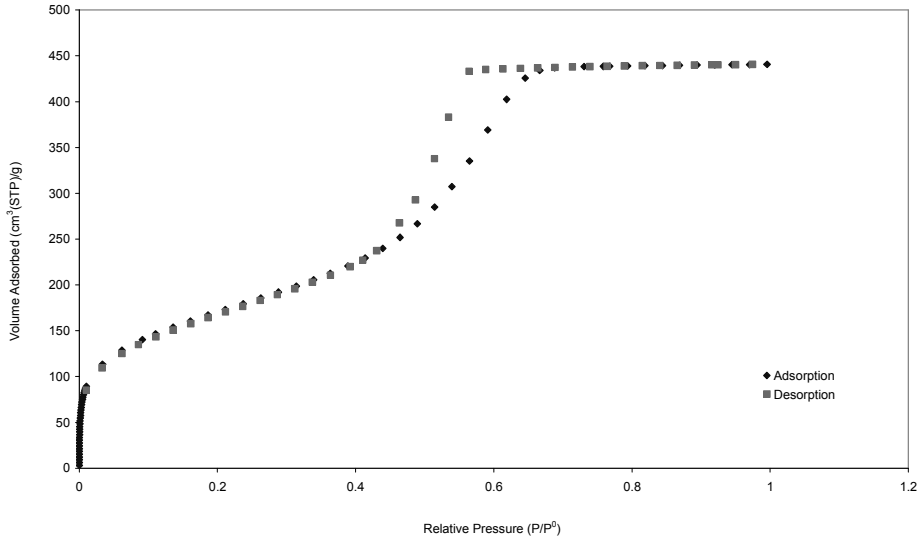

Figure 3.4: P123 core Expt. 1 N_2 isotherm at 77 K.

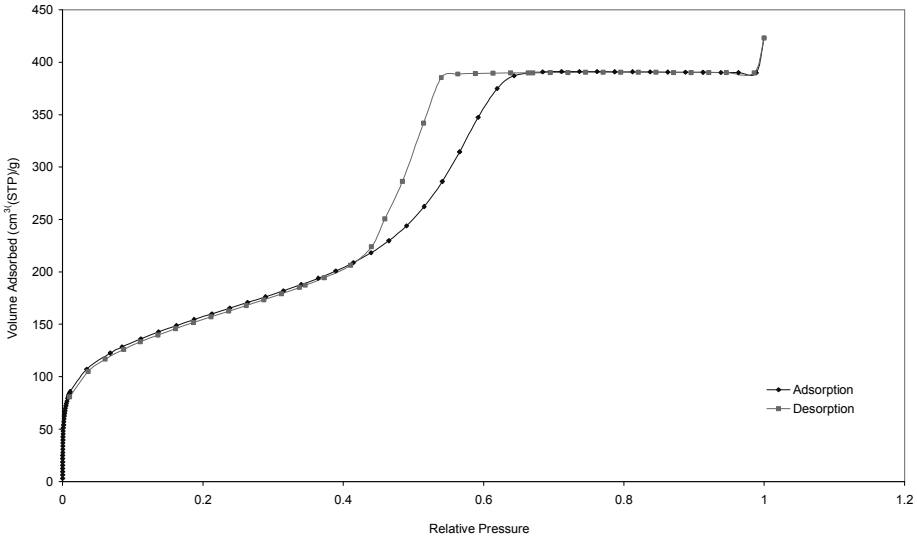

Figure 3.5: P123 core Expt. 2 N_2 isotherm at 77 K.

Both isotherms for P123 templated cores (Figure 3.4 and 3.5) produce a typical type IV isotherm, which implies the test material is predominately of a mesoporous structure. The high uptake of nitrogen at $P/P^0 = 1$, after what appears to be complete filling could be a result of high interaction strength between the adsorbent and adsorbate or the existence of some macroporosity. At relative pressure ($P/P^0 = 1$) in Figure 3.5 it can be seen that a further increase in mass uptake is possible, even though the final mass

uptake for both samples are close to 450 cm^3/g. At $P/P^0 = 1$, the further increase in mass uptake could be attributed to adsorption occurring on the outside of the sample. It is worth noting that the sample in expt. 2 (Figure 3.5) weighed 0.04 g while expt. 1 (Figure 3.4) weighed 0.09 g. The reason why specific quantities are used is to allow comparisons between samples of different mass. Therefore it can be assumed that the bulk condensation of the adsorbate at $P/P^0 = 1$ in expt. 2 suggests that perhaps the ASAP machine has got close enough to $P/P^0 = 1$ for bulk condensation or big macropores exists in the material, for example in the form of cracks. It is also very interesting to note that the shape of the hysteresis loop for both analysis is similar and occurs for both cases at relative pressures close to 0.5 which is within the region where the limit of the stability of condensed nitrogen in the pores is exceeded and hence becomes thermodynamically unstable. The produced hysteresis is of type H1 according to IUPAC classifications. The HK median pore diameter is 73.3 Å and 89.5 Å respectively. The surface area measurements for the samples are stated in Table 3.3 for expt.1 and expt.2 respectively.

Table 3.3 P123 Core Surface Area Measurements

Experiment 1	$594.0 \pm 4.7\ m^2/g$
Experiment 2	$535.0 \pm 4.9\ m^2/g$

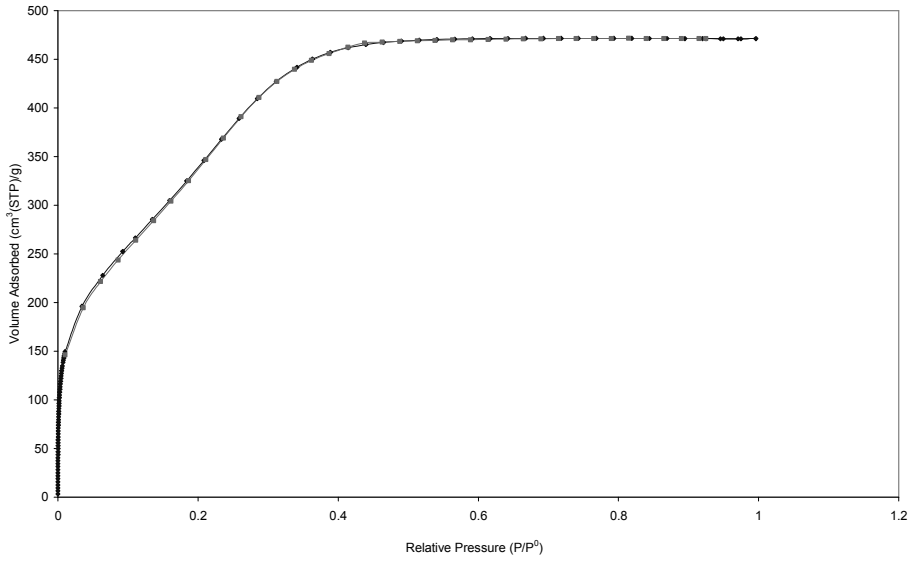

Figure 3.6: CTAB core Expt. 1 N_2 isotherm at 77 K.

Figure 3.6 shows the nitrogen sorption isotherm for a CTAB templated core which most closely matches the type I isotherm, typical of a microporous solid. The sample does not exhibit hysteresis, probably due to the fact that the maximum adsorbed volume occurred at a much lower relative pressure than in the previous pluronic P123 samples. It is worthy to note, that the lower limit for hysteresis for N_2 is ~ 0.4 and it is a property of the fluid itself (Rouquerol *et al.*, 1999). The complete reversibility is most likely due to the previously mentioned meniscus forces having an effect upon the condensing layer's on each side of the pore wall. This means that because the walls are much closer together in the smaller diameter pores condensation of multiple layers will occur much more rapidly and at lower relative pressures. The absence of hysteresis could also be explained by the successful attempt to achieve extremely ordered cylindrical mesopores in the hexagonal phase. Although it is hoped that the synthesized materials are highly ordered, it is highly unlikely that it will avoid hysteresis in one sample and not in the other sample of varying surfactant but similar method of synthesis. Hence one is led to think, that the multilayer condensation meniscus effect is the most likely cause. When micropores exist, the HK median pore diameter will be considered to be a more accurate estimate of the pore size. The measured HK median pore diameter for the CTAB material is 31.0369 Å. The BET surface area was calculated to be 1330.4 m^2/g (± 37.1), which is much higher than that of Pluronic P123 samples (~ 564.5 m^2/g) which have been to shown to possess very thick walls (Feng *et al.,* 2000) not likely present in CTAB materials.

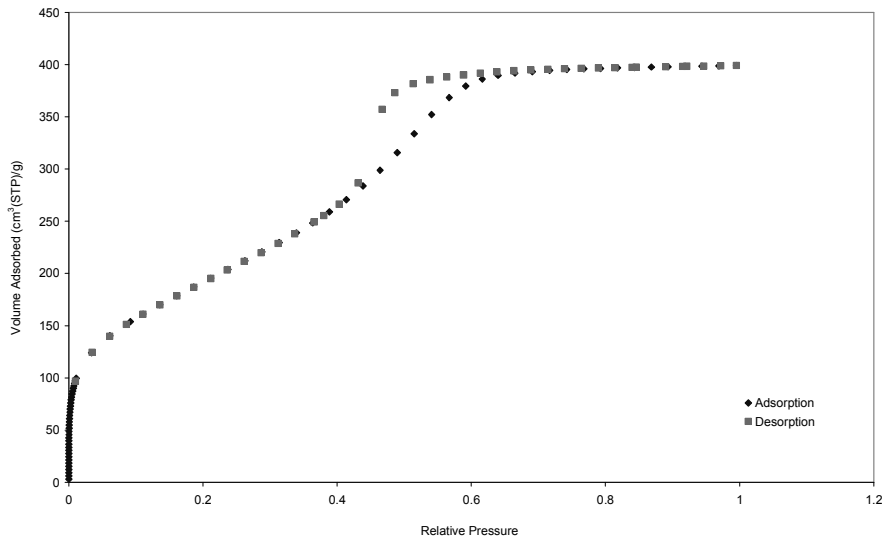

Figure 3.7: P123 coated in CTAB Expt. 2 N_2 isotherm at 77 K.

Figure 3.7 shows the isotherm of a mesoporous material of type IV according to the IUPAC classification, which is typical of the monolayer–multilayer coverage to capillary condensation pattern. The P123 coated in CTAB isotherm, reflects a material with a somewhat irregular cylindrical mesopores that are accessible only through permeable miroporous outer shell (CTAB templated). There is not an apparent step in the adsorption curve, which suggests the presence of a range of pore sizes, because although the progressive filling of a single sized pore is possible under the right conditions, it is however rare in literature. This is evident from the desorption branch of the isotherm and the shape of the hysteresis loop is characteristic of the of inkbottle pores Ravikovitch and Neimark (2002).

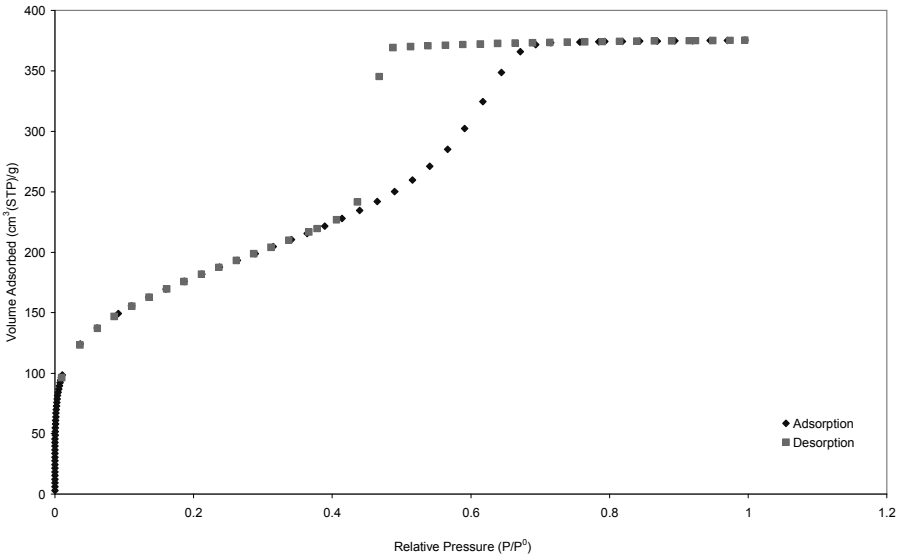

Figure 3.8: F127 core Expt. 1 N_2 isotherm at 77 K.

The Pluronic F127, which is a triblock copolymer like the Pluronic P123 produces a type IV isotherm as is expected, of surfactant micelles of same group. The broader hysteresis loop more closely resembles that of type H2 discussed previously in the adsorption isotherm section of Chapter 2. However the occurrence of this hysteresis loop at a relative pressure below the cut-off of 0.5 and the relatively steep decline in the desorption isotherm suggests that in this case, the evaporation of condensed nitrogen is caused by cavitation of the stretched metastable liquid ((Ravikovitch and Neimark, 2002). This is further supported by the work of Morrow and Harris (1965), where he

drew attention to the fact that the lower closure point of the hysteresis loop of nitrogen at 77 K is frequently situated at a relative pressure close to 0.42 but never below. The author examined over a hundred nitrogen isotherms, and half showed a sharp fall in adsorption, with loop closure, in the relative pressure range 0.42 - 0.52. Interpreted naively by a Kelvin type analysis, these observation would imply that a large proportion of adsorbents possess an extensive pore system in the very narrow range 17 Å < r_p < 20 Å with a sudden cut-off around 17 Å which corresponds to P/P^0 = 0.42. F127 templated solid has been shown to possess a very narrow neck size, in comparison to the pore body size as can be seen from the data set and one is led to think that this is probably the cause of the peculiar mechanism. The HK median pore diameter is 53.0 Å.

Bimodal materials were later created by dipping core samples still containing their templates in a viscous solution to ensure the formation of a thin layer of coat which should guarantee only a different pore size material on the outside and not on the inside.

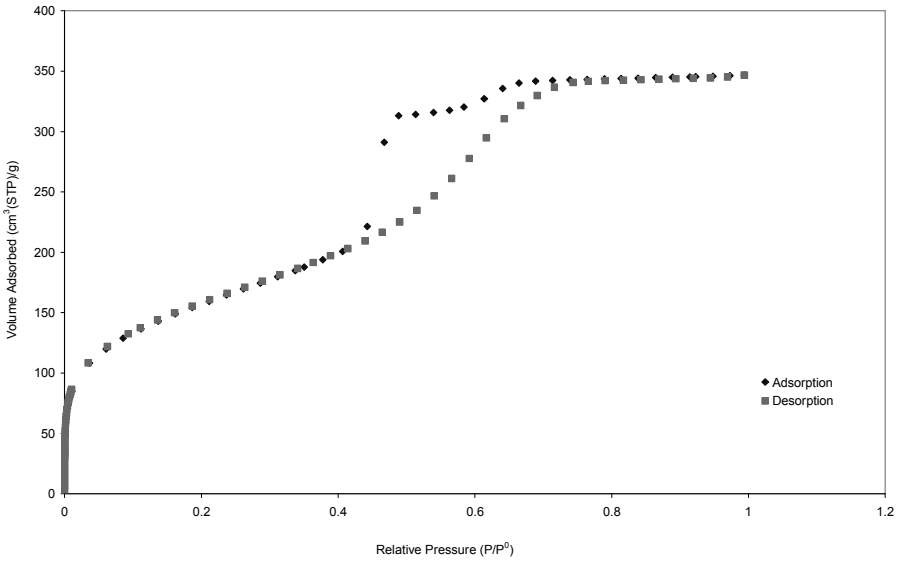

Figure 3.9: F127 coated in P123 N_2 isotherm at 77 K.

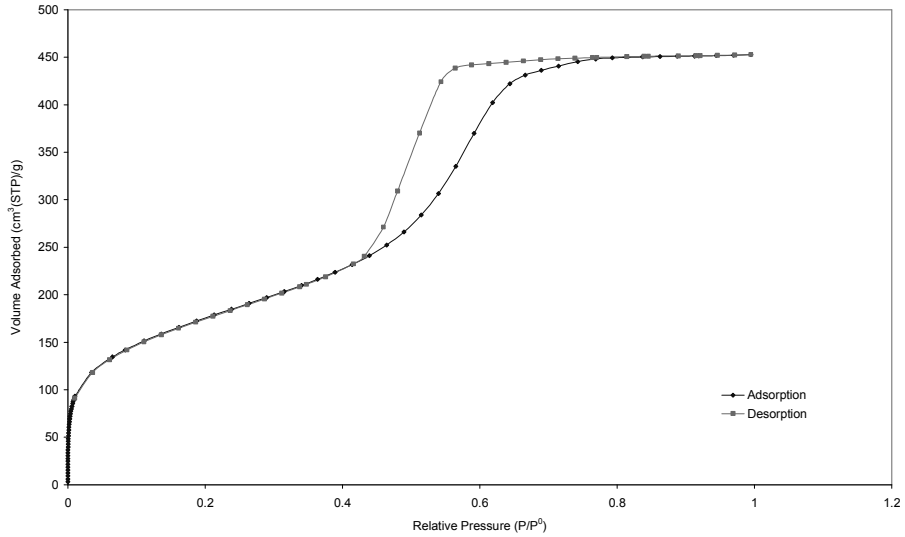

Figure 3.10: P123 coated in F127 N_2 isotherm at 77 K.

Samples from the same batch of core materials had been synthesised prior to coating, to obtain an independent record of the structural characteristics of the core materials only. Figure 3.9 shows the nitrogen sorption isotherm for F127 coated in P123, whilst Figure 3.10 shows the nitrogen sorption isotherm for another composite material (P123 coated in F127). Figure 3.11 shows the nitrogen sorption isotherms for samples taken from typical batches of the P123 and F127 core materials superimposed for ease of comparison whilst Figure 3.12 shows nitrogen sorption isotherms for the two different core-shell composite materials where P123 forms the core and F127 the shell, or vice-versa, as shown separately in Figures 3.9 and 3.10 for ease of comparison. It can be seen from the final volumes adsorbed at high relative pressures that the specific pore volume of P123 is much higher than that for F127 (see Figure 3.11). It can also be noted that the knee in the desorption isotherm of the F127 material occurs at a relative pressure of 0.47 and is followed by a near vertical drop (compared to the adsorption isotherm) in amount adsorbed. In contrast, the desorption knee for P123 occurs at the higher relative pressure of 0.54, and the subsequent drop in amount adsorbed is much less steep than for F127. Due to the particular position of the knee and the relatively steep subsequent decline in the desorption isotherm for F127, it is likely that, in this case, the evaporation of condensed nitrogen is caused by cavitation of the stretched metastable liquid (Ravikovitch and Neimark, 2002), whereas the evaporation of nitrogen from P123 is controlled by pore-blocking effects. Evaporation by spontaneous

cavitation is characteristic of a pore structure consisting of relatively large pore bodies guarded by narrower pore necks of diameters narrower than a characteristic size of ~ 4 nm. In general, it can be seen from Figure 3.11 that F127 and P123 have very characteristically different isotherms. From Figure 3.12, the desorption isotherm for F127 coated in P123 can be seen to have two steps, one at a relative pressure of ~ 0.6, and one at ~ 0.46. The occurrence of the two separate steps in the desorption isotherm suggests that the above synthesis procedure does lead to core-shell composites that contain two separate regions of differing porosity and pore geometry, one with the F127-type structure and one with the P123 structure. Hence, it is unlikely that either the shell solution, or the coating procedure, have filled or disrupted the pore structure of the core. The more rounded shape of the desorption knee for the P123 shell in Figure 3.11, when compared to that of the P123 core in Figure 3.12, is probably due to smaller thickness of the shell relative to the core. A more rounded desorption knee is associated with the more smeared out percolation transition that takes place in smaller pore networks. Since the condensed nitrogen evaporates from the shell before it does so from the core, the desorption behaviour of the nitrogen in the shell does not influence that in the core. In contrast, the desorption isotherm for the P123 core coated in the F127 shell does not contain two separate steps, and the position of the single desorption knee is delayed to lower relative pressures compared to the initial knee for F127 coated in P123. Figure 3.12 also suggests that the tail end of the hysteresis loop of the P123 core smoothly joins with the shape of the hysteresis loop of the F127 shell. For both composites, the cumulative amount adsorbed at the highest relative pressures is intermediate between the corresponding values for the separate F127 core and P123 core materials shown in Figure 3.11. It can be seen from Table 3.5 that the BET surface area data for the bimodal samples is close to an average of both core materials indicating the formation of a successful coat of smaller pores and also an inner core material of larger pore. More so it provides supporting information for pore blocking phenomena as the likely cause for reduction in the surface area measurement.

For P123 coated in CTAB material shown in Figure 3.13, the bulk of the sample is P123 core, and hence the adsorption properties exhibit a P123 trend, as the coat is only a thin layer added on. The adsorptive properties did not vary as much as one would expect following the large differences in the modal pore body sizes of P123 and CTAB core samples. This is probably because the coat is a thin layer and although it leads to a

reduction in maximum volume adsorbed it cannot totally change the shape of the isotherm, which is a direct behaviour of the bulk of the sample. The coating technique of applying a thin layer on the outside yields limited heterogeneity and hence the little microporous shell, is probably insufficient to effect major changes. Notwithstanding CTAB can be used to restrict the adsorption volume of P123. Figure 3.13 shows a reduction in the maximum volume adsorbed for the P123 coated in CTAB, in comparison to P123 core, suggesting that pore blocking effects may be causing a decrease in mass adsorbed. This can be explained by interconnectivity and percolation theories based on pore blocking effects. Since in the composite materials larger sized pores are covered by smaller pores, the coat will limit adsorption, until the pressure and conditions required to penetrate the micropores is reached, and also in the case of desorption until the pressure required for condensed nitrogen to evaporate from the micropores is reached. By comparing the cumulative pore area and the cumulative pore volume against a given pore diameter the relative spread of the coated samples and the core sample for large pore materials coated in smaller pore sizes (such as P123 coated in CTAB, Brij 76 coated in CTAB, and F127 + 1 g pentanol coated in CTAB), can be seen in the Appendix B. For all composite samples of CTAB, there is an increase in the cumulative pore area confirming existence of a coat of microporous nature. These outcome suggest that the coated sample lowers the pore volume and area for a given minimum pore diameter over the entire range. This is probably due to the fact that the smaller pores present in the CTAB sample though in a small proportion, are affecting the minimum pore diameter at which a given desorption occurs.

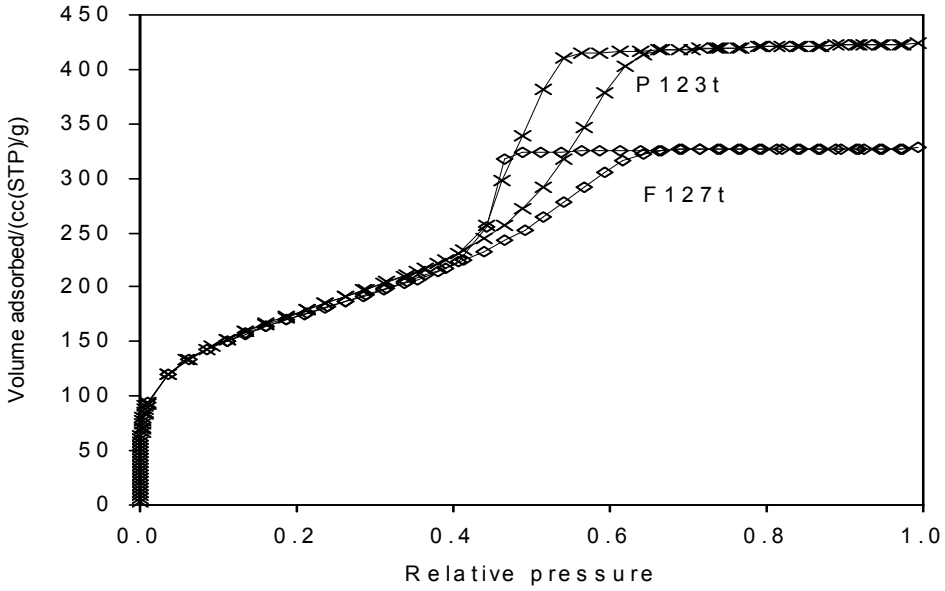

Figure 3.11: Nitrogen sorption isotherms for P123 and F127 core materials.

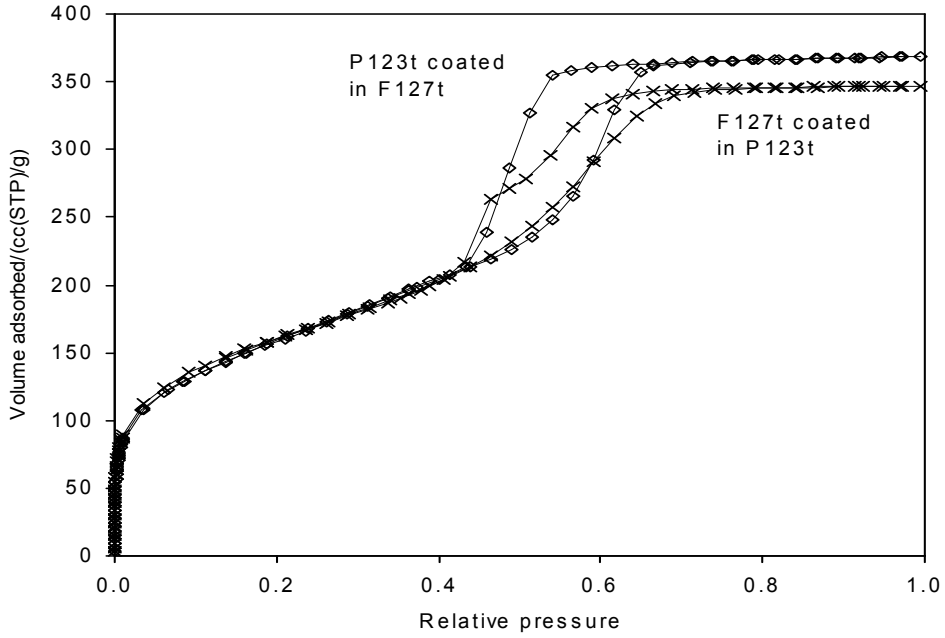

Figure 3.12: Nitrogen sorption isotherms for P123 and F127 composite materials superimposed.

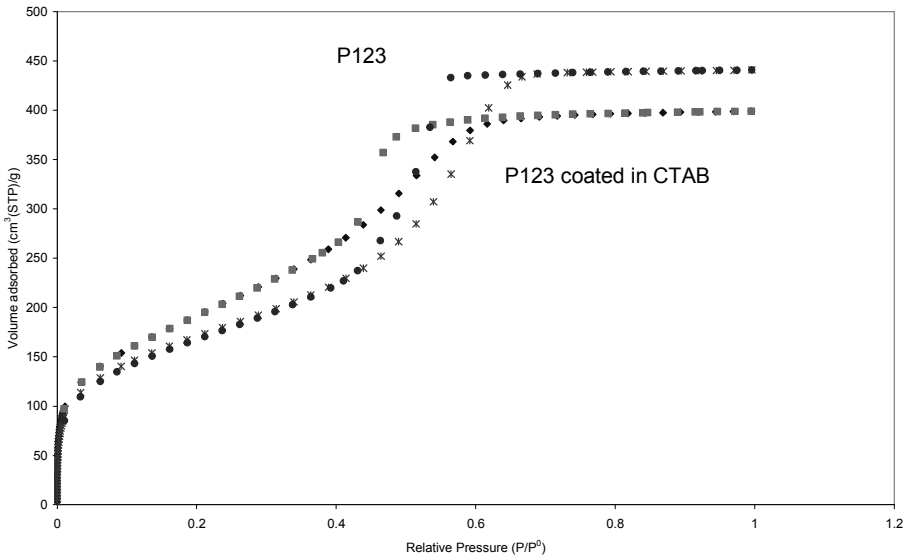

Figure 3.13: Nitrogen sorption isotherms for P123 and CTAB composite materials.

Table 3.4: Shows N_2 Sorption Results for Core Materials

	P123 core expt. 1	P123 core expt. 2	F127 core expt. 1	F127 core expt. 2	CTAB Core	Brij 76 Core	Brij 56 Core
BET Surface Area (m^2/g)	594.0	535.0	592.8	524.3	1330.4	914.1	909.9
BJH Adsorption Cumulative Surface Area of pores between 17 and 3000A Diameter (m^2/g)	583.0	534.4	448.1	413.6	779.7	701.3	534.9
BJH Desorption Cumulative Surface Area of pores between 17 and 3000A Diameter (m^2/g)	703.5	641.6	627.7	553.2	783.5	806.0	708.1
BJH Adsorption Cumulative Pore Volume of pores between 17 and 3000A Diameter (cm^3/g)	0.6	0.5	0.4	0.4	0.4	0.5	0.4
BJH Desorption Cumulative Pore Volume of pores between 17 and 3000A Diameter (cm^3/g)	0.6	0.6	0.5	0.4	0.4	0.5	0.4
BJH Adsorption Average Pore Diameter (4V/A) (Å)	37.9	40.5	36.9	34.9	21.6	26.7	26.8
BJH Desorption Average Pore Diameter (4V/A) (Å)	35.4	34.4	31.7	31.2	21.8	26.6	0.4
Horvath-Kawazoe Median Pore Diameter (Å)	73.3	89.5	53.0	51.3	31.0	45.3	37.5

Table 3.5: Shows N_2 Sorption Results for Coated Particles

Samples	P123 core expt. 1	P123 coated in CTAB expt. 1	F127 core expt. 1	CTAB	P123 coated in F127 expt. 1	F127 coated in P123 expt. 1
BET Surface Area (m^2/g)	594.0	735.69	592.75	1330.42	596.0	527.2
BJH Adsorption Cumulative Surface Area of pores between 17 and 3000A Diameter (m^2/g)	583.0	549.9	448.1	779.7	573.1	397.3
BJH Desorption Cumulative Surface Area of pores between 17 and 3000A Diameter (m^2/g)	703.5	678.2	627.7	783.5	719.5	555.5
BJH Adsorption Cumulative Pore Volume of pores between 17 and 3000A Diameter (cm^3/g)	0.6	0.4	0.4	0.4	0.6	0.4
BJH Desorption Cumulative Pore Volume of pores between 17 and 3000A Diameter ((cm^3/g))	0.6	0.5	0.5	0.4	0.6	0.4
BJH Adsorption Average Pore Diameter (4V/A) (Å)	37.9	31.3	36.9	21.6	39.3	38.8
BJH Desorption Average Pore Diameter (4V/A) (Å)	35.4	29.5	31.7	21.7	35.6	33.4
Horvath-Kawazoe Median Pore Diameter (Å)	73.3	45.0	53.0	31.0	84.2	59.4

Table 3.6: N_2 Sorption Results [After Enlarging Pore Sizes Of Triblock Co-Polymers by the Addition of Alcohol. (Third Method of Synthesis)]

	P123 + 0.349 Butanol	P123 + 0.21 Butanol	P123 + 0.18g Butanol	F127 + 1g Pentanol	F127 + 0.5004g Pentanol
BET Surface Area (m^2/g)	536.2	583.2	46.3	517.9	530.5
BJH Adsorption Cumulative Surface Area of pores between 17 and 3000A Diameter (m^2/g)	564.4	639.3	50.4	497.0	481.8
BJH Desorption Cumulative Surface Area of pores between 17 and 3000A Diameter (m^2/g)	675.3	750.0	58.4	600.9	591.6
BJH Adsorption Cumulative Pore Volume of pores between 17 and 3000A Diameter (cm^3/g)	0.6	0.7	0.1	0.6	0.5
BJH Desorption Cumulative Pore Volume of pores between 17 and 3000A Diameter (cm^3/g)	0.6	0.7	0.1	0.6	0.6
BJH Adsorption Average Pore Diameter (4V/A) (Å)	43.0	42.1	39.7	47.1	39.8
BJH Desorption Average Pore Diameter (4V/A) (Å)	38.0	39.5	37.3	42.2	36.9
Horvath-Kawazoe Median Pore Diameter (Å)	101.9	103.3	93.4	53.0	79.2

Table 3.7: N_2 Sorption Results for Coated Materials (Showing the Effect of Smaller Pores Coated Over the Largest Pores Achieved within this Research)

Samples	P123 + 0.349 Butanol	P123 + 0.21 Butanol	F127 + 1g Pentanol	F127 + 1g Pentanol Coated in P123	F127 + 1g Pentanol Coated in CTAB
BET Surface Area (m^2/g)	536.2	583.2	517.9	406.6	1187.5
BJH Adsorption Cumulative Surface Area of pores between 17 and 3000A Diameter (m^2/g)	564.40	639.31	496.95	383.15	634.4
BJH Desorption Cumulative Surface Area of pores between 17 and 3000A Diameter (m^2/g)	675.3	750.0	601.0	477.2	791.1
BJH Adsorption Cumulative Pore Volume of pores between 17 and 3000A Diameter (cm^3/g)	0.6	0.7	0.6	0.5	0.4
BJH Desorption Cumulative Pore Volume of pores between 17 and 3000A Diameter(cm^3/g)	0.6	0.7	0.6	0.5	0.5
BJH Adsorption Average Pore Diameter (4V/A) (Å)	43.1	42.1	47.1	50.2	27.0
BJH Desorption Average Pore Diameter (4V/A) (Å)	38.0	39.5	42.2	45.2	23.4
Horvath-Kawazoe Median Pore Diameter (Å)	101.9	103.3	53.0	117.8	19.1

Table 3.8: Shows N_2 Sorption Results for P123 Core Materials from First and Second Method of Synthesis

Samples	P123 core expt. 1 (Hydrophilic)	P123 core expt. 2 (Hydrophilic)	P123 expt.3 (Hydrophobic)
BET Surface Area (m^2/g)	594.0	535.0	229.3
BJH Adsorption Cumulative Surface Area of pores between 17 and 3000A Diameter (m^2/g)	583.0	534.4	121.8
BJH Desorption Cumulative Surface Area of pores between 17 and 3000A Diameter (m^2/g)	703.5	641.6	148.4
BJH Adsorption Cumulative Pore Volume of pores between 17 and 3000A Diameter (cm^3/g)	0.6	0.5	0.1
BJH Desorption Cumulative Pore Volume of pores between 17 and 3000A Diameter (cm^3/g)	0.6	0.6	0.1
BJH Adsorption Average Pore Diameter (4V/A) (Å)	37.8	40.5	23.8
BJH Desorption Average Pore Diameter (4V/A) (Å)	35.4	34.4	23.7
Horvath-Kawazoe Median Pore Diameter (Å)	73.3	89.5	27.7

3.8.1 – Images

The polystyrene latex spheres synthesised in section 3.6.6 (Sample a) and 3.6.7 (Sample B) are scanned using SEM and TEM prior to templating to confirm the size range and order of packing. Three TEM scans have been obtained for Sample a, denoted *a1*, *a2, and a3* and for Sample B, denoted *B1, B2, and B3* as shown in Figure 3.14. It can be seen from Figure 3.14 that Sample B has an average sphere size of ~150 nm whilst Sample a, has an average size of ~ 100 nm. The results of the TEM show that the addition of styrene before heating can lead to further polymerisation and thereby having a swelling effect on the already synthesised spheres. The SEM technique was used to obtain micrographs of the dried centrifuged PS spheres as seen in Figure 3.15. It is also interesting to note the level of highly ordered packing obtained for these materials evident from the alignment across the edges as well as the surface of the layered packing that is achieved by centrifuging.

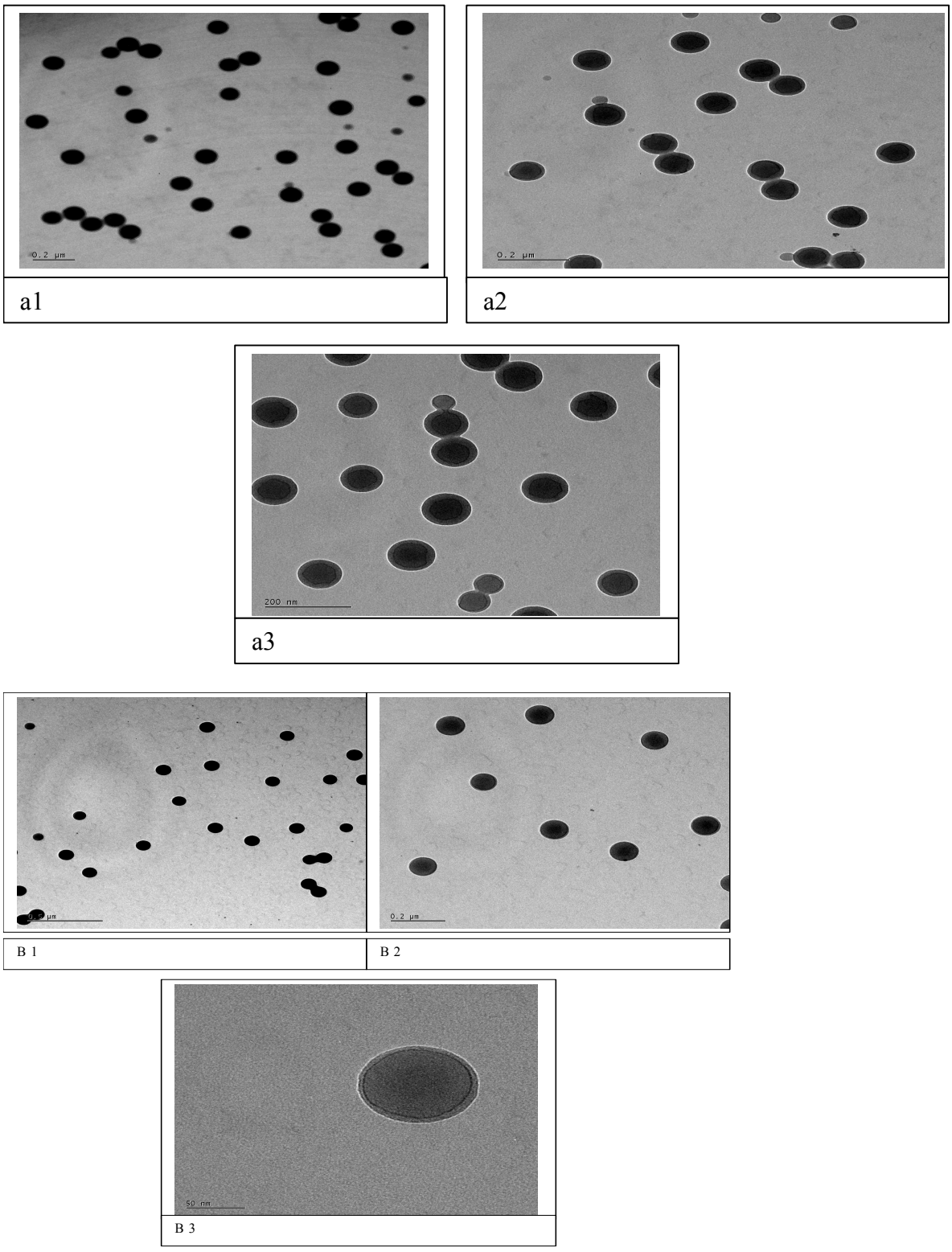

Figure 3.26: TEM images for sample 1 (a1, a2, a3) and TEM images for sample 2 (B1, B2, B3)

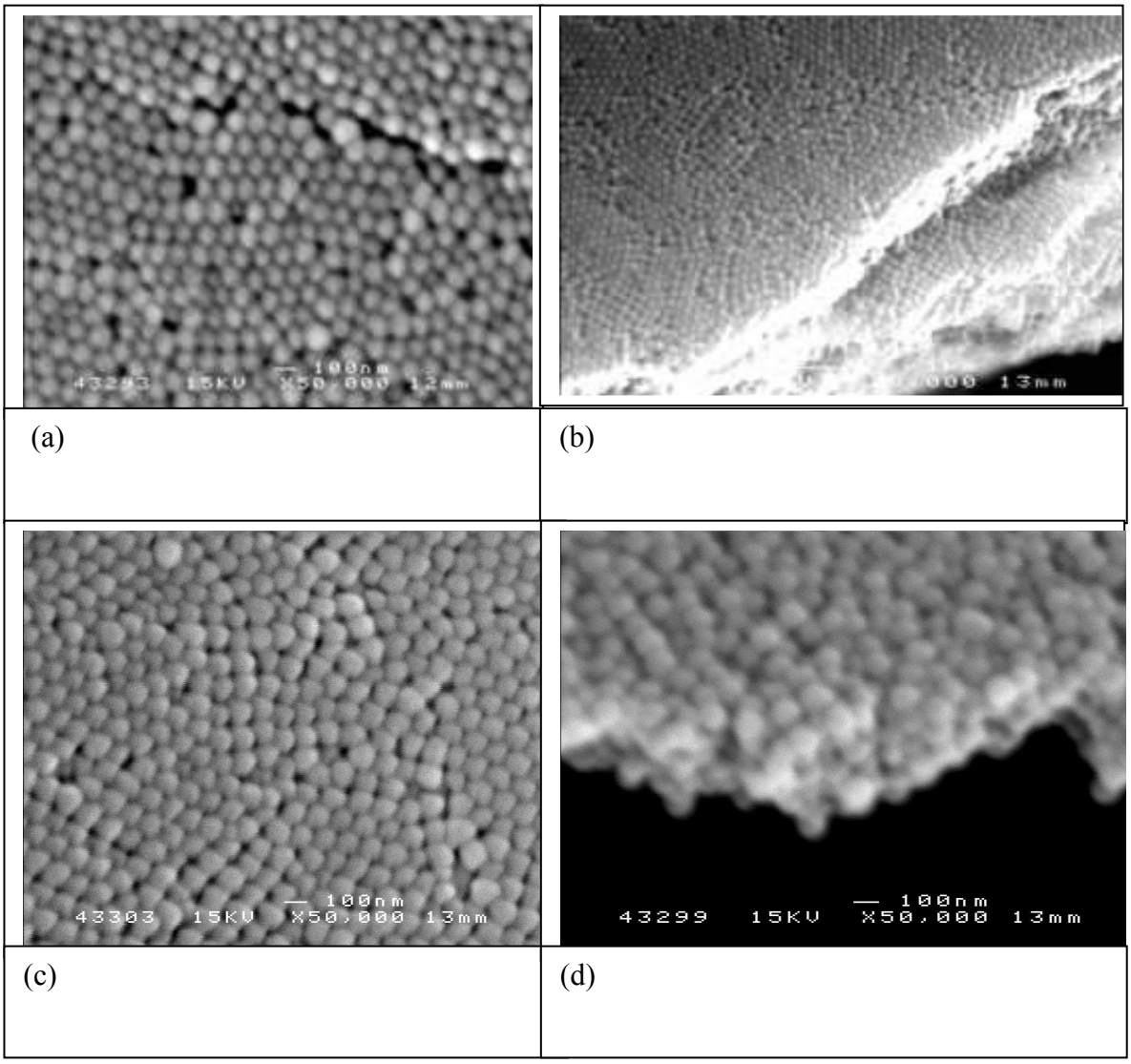

Figure 3.27: SEM images, (a) Dried centrifuged spheres of Sample 1 (b) image shows the pattern of packing towards the edges for Sample 1 (c) Dried centrifuged spheres of Sample 2 (d) image shows the pattern of packing towards the edges for Sample 2

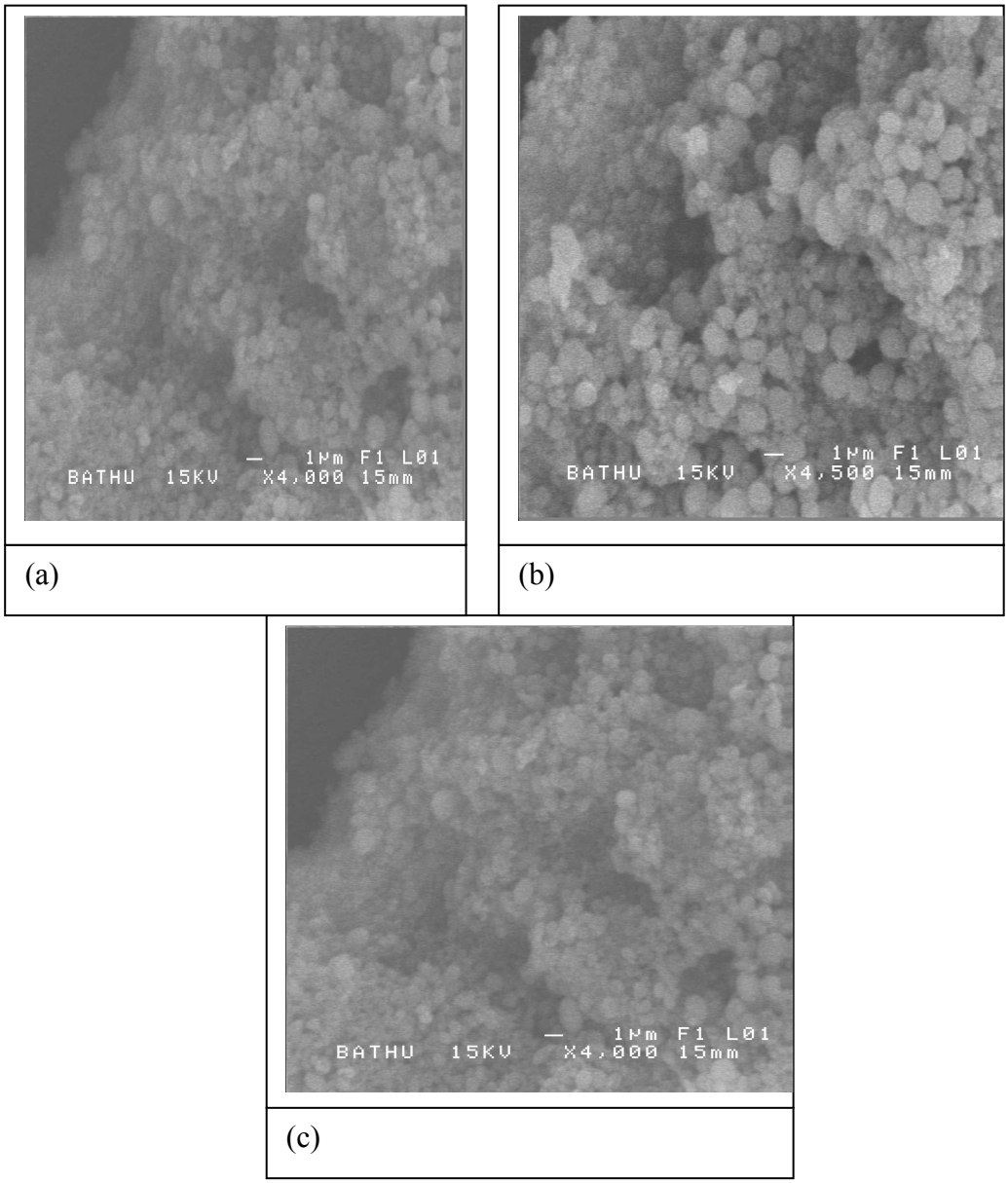

Figure 3.28: Shows three different SEM images (a, b and c) of the pore structure of the resulting PS templated silica solids from Sample 1.

Figure 3.16 shows the SEM images of the resulting silica solids produced from PS templating. It is evident from the micrographs that the templated solid possess spherical pores with a good level of ordering. This structure is a reflection of the voids within the spherical compacted PS beads.

Polystyrene synthesis stir rates of ~250 rpm produce beads of approximately 500 nm according to the method adopted by Holland *et al.* (1999) however SEM scans show beads of about 100 nm pore size which is a close match to the estimated pore size of 70

nm according to the standard recipe of the Edler group. The beads synthesised were enlarged by styrene polymerization, and the resulting SEM analysis shows a size increase of about ~10 nm for the smaller PS beads in sample 1 (which were about 80 nm) dispersed amongst the averagely sized ones (100 nm). Most of the spheres in sample 2 were about on average around 100 - 150 nm, there were also none smaller than 100 nm as was the case in sample 1. This technique shows some promising results, however it might be more successful, if a larger amount of styrene is added, and perhaps stirred for a much longer period in order to infiltrate the PS beads with more styrene prior to polymerisation. The process of styrene polymerization could result in secondary nucleation, which will produce several small spheres among a few big and hence defeats the purpose. This inconsistency was however, avoided within this research. If the beads are successfully and uniformly enlarged, macroscopic solids on a higher range can be prepared. Although there are some smaller spheres than the bulk visible in Figure 3.14, Figure 3.15 shows a somewhat uniform compacted PS spheres. Problems encountered with templating on packed polystyrene spheres include insufficient penetration of silica into the voids of the spheres, and hence a non- existent silica framework. This can result in a breakdown of solids during the calcining stage, as the polystyrene beads can get burnt off. It appeared that very close packing (i.e. centrifuging for long enough) of the spheres was a very essential part of the process, as the denser the packed spheres, the higher the chances of obtaining a strong dried latex chunk, and its survival of the templating process. This is also valid towards obtaining the highest level of ordered products.

3.9 - Conclusions

It can be concluded, that a range of highly ordered and mechanically stable mesoporous, microporous and macroporous materials have successfully been synthesised by surfactant templating and the use of polystyrene spheres. It has also been shown, that a range of size modification experiments can be performed, to produce materials independent of the standard surfactant chain lengths. Evidence has been provided in support of completely formed coats over synthesised and analysed core materials. The results within this section of the research provide supporting evidence for pore blocking effects in composite materials with a microporous outer shell and a mesoporous core.

Chapter 4: Transport Properties

4.1 – Introduction to Gas Adsorption Kinetics

This Chapter describes gas adsorption kinetics data, and the use of the 'Linear Driving Force Model' (LDF) to assess mass transfer coefficients for fluid transport in porous media. Gas adsorption kinetics can be used to estimate pore size, and reveal pore structure information relevant in determining the controlling mechanism and diffusivity factors of fluid transport in porous media. One reason why understanding adsorption kinetics and surface behaviour is important, is because it can be an effective means of characterizing the pore size distribution, as well as pore interconnectivity, and of identifying the location and deposition of pore types with regards to understanding the location of condensed vapours within a porous medium. This information can be used to understand the influence of condensed vapours on the transport rates of the displacing fluid in multiphase systems. It is also useful in catalytic reactions requiring manipulation of transport rates, as a gas adsorption kinetic study of various combinations of pore structure characteristics could reveal the means of attaining desired reactions.

Several researchers have studied adsorption kinetics using techniques such as gravimetric and volumetric gas adsorption analyser which makes it possible to measure adsorbed masses as a function of time. The adsorption kinetics of condensable vapours can be influenced by the behaviour of already adsorbed particles, and the physical properties as well as the initial saturation of the adsorbate, and this makes gas adsorption kinetics a useful tool for investigating the region of irreversibility (hysteresis) observed within the region of high pressure pore condensation. Rao *et al.* (1985) developed a model for the interaction potential of diffusing species in porous carbon molecular sieves, and concluded that two processes are involved in adsorption dynamics, namely diffusion along the pores and diffusion through the barrier at the pore entrance. Gas adsorption kinetic data was reported to have followed a LDF model, when the latter is the rate-determining step, or a Fickian diffusion model controls the kinetics when the former is the rate-determining step. For example in the case of carbon deposition, this

barrier results from constrictions in the porosity caused by the heterogeneous distribution of the deposited carbon (Chagger *et al.*, 1995).

4.1.1 – Applications of Adsorption Kinetics

The description of two-phase flow in porous materials is important in many applications, such as catalysis, fuel cells, membrane separations, and in understanding the mechanisms of enhanced oil recovery methods, as well as other areas involving heat and mass transfer, diffusion and reaction of condensable vapours, and capillarity and multiphase (vapour-liquid) flow in a porous media environment. In particular, transport in mesopores and the associated phenomena of multilayer adsorption and capillary condensation have been investigated extensively as a means of investigating catalyst effectiveness factors (Wood *et al.,* 2002), and as a separation mechanism for gas mixtures (Kainourgiakis *et al.*, 1996). More recent developments in manufacturing more complex mesoporous structures for applications in heterogeneous processes have, in turn, raised interest in the study of these underlying mechanisms. For effective application of such mesoporous media in chemical processes, such as membrane technology, a thorough determination is required. A number of equilibrium and dynamic techniques have been employed for this purpose. Gas adsorption techniques remains the most widely used due to the simplicity of the experimental procedure. The basic information that can be obtained from gas adsorption data includes surface area measurements, total pore volume and pore size distribution. In characterising mesoporous materials, if the adsorptive is below its critical point, it undergoes capillary condensation and, by using the Kelvin equation, the PSD can be obtained using the adsorption isotherm. In most cases, an assumption of a pore shape is necessary. An important topological property of a porous material is the interconnectivity, which gives information based on the interconnection between pores in the porous medium. Therefore, when calculating PSD from the desorption isotherm a different approach should be made based on the interconnectivity theory. The uncertainty in determining pore size distribution can be greatly reduced if all different methods give results in agreement with each other. However when focusing on dynamic flow methods, gas relative permeability is one of the most widely considered techniques due to its theoretical simplicity in relating gas permeability and pore structure characteristics. Gas

relative permeability is defined as the permeability of a fluid flowing through a porous medium in the presence of a second fluid (pore blockage), divided by the permeability of the same porous medium in the absence of the second fluid. In relating gas relative permeability to porous media topology, the experimental complication arising from the two component mixing requirement remains a problem, however kinetic data for systems containing condensable vapours have been studied in varying forms by several researchers (such as Kainourgiakis *et al.*, 1996; Tzevelekos *et al.*, 1998; Wood *et al.*, 2002) to highlight the link between pore structure and transport mechanisms.

Kainourgiakis *et al.* (1996) reported that although the static behaviour of the condensate in the capillaries is relatively well understood, the dynamic behaviour of both the adsorbed layer and the condensed phase, which determines the overall separation and transport efficiency, had not been adequately described yet. They measured permeability curves which were found to exhibit a maximum at some relative pressure, a fact that has been attributed to the occurrence of condensation (and hence blocking) in the main body of the pores. This was aimed at introducing a discrete network approach to modelling transport of condensable vapours in mesoporous structures. Such models posses the potential for improving the understanding of the mechanisms responsible for the observed transport behaviour.

Tzevelekos *et al.* (1998) proposed a method based on the permeability of a condensable vapour as an alternative method for pore structure characterisation to provide additional insight and information into the topology of the porous medium. Tzevelekos *et al.* (1998) reported the use of transport rates of condensable vapours in mesoporous materials, as a means of characterising pore structure. For a condensable vapour, as capillary condensation occurs the permeability of the vapour reaches its maximum at a pressure below its saturation pressure (Tzevelekos *et al.*, 1998). They collected experimental data of water and pentane vapour permeabilities on well defined mesoporous alumina membranes of similar pore structures but different porosities. They showed that the permeabilities of condensable vapours are a sensitive function of pore structure. It was observed that within a certain relative pressure range, a percolating cluster of capillary condensed pores is formed resulting in a dramatic increase in the permeability of the vapour. The limits of this pressure range can be related to the percolation threshold and thus to the topology of the medium.

The use of membrane technology is increasingly popular in a number of industrial sectors, in many cases successfully replacing traditional, energy-demanding and environmentally polluting separation techniques. An effective membrane system, for separation on a large scale, should provide high permeability values and satisfactory separation factors simultaneously. The use of microporous membranes as molecular sieves exhibit increased selectivity, but their applications are limited due to their low permeability. On the other hand mesoporous membranes exhibit the opposite characteristics in terms of selectivity and permeability. In an attempt to increase the selectivity of mesoporous membrane applications, Tzevelekos *et al.* (1999) proposed a means of improving the selectivity of mesoporous membranes for cases involving gas mixtures containing at least one condensable vapour, by taking advantage of the adsorption and capillary condensation phenomenon occurring within the pore structure of the membrane. They used a combination of the experimental findings of relative gas and condensable vapour permeabilities with kinetics data from equilibrium adsorption isotherms in order to develop a technique for selecting the optimum operation conditions (pressure, temperature, etc) for achieving the maximum selectivity and permeability values possible for a certain separation. He/H_2O and He/n-C_5H_{12} permeabilities as well as single-component permeabilities were measured on two mesoporous alumina membranes, in order to determine the optimum conditions for separating condensable from non-condensable vapours. The results show that, if the relative pressure of the condensable vapour in the condensable/non-condensable mixture is properly selected, very high selectivity and permeability values can be achieved simultaneously. The optimum relative pressure of the condensable vapour corresponded, in all cases studied, to the maximum condensable vapour permeability and to a relative gas permeability of zero.

Pore network models have also been used to study vapour diffusivity and reaction in porous media such as catalysts (Hollewand and Gladden, 1992a, b). Such models allowed investigations into the effects of topology of the pore network upon diffusion and reaction processes within porous materials such as a mesoporous catalyst pellets. Certain types of catalytic reactions are accompanied by capillary condensation of the vapour phase within the smaller pores of the catalyst pellet. For example capillary condensation has been found to accompany industrial hydro treatment reactions (Wood *et al.*, 2002). This process occurs in a fixed bed catalytic reactor, which operates in a

down flow mode to remove unwanted materials such as sulphur and nitrogen at high temperatures and pressures, typically 300 ^{o}C and 40 bar. At these hydrotreating conditions, reactants in the inter-particle void space and the larger pores of the catalyst are gas-filled, whilst capillary condensation occurs in the smaller pores of the catalyst (Wood *et al.*, 2002). The transport processes within the catalyst pellet then becomes a multiphase and hence much more complex. Wood *et al.* (2002) developed a model which simulates capillary condensation in porous media by combining a computational algorithm for calculating the critical radius below which capillary condensation occurs with a pore network model of vapour diffusion and reaction. The critical radius for capillary condensation was calculated using a multicomponent version of the Kelvin equation to determine which pores of the network fill with condensed liquid under specified conditions. A percolation analysis was used to determine whether regions of liquid-filled pores cause any vapour-filled pores to become blocked/disconnected from the network surface. Diffusion was simulated using Fick's law whilst reaction is assumed to be first order. The model was applied to the prediction of catalyst effectiveness factors for a first order reaction occurring over typical hydroprocessing catalysts with mean pore sizes within the mesoporous range (128 - 184Å). The model was used to demonstrate the influence of network topology (regular versus random) and pore structure parameters (mean pore size, standard deviation pore size and network connectivity) upon the catalysts effectiveness factor in the presence of a fraction of catalyst pores that are filled with capillary condensate. The results showed that a mixture of 5 mole% diethyl sulphide in hydrogen is prone to capillary condensation within the pores of the catalyst over the range of pressures 27.5 - 27:8 bar at 375 K. At low Thiele moduli, in the strong reaction-controlled limit, the presence of liquid-filled pores leads to a reduction in catalyst effectiveness of 4 – 7 % over the range of pressures simulated. However, at high Thiele moduli, in the strong diffusion-controlled limit, effectiveness factor was not significantly influenced by the presence of capillary condensate (Wood *et al.*, 2002).

Simulations of the kinetic uptake, adsorption and capillary condensation of butane vapour within the porous solid, conducted on a structural model already mapped out using MRI have successfully been used to predict experimental measurements of the effects of the onset of capillary condensation on mass transfer rates without the need of the various adjustable parameters prevalent in other models (Watt-Smith *et al.*, 2006).

Magnetic resonance (3-D) images were used to present a map of the spatial variation of porosity, pore sizes and network tortuosity within a porous solid and thence to construct a structural model for a mesoporous catalyst pellet. Gas sorption kinetics was then employed alongside MRI to interpret mass transport in systems with condensable vapours.

Krause *et al.* (2003) used PFG NMR to study the molecular diffusion of benzene in a mesoporous material of type MCM-41, and reported a sudden decrease in the effective diffusivity D_{eff} of benzene with increasing loading at medium pore filling factors. Over a very small benzene concentration range, at medium pore filling factors, the diffusivity dropped by up to one order of a magnitude, while it remained constant over the total remaining range from as little as nothing to over-saturation. Diffusivities in adsorbate-adsorbent systems exceeding those of the bulk liquid are generally believed to include the possibility of fast molecular propagation through the free space in the gas phase of the pore system (Karger, 1981). In this case the effective diffusivity as represented by NMR may be represented as the sum of two constituents ($D_{eff} = D_{surface} + P_{inter} D_{inter}$). P_{inter} and D_{inter} denote respectively the relative amount of molecules in the gas phase and their diffusivity, while the remaining contribution to molecular transportation is summarised in the term $D_{surface}$. P_{inter} is clearly much more smaller than 1, depending on the free volume of the pore system, and D_{inter} attains values which may significantly exceed all other contributions to mass transfer, such that $P_{inter} D_{inter}$ becomes the dominant term, possibly even exceeding the diffusivity of the bulk liquid. This surprising drop was associated with a dramatic drop in one of the constituents in the dominant term P_{inter} and or $D_{inter.}$ Since P_{inter} is proportional to the pressure of the adsorbate divided by the total amount adsorbed, an increase in the relative loading of about 10 % can not lead to a decrease in p_{inter} of up to an order of a magnitude. Hence the dramatic decrease in D_{eff} has to be associated with a decrease in D_{inter}. Krause *et al.* (2003) attributed this behaviour to the onset of capillary condensation. They observed that given the range of concentration, and the experimental conditions of loading, with an increasing relative loading, an increase in the adsorbate pressure will result in the onset of capillary condensation in the pore throats of MCM-41 hyper-structure. These pore throats will therefore connect the free space in the pore structure relevant for the large values of D_{inter} at smaller concentrations. Hence the onset of condensation explains the steep drop in diffusivity at medium pore filling factors. However for regions above

the onset of capillary condensation, the increase in D_{eff} with increasing loading is explained by the corresponding increase in P_{inter}. Subsequent experiments showed that the MCM-41 sample that was studied showed a more pronounced hysteresis loop in comparison to a reference MCM-41 specimen without secondary pore systems, suggesting the effect of capillary condensation on transport rates varies with pore topology.

Literature researchers have focused studies of adsorption kinetics of gases/vapours on several related materials such as on carbon molecular sieves (Braymer *et al.*, 1994), on active carbons (Harding *et al.*,1998)) and on porous metal organic framework materials (Flecther *et al.*, 2001), but very little has been done with regards to transport (adsorption kinetics) in silicate structures of MCM-41 type materials, and hence this research aims to investigate the kinetics of adsorption on mesoporous materials, as well as to investigate the effect of engineered diffusion barriers on transport rates for dual-structured synthesised materials. Investigations into the adsorption dynamics for mesopores (core materials), which have a well-defined mesoporous structure, will be carried out by running experimental studies of gas adsorption and then comparing the adsorption kinetics at different steps of the process, for a range of sol gel silicas with varying size and shape, to establish the relation between sorption kinetics and the pore structure/topology. Particular emphasis will be placed on the region of capillary condensation as there is still a need to further understand the influence of capillary condensation upon diffusion of condensable vapours in mesoporous media, and in particular the role of pore geometry and topology on capillary condensation and hence overall diffusivity and effectiveness in porous media transport processes. These measured diffusivity factors will also be used to investigate pore structure models such as the pore blocking phenomenon and the effect of capillary condensation on transport rates in gas adsorption and desorption (evaporation of condensable vapours) in the presence of adsorbed gas.

4.1.2 - Calculation of Diffusivity - Linear Driving Force (LDF) Model

Rates of adsorption and desorption in porous solids, are generally controlled by transport within the pore network, rather than by the intrinsic kinetics of sorption at the surface. Since there is little bulk flow through the pore, it is convenient to consider intraparticle transport as a diffusive process and to correlate kinetic data in terms of a diffusivity defined according to Fick's first equation (Equation 4.1).

$$J = -D(c)\frac{\partial c}{\partial x} \quad \textbf{(4. 1)}$$

The Linear Driving Force (LDF) model was originally proposed by Gleuckauf and Coates (1947) based on the Fick's law for adsorption chromatography. It is frequently used for analysis of dynamic adsorption data and for adsorptive process designs because it is simple, analytical and physically consistent (Sircar *et al.*, 2000). The model can be used to analyse the transport properties of the designed porous structures, from sets of gas uptake data acquired from low-pressure experiments (~100 pa), which ensures diffusion is restricted to the Knudsen regime and interference from the adsorbed phase is avoided. For a sequence of mass uptake measurements of an adsorbate, M_t, taken over time, after a step increase in the external gas pressure, an equilibrium value of uptake M_f is eventually attained. An assumption was made, that the surface concentration of gas is constant, and that the diffusion is controlled by the concentration gradient through the particle. The resulting empirical diffusion equation was:

$$M_t / M_\infty = Kt^n \quad \textbf{(4. 2)}$$

M_t = Gas uptake at time t

M_∞ = Gas uptake at equilibrium

K = constant and t = time

A model for Fickian diffusion in a spherical particle was adopted, as explained by Thomas *et al.* (1995), for short and long time behaviour. Based on Fick's law for

isothermal diffusion the concentration *c* into a homogenous sphere of radius *a*, with a diffusivity constant *D* is described by.

$$\frac{\partial c}{\partial t} = D\left(\frac{\partial^2 c}{\partial a^2} + \frac{2}{a}\frac{\partial c}{\partial a}\right) \quad \textbf{(4. 3)}$$

Approximate solutions for this equation for mass uptake are stated below;

At small times ($M_t/M_f<0.25$), this approximates to:

$$M_t / M_f = 6\, D^{1/2}\, t^{1/2} / \pi^{1/2}\, a \quad \textbf{(4. 4)}$$

For $M_t / M_f > 0.5$ the gas uptake can be approximated by an equation of the form of the LDF model:

$$M_t \Big/ M_f = 1 - e^{-kt} \quad \textbf{(4. 5)}$$

Where k is essentially comparable to $D^2 \pi / a^2$

Thomas *et al.* (1995) had reported the experimental analysis of oxygen and nitrogen adsorption data on heterogeneous carbon molecular sieves (CMS) prepared by carbon deposition methods through the use of the Linear Driving Force model, to assess the diffusivity of the adsorbed molecules into a homogeneous spherical particles of radius a, in the range of $M_t / M_f > 0.5$. The range of newly designed novel structured porous materials synthesised within this research include core particles of a uniform pore structure and composite particles which were intended to have two distinctive regions of diffusion, and as a result, the previously adopted LDF model is not directly applicable, for the dual-structured particles. These materials were also not perfect spheres, and hence a two-fraction LDF model is developed, and fitted to the uptake curves by the least possible square difference method for $M_t / M_f > 0.5$ and < 1. After a step increase in

the external gas pressure, a range of mass uptake of adsorbate measurements M_t, were taken over time until an equilibrium (M_f) was obtained. Equation 4.6 was developed for the fractional mass uptake with time and fitted to the data, to calculate the effective diffusivity of water, butane, and cyclohexane:

$$\frac{M_t}{M_f} = p\left(1 - e^{-k_1 t}\right) + (1 - p)\left(1 - e^{-k_2 t}\right) \quad \textbf{(4. 6)}$$

Where p, k_1 and k_2 are fitting parameters, where $k_i = D_i \pi^2 / a^2$, and

p = Fraction of component i

D = Diffusion coefficient

a = Particle size parameter, this is a mean of three different measurements of the linear dimension of the particle (taken to represent the diameter of a sphere).

At constant temperature and molecular mass, the Knudsen diffusivity is proportional to the pore radius.

4.1.3 - Experimental Procedure

Gas adsorption gravimetry is particularly useful for studying the transport mechanisms of adsorption, as well as desorption of vapours e.g. water, organic adsorptives such as cyclohexane and butane, because it enables the change in mass uptake of the adsorbent (kinetics) to be recorded during the out-gassing and both stages of the sorption process. An Intelligent Gravimetric Analyser (IGA) supplied by Hiden Ltd U.K., was used in this study. This apparatus is an ultra high vacuum system, which combines computer control and uptake measurement by weight change, pressure and temperature to produce adsorption and desorption curves, as well as the kinetics of each pressure increment in diverse operating conditions. The mass uptake is measured as a function of time and the approach to equilibrium is monitored by a computer-controlled algorithm. The balance and pressure control system were fully thermostated to ± 0.2 K to eliminate changes in the external environment. The adsorbent sample was out-gassed until constant weight

(typical sample mass was ~100 mg), at a pressure of < 10^{-6} mbar at 100 ^{o}C for nitrogen, cyclohexane, and butane experiments, and at 25 ^{o}C for water vapour experiments. Except for the nitrogen experiment, where the temperature control fluctuated as a result of the difficulties involved in dealing with liquid nitrogen drawn from a Dewar flask under manual temperature control, all other experiments were conducted by using a computer controlled bath containing a mixture of ethylene glycol and water around a stainless steel cylinder for maintaining low temperatures < 30 ^{o}C whilst a furnace was used for temperatures above 30 ^{o}C. The first pressure increment involves a change from the ultrahigh vacuum already attained, to the pressure of gas/vapour, and this introduces conduction through the gas phase to the sample, which in turn results in a slight temperature variation until equilibrium is achieved. The liquid used to generate the adsorptive vapours for cyclohexane and water vapour adsorption experiment was degassed fully by repeating the evacuation and vapour equilibration cycles of the liquid supply side of the vapour reservoir for cyclohexane and water vapour. The butane and nitrogen gases were used directly from cylinder by connecting to the gas supply pipe. The vapour pressure was gradually increased, over an equilibration time of 45 s to prevent disruption to the microbalance, until the desired value was achieved. The pressure was controlled by the use of three transducers with ranges 0 - 0.2, 0 - 10, and 0 - 200 kpa, each with an accuracy of 0.02 % of the specified range. The pressure was maintained at the set point by computer control of the inlet/outlet valves throughout the duration of the experiment. The mass uptake was measured as a function of time and the approach to equilibrium of the mass relaxation curve was monitored in real time using a computer algorithm. After equilibrium was reached, the vapour pressure was raised to the next pressure value and the subsequent uptake was measured until equilibrium was re-established. The increase in weight as a result of the uptake for each pressure step was used to calculate the kinetic parameters for adsorption using an appropriate kinetic model.

4.1.4 - Cyclohexane Adsorption Experiment

The IGA is also used to perform the cyclohexane adsorption analysis. The sample was put in a pre-weighed pan and loaded onto the IGA reactor, and sealed tightly. The first stage was to outgas the sample, to free it of any physisorbed water. The sample is heated under vacuum to 170 ^{o}C overnight, until the sample weight remains unchanged and then the dry mass is set. The reactor and sample is then allowed to cool down to room temperature, before the water bath is attached and set to 30 ^{o}C and 10 ^{o}C for the second batch to assess the effect of temperature on the adsorption rate of cyclohexane. Once the temperature set reaches the target temperature, the isothermal analysis begins with the mass relaxation for a set of pressures over a range within the saturated vapour pressure of cyclohexane (~160 and 80 mbar at 30 ^{o}C and 10 ^{o}C respectively). The kinetic data obtained was used to assess the fluid transport properties of the sample, and to measure the surface area of the materials. The cross-sectional area for one molecule of cyclohexane was assumed to be 0.369 nm^2 (Lowell and Shields 1984).

4.1.5 - Butane Gas Adsorption Experiment

The butane adsorption experiment follows the same technique, as the cyclohexane adsorption analysis, using the IGA. The sample was put in a pre-weighed pan and loaded onto the IGA reactor, and sealed tightly. The first stage again is to outgas the sample, to free it of any physisorbed water. The sample is heated under vacuum to 170 ^{o}C overnight, until the sample weight remains unchanged and the dry mass is set. The reactor and sample is then allowed to cool down to room temperature, before the water bath is attached and set to 0 ^{o}C prior to the mass uptake analysis. Once the temperature set reaches the target temperature, the mass relaxation begins, and the uptake for a set of pressure points over the range from 0.054 mbar to the saturated vapour pressure of butane (~1000 mbar at 0 ^{o}C) is obtained. The kinetic data again is used to assess the fluid transport properties of the sample, and the surface area. The cross-sectional area for one molecule of butane was assumed to be 0.469 nm^2 (Lowell and Shields 1984).

4.1.6 - Drawbacks in Methodology (LDF Theory)

The gas adsorption data obtained from the IGA is processed based on the Kelvin equation, to yield the PDD and the Kelvin equation makes assumptions that the pores are rigid and of well defined shape (such as cylindrical or slit shaped) and that a hemispherical meniscus with zero contact angle controls adsorption. However this is never the case with most complex structures. Despite this highlighted inconsistencies it is however the best model available. Drawbacks to the application of the LDF model also exist and are also listed below:

There is no guarantee that for every material on every surface, the contact angle is zero and that it is known that contact angle and surface tension are functions of pore structure. As the pores become smaller, the contact of the meniscus is less well defined.

1. The initial uptake data are less accurate due to the fact that the step increase is not exactly vertical (see diagrammatic representation below). Some of the pressure steps of the gas uptake curves obtained (e.g. Figures 4.6 and 4.7) show a few wiggles as the pressure rises towards equilibrium and these inconsistencies could lead to errors in data interpretation.

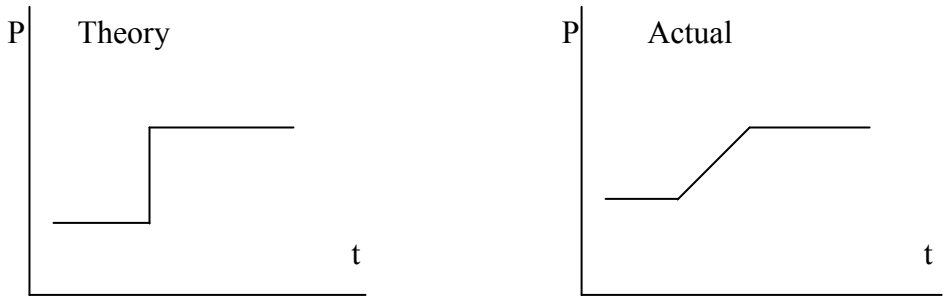

2. The solution to the equation assumes an isothermal behaviour, which is not always the case. Limitations could arise depending on how big temperature variations were and whether they were random or systematic. However the IGA

monitors the temperature variation, and shows minimal variation for the experiments within this research, it is not very clear as to what difference minor temperature variations could make.

3. Also the presence of extra-crystalline resistance arising from the interfacial discontinuity within the crystallised silica samples can easily retard the initial uptake rate.

In an attempt to address some of the above drawbacks, a modification to the LDF model was developed to account for the difficulties leading to a more accurate estimate of the transport properties. The two coefficient model is implemented, to check the possibilities of two-component diffusion. The sensitivity of the fits of an LDF model is also investigated, and the details are included in the sensitivity analysis in Section 4.2.8.1.

4.1.7 - Results and Discussions

For each experimental data set analysed within Section 4.1, the one component (*k* at small times or *k* at large times) or two component *k* methods were used to obtain the diffusivities. A typical IGA gas adsorption uptake curve as shown in Graph A1 in Appendix A is analysed in order of increasing pressure steps for each of the pressure steps. The plateau at each uptake step represents the equilibrium value (M_f). After all data has been obtained for the relevant region, Graphs A3 and A4 (see Appendix A) are plotted in the case of the one component (*k* at small times or *k* at large times). The time of uptake and mass adsorbed is renormalized for each pressure step, so that the *k* is the mass transfer coefficient at a specific pressure step. For the two component *k* method, Graph A5 (see Appendix A) is plotted to access the fit of the adsorption data to the LDF model. Since the particles synthesised in this work were not perfect spheres and were intentionally inhomogeneous a two-fraction LDF model was fitted to the uptake curves for ($0.5 > M_t/M_f > 0.9$) such that the fractional mass uptake with time is represented by Equation 4.6. The LDF model is used to calculate M_t/M_f values for each pressure step, and the experimental result is also used to calculate a set of M_t/M_f values from the plateau of each step. The square root of the difference between both sets (sum

residuals) with P and k_1 and k_2 being adjustable parameters is obtained and minimised using the excel solver.

4.1.7.1 - One Component Fit

At first attempt, the effective diffusivities for the synthesised materials were calculated by a method of determining a one component k value by the use of Equation 4.4 to obtain k for small times (M_t/M_f <0.25), and a one component k for large times (M_t/M_f > 0.5) by using Equation 4.5. For more details including graphs see Appendix A. Tables 4.1 - 4.3 shows the results of calculated k values for small and large times with their corresponding R^2 values, which is a reflection of the goodness of data fit. Tables 4.1 – 4.3 show the resulting k values for the first five pressure steps/points, followed by two high pressure points which fall within the region of capillary condensation. Tables 4.1 and 4.2 indicate that for both cyclohexane and butane gas adsorption, the existence of a $P123_t$ coat over $F127_t$ appears to have lead to an increase in the mass transfer coefficient. This can be attributed to the existence of an additional region (coat) which possesses a higher mass transfer coefficient in comparison to the core material. The increase in k, for small and large times in Tables 4.1 and 4.2 could also be linked to the fact that they are functions of the diffusion coefficient D, and particle size a, such that a decrease in the particle size a, will result in an increase in k and vice versa. However, as the particle sizes of the composite materials are only slightly less than the core material, the increase in k both for small and large times is somewhat more than can be expected from the slight decrease in particle size and hence a result of the effect of the $P123_t$ coat. Although both $P123_t$ and $F127_t$ have similar pore body sizes, the smaller necks present in $F127_t$ may lead to the lower rate of diffusion into $F127_t$. The pore neck size has been shown to control the desorption branch of the isotherm; however it is not completely clear whether there is any influence of the $F127_t$ coat on the adsorption properties of the composite material. This method has shown little success, because of the drawbacks to the LDF model as explained in Section 4.1.6. The pressure steps exhibits a slightly slanted rise as opposed to a vertical increase, and hence leads to a difficulty in obtaining the M_t values since the 'zero' time could be reasonably taken as either the beginning of the pressure increase or half way through. This feature, in addition to the fact that very little uptake occurs at the so called small

times *(M_t /M_f < 0.25)*, has resulted in insufficient data in the small times region, to accurately determine the *k* in this region. Table 4.3 shows a comparison of the effective diffusivity values obtained for $P123_t$ core samples as well as $P123_t$ coated in $F127_t$ (mesopores shielded by much smaller necks) and $P123_t$ coated in CTAB (micropores). The results in table 4.3 show a decrease in the effective diffusivity for coated materials with the coat material having the smallest pores showing the largest decrease on $P123_t$ core material. Previous nitrogen adsorption experiments in Chapter 3 suggest that the adsorption properties of the coated material, is a reflection of a combination of the properties of the two constituents. Although this is understandably correct to an extent, the results from this section seem to show in particular that at low pressure filling, the effective diffusivity is dominated by the coating material. This study of the kinetics of gas adsorption on the synthesized silica materials has shown that the method of synthesis of a bimodal material by introducing a shell of a different structure over a coat of uniform pores affects the adsorption properties of the materials and could lead to a reduced or increased rate.

Table 4.1: Butane Gas Adsorption $F127_t$ core and $F127_t$ coated in $P123_t$

	D (m^2/s) (F127 core expt.1)	R^2	D (m^2/s) F127/P123 expt. 1	R^2
Diffusivities obtained from k For M_t/M_f values < 0.25				
Step 1	$5.17 (\pm 0.021) \times 10^{-9}$	0.9376	$3.40 (\pm 0.011) \times 10^{-9}$	0.9419
Step 2	$2.68 (\pm 0.015) \times 10^{-9}$	0.9144	$9.85 (\pm 0.006) \times 10^{-10}$	0.8494
Step 3	$1.82 (\pm 0.012) \times 10^{-9}$	0.8463	$1.65 (\pm 0.008) \times 10^{-9}$	0.8916
Step 4	$4.15 (\pm 0.019) \times 10^{-9}$	0.6387	$3.39 (\pm 0.011) \times 10^{-9}$	0.6282
Step 5	$5.17 (\pm 0.0210 \times 10^{-9}$	0.7968	$3.25 (\pm 0.113) \times 10^{-9}$	0.6291
Step 19*	$2.47 (\pm 0.014) \times 10^{-9}$	0.9558	$7.82 (\pm 0.1750 \times 10^{-7}$	0.9858
Step 20*	$1.23 (\pm 0.010) \times 10^{-9}$	0.9413	$8.28 (\pm 0.179) \times 10^{-7}$	0.9901
Diffusivities obtained from k For M_t/M_f values > 0.5				
Step 1	$2.81 (\pm 0.049) \times 10^{-8}$	0.9931	$1.64 (\pm 0.025) \times 10^{-5}$	0.9884
Step 2	$2.53 (\pm 0.047) \times 10^{-8}$	0.9919	$1.64 (\pm 0.024) \times 10^{-5}$	0.9952
Step 3	$2.39 (\pm 0.045) \times 10^{-8}$	0.9952	$1.64 (\pm 0.254) \times 10^{-5}$	0.9960
Step 4	$2.70 (\pm 0.048) \times 10^{-8}$	0.8887	$1.64 (\pm 0.026) \times 10^{-5}$	0.9490
Step 5	$2.22 (\pm 0.044) \times 10^{-8}$	0.9359	$1.64 (\pm 0.025) \times 10^{-5}$	0.5032
Step 19*	$5.97 (\pm 0.023) \times 10^{-9}$	0.9906	$8.21 (\pm 0.004) \times 10^{-6}$	0.9571
Step 20*	$4.26 (\pm 0.019) \times 10^{-9}$	0.9852	$8.28 (\pm 0.004) \times 10^{-6}$	0.9964

Note: For F127 core expt. 1 ($a = 5.29 \times 10^{-3}$ m) and For F127 coated in P123 expt. 1 ($a = 4.06 \times 10^{-3}$ m)

*within the region of condensation

Table 4.2: Cyclohexane Gas Adsorption $F127_t$ Expt. 2 and $F127_t/P123_t$ Expt. 2

Steps	D (m^2/s) (F127 expt. 2)	R^2	D (m^2/s) (F127/P123 expt. 2)	R^2
Diffusivities obtained from k For M_t/M_f values < 0.25				
Step 1	$4.91 (\pm 0.024) \times 10^{-9}$	0.7935	$2.89 (\pm 0.007) \times 10^{-10}$	0.4546
Step 2	$6.08 (\pm 0.027) \times 10^{-9}$	0.8052	$1.64 (\pm 0.017) \times 10^{-9}$	0.6925
Step 3	$4.25 (\pm 0.022) \times 10^{-9}$	0.7991	$1.99 (\pm 0.018) \times 10^{-9}$	0.7776
Step 4	$2.08 (\pm 0.016) \times 10^{-9}$	0.7230	$1.21 (\pm 0.014) \times 10^{-9}$	0.7327
Step 5	$2.68 (\pm 0.018) \times 10^{-9}$	0.7062	$2.45 (\pm 0.02) \times 10^{-9}$	0.9250
Step 20*	$4.52 (\pm 0.007) \times 10^{-10}$	0.5791	$2.34 (\pm 0.006) \times 10^{-10}$	0.8643
Step 21*	$1.10\ 9\pm 0.004) \times 10^{-10}$	0.9873	$1.62 (\pm 0.005) \times 10^{-10}$	0.5788
Diffusivities obtained from k For M_t/M_f values > 0.5				
Step 1	$4.06 (\pm 0.069) \times 10^{-8}$	0.9148	$1.30 (\pm 0.047) \times 10^{-8}$	0.1973
Step 2	$2.02 (\pm 0.069) \times 10^{-4}$	0.9753	$1.17 (\pm 0.044) \times 10^{-8}$	0.7013
Step 3	$2.42 (\pm 0.053) \times 10^{-8}$	0.8776	$1.33 (\pm 0.047) \times 10^{-8}$	0.6089
Step 4	$2.49 (\pm 0.054) \times 10^{-8}$	0.4248	$7.78 (\pm 0.036) \times 10^{-9}$	0.6940
Step 5	$2.18 (\pm 0.051) \times 10^{-8}$	0.9694	$6.57 (\pm 0.033) \times 10^{-8}$	0.6847
Step 20*	$8.29 (\pm 0.009) \times 10^{-10}$	0.8848	$1.13 (\pm 0.013) \times 10^{-9}$	0.9999
Step 21*	$9.68 (\pm 0.010) \times 10^{-10}$	0.9931	$3.25 (\pm 0.013) \times 10^{-9}$	0.9931

Note: For F127 core expt. 2 ($a = 3.69 \times 10^{-3}$ m) and For F127 coated in P123 expt. 2 ($a = 2.73 \times 10^{-3}$ m)

*within the region of condensation

Table 4.3: Cyclohexane Gas Adsorption $P123_t$ Core Expt. 1, $P123_t/F127_t$ Expt. 1 & $P123_t/CTAB_t$ Expt. 1

***k* For M_t/M_f values < 0.25**						
	P123 Core expt.1 D (m^2/s)	R^2	P123/F127 expt. 1 D (m^2/s)	R^2	P123/CTAB expt.1 D (m^2/s)	R^2
Step 1	$7.74 (\pm 0.048) \times 10^{-9}$	0.9063	$1.22 (\pm 0.007) \times 10^{-9}$	0.6328	$3.53 (\pm 0.012) \times 10^{-9}$	0.9683
Step 2	$4.70 (\pm 1.195) \times 10^{-6}$	0.6396	$2.09 (\pm 0.003) \times 10^{-9}$	0.5897	$1.97 (\pm 0.009) \times 10^{-9}$	0.6338
Step 3	$1.16 (\pm 0.059) \times 10^{-8}$	0.931	$3.32 (\pm 0.011) \times 10^{-9}$	0.7753	$2.80 (\pm 0.011) \times 10^{-9}$	0.6897
Step 4	$1.00 (\pm 0.017) \times 10^{-9}$	0.3204	N/A	N/A	$7.69 (\pm 0.006) \times 10^{-10}$	0.7853
Step 5	$3.87 (\pm 0.034) \times 10^{-9}$	0.6013	N/A	N/A	$4.05 (\pm 0.013) \times 10^{-9}$	0.9005
Step 14*	$1.49 (\pm 0.021) \times 10^{-9}$	0.9113	N/A	N/A	N/A	N/A
Step 15*	$5.74 (\pm 0.004) \times 10^{-11}$	0.7714	N/A	N/A	N/A	_N/A
***k* For M_t/M_f values > 0.5**						
Step 1	$3.94 \pm 0.048 \times 10^{-8}$	0.9104	$2.96 (\pm 0.001) \times 10^{-8}$	0.9915	$3.51 \pm 0.038 \times 10^{-8}$	0.9834
Step 2	$4.68 \pm 0.048 \times 10^{-7}$	0.9892	$1.07 (\pm 0.012) \times 10^{-8}$	0.9692	$2.01 \pm 0.029 \times 10^{-8}$	0.9965
Step 3	$8.28 \pm 0.048 \times 10^{-8}$	0.9915	$9.96 (\pm 0.013) \times 10^{-8}$	0.9623	$2.84 \pm 0.034 \times 10^{-8}$	0.9904
Step 4	$3.35 \pm 0.048 \times 10^{-8}$	0.9692	N/A	N/A	$2.12 \pm 0.029 \times 10^{-8}$	0.9970
Step 5	$3.78 \pm 0.048 \times 10^{-8}$	0.9623	N/A	N/A	$2.06 \pm 0.048 \times 10^{-8}$	0.8835
Step 14*	$3.12 \pm 0.048 \times 10^{-9}$	0.9698	N/A	N/A	N/A	N/A
Step 15*	$1.04 \pm 0.048 \times 10^{-9}$	0.9766	N/A	N/A	N/A	N/A

Note: For P123 core expt. 1 ($a = 4.14 \times 10^{-3}$ m), for P123 coated in F127 expt. 1 ($a = 3.63 \times 10^{-3}$ m) and for P123 coated in CTAB expt. 1 ($a = 3.44 \times 10^{-3}$ m)

*within the region of condensation

Table 4.4: Cyclohexane Sorption at 30^0C (Two Component Fit $Brij\ 76_t$ Expt. 1)

Steps	***P***	k_1 (s^{-1})	k_2 (s^{-1})	D_1 (m^2/s)	D_2 (m^2/s)
step 1	1.000	0.018	0.003	$1.87 (\pm 3.73) \times 10^{-4}$	$3.08 (\pm 1.36) \times 10^{-5}$
step 2	1.000	0.022	0.003	$2.30 (\pm 3.73) \times 10^{-4}$	$3.08 (\pm 1.36) \times 10^{-5}$
step 3	1.000	0.023	0.003	$2.40 (\pm 3.81) \times 10^{-4}$	$3.08 (\pm 1.36) \times 10^{-5}$
step 4	1.000	0.024	0.003	$2.47 (\pm 3.87) \times 10^{-4}$	$3.08 (\pm 1.36) \times 10^{-5}$
step 5	1.000	0.024	0.003	$2.44 (\pm 3.84) \times 10^{-4}$	$3.08 (\pm 1.36) \times 10^{-5}$

Note: $a = 4.27 \times 10^{-3}$m

Table 4.5: Cyclohexane Sorption at 10^0C (Two Component Fit $Brij\ 76_t$ Expt. 2)

Steps	***P***	k_1 (s^{-1})	k_2 (s^{-1})	D_1 (m^2/s)	D_2 (m^2/s)
step 1	1.000	0.024	0.003	$2.42 (\pm 3.83) \times 10^{-4}$	$3.08 (\pm 1.36) \times 10^{-5}$
step 2	1.000	0.023	0.003	$2.36 (\pm 3.77) \times 10^{-4}$	$3.08 (\pm 1.36) \times 10^{-5}$
step 3	1.000	0.028	0.003	$2.84 (\pm 4.15) \times 10^{-4}$	$3.08 (\pm 1.36) \times 10^{-5}$
step 4	1.000	0.031	0.003	$3.17 (\pm 4.38) \times 10^{-4}$	$3.08 (\pm 1.36) \times 10^{-5}$
step 5	1.000	0.036	0.014	$3.66 (\pm 3.66) \times 10^{-4}$	$1.43 (\pm 2.94) \times 10^{-4}$

Note: $a = 4.27 \times 10^{-3}$m

Table 4.6: Cyclohexane Sorption at 30^0C (Two Component Fit $CTAB_t$ Expt. 1)

Steps	P	k_1 (s^{-1})	k_2 (s^{-1})	D_1 (m^2/s)	D_2 (m^2/s)
step 1	1.000	0.035	11.000	$1.06 (\pm 0.04) \times 10^{-8}$	$3.32 (\pm 0.71) \times 10^{-6}$
step 2	1.000	0.038	0.003	$1.13 (\pm 0.04) \times 10^{-8}$	$9.05 (\pm 0.01) \times 10^{-10}$
step 3	0.861	0.032	0.032	$9.62 (\pm 0.04) \times 10^{-9}$	$9.62 (\pm 0.04) \times 10^{-9}$
step 4	1.000	0.028	0.029	$8.52 (\pm 0.04) \times 10^{-9}$	$8.69 (\pm 0.04) \times 10^{-9}$
Step 5	0.976	0.030	0.000	$8.93 (\pm 0.04) \times 10^{-9}$	0

Note: $a = 1.73 \times 10^{-3}$ m

Table 4.7: Cyclohexane Sorption at 30^0C (Two Component Fit $CTAB_t$ Expt. 2)

Steps	P	k_1 (s^{-1})	k_2 (s^{-1})	D_1 (m^2/s)	D_2 (m^2/s)
step 1	1.000	0.018	0.023	$1.88 (\pm 0.08) \times 10^{-8}$	$2.45 (\pm 0.09) \times 10^{-8}$
step 2	1.000	0.026	0.002	$2.69 (\pm 0.09) \times 10^{-8}$	$2.43 (\pm 0.02) \times 10^{-9}$
step 3	0.990	0.022	0.000	$2.29 (\pm 0.08) \times 10^{-8}$	0
step 4	1.000	0.023	0.003	$2.41 (\pm 0.09) \times 10^{-8}$	$3.16 (\pm 0.03) \times 10^{-9}$
step 5	0.938	0.025	0.010	$2.64 (\pm 0.09) \times 10^{-8}$	$1.07 (\pm 0.06) \times 10^{-8}$

Note: $a = 3.23 \times 10^{-3}$ m

Table 4.8: Cyclohexane Sorption at 30^0C (Two Component Fit $CTAB_t$ coated in $P123_t$ Expt. 1)

Steps	P	k_1 (s^{-1})	k_2 (s^{-1})	D_1 (m^2/s)	D_2 (m^2/s)
step 1	N/A	N/A	N/A	N/A	N/A
step 2	0.127	0.859	0.019	$9.61 (\pm 0.50) \times 10^{-7}$	$2.09 (\pm 0.07) \times 10^{-8}$
step 3	0.500	0.029	0.029	$3.29 (\pm 0.09) \times 10^{-8}$	$3.29 (\pm 0.09) \times 10^{-8}$
step 4	0.493	0.060	0.015	$6.68 (\pm 0.13) \times 10^{-8}$	$1.68 (\pm 0.06) \times 10^{-8}$
step 5	0.500	0.033	0.033	$3.67 (\pm 0.10) \times 10^{-8}$	$3.67 (\pm 0.10) \times 10^{-8}$
step 6	0.292	0.049	0.028	$5.50 (\pm 0.12) \times 10^{-8}$	$3.19 (\pm 0.90) \times 10^{-8}$
step 7	0.500	0.028	0.028	$3.16 (\pm 0.09) \times 10^{-8}$	$3.16 (\pm 0.90) \times 10^{-8}$
step 23*	0.517	0.019	0.019	$2.17 (\pm 0.07) \times 10^{-8}$	$2.17 (\pm 0.80) \times 10^{-8}$
step 24*	0.316	0.013	0.013	$1.44 (\pm 0.06) \times 10^{-8}$	$1.44 (\pm 0.60) \times 10^{-8}$
step 25*	0.500	0.017	0.017	$1.86 (\pm 0.07) \times 10^{-8}$	$1.86 (\pm 0.70) \times 10^{-8}$

Note: $a = 3.32 \times 10^{-3}$ m

*within the region of condensation

Table 4.9: Cyclohexane Sorption at 30^0C (Two Component Fit $F127_t$ Expt. 1)

Steps	P	k_1 (s^{-1})	k_2 (s^{-1})	D_1 (m^2/s)	D_2 (m^2/s)
step 1	0.500	0.010	0.010	$2.77 (\pm 0.04) \times 10^{-8}$	$2.77 (\pm 0.04) \times 10^{-8}$
step 2	1.000	0.009	0.000	$2.56 (\pm 0.04) \times 10^{-8}$	0.00E+00
step 3	1.000	0.009	0.000	$2.48 (\pm 0.04) \times 10^{-8}$	0.00E+00
step 4	0.633	0.008	0.063	$2.33 (\pm 0.04) \times 10^{-8}$	$1.78 (\pm 0.10) \times 10^{-7}$
step 5	0.697	0.009	0.363	$2.43 (\pm 0.04) \times 10^{-8}$	$1.03 (\pm 0.25) \times 10^{-6}$

Note: $a = 5.29 \times 10^{-3}$ m

*within the region of condensation

Table 4.10: Cyclohexane Sorption at 30^0C (Two Component Fit $F127_t$ Expt. 2)

Steps	P	k_1 (s^{-1})	k_2 (s^{-1})	D_1 (m^2/s)	D_2 (m^2/s)
step 1	1.000	0.033	0.033	$4.58 (\pm 0.04) \times 10^{-8}$	$4.58 (\pm 0.04) \times 10^{-8}$
step 2	1.000	0.025	0.038	$3.47 (\pm 0.04) \times 10^{-8}$	$5.29 (\pm 0.04) \times 10^{-8}$
step 3	1.000	0.031	0.031	$4.33 (\pm 0.04) \times 10^{-8}$	$4.33 (\pm 0.04) \times 10^{-8}$
step 4	1.000	0.022	0.033	$3.06 (\pm 0.04) \times 10^{-8}$	$4.62 (\pm 0.04) \times 10^{-8}$
step 5	1.000	0.024	0.034	$3.35 (\pm 0.04) \times 10^{-8}$	$4.67 (\pm 0.04) \times 10^{-8}$
step 6	1.000	0.038	0.034	$5.32 (\pm 0.04) \times 10^{-8}$	$4.67 (\pm 0.04) \times 10^{-8}$
step 7	1.000	0.052	0.034	$7.22 (\pm 0.04) \times 10^{-8}$	$4.67 (\pm 0.04) \times 10^{-8}$
step 8	1.000	0.045	0.034	$6.22 (\pm 0.04) \times 10^{-8}$	$4.67 (\pm 0.04) \times 10^{-8}$
step 9	1.000	0.022	0.034	$3.08 (\pm 0.04) \times 10^{-8}$	$4.67 (\pm 0.04) \times 10^{-8}$
step 10	1.000	0.033	0.034	$4.62 (\pm 0.04) \times 10^{-8}$	$4.67 (\pm 0.04) \times 10^{-8}$
step 11	1.000	0.014	0.034	$1.92 (\pm 0.04) \times 10^{-8}$	$4.67 (\pm 0.04) \times 10^{-8}$
step 12	1.000	0.042	0.034	$5.85 (\pm 0.04) \times 10^{-8}$	$4.67 (\pm 0.04) \times 10^{-8}$
step 13	1.000	0.033	0.034	$4.56 (\pm 0.04) \times 10^{-8}$	$4.67 (\pm 0.04) \times 10^{-8}$
step 14	1.000	0.033	0.034	$4.58 (\pm 0.04) \times 10^{-8}$	$4.67 (\pm 0.04) \times 10^{-8}$
step 15*	1.000	0.040	0.040	$5.60 (\pm 0.04) \times 10^{-8}$	$5.60 (\pm 0.04) \times 10^{-8}$
step 16*	1.000	0.014	0.014	$1.92 (\pm 0.04) \times 10^{-8}$	$1.92 (\pm 0.04) \times 10^{-8}$
step 17*	1.000	0.033	0.033	$4.58 (\pm 0.040) \times 10^{-8}$	$4.58 (\pm 0.04) \times 10^{-8}$
step 18*	1.000	0.015	0.015	$2.11 (\pm 0.04) \times 10^{-8}$	$2.11 (\pm 0.04) \times 10^{-8}$
step 19*	1.000	0.031	0.031	$4.33 (\pm 0.04) \times 10^{-8}$	$4.33 (\pm 0.04) \times 10^{-8}$
step 20*	1.000	0.016	0.016	$2.25 (\pm 0.04) \times 10^{-8}$	$2.25 (\pm 0.04) \times 10^{-8}$
step 21*	1.000	0.037	0.037	$5.17 (\pm 0.04) \times 10^{-8}$	$5.17 (\pm 0.04) \times 10^{-8}$
step 22*	1.000	0.037	0.037	$5.06 (\pm 0.04) \times 10^{-8}$	$5.06 (\pm 0.04) \times 10^{-8}$

Note: $a = 3.69 \times 10^{-3}$ m

*within the region of condensation

Table 4.11: Butane Sorption at 0^0C (Two Component Fit $F127_t$ coated in $P123_t$ Expt. 1)

Steps	P	k_1 (s^{-1})	k_2 (s^{-1})	D_1 (m^2/s)	D_2 (m^2/s)
step 1	0.519	0.009	0.018	$1.42 (\pm 0.01) \times 10^{-8}$	$3.00 (\pm 0.02) \times 10^{-8}$
step 2	0.518	0.008	0.012	$1.42 (\pm 0.01) \times 10^{-8}$	$2.00 (\pm 0.02) \times 10^{-8}$
step 3	0.478	0.007	0.013	$1.19 (\pm 0.01) \times 10^{-8}$	$2.13 (\pm 0.01) \times 10^{-8}$
step 4	0.373	0.106	0.008	$1.77 (\pm 0.02) \times 10^{-7}$	$1.36 (\pm 0.02) \times 10^{-8}$
step 5	0.619	0.007	0.488	$1.12 (\pm 0.02) \times 10^{-9}$	$8.14 (\pm 0.01) \times 10^{-7}$
step 21*	1.000	0.004	0.000	$5.98 (\pm 0.01) \times 10^{-9}$	$5.01 (\pm 0.02) \times 10^{-10}$
step 22*	1.000	0.005	0.000	$8.47 (\pm 0.01) \times 110^{-9}$	$5.01 (\pm 0.01) \times 10^{-10}$
step 23*	0.272	0.080	0.013	$1.34 (\pm 0.02) \times 10^{-7}$	$2.16 (\pm 0.02) \times 10^{-8}$

Note: $a = 4.06 \times 10^{-3}$ m

*within the region of condensation

Table 4.12: Cyclohexane Sorption at 30^0C (Two Component Fit $F127_t$ coated in $P123_t$ Expt. 2)

Steps	P	k_1 (s^{-1})	k_2 (s^{-1})	D_1 (m^2/s)	D_2 (m^2/s)
step 1	N/A	N/A	N/A	N/A	N/A
step 2	0.421	0.007	0.046	$5.59 (\pm 0.03) \times 10^{-9}$	$3.44 (\pm 0.02) \times 10^{-8}$
step 3	0.500	0.006	0.044	$4.83 9\pm 0.03) \times 10^{-9}$	$3.35 (\pm 0.01) \times 10^{-8}$
step 4	0.547	0.006	0.038	$4.36 (\pm 0.01) \times 10^{-9}$	$2.84 (\pm 0.02) \times 10^{-8}$
step 5	0.581	0.005	0.035	$3.99 (\pm 0.02) \times 10^{-9}$	$2.61 (\pm 0.01) \times 10^{-8}$
step 6	0.633	0.005	0.200	$3.58 (\pm 0.03) \times 10^{-9}$	$1.51 (\pm 0.02) \times 10^{-7}$
step 7	1.000	0.012	0.030	$9.11 (\pm 0.03) \times 10^{-9}$	$2.26 (\pm 0.02) \times 10^{-8}$
step 8	0.486	0.020	0.020	$1.54 (\pm 0.03) \times 10^{-8}$	$1.54 (\pm 0.020 \times 10^{-8}$
step 9	1.000	0.026	0.026	$1.96 (\pm 0.03) \times 10^{-8}$	$1.96 (\pm 0.02) \times 10^{-8}$

Note: $a = 2.73 \times 10^{-3}$ m

Table 4.13: Cyclohexane Sorption at 30^0C (Two Component Fit $P123_t$ Core Expt. 1)

Steps	P	k_1 (s^{-1})	k_2 (s^{-1})	D_1 (m^2/s)	D_2 (m^2/s)
step 1	0.441	0.009	0.052	$1.61 (\pm 0.06) \times 10^{-8}$	$8.96 (\pm 0.17) \times 10^{-8}$
step 2	0.687	0.091	0.028	$1.58 (\pm 0.05) \times 10^{-7}$	$4.89 (\pm 0.12) \times 10^{-8}$
step 3	0.274	0.004	0.070	$7.67 (\pm 0.19) \times 10^{-9}$	$1.22 (\pm 0.19) \times 10^{-7}$
step 4	0.588	0.073	0.006	$1.26 (\pm 0.05) \times 10^{-7}$	$9.62 (\pm 0.05) \times 10^{-9}$
step 5	0.512	0.006	0.093	$1.00 (\pm 0.36) \times 10^{-8}$	$1.62 (\pm 0.22) \times 10^{-7}$
step 6	1.000	0.250	0.101	$4.34 (\pm 0.21) \times 10^{-7}$	$1.75 (\pm 0.23) \times 10^{-7}$
step 7	1.000	0.091	0.020	$1.58 (\pm 0.04) \times 10^{-7}$	$3.47 (\pm 0.10) \times 10^{-8}$
step 8	0.680	0.009	0.330	$1.59 (\pm 0.04) \times 10^{-8}$	$5.73 (\pm 0. 41) \times 10^{-7}$
step 9	1.000	0.015	0.020	$2.58 (\pm 0.04) \times 10^{-8}$	$3.47 (\pm 0.10) \times 10^{-8}$
step 10	0.146	0.509	0.023	$8.83 (\pm 0.04) \times 10^{-7}$	$4.04 (\pm 0.11) \times 10^{-8}$

Note: $a = 4.14 \times 10^{-3}$ m

Table 4.14: Cyclohexane Sorption at 30^0C (Two Component Fit $P123_t$ Coated in Brij 76_t Expt. 1)

Steps	P	k_1 (s^{-1})	k_2 (s^{-1})	D_1 (m^2/s)	D_2 (m^2/s)
step 1	0.856	0.018	0.139	1.92 (± .003)× 10^{-8}	1.49 (± 0.06)× 10^{-7}
step 2	1.000	0.020	0.038	2.19 (± 0.03) × 10^{-8}	4.12 (± 0.06)× 10^{-8}
step 3	0.986	0.024	0.024	2.56 (± 0.03) × 10^{-8}	2.55 (± 0.06)× 10^{8}
step 4	0.981	0.023	0.023	2.43 (± 0.03) × 10^{-8}	2.43 (± 0.06)× 10^{-8}
step 5	0.973	0.022	0.022	2.40 (± 0.03) × 10^{-8}	2.40 (± 0.06) 10^{-8}
step 6	0.947	0.025	0.265	2.65 (± 0.03) × 10^{-8}	2.85 (± 0.05)× 10^{-7}
step 7	0.942	0.025	0.024	2.65 (± 0.04) × 10^{-8}	2.54 (± 0.04)× 10^{-8}
step 8	0.770	0.010	0.010	1.07 (± 0.02) × 10^{-8}	1.07 (± 0.04)× 10^{-8}
step 9	0.894	0.024	0.024	2.58 (± 0.02) × 10^{-8}	2.58 (± 0.04) 10^{-8}
step 10	0.949	0.030	0.015	3.26 (± 0.02) × 10^{-8}	1.66 (± 0.04)× 10^{-8}
step 11	0.951	0.020	0.008	2.15 (± 0.02) × 10^{-8}	8.54 (± 0.04)× 10^{-8}
step 12	0.962	0.019	0.020	2.01 (± 0.03) × 10^{-8}	2.14 (± 0.04)× 10^{-8}
step 13	0.988	0.029	0.036	3.13 (± 0.03) × 10^{-8}	3.86 (± 0.06)× 10^{-8}
step 14	1.000	0.023	0.031	2.53 (± 0.03) × 10^{-8}	3.38 (± 0.06)× 10^{-8}
step 15*	1.000	0.021	0.034	2.27 (± 0.03) × 10^{-8}	3.70 (± 0.06)× 10^{-8}
step 16*	0.953	0.031	0.016	3.38 (± 0.03) × 10^{-8}	1.77 (± 0.04)× 10^{-8}
step 17*	1.000	0.022	0.034	2.38 (± 0.02) × 10^{-8}	3.71 (± 0.04) × 10^{-8}
step 18*	1.000	0.020	0.042	2.16 (± 0.010 × 10^{-8}	4.50 (± 0.11) × 10^{-8}
step 19*	1.000	0.019	0.037	2.09 (± 0.03) × 10^{-8}	4.04 (± 0.12) × 10^{-8}
step 20*	1.000	0.015	0.033	1.58 (± 0.03) × 10^{-8}	3.60 (± 0.12) × 10^{-8}
step 21*	1.000	0.015	0.034	1.66 (± 0.03) × 10^{-8}	3.71 (± 0.10) × 10^{-8}
step 22*	0.977	0.026	0.028	2.80 (± 0.02) × 10^{-8}	3.03 (± 0.06) × 10^{-8}
step 23*	1.000	0.019	0.019	2.07 (± 0.01) × 10^{-8}	2.07 (± 0.06) × 10^{-8}
step 24*	1.000	0.037	0.010	4.02 (± 0.01) × 10^{-8}	1.09 (± 0.06) × 10^{-8}
step 25*	1.000	0.033	0.005	3.58 (± 0.01) × 10^{-8}	5.55 (± 0.06) × 10^{-9}
step 26*	0.897	0.038	0.020	4.09 (± 0.01) × 10^{-8}	2.18 (± 0.05) × 10^{-8}
step 27*	0.855	0.024	0.024	2.55 (± 0.01) × 10^{-8}	2.55 (± 0.06) × 10^{-8}
step 28*	0.935	0.035	0.034	3.72 (± 0.01) × 10^{-8}	3.71 (± 0.06) × 10^{-8}

Note: a = 3.26 × 10^{-3} m

*within the region of condensation

Table 4.15: Cyclohexane Sorption at 30^0C (Two Component Fit $P123_t$ Coated in $CTAB_t$ Expt. 1)

Steps	P	k_1 (s^{-1})	k_2 (s^{-1})	D_1 (m^2/s)	D_2 (m^2/s)
step 1	N/A	N/A	N/A	N/A	N/A
step 2	1.000	0.016	0.000	$1.96 (\pm 0.03) \times 10^{-8}$	0
step 3	0.656	0.013	33.451	$1.58 (\pm 0.03) \times 10^{-8}$	$4.01 (\pm 1.27) \times 10^{-5}$
step 4	0.791	0.032	0.002	$3.88 (\pm 0.04) \times 10^{-8}$	$2.60 (\pm 0.01) \times 10^{-9}$
step 5	0.721	0.032	0.003	$3.81 (\pm 0.04) \times 10^{-8}$	$3.17 (\pm 0.01) \times 10^{-9}$
step 6	0.674	0.030	0.003	$3.57 (\pm 0.04) \times 10^{-8}$	$3.47 (\pm 0.01) \times 10^{-9}$
step 7	0.209	0.267	0.010	$3.21 (\pm 0.11) \times 10^{-7}$	$1.16 (\pm 0.02) \times 10^{-8}$
step 8	0.371	0.022	0.004	$2.59 (\pm 0.03) \times 10^{-8}$	$4.42 (\pm 0.01) \times 10^{-9}$
step 9	0.528	0.003	0.022	$3.30 (\pm 0.01) \times 10^{-9}$	$2.68 (\pm 0.03) \times 10^{-8}$
step 10	0.841	0.005	0.005	$6.46 (\pm 0.02) \times 10^{-9}$	$6.47 (\pm 0.02) \times 10^{-9}$
step 11	1.000	0.050	0.050	$6.00 (\pm 0.05) \times 10^{-8}$	$6.00 (\pm 0.05) \times 10^{-8}$
step 12	0.211	2.559	0.010	$3.07 (\pm 0.35) \times 10^{-6}$	$1.20 (\pm 0.02) \times 10^{-8}$
step 13	0.802	0.004	0.004	$4.79 (\pm 0.01) \times 10^{-9}$	$4.80 (\pm 0.01) \times 10^{-9}$
step 14	0.586	0.010	0.010	$1.15 (\pm 0.02) \times 10^{-8}$	$1.15 (\pm 0.01) \times 10^{-8}$
step 15*	0.525	0.006	0.006	$7.79 (\pm 0.01) \times 10^{-9}$	$7.79 (\pm 0.02) \times 10^{-9}$
step 16*	0.801	0.008	0.008	$1.00 (\pm 0.02) \times 10^{-8}$	$1.00 (\pm 0.03) \times 10^{-8}$
step 17*	0.509	0.005	0.005	$5.83 (\pm 0.02) \times 10^{-9}$	$5.83 (\pm 0.02) \times 10^{-9}$
step 18*	0.517	0.006	0.006	$6.99 (\pm 0.02) \times 10^{-9}$	$6.99 (\pm 0.02) \times 10^{-9}$
step 19*	0.541	0.006	0.006	$6.77 (\pm 0.02) \times 10^{-9}$	$6.77 (\pm 0.03) \times 10^{-9}$
step 20*	1.000	0.020	0.030	$2.40 (\pm 0.03) \times 10^{-8}$	$3.60 (\pm 0.03) \times 10^{-8}$
step 21*	0.512	0.005	0.005	$6.25 (\pm 0.02) \times 10^{-9}$	$6.25 (\pm 0.02) \times 10^{-9}$

Note: $a = 3.44 \times 10^{-3}$ m

*within the region of condensation

Table 4.16: Butane Sorption at 0^0C (Two Component Fit $P123_t$ Coated in $CTAB_t$ Expt. 2)

Steps	P	k_1 (s^{-1})	k_2 (s^{-1})	D_1 (m^2/s)	D_2 (m^2/s)
step 1	0.000	0.056	0.013	$8.79 (\pm 0.05) \times 10^{-8}$	$2.11 (\pm 0.03) \times 10^{-8}$
step 2	0.500	0.016	0.016	$2.43 (\pm 0.03) \times 10^{-8}$	$2.43 (\pm 0.03) \times 10^{-8}$
step 3	0.500	0.015	0.015	$2.39 (\pm 0.03) \times 10^{-8}$	$2.39 (\pm 0.03) \times 10^{-8}$
step 4	0.499	0.015	0.015	$2.36 (\pm 0.03) \times 10^{-8}$	$2.36 (\pm 0.03) \times 10^{-8}$
step 5	0.375	0.012	0.012	$1.82 (\pm 0.03) \times 10^{-8}$	$1.82 (\pm 0.03) \times 10^{-8}$
step 6	0.664	0.013	0.021	$2.06 (\pm 0.03) \times 10^{-8}$	$3.27 (\pm 0.03) \times 10^{-8}$
step 7	0.701	0.017	0.017	$2.64 (\pm 0.03) \times 10^{-8}$	$2.64 (\pm 0.03) \times 10^{-8}$
step 8	0.677	0.016	0.016	$2.55 (\pm 0.03) \times 10^{-8}$	$2.55 (\pm 0.03) \times 10^{-8}$
step 9	1.000	0.013	0.027	$2.08 (\pm 0.03) \times 10^{-8}$	$4.24 (\pm 0.04) \times 10^{-8}$
step 10*	1.000	0.012	0.012	$1.85 (\pm 0.03) \times 10^{-8}$	$1.89 (\pm 0.03) \times 10^{-8}$
step 11*	0.590	0.011	0.011	$1.77 (\pm 0.03) \times 10^{-8}$	$1.77 (\pm 0.03) \times 10^{-8}$
step 12*	0.815	0.011	0.011	$1.69 (\pm 0.03) \times 10^{-8}$	$1.69 (\pm 0.03) \times 10^{-8}$
step 13*	1.000	0.011	0.088	$1.75 (\pm 0.03) \times 10^{8}$	$1.37 \pm 0.07 \times 10^{7}$
step 14*	1.000	0.011	0.011	$1.65 (\pm 0.03) \times 10^{8}$	$1.65 \pm 0.03 \times 10^{8}$
step 15*	1.000	0.011	0.011	$1.76 (\pm 0.03) \times 10^{8}$	$1.65 \pm 0.03 \times 10^{8}$

Note: $a = 3.93 \times 10^{-3}$ m

*within the region of condensation

Table 4.17: Cyclohexane Sorption at 0^0C (Two Component Fit $P123_t$ Coated in $F127_t$ Expt. 1)

Steps	P	k_1 (s^{-1})	k_2 (s^{-1})	D_1 (m^2/s)	D_2 (m^2/s)
step 1	0.482	0.044	0.007	$5.83 (\pm 0.06) \times 10^{-8}$	$9.93 (\pm 0.02) \times 10^{-9}$
step 2	0.482	0.044	0.007	$5.83 (\pm 0.06) \times 10^{-8}$	$9.93 (\pm 0.02) \times 10^{-9}$
step 3	1.000	0.078	0.078	$1.04 (\pm 0.08) \times 10^{-7}$	$1.04 (\pm 0.08) \times 10^{-7}$

Note: $a = 3.63 \times 10^{-3}$ m

Table 4.18: Butane Sorption at 0^0C (Two Component Fit $P123_t$ Coated in $F127_t$ Expt. 2)

Steps	P	k_1 (s^{-1})	k_2 (s^{-1})	D_1 (m^2/s)	D_2 (m^2/s)
step 1	1.000	0.034	0.069	$4.74 (\pm 0.06) \times 10^{-8}$	$9.53 (\pm 0.03) \times 10^{-8}$
step 2	0.783	0.037	0.009	$5.09 (\pm 0.02) \times 10^{-8}$	$1.19 9\pm 0.06) \times 10^{-8}$
step 3	0.346	0.044	0.017	$6.05 (\pm 0.02) \times 10^{-8}$	$2.31 (\pm 0.06) \times 10^{-8}$
step 4	1.000	0.018	0.061	$2.51 (\pm 0.01) \times 10^{-8}$	$8.45 (\pm 0.03) \times 10^{-8}$
step 5	0.726	0.032	0.006	$4.40 (\pm 0.02) \times 10^{-8}$	$8.55 (\pm 0.02) \times 10^{-9}$
step 6	0.461	0.013	0.019	$1.81 (\pm 0.05) \times 10^{-8}$	$2.62 (\pm 0.03) \times 10^{-8}$
step 7	1.000	0.013	0.019	$1.85 (\pm 0.04) \times 10^{-8}$	$2.67 (\pm 0.01) \times 10^{-8}$
step 8	0.567	0.013	0.024	$1.77 (\pm 0.03) \times 10^{-8}$	$3.38 (\pm 0.02) \times 10^{-8}$
step 9	0.862	0.013	0.198	$1.84 (\pm 0.02) \times 10^{-8}$	$2.75 (\pm 0.01) \times 10^{-7}$
step 10	0.916	0.014	0.188	$1.94 (\pm 0.01) \times 10^{-8}$	$2.62 (\pm 0.02) \times 10^{-7}$
step 11	0.108	0.308	0.014	$4.28 (\pm 0.01) \times 10^{-7}$	$1.97 (\pm 0.02) \times 10^{-8}$
step 12	0.892	0.014	0.205	$1.90 (\pm 0.02) \times 10^{-8}$	$2.85 (\pm 0.06) \times 10^{-7}$
step 13	0.873	0.010	0.010	$1.46 (\pm 0.03) \times 10^{-8}$	$1.46 (\pm 0.06) \times 10^{-8}$
step 14	0.905	0.012	0.166	$1.66 (\pm 0.03) \times 10^{-8}$	$2.30 (\pm 0.05) \times 10^{-7}$
step 15	0.533	0.007	0.011	$1.04 (\pm 0.05) \times 10^{-8}$	$1.48 (\pm 0.06) \times 10^{-8}$
step 16	0.928	0.007	0.024	$1.02 (\pm 0.06) \times 10^{-8}$	$3.29 (\pm 0.05) \times 10^{-8}$
step 17	1.000	0.009	0.030	$1.22 (\pm 0.06) \times 10^{-8}$	$4.23 (\pm 0.06) \times 10^{-8}$
step 18	1.000	0.013	0.021	$1.74 (\pm 0.05) \times 10^{-8}$	$2.89 (\pm 0.06) \times 10^{-8}$
step 19	1.000	0.014	0.027	$1.88 (\pm 0.04) \times 10^{-8}$	$3.77 (\pm 0.05) \times 10^{-8}$
step 20*	0.929	0.012	0.012	$1.68 (\pm 0.02) \times 10^{-8}$	$1.68 (\pm 0.05) \times 10^{-8}$
step 21*	0.760	0.010	0.010	$1.40 (\pm 0.01) \times 10^{-8}$	$1.40 (\pm 0.04) \times 10^{-8}$
step 22*	1.000	0.009	0.010	$1.20 (\pm 0.02) \times 10^{-8}$	$1.43 (\pm 0.04) \times 10^{-8}$
step 23*	1.000	0.008	0.031	$1.13 (\pm 0.02) \times 10^{-8}$	$4.29 (\pm 0.05) \times 10^{-8}$
step 24*	0.835	0.011	0.022	$1.52 (\pm 0.01) \times 10^{-8}$	$3.07 (\pm 0.06) \times 10^{-8}$
step 25*	0.918	0.012	0.031	$1.68 (\pm 0.04) \times 10^{-8}$	$4.34 (\pm 0.05) \times 10^{-8}$
step 26*	0.672	0.016	0.016	$2.26 (\pm 0.06) \times 10^{-8}$	$2.26 (\pm 0.05) \times 10^{-8}$

Note: $a = 3.70 \times 10^{-3}$ m

*within the region of condensation

Table 4.19: Cyclohexane Sorption at 30^0C (Two Component Fit $F127_t$ + 1.008g Pentanol Expt. 1)

Steps	P	k_1 (s^{-1})	k_2 (s^{-1})	D_1 (m^2/s)	D_2 (m^2/s)
step 1	0.000	0.050	0.039	5.91 (± 0.0080 × 10^{-8}	4.62 (± 0.006) × 10^{-8}
step 2	1.000	0.055	0.055	6.51 (± 0.008) × 10^{-8}	6.51 (± 0.008) × 10^{-8}
step 3	0.634	0.032	0.041	3.74 9± 0.006) × 10^{-8}	4.91 (± 0.007) × 10^{-8}
step 4	1.000	0.045	0.045	5.35 (± 0.007) × 10^{-8}	5.35 (± 0.007) × 10^{-8}
step 5	1.000	0.026	0.000	3.03 9± 0.006) × 10^{-8}	0
step 6	1.000	0.065	0.060	7.71 (± 0.008) × 10^{-8}	7.14 (± 0.008) × 10^{-8}

Note: a = 3.42 × 10^{-3} m

Table 4.20: Cyclohexane Sorption at 30^0C ($F127_t$ + 1.008g Pentanol Coated in $P123_t$ Expt. 1)

Steps	P	k_1 (s^{-1})	k_2 (s^{-1})	D_1 (m^2/s)	D_2 (m^2/s)
step 1	0.323	0.004	0.004	3.16 (± 0.02) × 10^{-9}	3.16 (± 0.03) × 10^{-9}
step 2	0.500	0.006	0.006	4.05 (± 0.02) × 10^{-9}	4.05 (± 0.03) × 10^{-9}
step 3	0.505	0.018	0.018	1.29 (± 0.04) × 10^{-8}	1.29 (± 0.06) × 10^{-8}
step 4	0.500	0.014	0.014	1.03 (± 0.05) × 10^{-8}	1.03 (± 0.05) × 10^{-8}
step 5	0.500	0.017	0.017	1.22 (± 0.04) × 10^{-8}	1.22 (± 0.05) × 10^{-8}
step 6	0.500	0.031	0.031	2.19 (± 0.05) × 10^{-8}	2.19 (± 0.07) × 10^{-8}
step 7	0.500	0.015	0.015	1.08 (± 0.04) × 10^{-8}	1.08 (± 0.05) × 10^{-8}
step 8	0.500	0.013	0.013	8.91 (± 0.03) × 10^{-9}	8.91 (± 0.05) × 10^{-9}
step 9	0.500	0.004	0.004	2.83 (± 0.02) × 10^{-9}	2.83 (± 0.03) × 10^{-9}

Note: a = 2.64 × 10^{-3} m

Table 4.21: Cyclohexane Sorption at 30^0C ($F127_t$ + 1.008g Pentanol Coated in $CTAB_t$ Expt. 1)

Steps	P	kK_1 (s^{-1})	k_2 (s^{-1})	D_1 (m^2/s)	D_2 (m^2/s)
step 1	0.550	0.001	0.134	1.09 (± 0.006) × 10^{-9}	1.43 (± 0.06) × 10^{-9}
step 2	0.380	0.113	0.022	1.21 (± 0.06) × 10^{-7}	2.38 (± 0.02) × 10^{-8}
step 3	0.410	0.036	0.005	3.87 (± 0.03) × 10^{-8}	5.79 (± 0.01) × 10^{-9}
step 4	0.434	0.018	0.018	1.95 (± 0.02) × 10^{-8}	1.95 (± 0.02) × 10^{-8}
step 5	0.500	0.004	0.004	3.76 (± 0.01) × 10^{-9}	3.76 (± 0.01) × 10^{-9}
step 6	0.500	0.044	0.044	4.76 (± 0.03) × 10^{-8}	4.76 (± 0.04) × 10^{-8}
Step 21*	0.500	0.007	0.007	8.00 (± 0.02) × 10^{-9}	8.00 (± 0.02) × 10^{-9}
step 22*	0.500	0.040	0.040	4.29 (± 0.04) × 10^{-8}	4.29 (± 0.04) × 10^{-8}
step 23*	0.500	0.069	0.069	7.35 (± 0.05) × 10^{-8}	7.35 (± 0.05) × 10^{-8}

Note: a = 3.25 × 10^{-3} m

*within the region of condensation

4.1.7.2 - Two Component k Mass Transfer Coefficient

In order to improve upon the accuracy of the assessment of the transport properties of the synthesised core and bimodal silica materials, a second attempt was made by using the two component LDF model to measure k_1 and k_2 (see Equation 4.6). The quoted error for the pellet diameters is one standard deviation for the set of measurements taken of the linear dimension of each pellet, and is thus an estimate of the deviation of the particle from a spherical shape. This is the largest contributor of error to the measured diffusivity values. The calculated diffusivity is directly proportional to Ka^2, and within this research the constant of proportionality is assumed to be $1/\pi^2$. Although the chosen value of the constant is arguable, it is worth noting that for the purpose of this research the emphasis is on a comparative basis and hence the value of the chosen constant does not affect the validity of the results. The modal pore body size for $CTAB_t$ was found to be ~2 - 4 times smaller than the modal pore size of $P123_t$, hence the statistically significant drop in diffusivity of cyclohexane between the $P123_t$ core (see Table 4.13) in comparison to the $P123_t$ coated in $CTAB_t$ shown in Tables 4.15, and 4.16 is a result of the shielding effect of the smaller pores of $CTAB_t$. However there is relatively little difference between the transport properties of the $P123_t$ core and the $P123_t$ coated in $F127_t$ composite. This again suggests that since $P123_t$ and $F127_t$ have similar pore body sizes, the narrower pore necks present in $F127_t$ has a slight effect on the adsorption, but does not greatly affect the diffusion process. $F127_t$ + ~1 g of pentanol as shown in Table 4.19 has an average diffusivity of $\sim 5.1\times10^{-8}$ m^2 s^{-1}, and Table 4.21 shows a reduction to an average of 3.8×10^{-8} m^2s^{-1} on coating with $CTAB_t$. The existence of a full coat has not been confirmed by other imaging methods, and however one could be led to think that decrease in diffusivity is linked to the $CTAB_t$ pores, and also by ensuring a full coat has been applied or even increasing the thickness of the coat, could lead to a more pronounced effect. Again a $CTAB_t$ coat of modal pore body size of 31 Å (HK) has been shown to reduce the effective diffusivity of $F127_t$ + ~1 g of pentanol core of a modal pore body size of 53 Å (HK). The effective diffusivity of cyclohexane in $F127_t$ + ~1 g of pentanol coated in P123 experiment 1 are higher than observed for the core material (see Table 4.19 and 4.20). This is consistent with the presence of a complete coat with a higher pore neck size, as the adsorption/desorption data for F127 templated material suggests a pore structure of large pores surrounded by much smaller necks, therefore

much small neck size exists for $F127_t$ in comparison to $P123_t$. The composite is calculated to have a modal pore body size of 45.2 Å, whereas the core material had a modal pore body size of 42.2 Å. Table 4.6 and Table 4.7 show the results of subsequent cyclohexane adsorption experiments on two $CTAB_t$ core materials. On coating a sample from the same batch as $CTAB_t$ experiment 1 with $P123_t$, the resulting composite gives diffusivity values much higher than that obtained for the $CTAB_t$ core. This result suggests that a distinctive region of larger pore sizes has been created around the $CTAB_t$, and it leads to a higher diffusivity than expected for the smaller pores of the $CTAB_t$ material alone. Further along the adsorption isotherm the diffusivity begins to drop, nearer the diffusivity values expected for $CTAB_t$, confirming the presence of a core material with a smaller modal pore body size on the interior. Table 4.11 shows a significant drop in the diffusivity of butane in $F127_t$ coated in $P123_t$ for steps 21-23 (region of condensation) in comparison to the first five steps. This result suggest that the coat material contributes to the diffusivity at low pressure filling, prior to the start of capillary condensation in those pores, when most of the pores would begin to fill and lead to a steady slowing down of the adsorption rate. Condensate can either block access for gas phase mass transport, or because liquids are denser, if it flows it can make a big difference to mass transport rates. However due to the composite nature of the material, one could be led to think that around the point where capillary condensation begins in those pores the core material starts to dominate the adsorption process, and the narrow necks in $F127_t$ core material may have lead to the significant drop.

For $P123_t$ coated in $F127_t$, experiment 1 and 2 (see tables 4.17 and 4.18) similar diffusivities are calculated for cyclohexane and butane respectively, indicating that both butane and cyclohexane share similar adsorptive properties. This is consistent with the fact that butane is a non-polar alkane, and cyclohexane is similar to butane as it is an alkane compound too. There is also a molecular mass dependency of diffusivity and as the molar mass of butane is close to cyclohexane, which is 58.1 g/mol. and 84.16 g/mol, similar rates of diffusivity can be expected, as seen in the results section (Tables 4.1 - 4.21). Ideally butane molecules are smaller and should hence have a faster rate of diffusion, this is also consistent with the measured diffusivities of the first step in the region of condensation as shown in Table 4.1 and 4.2, where butane and cyclohexane

diffusivity in $F127_t$ coated in $P123_t$ were measured to be 7.82×10^{-7} m^2s^{-1}, and 2.34×10^{-10} m^2s^{-1} respectively.

Tables 4.19, 4.20, and 4.21 show the data set for $F127_t$ +1.0008 g of pentanol core material and their composite with $P123_t$ and $CTAB_t$ respectively. This material has pore body size greater than that of the ordinary $F127_t$ (see synthesis method section), and hence also produces a material with a larger pore body size than $CTAB_t$. $F127_t$ and $P123_t$ have already been shown to produces pore bodies of similar sizes, but the differing factor is the small constricting necks of $F127_t$. It can be seen from the results of $F127_t$ +1.0008 g of pentanol core material, that the coat with the smallest pore body produces a more pronounced shielding effect, as desorption from the big pores are delayed until the smaller shielding pores are emptied and hence the decrease in the diffusivity. Two experiments were performed on the same sample of Brij 76_t, at two different temperatures to characterise the temperature dependence of the mass transfer coefficient of the material. The results of the two component fits on these materials are shown in Table 4.4 and 4.5. There is a higher mass transfer coefficient (*k* value) for cyclohexane adsorption at 10 ^oC in Brij 76_t experiment 2. The D_2 values obtained using the two component model for both experiments ($\sim4\times10^{-4}$ m^2s^{-1}) are consistent with the guess values used to run the Excel Solver, for the analysis of the two experimental results. Hence the mass uptake is dominated by one component, making the D_1 values an accurate estimation of the diffusivity which was $\sim5\times10^{-4}$ m^2s^{-1} for Brij 76_t experiment 1 and $\sim 7\times10^{-4}$ m^2s^{-1} for Brij 76_t experiment 2.

The linear driving force (LDF) model as adapted by Thomas *et al.*, (1995) describes the gas adsorption uptake curve for most parts of the adsorption curve for all surfactant templated silica solids analysed within this research, with a slightly less than 99 % fit for certain regions of the isotherm as can be seen in Graph A5 (Appendix A). This slight variation in the behaviour of some parts has been attributed to the effect of inhomogeniety caused by the percentage of surface coverage. At medium desorption factors, when the pressure for the emptying of larger pores is being approached, the linear fit drops slightly below 99 % and this is probably because at this point, some randomly dispersed large pores will still contain some condensed liquid. This behaviour has been repeated across all the experiments being discussed within this research. One is

led to believe that these filled large pores causes a temporary heterogeneous effect on the pores that reduces the accuracy of the LDF model, as the LDF model was developed for a perfectly homogeneous spherical surface.

4.1.8 - Conclusions

The results presented in this section have shown the kinetic study of a range of synthesised porous materials. The kinetics of the porous materials have been shown to follow the linear driving force (LDF) model, and it has been used to obtain values of the mass transfer coefficient of butane and cyclohexane in the synthesised materials and hence their diffusivities. It can therefore, be concluded that core-coat composite particles that retain different pore structures in each zone, can be manufactured. Adding a microporous coat ($CTAB_t$) to a mesoporous core (such as $P123_t$, $F127_t$ and Brij 76_t) brings down the diffusion coefficient in line with the decrease in modal pore diameter. The modal pore diameter for $P123_t$ is larger than the $CTAB_t$ for instance, and these features are reflected in the diffusion coefficients.

4.2 – Investigative Studies of Hysteresis using Gas Adsorption Kinetics

Adsorption can be seen as the increase in concentration or density of one or more gaseous components in the vicinity of a gas-solid interface. Gas adsorption kinetics study will be applied to a range of adsorbate - adsorbent systems to investigate the pore filling mechanisms, and although it is hoped that a physical adsorption mechanism will control the uptake of gas within this systems, chemisorption effects cannot be totally ruled out. The forces involved in physisorption (which occurs when a clean solid (adsorbate) is exposed to a gas (adsorptive)) are the same as those responsible for the condensation of vapours and their deviation from ideal gas behaviour. Unlike chemisorption, physisorption involves no chemical bonding to the surface. However if they are polar, the physisorbed molecules may undergo specific interactions with particular functional groups (e.g. surface hydroxyls on silica pellets prior to heat treatment) as explained further within this Chapter. The chemical nature of a solid will

influence its adsorption properties, as the energy of immersion in the fluid depends directly on the surface chemistry and also to some extent on the nature of the bulk solid. For example the interaction between water and silica may have contributions from the bulk SiO_2 and contributions from the silanol groups of the interface. The purpose of this section is to increase our understanding of adsorption kinetics, high pressure hysteresis and multi-layer adsorption for cyclohexane (C_6H_{12}), butane and water vapours. The adsorption and desorption kinetics will be assessed to investigate the geometry connectivity of the condensed phase within mesoporous sol gel silica pellets. The LDF model is used to determine rate constants for adsorption/desorption in C10, which is a sol gel silica.

There are few reports to date on the comparisons of the rate constants of adsorption/desorption kinetics for the purpose of investigating high-pressure hysteresis. One report by Barrer *et al.* (1958) showed that for an adequate description of the transient and steady states of volume and surface flow of gases and vapours in microporous media, four different diffusion coefficients are required, namely; a surface and a gas phase coefficient for transient and a surface and a gas phase coefficient for steady flow. The distinction between steady and transient flow arises in part because of the role of blind pores. Similarly two different porosities and two different surface areas govern transient and steady-state flow respectively. By comparing the two gas-phase and the two surface diffusion coefficients with gas-phase and surface diffusion coefficients in a smooth cylindrical capillary having porosity/area equal to that of the porous medium, four structure factors can be defined, in terms of which the transport/pore properties of microporous media can be discussed. They presented sorption data for transient flow (time lag) and steady flow of He, Ne, A and N_2 in compressed alumina catalyst plugs analysed according to the above procedure and pore properties compared. This made it possible to obtain information regarding pore structure which could not have been derived by an alternative method. Barrer *et al.*, (1958) used diffusion coefficients measured for sorption data to further emphasise the differences between transient and steady states of flow, which can help characterise blind pores as distinct from open pores. They suggested that surface diffusion coefficients derived by Fick's law from the measured surface fluxes, for microporous media having rough and interrupted surfaces are likely to be about an order of magnitude less than diffusion coefficients on molecularly smooth straight surfaces of

the same substrate. They also found that on such smooth surfaces the true diffusion coefficient also has a smaller Arrhenius energy of activation than the experimental diffusion coefficients.

4.2.1 - Theory/Background

Rigby *et al.* (2004) used integrated mercury porosimetry and nitrogen sorption to investigate the existence of the pore blocking effect within the mesoporous C10 silica sol gel. Pore blocking has some similarities to pore shadowing or pore shielding, which also arises in mercury intrusion porosimetry (Androutsopoulos 1979). So if pore blocking also arises in mercury porosimetry then the PSD from gas desorption should match those obtained from mercury porosimetry. This provides a simple test for pore blocking effects, as long as the necessary correction for the contact angle and surface tension has been implemented. Based on the above assessment, Rigby and Fletcher, (2004) reported the existence of pore blocking effects in nitrogen desorption of the tested material.

Smarsly *et al.* (2001) used in-situ small angle neutron scattering (SANS) to investigate gas adsorption within larger mesopores which consists of multilayer build-up and then capillary condensation, according to the Kelvin equation. The SANS studies supported the assumption, that capillary condensation is governed by the structural properties of the single pores and is less affected by network effects in contrast to desorption and therefore suggests that gas adsorption hysteresis could be a result of networking effects (pore blocking).

NMR investigation of adsorption/desorption hysteresis was carried out on porous silicas by Porion *et al.* (1998) where they analysed the possible differences in the connectivity of the liquid phase in a partially water-saturated porous medium between the adsorption and the desorption branches. This was done by comparing the T_1 and T_2 relaxation times in ^1H and ^2H nuclear magnetic resonance (NMR) relaxation, as well as the water self diffusion coefficient D (in ^1H), along the two branches of the adsorption/desorption isotherms. By using the results of adsorption/desorption isotherms, and within the framework of the fast exchange model as developed by Brownstein and Tarr (1979), the

relaxation rates should be sensitive to the solid/liquid interface area, whereas the self diffusion coefficient should depend on adsorbed phase tortuosity. The water sorption experiment was performed on silica gels with pore sizes of ~10 nm which has a similar PSD, surface chemistry (in the sense that they both contain SiO_2 sites), and synthesis method to the test samples used in this research. They showed that at equivalent water saturation levels, there was no difference between NMR relaxation times and self diffusion coefficients for the condensed liquid phase obtained, hence suggesting that the geometry and connectivity of the liquid phase was the same for both the adsorption and desorption branches. If pore blocking effects were occurring during desorption there should be differences in the geometry and topology of the condensed liquid phase between the two branches of the hysteresis loops. A review of the above studies indicates a discrepancy in the existence of pore blocking effect during gas desorption. The pore blocking theory suggests that desorption of the condensed liquid from a pore network is a cooperative process, whereby the evaporation of the condensed liquid from a large pore is delayed if access to the vapour phase is only via a smaller adjacent pore (classic ink-bottle theory). The ink bottle and network effect in capillary condensation has been extensively reviewed by several researchers (Everett, 1967; Gregg and Sing, 1982). In this investigation of the pore blocking effect, C10, an irregular amorphous solid with increased likelihood of exhibiting networking effects than a structured mesoporous material like the SBA-type is employed as the test material. An irregular amorphous solid such as C10 can also exhibit cooperative effects on adsorption such as advanced condensation, where if pore neck radius is greater than half body size, both adsorption and desorption would be a single step and hence no pore blocking effects would be evident. This is worth noting, and will be discussed further at a later stage within this research.

Many mesoporous materials with Type IV or III gas sorption isotherms, often exhibit a region of irreversibility, where two different relative pressures produce the same mass of adsorbed gas on the adsorption or desorption branches, known as the region of hysteresis. Hysteresis occurs in the capillary condensation region of the sorption isotherms for a number of reasons peculiar to the adsorbate-adsorbent pairs, and in some cases it remains unknown (Rouquerol *et al.*, 1999) and hence a need for further investigations exists. Wallacher *et al.* (2004) created a material from silicon wafers with ink bottle type pores, starting with an outer thinner section at the angle and a wider

section with a blind end in the regular part of the wafer. They obtained N_2 and Ar isotherms to confirm that the crucial geometry is of inkbottle type. If capillary condensation is considered a first order phase transition, then the geometry should result in pore blocking effects. For the region of irreversibility in some adsorption isotherms, they ascribed no other reason than the effect of a broken chain of condensed liquid, which is due to the liquid-matrix interaction in combination with random field disorder (heterogeneities).The concept of pore blocking in the most rigorous form assumes that a pore segment with diameter D can only evaporate, when on lowering the vapour pressure to the corresponding Kelvin pressure of D, there is free access to the vapour reservoir outside the porous matrix. Hence, for inkbottle type pores, the evaporation of the segment with larger diameter D_1 is delayed until condensed nitrogen in the segment with the smaller diameter D_s evaporates at a lower pressure. Pore blocking is considered as the basis of percolation models (Mason, 1983), which explains the sharp phase-transition-like onset of desorption in pore networks such as Vycor. Many researchers such as Mason (1983) and Seaton (1991) believe hysteresis in nitrogen adsorption is due to the pore interconnectivity on nitrogen desorption. In addition to the hysteresis due to finite connectivity, there is also a 'single pore' contribution to the hysteresis, due to a delay in capillary condensation during the adsorption process. Measurements on unconnected porous materials of type MCM-41 show that the effect of 'single pore' hysteresis loop exists and is smaller than that found in porous solids that have interconnected pores (Ravikovitch *et al.* 1997). In addition to the effect of the connectivity of the pore network, the hysteresis that is observed in sorption measurements on porous materials of various shapes and structure may contain a purely thermodynamic contribution. Measurements of adsorption on solids which have very narrow pore size distributions, have shown that hysteresis can exist even when there is no structural impediment to desorption (Godshalk and Hallock, 1987).

Cohan (1938) suggested that hysteresis might arise for pores consisting of cylinders open at both ends because of the difference in the shapes of the meniscus during adsorption and desorption. Prior to adsorption the meniscus is cylindrical in shape, while prior to desorption the meniscus is hemispherical in shape. However, most real materials such as alumina catalyst supports and sol gel silicas are known to have a more complex pore structure consisting of interconnecting networks of pore bonds, or of voids and necks. (Ravikovitch *et al.*, 2002) describes capillary hysteresis as being more

pronounced in the inkbottle type pores, following preliminary work by researchers (such as Kraemer, 1931; Mc Bain, 1935; Cohan, 1938). The pore filling in the process of condensation follows the formation of a liquid film on the cavity wall and thus is controlled by the radius of curvature of the cavity, r_c. The pressure of condensation is given by the Kelvin–Laplace equation. During desorption, evaporation occurs after the formation of a hemispherical meniscus, in the pore neck and thus is controlled by the radius of the neck r_n. The pressure for evaporation is also represented in a similar manner to condensation with r_c being replaced by r_n.

The study of gas adsorption kinetics of the hysteresis loops will provide valuable information, which can be compared to the low pressure region of reversibility to identify any mechanistic differences. Berenguer-Murcia *et al.* (2003) compared the adsorption kinetics of carbon dioxide, n-nonane, and α-pinene, showing a variation of the diffusion rate constant with relative pressure for the test samples of MCM-41 and precipitated silica. Their results fit the LDF model, and were consistent with diffusion through a barrier as the rate-determining step despite the large variation in the size and shape and structure of adsorptive. The variation in the rate constant could either be associated with either a surface barrier or diffusion through molecular constrictions (narrow pore necks) in the porosity. At low surface coverage, a much larger molecule (α-pinene) had a faster rate constant in comparison to a smaller molecule (n-nonane). This led the authors to the conclusion that the constrictions are not the determining factor, and hence proposed a surface diffusion barrier is present in adsorption in a mesoporous structure, which was attributed to the alignment of molecules in the mesopores leading to a pore blocking effect. In activated carbons with either Type III or Type IV isotherms, the adsorption kinetics for water vapour adsorption also followed the LDF model, and showed a decrease in the rate constant with increasing surface coverage. The authors attributed this behaviour to the formation of water molecule clusters around functional groups which causes the development of barriers to diffusion and hence a decrease in the rate constants. Different dependencies of tortuosity on volume of condensate adsorbed might indicate a different spatial disposition of condensates for different adsorptives on the adsorption branch. Therefore if there were a surface barrier as a result of pore blocking effect and poor connectivity, one would expect, if pore blocking effect is the cause of high pressure hysteresis, the mass transfer

coefficient will differ for the same region in adsorption and desorption, since the mass transfer coefficient depends on the tortuosity and pathway of evaporation or condensation. If the gas molecules are adsorbed through a certain pathway in accordance with gas uptake, and the condensed liquid follows the theory of pore blocking (i.e. larger pores accessible only through one narrow exit), then surely the pathway and tortuosity will be different between adsorption and desorption. This is because the diffusion coefficient is reduced for liquids in comparison to the gas phase. One can assume that if the pathways for gas phase transport are different, then surely the mass transfer coefficient will differ between adsorption and desorption. If they don't, then it is evident that the pathway of uptake is the same for desorption and hence pore blocking effects were not occurring in this system. For the same C10 silica pellets as used within this research pore blocking effects were reported to exist when an integrated nitrogen adsorption and mercury porosimetry was performed (Rigby *et al.*, 2004), whilst NMR studies for water sorption on a similar silica pellet showed no difference in the adsorption/desorption branches, attributable to pore blocking (Porion *et al.*, 1998). Nitrogen and water vapour sorption will be used in this investigation, to represent both of the above adsorbate-adsorbent systems of previous studies.

Water adsorption experiments by Branton *et al.* (1995) reported low values of BET monolayer coverage (n_m) for water adsorption on MCM-41 which resulted in a typical Type III isotherm confirming the low adsorbent-adsorbate interactions associated with a 'hydrophobic' surface in comparison to other adsorptives such as nitrogen indicating a low affinity for the surface. The initial monolayer adsorption was evidently confined to a very small part of the total internal surface, however capillary condensation occurred in the mesopores in an apparently normal manner around P/P^0 = 0.6. The authors concluded that the low affinity of the MCM-41 for water vapour is an important property of this adsorbent and another interesting feature is its reversibility in the pre-hysteresis region. With respect to these qualities they quote, that MCM-41 behaves more like a mesoporous carbon than dehdroxylated silica, and hence there appears to be no indication of any dissociative chemisorption of water on the internal surface.

4.2.2 - Water Adsorption Theory

Water is one of the most plentiful and essential compounds occurring in nature, which makes its interaction with porous solids and metal surfaces of interest to various fields of science and is of particular relevance to heterogeneous catalysis. The adsorption mechanism for water on surfaces with active sites; such as hydroxyl silanols as seen on silicates or carboxyl groups on carbons, is markedly different from that of simple non-associating molecules such as hydrocarbons or nitrogen.

In contrast to the usual build up of adsorbed layers on the surface, water adsorption is characterised by the ability of water molecules to form H-bonds with the surface sites, and then with subsequently adsorbed molecules which results in the formation of three dimensional water clusters and networks, whose formation relies on a cooperative effect involving both fluid-fluid and fluid-solid interactions with suitably placed active sites. The density and arrangement of these active sites on the surface of the adsorbate have a pronounced effect on the adsorption of water (Muller *et al.*, 1996). Under this mechanism of adsorption, capillary condensation is observed only for adsorbents with low densities of active sites, whereas in adsorbents with higher density of active sites, continuous filling occurs. Muller *et al.* (1996) reported a molecular simulation of a model of water adsorption on nonporous and porous activated carbons. The authors were able to use the Monte-Carlo (GCMC) method, at a fixed temperature of 300K, to model the water molecules as a Lenard-Jones ((LJ) atom) sphere with four square-well sites as shown in Figure 4.1.l. Two sites correspond to the hydrogen atoms (H type), the other two corresponding to the lone pair electrons in the oxygen atom (O type). The square well (SW) sites represent the associating sites. The carbon surfaces were shown to consist of planar graphite sheets consistent with slit shaped pores that possess active chemical sites on the square well sites. The authors carried out a systematic study using molecular simulation to understand the mechanism of adsorption of water and aqueous solutions in model activated carbons and to answer the questions at hand regarding the molecular mechanisms involved: how it occurs and why it differs from that of simple fluids, and if it does?

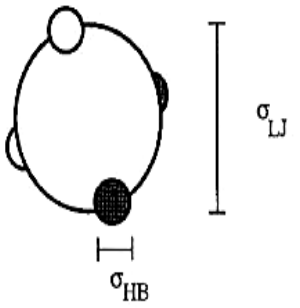

Figure 4.1: Sketch of the water molecule, the large open circle represents the LJ core of the molecule. The small open (H-type) and shaded (O-type) circles are the square well sites (SW) associating sites. O-type sites bond only to H-type sites. H-type sites also bond to sites placed on the surface. (Muller *et al.*, 1996) (With kind permission of the American Chemical Society).

Using the Werthiems theory (Muller *et al.*, 1996) to calculate the area occupied by an adsorbed water molecule based on a model of non associating water molecules (LJ spheres), of site diameter 0.306nm within a closed packed hexagonal monolayer is 0.081nm^2, which is in poor agreement with the commonly sited estimate of 0.105nm ^{2}. However, the tetrahedral hydrogen bonding of water implies a much more open structure with a coordination number of four and a corrugated monolayer, which will result in each molecule occupying 0.1nm^2, which is in close agreement with the commonly quoted value (Muller *et al.*, 1996). This confirms that modelling water adsorption in terms of a monolayer leads to an incorrect picture of the actual physical process. Water turned out to be a very poor adsorbate for un-activated walls (less active site) and only at high pressures is any noticeable amount adsorbed. For activated walls, which were achieved by randomly placing spherical SW sites on the surface, the amount of water adsorbed increased as a result of the decreasing hydrophobic nature of the surface. They authors also showed that in the low pressure regimes the sites each adsorb a water molecule, and that at high coverage some cooperative effects take place and water molecules may now adsorb onto sites as well as onto adsorbed molecules. Once groups of water clusters are formed around active sites they are shown to connect producing a large bonded molecule, with pressure increase leading to capillary condensation (see Figures 4.2 and 4.3).

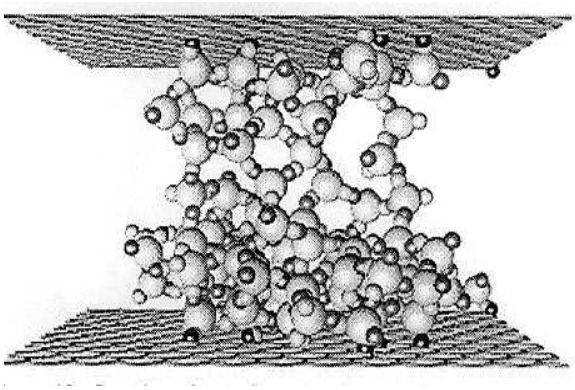

Figure 4.2: Showing the snapshot of a configuration from a GCMC simulation at P/P^0 = 0.0631, which according to the adsorption isotherm is within the region of capillary condensation for the carbon slit pores (Muller at al., 1996) (With kind permission of the American Chemical Society).

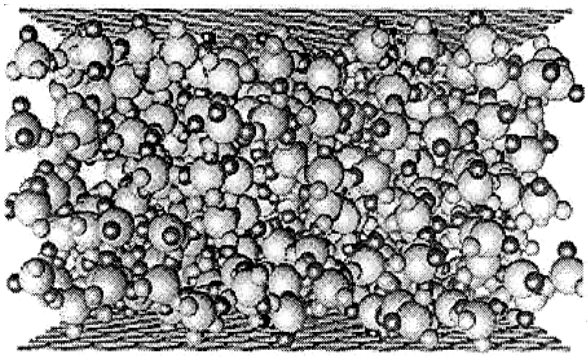

Figure 4.3: Showing the snapshot of a configuration from a GCMC simulation at P/P^0 = 0.0932, (Muller at al., 1996) (With kind permission of the American Chemical Society).

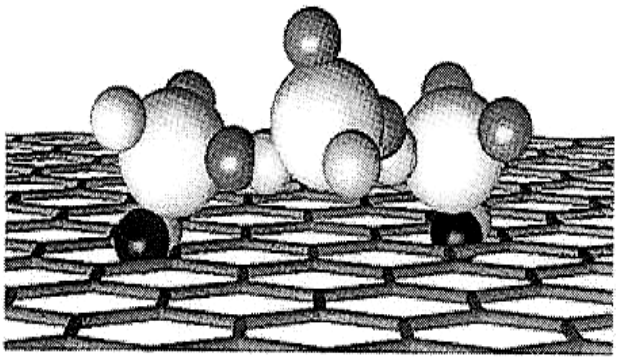

Figure 4.4: Bridging between two molecules which are H bonded onto sites on the surface. The cluster in the middle is isolated from an equilibrium configuration, (Muller at al., 1996) (With kind permission of the American Chemical Society).

A feature evident from Figure 4.2 is the availability not only of free surface in the pore, but also of free associating sites such as the one in the far right corner. It confirms that this type of adsorption is of cooperative effects and the position of the sites is crucial to the overall behaviour of the system. A snapshot of the filled pores for an activated surface (see Figure 4.3) also showed that when the pore is filled with a dense liquid like adsorbate phase, the phase is very stable and hence produces large hysteresis loops in gas adsorption. The non-activated surface presents a somewhat similar hysteresis, however this is caused by the fluid-fluid interactions, which allow a metastable condition (Muller *et al.*, 1996). Figure 4.4 shows the mechanistic bridging that occurs in water adsorption, which leads to the so-called 'selective' or 'cooperative adsorption' mechanism proposed for water adsorption. So therefore, in the absence of active sites, molecules could be adsorbed onto molecules.

Iiyama *et al.* (2004) also carried out similar studies by using in-situ small-angle X-ray scattering (SAXS) to study water and CCl_4 adsorption on pitch-based activated carbon fibres (ACF) at different relative pressures at 303 K. The authors extended the Debye-Bueche theory to the three-phase mixed system (carbon, adsorbed phase, and vacant space) to obtain the average dimension of the adsorbed phase *I(a)* (where *I(a)* is a correlation function parameter from a Debye-Bueche fit) . The zero-angle intensity of X-ray scattering *I-0* and *I(a)* gave direct information on the shape and size of molecular assemblies in the micropores. CCl_4 molecules uniformly fill the micropores, while water molecules fill the micropores via the formation of cluster-like assemblies comprising about 12 molecules, irrespective of pore width. In the small pore system (w = 0.75 nm) the cluster size was unchanged with increase in the fractional filling. On the other hand, in the wider pore system (w = 1.13 nm), the cluster grew with increased fractional filling. It seems that the difference in the size and shape of water clusters in the adsorption and desorption processes could lead to adsorption hysteresis. Thus, the *I-0*, *I(a)*, and average dimension of vacant space *I(v)* from in situ SAXS measurements may give direct information on molecular assemblies in micropores (Iiyama *et al.*, 2004).

4.2.3 - Nitrogen Adsorption

Several researchers including Seaton (1991), Liu *et al.* (1994), and Rouquerol *et al.* (1999) assume that nitrogen is completely wetting of most porous solid surfaces, and hence exhibits a zero contact angle. This is one of the reasons why nitrogen is used to probe most solids for structural characterization. It is therefore not surprising that most of the investigative work into the existence of hysteresis is performed using nitrogen. Water vapour and cyclohexane show a lower strength of interaction with silicas, in comparison to nitrogen, and they also exhibit similar shaped BET regions as can be seen for isotherms run within this research in Figures 4.13 - 4.17 in the results section.

Nitrogen adsorption isotherms were obtained using the Micrometric ASAP, and a scanning loop was also obtained using the IGA. The limited N_2 scanning loop was targeted to the point of the onset of hysteresis. The kinetics data was collected and the mass transfer coefficient k was calculated for both branches of the scanning loops to identify if at all any differences exist in the tortuosity and pathways of the adsorbed phase. During the scanning experiment, there will be certain unoccupied small pores adjacent to large pores containing condensed nitrogen, and according to the percolation theory if these large pores link to the surface and/or also have an adjacent unoccupied pore with access to the surface then pore blocking hysteresis is limited. So therefore under the circumstances, if a region of irreversibility is observed in the scanning loops, then it will confirm the effects of pore blocking, since it is evident even under the least likely circumstance.

A further look into the theory of hysteresis shows that if the pore width is sufficiently large, a first-order phase transition should occur at an appropriate chemical potential from gas to metastable bulk liquid, with an accompanying jump in the adsorption. Evans *et al.* (1986) suggested that adsorption hysteresis was likely to be associated with this discontinuous jump. The expectation that the magnitude of the first-order transition should be reduced with increase in temperature would explain the experimental observation of the effect of temperature in decreasing the size of the hysteresis loops (Machin, 1994).

Attempts were made by Everett (1955, 1965) to formulate the behaviour of groups of pores in terms of 'domain theory'. The independent domain theory assumed that each pore behaves as though it was interacting in isolation with the vapour, and therefore the overall behaviour was considered to depend on the statistical distribution of the individual pore properties. When the scanning loops were traced within given limits, the areas of these subsidiary loops were neither constant nor independent of their location within the main loop, and hence it was concluded that the domains do not behave independently. In addition as most mesoporous adsorbents possess complex networks of pores of different size it is therefore unlikely that the condensation-evaporation processes can occur independently for each pore. Following Monte-Carlo simulation studies of the complexity of porous materials by Page and Monson (1996) and Gelb and Gubbins (1998), the well-defined hysteresis loops observed were attributed to the presence of thermodynamic metastable states and not to kinetic effects. Rouquerol *et al.* (1999) concluded that the extent of hysteresis was associated with the overall heterogeneity of the adsorbent structure and not simply due to capillary condensation within individual pores. The fact that the condensate cannot leave a pore at the 'Kelvin relative pressure' unless there is a continuous channel of vapour leading to the adsorbent surface supports the conclusions of the work of Rouquerol *et al.* (1999), suggesting that the probability of a portion of the condensate being trapped if any, will depend on the nature of the pore network and the numerical and spatial distribution of pore size. Thus a large amount of entrapment and hence a more pronounced hysteresis will be observed if a high proportion of the pore volume is only accessible through narrow channels with relatively low level of pore connectivity.

The percolation theory has been applied to adsorption in porous solids by several researchers (Liu *et al.*, 1994; Mason *et al.*, 1988; Seaton, 1991) who consider the pore space as a three- dimensional network of cavities and necks. If the total neck volume is relatively small, the location of the adsorption branch should be mainly determined by the cavity size distribution. On the other hand, if the evaporation process is controlled by percolation, the location of the desorption branch, is determined by the network coordination number and the neck size distribution. The alternative structural model adopted by Seaton (1991) to estimate interconnectivity, represented the mesopore network by a simple cubic lattice where each pore is regarded as a bond in the lattice and each junction is a node, and the average size of the small particles is expressed as

the number of pore lengths *l*. Seaton and co workers (Liu *et al.*, 1992) have simulated the desorption percolation for nitrogen from a simple cubic lattice, and their hypothetical results were plotted in the form of the fraction of the pores retaining liquid nitrogen $(1\text{-}x^A)$ against the fraction of the pores containing nitrogen in its stable condensed state. Here x is defined, as the fraction of the pores large enough to allow evaporation at P/P^0 and x^A is the fraction of pores from which nitrogen is able to evaporate at P/P^0. As the adsorption run is not influenced by the connectivity, *x* over the adsorption branch of the hysteresis loop represents the fraction of pores in which condensation has not yet occurred at P/P^0 and thus the linear relationship $(1\text{-}x^A) = (1\text{-}x)$ represents the adsorption branch, assuming no advanced condensation effects exist. A plot was generated for a given value of lattice size *L* with these coordinates, and the simulation data gives a series of transformed desorption isotherms, which provide an indication of vapour accessibility as a function of bond occupation probability (see Figure 4.5 below). As one would expect, the results showed that over a certain fraction of occupation, the location of the accessibility curve is highly dependent on the value of *L*. Subsequent experiments by Lui *et al.* (1992) showed that an increasing value of the coordination number *Z* causes the percolation threshold to move to the right, and this is because there is a greater chance that the liquid in a given pore can find a pathway of vapour-filled pores to the surface. It can therefore be concluded that the size of hysteresis loop is increased as the mean coordination number is reduced.

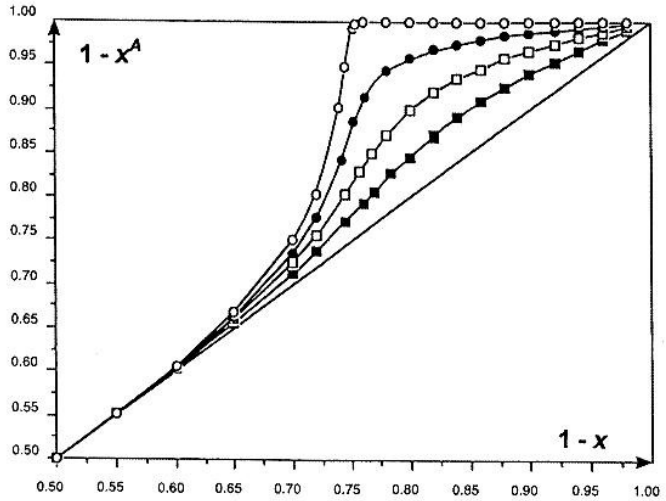

Figure 4.5: Showing fraction of pores retaining liquid nitrogen $(1\text{-}x^A)$ against the fraction of the pores containing nitrogen in its stable condensed state (1-x) (Liu *et al.*, 1992). The different lines shown are for different scanning loops (With kind permission of Elsevier).

It can be seen from Figure 4.5 that it is harder to achieve pore blocking effect in scanning loops, than in a full adsorption/desorption isotherm. The variation from the equilibrium line is less pronounced for the smallest scanning loops, and it's shown to reach a maximum for the complete isotherm. Following on from the work of Liu *et al.* (1992), the limited nitrogen scanning loop run within this research is therefore expected to show just a fraction of the region of irreversibility that is expected, or associated with this particular adsorbate-adsorbent system.

4.2.4 - Experimental Procedure

This Study has been performed on a series of mesoporous silica pellets (C10), with an estimated average pore diameter of 10nm, and an average pore volume of ~1.05 cc/g determined from nitrogen gas adsorption BJH PSD. Water vapour and cyclohexane adsorption experiments were performed on the same set of silica pellets using the Intelligent Gravimetric Analyzer (IGA). In the case of cyclohexane adsorption on C10 silica pellets, the analysis were ran on a partially dehdroxylated sample at a temperature of 30 ^{o}C. The silica pellet was prepared by evacuating to vacuum at a temperature of 100 ^{o}C for an hour, to drive off any physisorbed molecules and was denoted (experiment 1). For water adsorption on C10, four sets were run denoted, experiment 1, 2, 3 and 4. The first sample was prepared by evacuation at room temperature, to a vacuum of (1×10^{-5} kP_a) for a few hours, and ran at 10 ^{o}C. There was no heat application, during the degassing process, in an attempt to preserve the silanol groups of the interface as surface chemistries can be altered by heat. The second sample was exposed to the atmosphere overnight, to allow for adsorption of moisture in an attempt to eliminate interference to the adsorption isotherm as a result of the chemisorption effects (i.e. re-hydroxylation reactions that may occur) prior to the experiment which was ran at 10 ^{o}C. The third sample was heated to 100 ^{o}C during evacuation for a few hours, which should lead to a loss of hydroxyl surfaces, prior to the experiment being run at 20 ^{o}C. The fourth sample was run at 10 ^{o}C and was prepared by soaking in water overnight and then allowed to dry over several days prior to being evacuated at room temperature. The sample would then have been exposed, to high water content, which should further eliminate the possibility of chemisorption, and hence the adsorption process will be

attributed to physisorption and the nature of the interaction strengths between the adsorbent and adsorbate. Type IV isotherms have been obtained for the set of experiments run, and their specific surface area has been calculated using the classical Brunauer-Emmet-Teller (BET) model. Water vapour was adsorbed to fill up a substantial fraction of the estimated pore volume. A nitrogen adsorption desorption scanning loop was also run to act as a control experiment to investigate hysteresis as an effect of pore blocking under the least likely case scenario.

The nitrogen adsorption/desorption scanning loops were performed at 77 K using the IGA. The sample used for the nitrogen experiment is the same as the one used for the cyclohexane experiment and hence has the same sample pre-treatment history. The experimental procedure is also the same as in Chapter 3, where the technique is explained in detail, except for the method employed for the temperature control because the required temperature (-195 ^{o}C) is significantly lower than previously with butane (0 ^{o}C) or cyclohexane (30 ^{o}C). A manual temperature control was adopted by employing a Dewar full of liquid nitrogen, insulated tightly and made to cover the entire reactor section where the adsorbent sits. The problems of evaporation and stability encountered with this option, makes it paramount to avoid running a more prolonged full isotherm analysis. When target temperature is reached, it is very important to maintain a tight temperature control as the 'Kelvin equation pressure' is dependent on the temperature and hence the amount adsorbed will be affected. The above reasons have contributed to the decision to run a short scanning loop as opposed to the alternative of running a complete isotherm. As a full nitrogen adsorption/desorption isotherm has been run on the micrometrics ASAP for the characterisation of the PSD of the C10 silica pellets, the relevant relative pressure for the onset of hysteresis has been noted and implemented as a starting pressure point for adsorption in the IGA since the adsorption process is an equilibration process and the amount adsorbed is a function of the temperature and pressure. The resulting scanning loop is a true picture of the selected region of capillary condensation, and represents the onset of hysteresis.

4.2.5 - Analysis

This section discusses the details of the experimental analysis of the uptake mass transfer coefficient of the adsorbates (cyclohexane water vapour and nitrogen), transport properties and the total pore volume of the adsorbent (C10 silica pellets).

Nitrogen shows high interaction strength with hydroxylated silica walls, as can be seen in the resulting Type IV isotherm shown in the results section (Figure 4.12). Cyclohexane has a similar BET region to all of the water isotherms run (Figures 4.13 - 4.16 and 4.39), and so their isotherm shapes are similar, indicating a lower strength of adsorbate-adsorbent interaction. For this reason, the cyclohexane mass transfer coefficient is being compared to that of water, since a similar adsorption mechanism might be occurring in the region of monolayer coverage. If there is a difference in the observed trends of the variation of mass transfer coefficient with amount adsorbed for water vapour and nitrogen gas, it could be due to the same causes giving rise to the differences in the shapes of their equilibrium isotherms. However a difference in the analogous trends of mass transfer coefficient for water vapour and cyclohexane cannot be explained by the strength of adsorbate-adsorbent interaction. This suggests that a peculiar mechanism governs water vapour sorption. As water adsorbs, if it follows the same mechanism as nitrogen adsorption on mesoporous silica pellets, the mass transfer coefficient will be expected to drop as the vapour begins to condense, since liquid diffusion rates are much slower than gas diffusion. Assuming water vapour behaves like nitrogen gas, the pores are expected to fill up with the condensed liquid, blocking the passage ways for gas to be adsorbed onto other pores, hence k should decline steadily. Following the maximum volume adsorbed, the pressure is reduced to that required for desorption. If this system has pore blocking effects, a different set of pores should be filled, at a particular value of amount adsorbed on adsorption compared to desorption. At the same time, if pore blocking exists, the passage way for desorption will have a different tortuosity factor to that of adsorption, and hence one will expect a change in the k. If an isotherm shows no hysteresis, then one will expect no variations in the k, whereas if the isotherm shows a region of irreversibility, as a result of pore blocking phenomenon, then the k values are expected to differ.

4.2.6 - Calculations of V/Vo

A dimensionless factor $\frac{v}{v_0}$ is used to represent the fraction of the pore space occupied by the adsorbed fluid for the analysis of both vapour sorption and cyclohexane adsorption. The value of v_0 represents the total pore volume of the c10 silica pellets as deduced by nitrogen adsorption.

$$\frac{v}{v_0} = \frac{\frac{m^f - m}{m \times \rho}}{v_0} \qquad \textbf{(4. 7)}$$

Where v = Volume of adsorbate/gram of sample

m^f = mass of sample + adsorbate at equilibrium

m = dry mass of adsorbent

ρ = density of the adsorbate

v_0 = total specific pore volume of C10 silica pellets obtained from N_2 adsorption

4.2.7 - Mass Transfer Coefficient

The linear driving force model is being adopted to calculate the mass transfer coefficients across the pressure points on both the adsorption and desorption branch of the isotherm. The work of Berenguer-Murcia *et al.* (2003) shows that for the adsorption kinetics of water vapour on MCM-41 type which have either a Type III or Type IV isotherms, the linear driving force model holds, and there is a decrease in the rate constant with increasing surface coverage, and for this reason, it is assumed that this model is sufficient to describe the fluid transfer rates for cyclohexane and water vapour adsorption this silica sol gel. This method has previously been explained in Chapter 3, and exactly the same experimental procedures apply here. For an overall graph of mass uptake vs. time, a series of stepwise increases occurs for adsorption, and stepwise decreases for desorption. Each step is considered as independent, assuming the previous step has reached equilibrium, and then time and weight increase or decrease can be

renormalized. A data set from water vapour experiment 2 will be used to show how the mass transfer coefficient is obtained. A plot of the overall kinetic data is broken down to steps and each step looks like either one of the two (Figures 4.6 - 4.8) below, depending on whether it is an adsorption or desorption process. For some pressure steps the pressure increase towards equilibrium fluctuates (Figures 4.6 and 4.7 shows a few wiggles). These fluctuations could be a result of either a bit of error in weight measurement or under damping of the pressure step control, but mainly the latter.

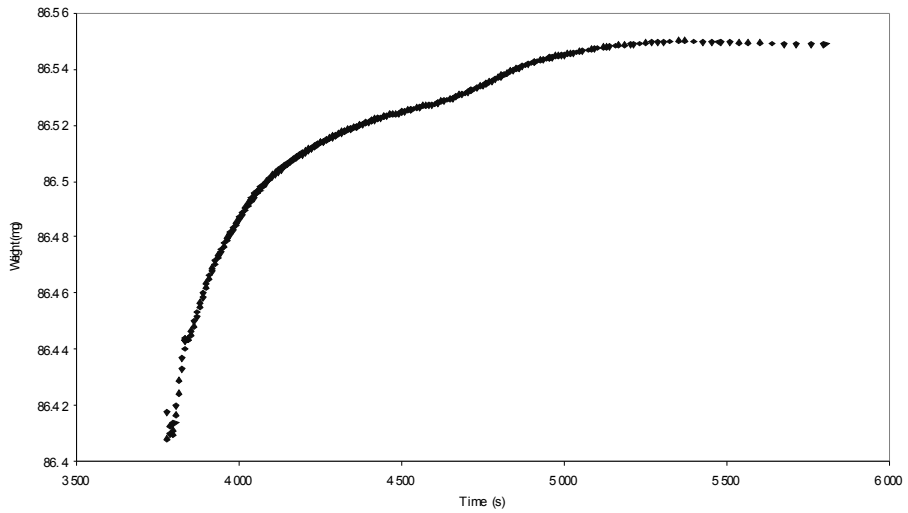

Figure 4.6: Adsorption step 1 for water vapour sorption experiment 1on C10 (see Figure 4.13).

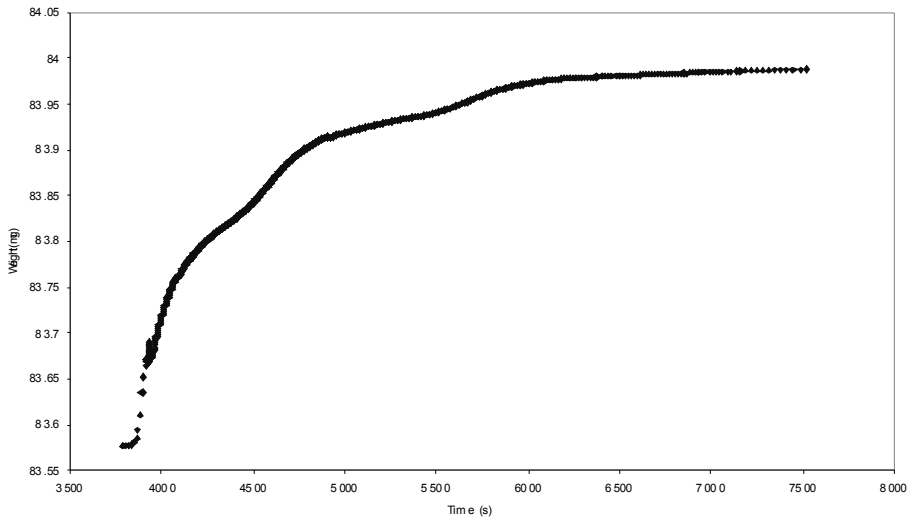

Figure 4.7: Adsorption step 1 for water vapour sorption experiment 4 on C10 (see Figure 4.16).

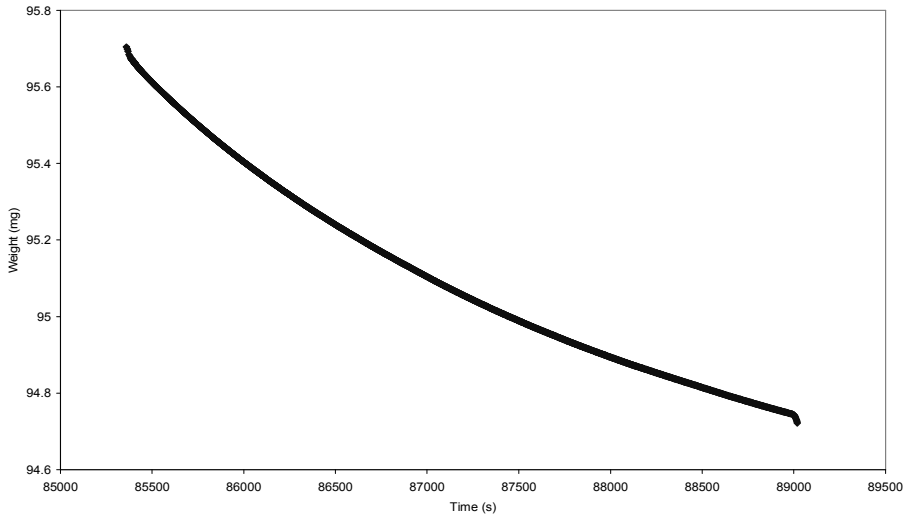

Figure 4.8: Desorption step 1 for water vapour sorption experiment 1(see Figure 4.13).

For $M_t / M_f > 0.5$ the gas uptake can be approximated by Equation 4.5, hence a plot f $ln (1- M_t/M_f)$ vs. t (time) will give a slope with a gradient, which represents k, where k is essentially comparable to $D\pi^2/ a^2$. For a set of M_t values, where M_f is the equilibrium uptake at the plateau, k is obtained subsequently for all steps. Typical examples are show below (Figures 4.9-4.11). The model is also shown to vary slightly when applied outside its range of linearity $(M_t /M_f < 0.5)$. Equation 4.5 does not hold for small times $(M_t /M_f < 0.5)$ as a different equation is approximated for small times $(M_t/M_f < 0.25)$ as shown in Equation 4.4). However Figure 4.9 shows a good fit of Equation 4.5 for $(M_t/M_f < 0.25)$ which is outside its region of validity, it also gives a better fit in comparison to Figures 4.10 and 4.11 for ranges $(M_t /M_f = 0.5 -< 0.7)$ and $(M_t /M_f = 0 -< 0.9)$ respectively (both within its region of validity). There is also some systematic variation from the fitting line in Figures 4.10 and 4.11, which could be attributed to the drawbacks of the LDF model as well as inconsistencies associated with the inaccurate representation of the adsorption theory by the Kelvin equation and subsequent models.

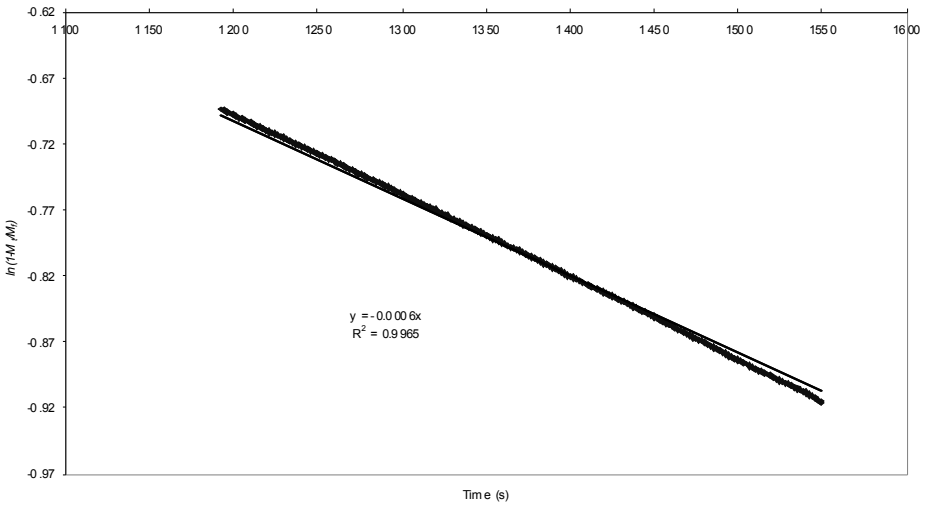

Figure 4.9: Shows a typical Plot of *ln (1-M_t/M_f)* Vs Time for *M_t/M_f = 0- < 0.25* (Water Vapour Experiment 1 as shown in Figure 4.13).

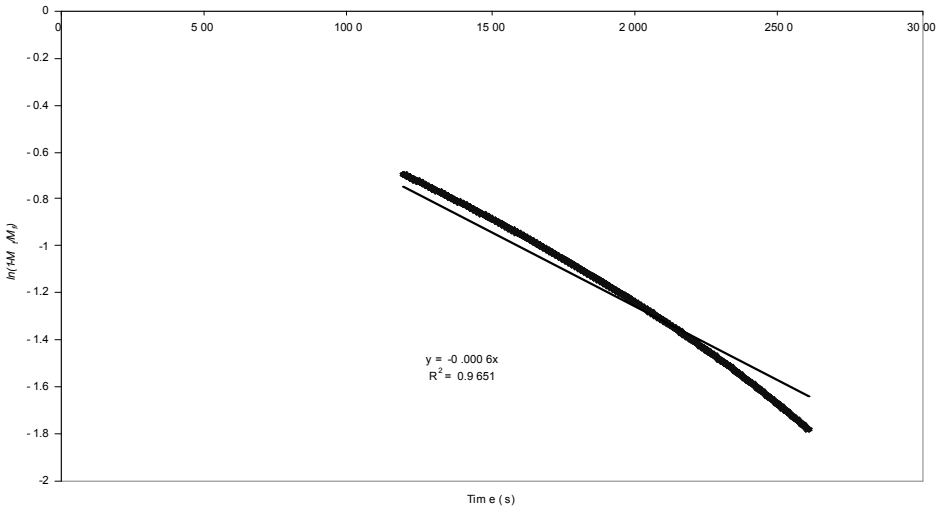

Figure 4.10: Shows a typical Plot of *ln (1- M_t/M_f)* Vs Time for *M_t/M_f = 0.5 -< 0.7* (Water Vapour Experiment 1 as shown in Figure 4.13).

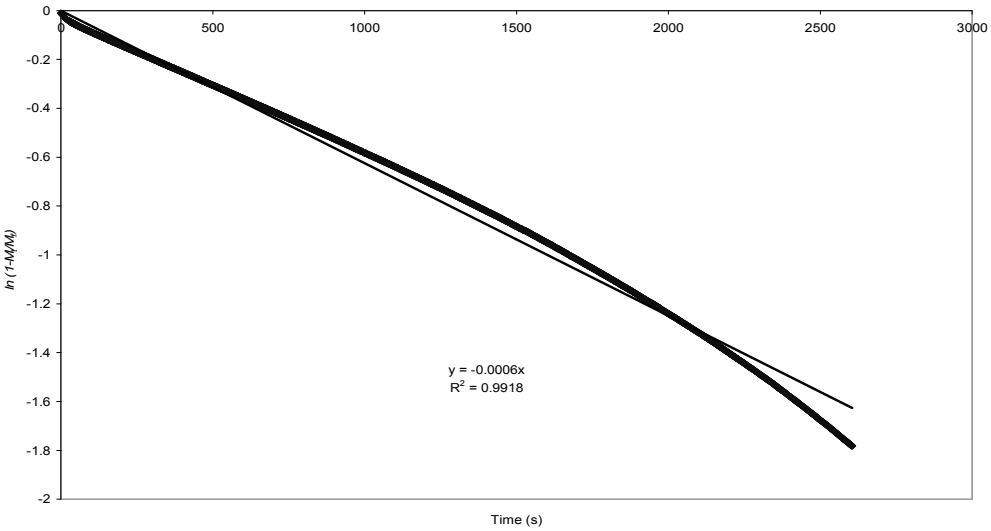

Figure 4.11: Shows a typical Plot of *ln (1- M_t/M_f)* Vs Time for *M_t/M_f = 0 - < 0.9* (Water Vapour Experiment 1 as shown in Figure 4.13).

4.2.8 - Results

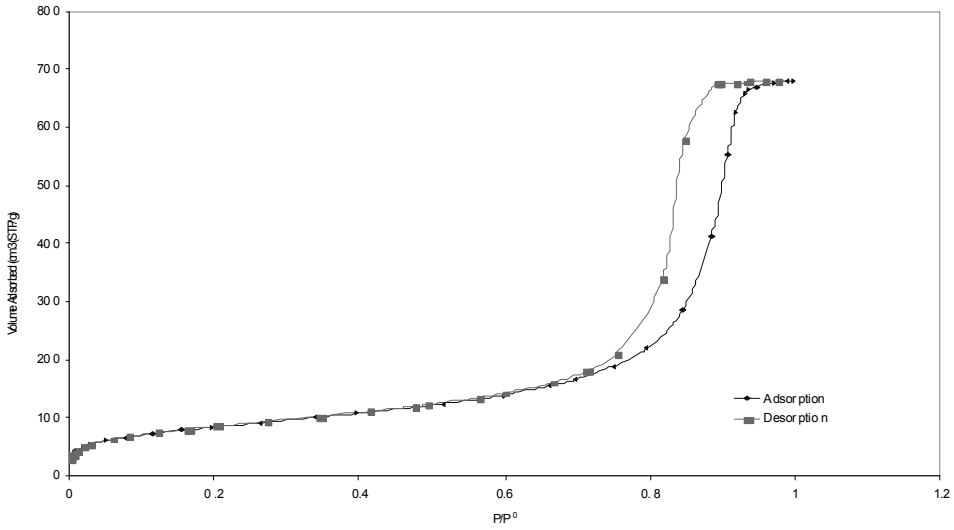

Figure 4.12: Nitrogen sorption experiment 1 at 77 K on C10 silica pellets.

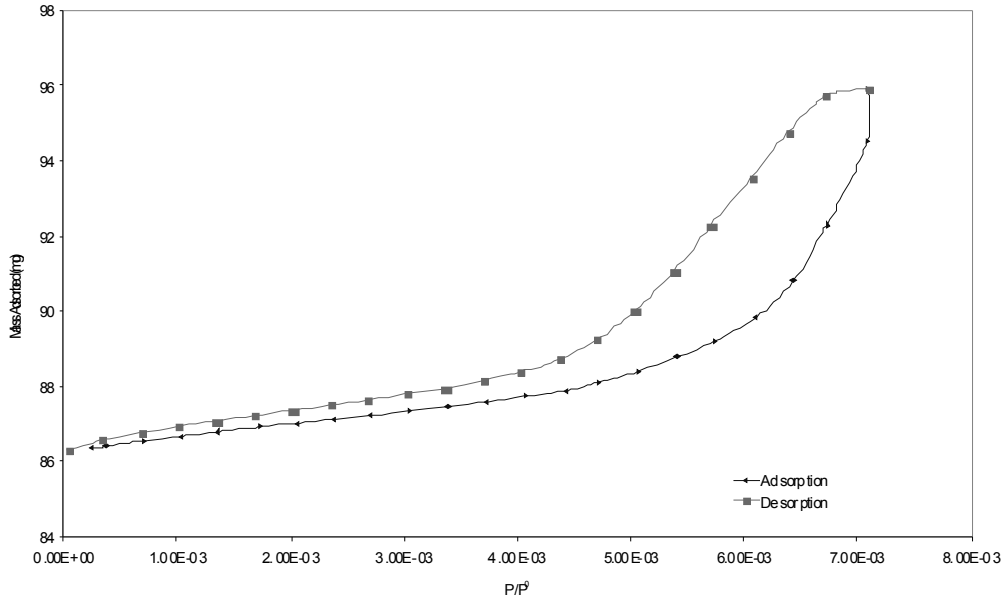

Figure 4.13: Water vapour sorption experiment 1 at 10 ^{o}C on C10 silica pellets.

The first water vapour isotherm results in a Type V isotherm as shown in Figure 4.13, indicating a weak adsorbate-adsorbent interaction. A very slight low pressure hysteresis is evident on this isotherm, and this behaviour is probably due to the limited chemisorption that might have occurred between the silica hydroxyl groups and the water molecules. Although prior to the experiment, the sample did not undergo thermal treatment, and hence the hydroxyl surfaces should be preserved, it is likely that in the course of manufacture, the calcining to free up pores could have resulted in dehydroxylated surfaces. The low pressure hysteresis is much smaller than that within the region of capillary condensation, and can be ignored, as it could be a result of the amount of water lost to reaction. The result isotherm is hence extremely likely to be a true reflection of this sample, and the high pressure hysteresis loop evident is just as well.

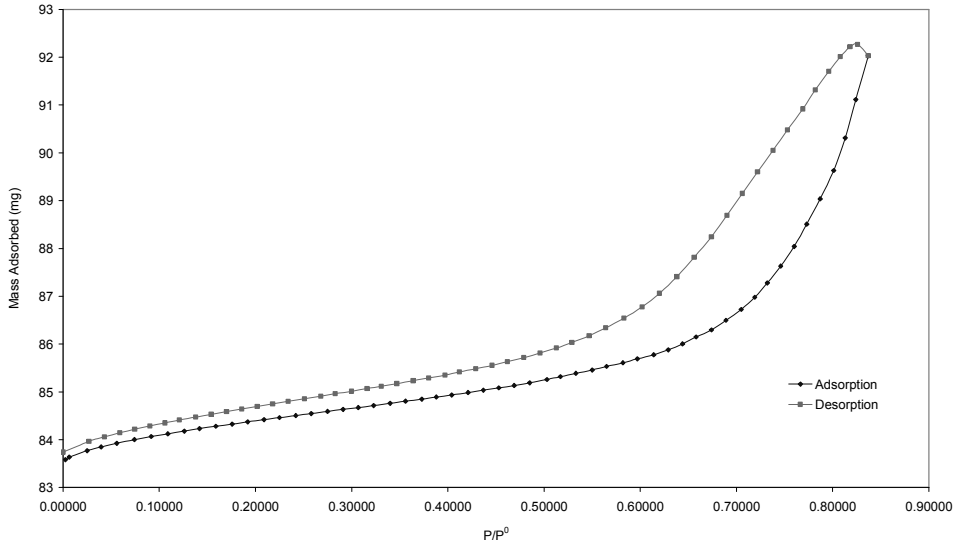

Figure 4.14: Water vapour sorption experiment 2 at 10 °C on C10 silica pellets.

Following water vapour experiment 1, a second experiment is run, and the resulting isotherm (Figure 4.14) is as well a Type V isotherm according to the IUPAC 1985 classification. This experiment has more pressure points at smaller pressure intervals, which will help emphasize the existence of any trends particular to the adsorbate-adsorbent system, and also decreases any endotherms and exotherms due to heat of adsorption. Although this sample was exposed to the atmosphere for moisture uptake, in an attempt to get rid of the low pressure hysteresis, it is still evident, although slightly less emphasised than that of the water vapour experiment 1. The size of the discrepancy evident at the top of the isotherm (Figure 4.14) almost matches the size of the fluid's low pressure hysteresis. This may be as a result of chemisorbed water that does not come back off the surface.

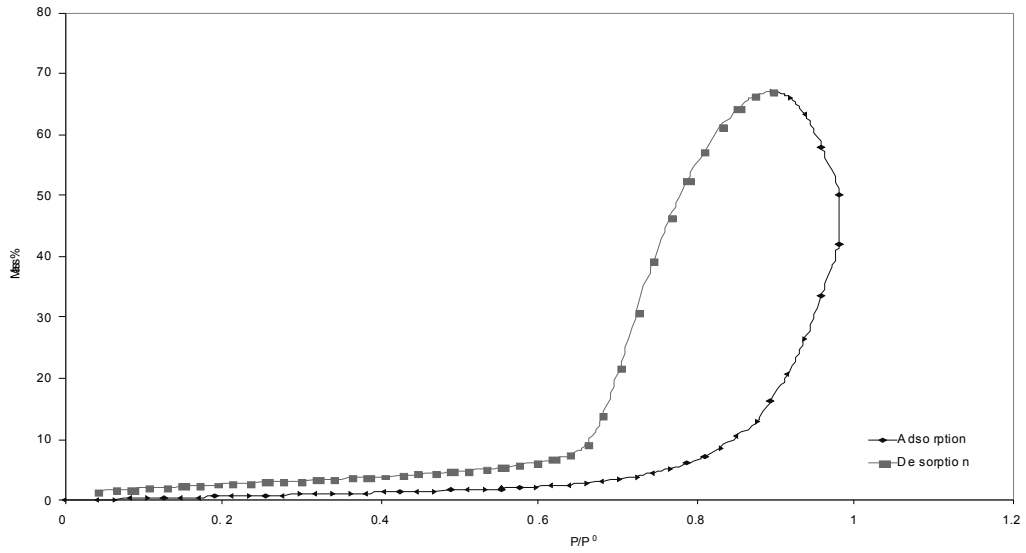

Figure 4.15: Water vapour sorption experiment 3 at 20 ^{o}C on C10 silica pellets.

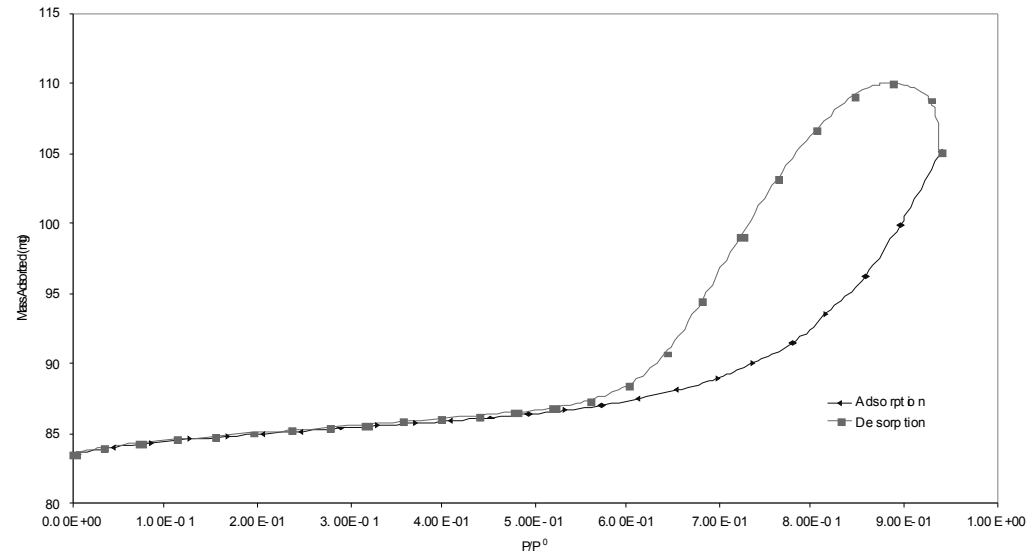

Figure 4.16: Water vapour sorption experiment 4 at 10 ^{o}C on C10 silica pellets.

Water vapour experiment 3, results in a Type V isotherm as well as shown in Figure 4.15. Although this sample under went thermal pre-treatment at 100 ^{o}C, it has a similar low pressure hysteresis to water vapour experiment 1. This suggests that either some chemisorption effects are occurring, or most of the hydroxyl surfaces had been previously removed by thermal treatment hence reducing its affinity for water

molecules. However, further thermal treatment might explain the variation in the shape of the hysteresis loop observed. Water vapour experiment 4 (see Figure 4.16) is the final experiment in the series of water vapour experiments. This experiment aims at achieving a higher density of active sites by fully hydroxylating the sample. The sample is soaked in distilled water as previously stated, and this will prevent any further reaction during the adsorption experiment. The resulting isotherm best resembles a Type V isotherm according to the IUPAC 1985 classification of physisorption isotherms, characterised by its low initial uptake or monolayer coverage, and confirming the existence of a low adsorbent-adsorbate interactions (as in the case of water vapour and C10 silica pellets). Capillary condensation occurs at a normal relative pressure of P/P^0 = 0.6 for mesopores. Experiment 4 shows no low pressure hysteresis loops and also shows a somewhat larger high pressure hysteresis loops than seen in the samples of the three previous water adsorption isotherm runs. After the pressure has been reduced for desorption, there is an increase of about 5 mg in mass of adsorbate, before the beginning of a steady mass reduction. The mechanism of the adsorption of water vapour onto C10 silica pellets with in this research provides strong evidence for the adsorption mechanism described by Muller *et al.* (1996).

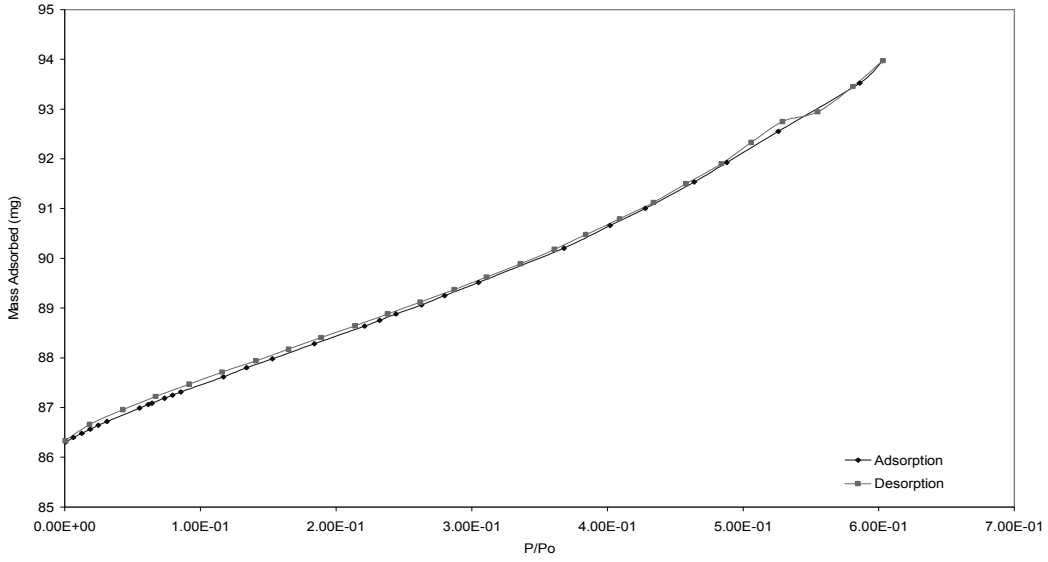

Figure 4.17: Cyclohexane vapour sorption at 30 °C on C10 silica pellets.

The isotherm in Figure 4.17 is best described by a Type III isotherm according to the IUPAC 1985 classification. It is also typical for a low adsorbent-adsorbate interaction. The isotherm appears completely reversible, except for a little pinch around the relative pressures of 0.5 – 0.6 which could be due to experimental error. This complete reversibility indicates that there is no pore blocking effects observed for C10 cyclohexane adsorption. Hence the mass transfer coefficient will be expected to show very little variation, if at all with mass uptake, as the isotherm indicates that both branches follow a similar pathway, and that the pressure required to fill pores is the same required to empty the pores with little or no effects of delays as seen in the capillary condensation regions of Type IV isotherms.

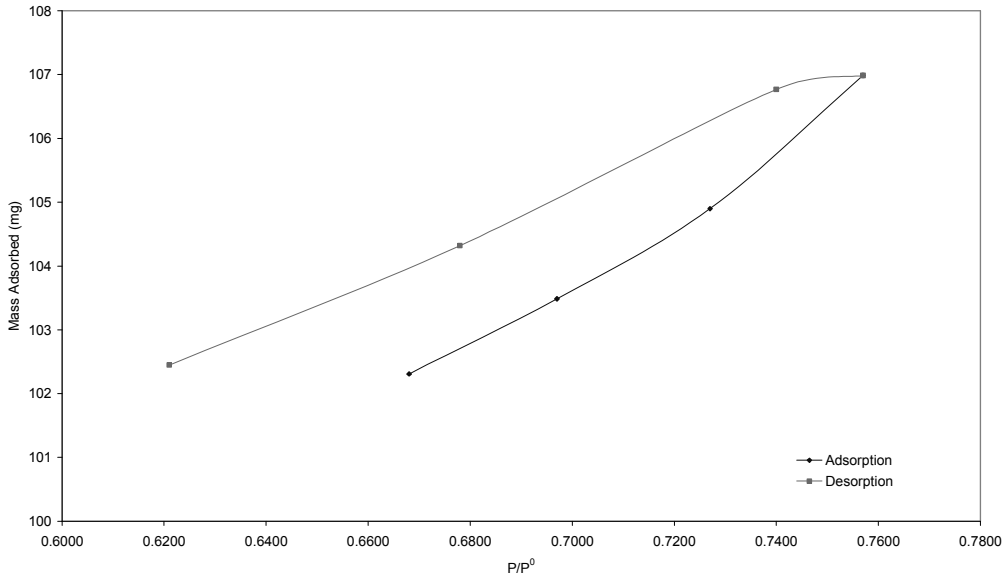

Figure 4.18: Nitrogen sorption experiment 2 at 77 K on C10 silica pellets (Scanning Loop).

The adsorption/desorption scanning loop for nitrogen shown in Figure 4.18 exhibits a region of irreversibility around the region of capillary condensation as would be expected, since the full isotherm run using the Micrometrics ASAP has already shown (see Figure 4.12) hysteresis. As discussed earlier, since the fraction of occupied pores has a positive effect on the occurrence of hysteresis loops, a scanning loop is least likely to exhibit a hysteresis loop. Hence if this region of hysteresis shows a difference in mass transfer coefficient, it will confirm the existence of pore blocking effects in C10 N_2 adsorption. The observed irreversibility is expected to reflect a variation in the k

values for adsorption and desorption, as different pathways exist for mass transfer during adsorption (controlled by pore body size) and desorption (controlled by pore neck size and subject to pore blocking effect).

4.2.8.1 - Sensitivity Analysis

The set of kinetic uptake constants obtained for the variety of adsorbate discussed in this section have been determined using the LDF model described in Chapter 3, over two ranges of M_t/M_f data and three in the case of the nitrogen adsorption desorption scanning loops. The three ranges include $0.5< M_t/M_f < 0.7$, $0.5< M_t/M_f < 0.9$, and $0< M_t/M_f < 0.9$. The different ranges were used to show the level of sensitivity of the linear fits to the range of validity of the LDF model which is said to hold for $M_t/M_f > 0.5$ (Thomas *et al.*, 1995). While a different relationship is shown to exist for $M_t/M_f < 0.25$ (Thomas *et al.*, 1995), it has also been found that the LDF model is a close fit over the M_t/M_f to data in the range < 0.25 despite the fact that two regions are normally described by different relationships. The fitted curves below resulting from fits to the two different ranges both give good agreement with experimental data which supports the validity of the LDF model up to $M_t/M_f < 0.9$. The experimental data was not fitted for $M_t/M_f > 0.9$ because of the noise. The mass transfer coefficients were determined from the gradient of the linear fit to a plot of $ln\ (1- M_t/M_f)$ vs. renormalized time for each pressure step increase, with zero intercept. For fits with a non-zero intercept the variation in mass transfer coefficients observed is negligible. Excel solver was also used to perform a fit with the extra flexibility of M_f also being an adjustable parameter. This was carried out, to show that the mass uptake has reached equilibrium for each data set. If the fitted value of M_f matched the plateau value at long times then equilibrium had been reached.

Error calculations for the rate constants were performed, and subsequent error bars have been included in the resulting plots for the two branches of the isotherm, so that any real difference that cannot be explained by the errors within the calculation is made evident. The kink evident at the top of water vapour experiment 4 isotherm (see Figure 4.16), has been analysed to explain the discrepancy, as when the pressure has been reduced for

desorption, an increase in uptake occurs. There are a few possible explanations for this behaviour, and they are discussed below. A possible explanation for the rising water vapour desorption isotherm could be the variations in pressure. Looking at the mass uptake curves, the plateau at the top around M_f had a bit of scatter. Since the IGA also provides pressure vs. time data, this can be plotted to visualise equilibrium conditions on each uptake step. The P/P^0 data plotted on the isotherm graph coming from the IGA is the pressure point in the original pressure table that it aims to achieve. How closely the IGA actually gets to the required pressure and the intensity of the 'scatter' in the final pressure point, if any could explain the discrepancy. However the variation in the pressure is very little and cannot be solely responsible for this variation, the pressure vs. time data for the last adsorption isotherm is shown in Figure 4.19, and the pressure necessary for the first desorption point has been included (in Figure 4.20) to confirm that the IGA had reached close enough to the required pressure.

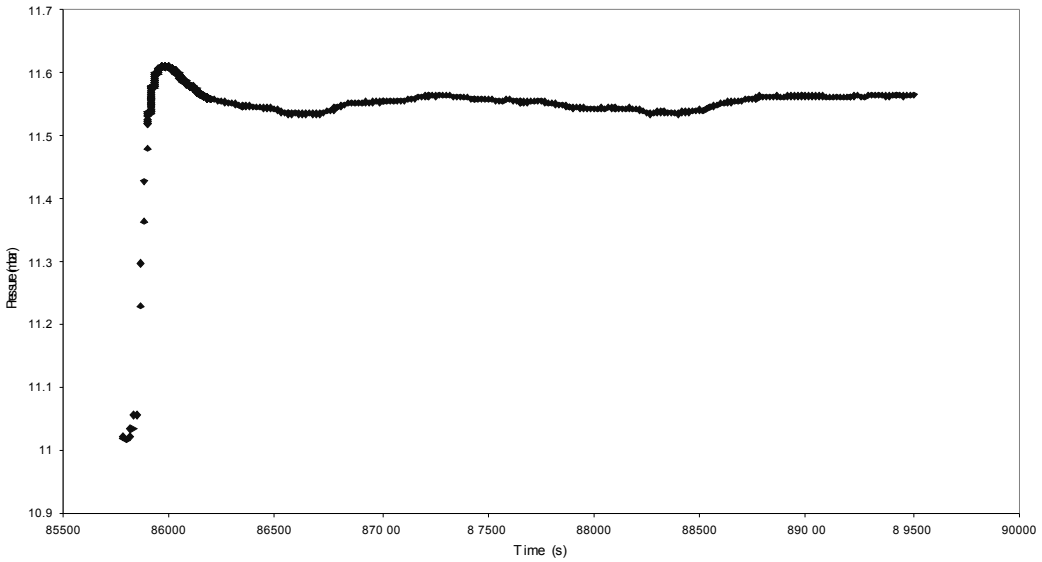

Figure 4.19: Plot of Pressure Vs time for last adsorption point water vapour experiment 4 isotherm.

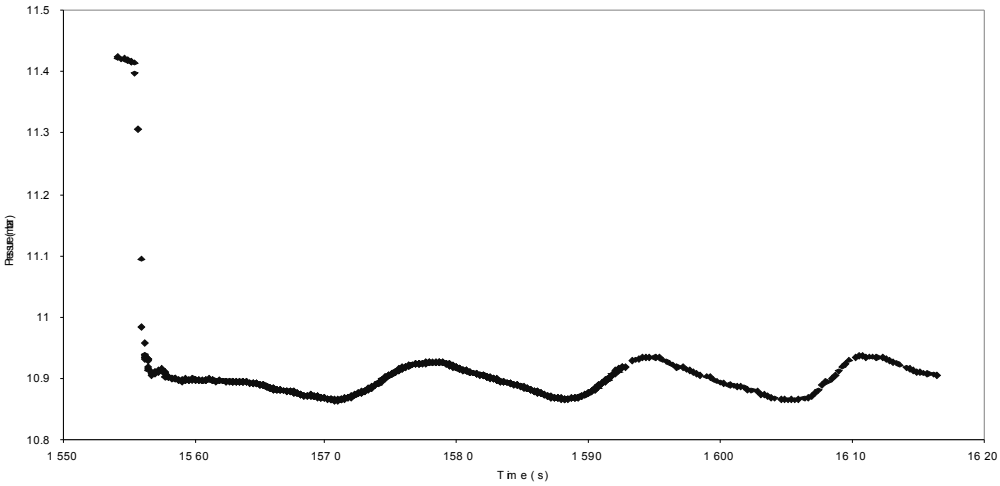

Figure 4.20: Plot of Pressure Vs time for first desorption point water vapour experiment 4 isotherm.

Pressure scatter at the top points of the isotherm of Figure 4.16, could be attributed to the fact that pressure is more sensitive at the region of capillary condensation, since the rise is steeper at the stage of involving the biggest pore regions. The Kelvin equation (see Equation 2.3) presents an inversely proportional relationship for the pressure and radius. So as r gets bigger the Kelvin equation becomes more sensitive to scatter (unstable). Another possible explanation for this rise in the water vapour isotherm could be that this is a direct result of the peculiar adsorption isotherm of water vapour, because if all pore surfaces or sites are covered with condensed water vapour, it will provide the highest achievable density of active sites, assuming all clusters have formed a film. So when pressure is being reduced for desorption, the cooperative effects is stronger, than or opposes the effect of pressure decrease until it eventually balances out. This rise in amount adsorbed, seen at the top of isotherm does not occur for cyclohexane adsorption.

The value of the M_f used in the LDF model was taken as average of the last ten points of the data set, and usually represents the equilibrium uptake for a system which has reached equilibrium. However if the system is yet to reach equilibrium and is likely to have more mass uptake, then the M_f obtained by this method from the data set is inaccurate, and hence does not fully represent the system. In order to ascertain if the pressure points within the region of capillary condensation of the equilibrium isotherm has actually reached equilibrium, the LDF model is used as to calculate M_t using

Equation 4.5 and compared with the value of M_t from the mass uptake kinetic data. For each data point the square root of M_t (mass uptake) - M_t (model) is summed up (sum of residuals) with the value of M_f and k being adjustable parameters. The excel solver is used to obtain the M_f and k and a check of the plateau value estimated as described above. If the system at a certain pressure point has failed to reach equilibrium, then the M_f value required to produce the least sum of residuals will be much higher than the value obtained from the kinetics data. By using this technique, it was found that equilibrium was attained for all the experiments in this work except for the top five points of the adsorption isotherm and the first five points of the desorption isotherm in Figure 4.16. For the last adsorption point, the system was shown to be just about half way to reach equilibrium, as the M_f (mass uptake) is 5.15 and the M_f (model) which was a variable parameter estimated 12.64. As this adsorption and desorption process is generally an equilibrium process, and it is computed by an inbuilt software in the IGA, the method of identifying that equilibrium has been reached for each pressure point is somewhat questionable. In the future, it is worth attempting several equilibration models as some might work better with a different adsorbent-adsorbate relationship. As a result of the above discrepancies, the trends of the k values within the affected region in water vapour sorption experiment 4 are not considered to be the main basis of the conclusions put forward in the results section, but it is used in support of the proposition. Also it is worthy to note that if the affected region of both branches has failed to reach equilibrium one could say they represent the partial behaviour of both branches within the upper part of the region of condensation. As has been mentioned, previously, the aim here is to compare the adsorption/desorption branches, especially within the region of condensation. So for the set of k values of water vapour experiment 4, those obtained at the lower pressure points of the region of capillary condensation (P/P^0 = 0.735 - 0.532 when the loop begins to shut down for adsorption), and (P/P^0 = 0.681 - 0.520 when the loop begins to shut down for desorption) remain valid as mass uptake for those points reach equilibrium. For the 19th adsorption point (P/P^0 = 0.735) the M_f (mass uptake) is 1.0668527 mg and the M_f (model), which was a variable parameter was 1.0138855 mg. For the 7th desorption point (P/P^0 = 0.681) the M_f (mass uptake) is -0.2031455 mg and the M_f (model), which is allowed to be a variable parameter is -0.16349 mg. It can therefore be concluded that the close similarities in these two values suggests that, for the relative pressure point 0.7 and lower P/P^0, the system reaches equilibrium because their M_f (mass uptake) is well described by the LDF model.

Further analytical studies suggest that the higher pressure points of the water adsorption isotherm had failed to reach equilibrium, because at relative pressures higher than 0.85, the diffusivity of water vapour in the pores of C10 is extremely small. This could be a result of the effect of the filling of smaller pores at high pressures. The mass transfer coefficient *k* is seen to approach a minimum for higher pressures, and these slow uptake rate could result in the instability. The work of Rigby *et al.* (2004) showed mercury entrapment in large pores within the silica pellets, indicating that the surrounding pores on the outer shell are the smallest with no entrapment. So if pressures have been raised enough in water vapour experiment 4 as shown in Figure 4.16, for the smallest pores to be filled, then capillary condensation in these pores can severely drop the uptake rate, and possibly result in the above discrepancy. The filling of these small pores would also increase the pore blocking effect, and could explain the gradual decline in mass transfer coefficient for C10 silica pellets. As the pressure is increased to a maximum, the smallest of pores are filled, and these small pores are dispersed around the outer surface for C10 silica pellets (Rigby *et al.*, 2004). This will reduce the diffusivity to a minimum, and the mass transfer coefficient is subsequently reduced significantly and could explain why the high pressure points, of water vapour experiment 4 (see Figure 4.16), was unable to reach equilibrium. Although water vapour experiment 4 was intended to be the last in the series, the problem encountered around the higher pressure points has led to running another experiment. Water vapour experiment 5 (see Figure 4.39), is therefore carried out by preparing a test sample in exactly the same manner as done for experiment 4 (pre-soaking in water and then dried and out-gassed). The test sample is then used to run an experiment within the same pressure range as experiment 2. The resulting isotherm for water vapour experiment 5 is shown in Figure 4.39. There is no kink at the top of the isotherm, and the mass uptake has been confirmed to have reached equilibrium for high pressures, just as was the case for water vapour experiment 2. The only difference in both isotherms is the non-existence of low pressure hysteresis in water vapour experiment 5. This result suggests that the low pressure hysteresis seen in water vapour experiment 2 is a result of inadequate hydroxylation of the silica surfaces of C10, as exposure to large amounts of water in experiment 5 has prevented any losses in adsorbed water. Since all pressure points have reached equilibrium in water vapour experiment 5, the results provide supporting information for the proposal that at relative pressures above 0.85, the diffusivity of water vapour in the pores of C10 is extremely

small, and as the mass transfer coefficient *k* approaches a minimum for higher pressures, the slow uptake rate could result in the instability.

4.2.9 - The Analysis of *k* Values

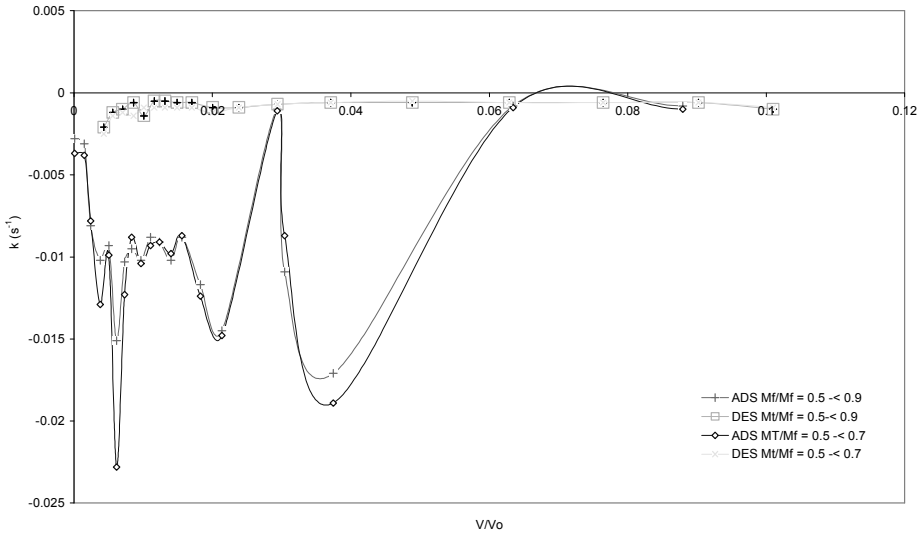

Figure 4.21: C10 water vapour experiment 1Plot of *k* values adsorption/desorption vs. V/Vo.

Figure 4.21 shows the trend exhibited by the *k* values in relation to the fraction of pore volume occupied by adsorbent, calculated for the water vapour sorption experiment 1 at 10 ^{o}C on C10 pellets. The trend of the mass transfer coefficient of water vapour from the onset of adsorption through to the region of condensation for both branches of the isotherm, shows only a slight variation within the region of low pressure uptake (the region of monolayer coverage), which indicates there's a difference in the pattern followed for monolayer coverage in comparison to the desorption of water vapour at low pressures. However there is no region of substantial irreversibility noticed in the isotherm within this region. The small region of irreversibility noticed for the low pressure region is negligible compared to the hysteresis loop observed within the region of condensation, and is attributed to the loss of water vapour due to chemisorption and reactions with the silica surfaces, as this sample has been calcined at temperatures close to silica sintering temperature (~600 ^{o}C) and has no previous history of hydration, either by being exposed to the atmosphere long enough or by soaking in water. This

observation, (variation in *k* values) could be explained by the peculiar pattern of selective monolayer coverage as described by Monte-Carlo simulations of Muller *et al.* (1996). One could conclude, that perhaps the water molecules are adsorbed by selective adsorption, and may be dispersed during desorption by a more random pattern probably due to delays in evaporation caused by surrounding pores. The *k* value, as mentioned previously, is a function of the diffusivity of molecules, a drop in the *k* occurs as the system approaches the region of condensation, which is consistent with the fact that the diffusion in the gas phase is much faster than in the liquid phase. This experiment however does not fully represent the region of condensation since it did not reach high relative pressures (~1), and hence cannot be used to draw conclusions as to whether there is a significant difference, or not, in the *k* values for both branches. This experiment has been shown to present reflective picture of the diffusivity of water vapour in C10 silica pellets, however further analysis is required to investigate the hysteresis loops. It can be seen, nearer to $P/P^0 = 0.7$ that there is a close overlap of some *k* values, and this raises suspicion already, that there is no difference in the diffusivity of water on the adsorption to that of water on the desorption branch.

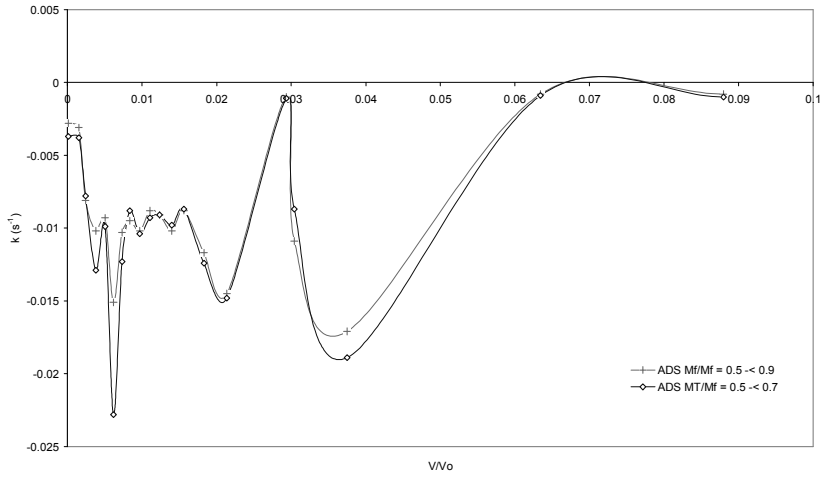

Figure 4.22: C10 water vapour experiment 1 *k* values vs. V/Vo for Adsorption.

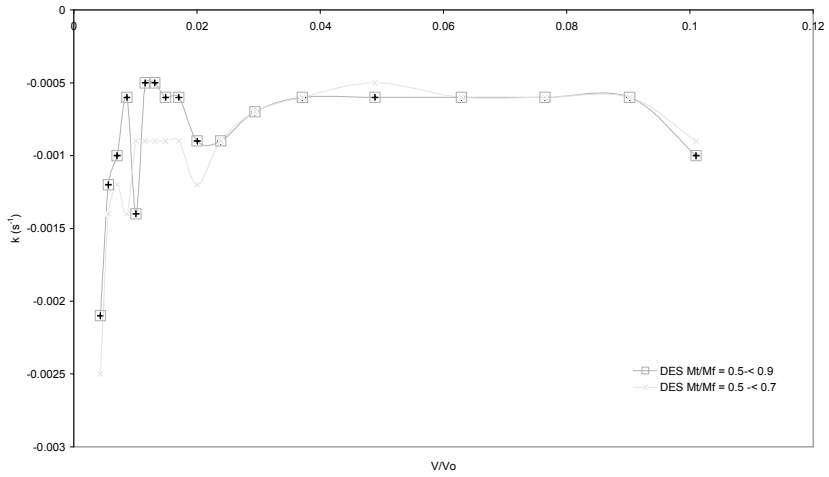

Figure 4.23: C10 water vapour experiment 1*k* values vs. V/Vo for Desorption.

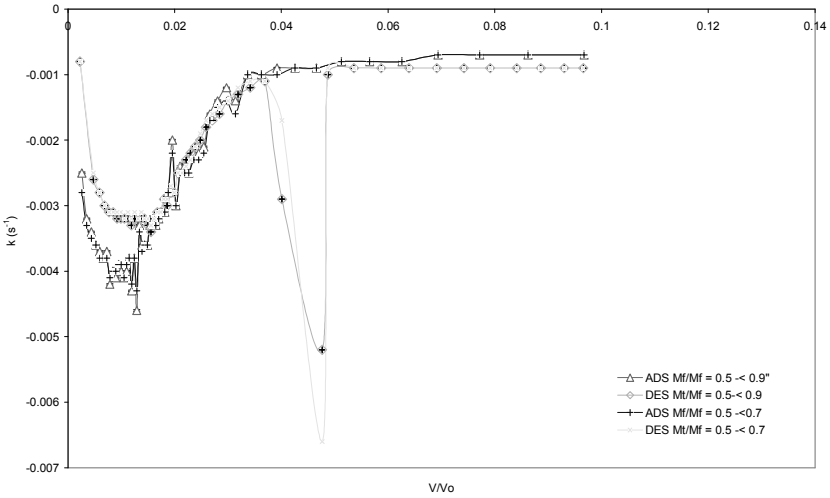

Figure 4.24: C10 water vapour experiment 2 *k* values vs. V/Vo for adsorption/desorption.

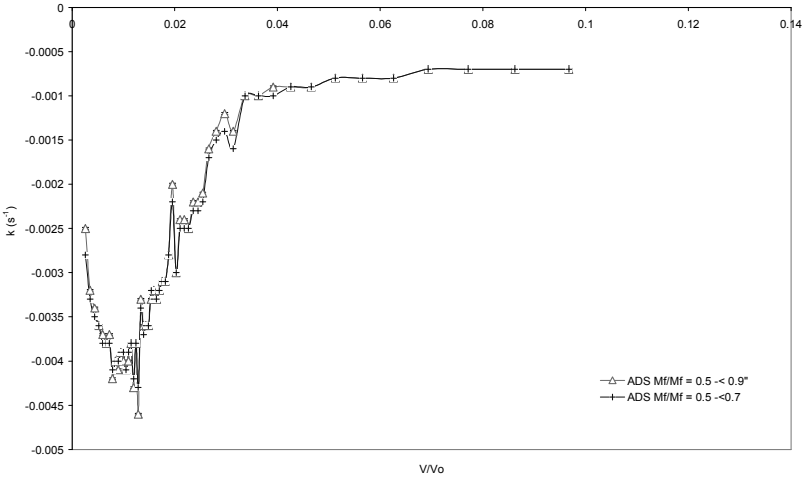

Figure 4.25: C10 Water Vapour Experiment 2 *k* Values vs. V/Vo for adsorption.

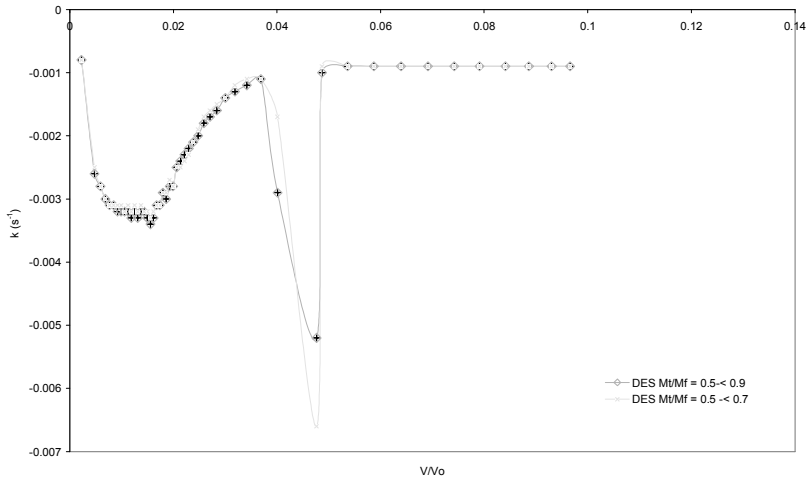

Figure 4.26: C10 Water Vapour Experiment 2 *k* Values vs. V/Vo for desorption.

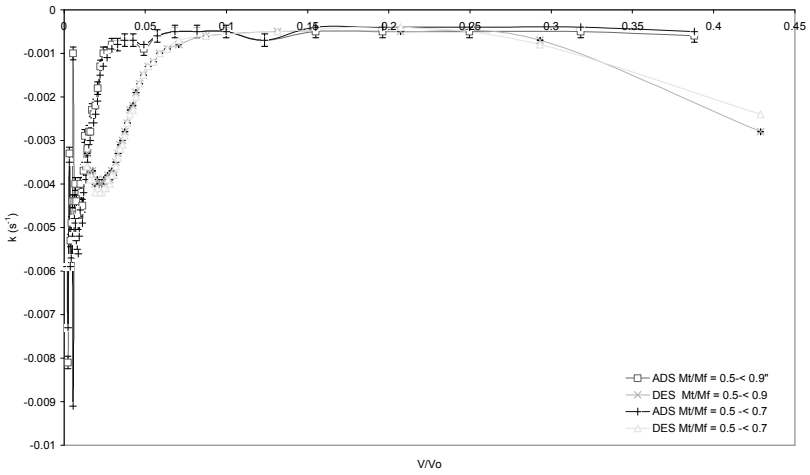

Figure 4.27: C10 Water Vapour Experiment 3 *k* vs. V/Vo for adsorption/desorption.

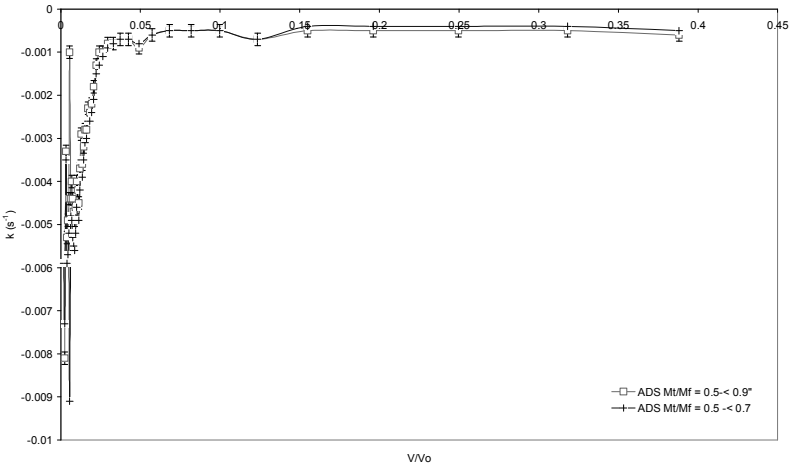

Figure 4.28: C10 Water Vapour Experiment 3 *k* Values vs. V/Vo for adsorption.

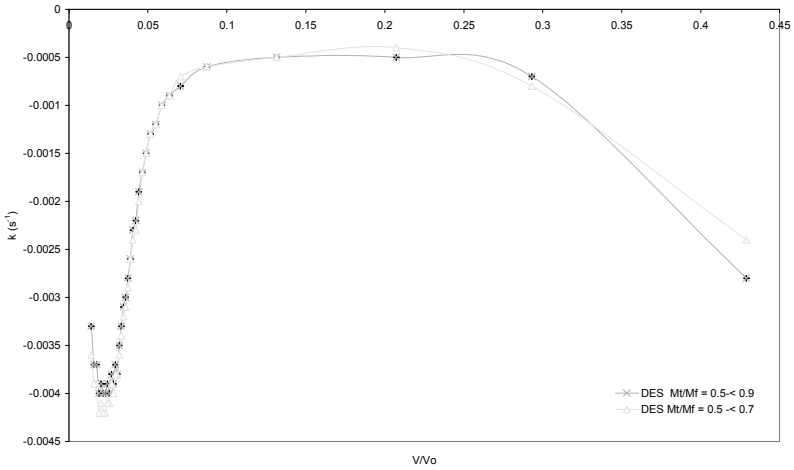

Figure 4.29: C10 Water Vapour Experiment 3 *k* Values vs. V/Vo for desorption.

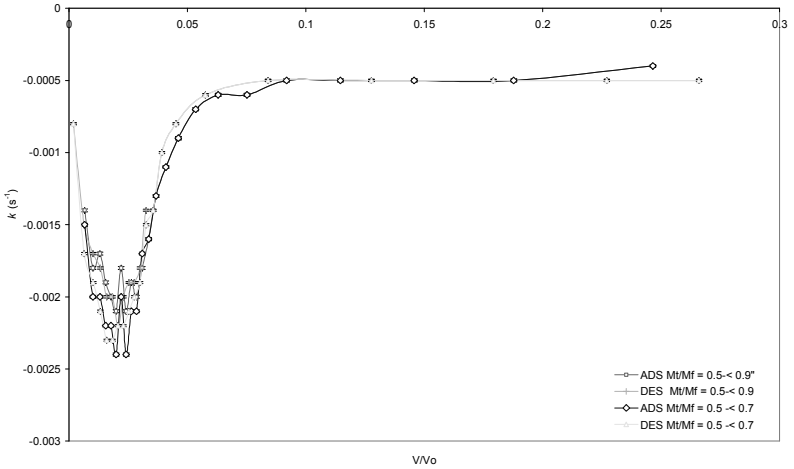

Figure 4.30: C10 Water Vapour Experiment 4 *k* Values vs. V/Vo for adsorption/desorption.

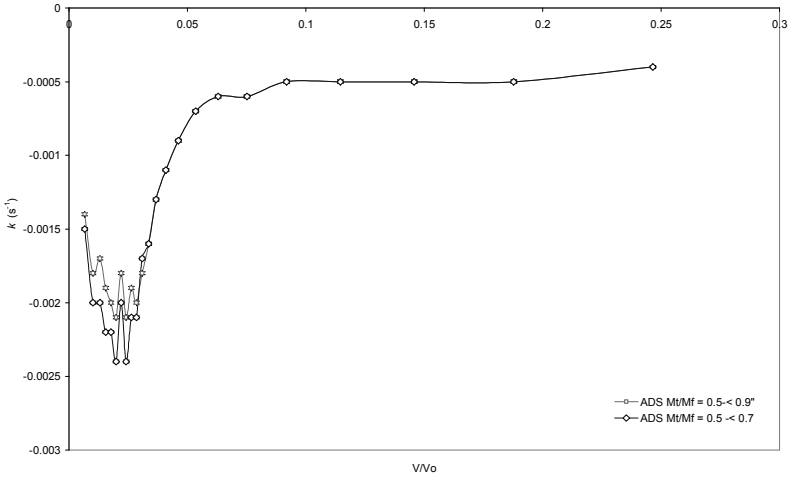

Figure 4.31: Shows *k* Values vs. V/Vo for adsorption for C10 Water Vapour Experiment 4.

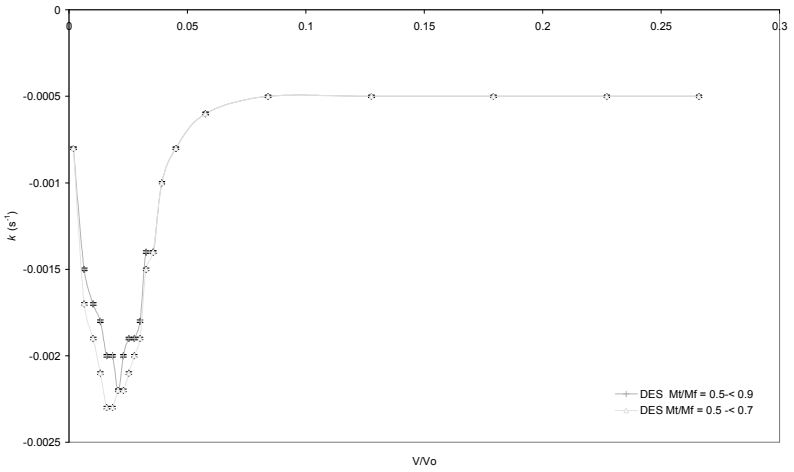

Figure 4.32: Shows *k* Values vs. V/Vo for desorption for C10 Water Vapour Experiment 4

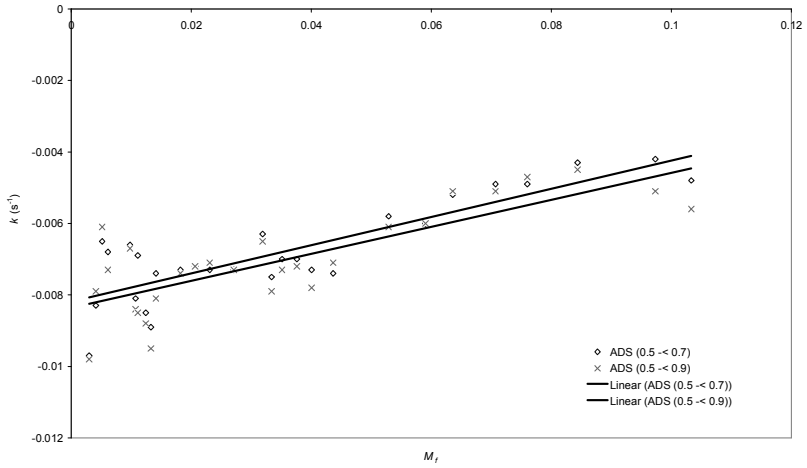

Figure 4.33: Shows *k* Values vs. V/Vo for Adsorption for C10 Cyclohexane Experiment 1.

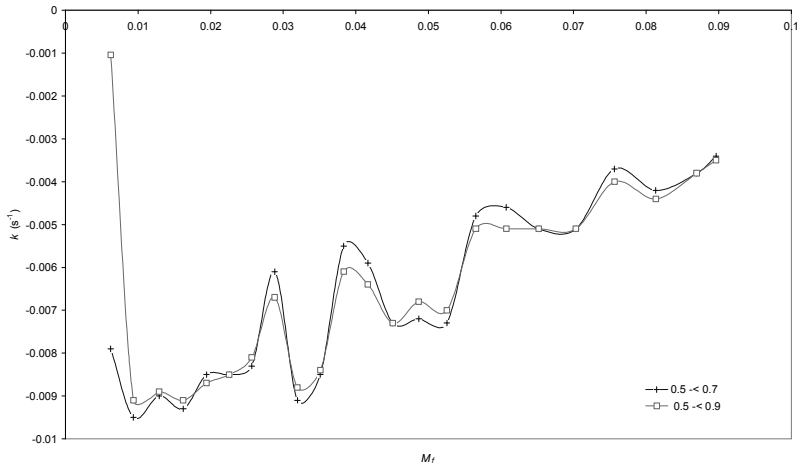

Figure 4.34: Shows the variation of *k* values with V/Vo for the desorption branch of C10 Cyclohexane experiment 1.

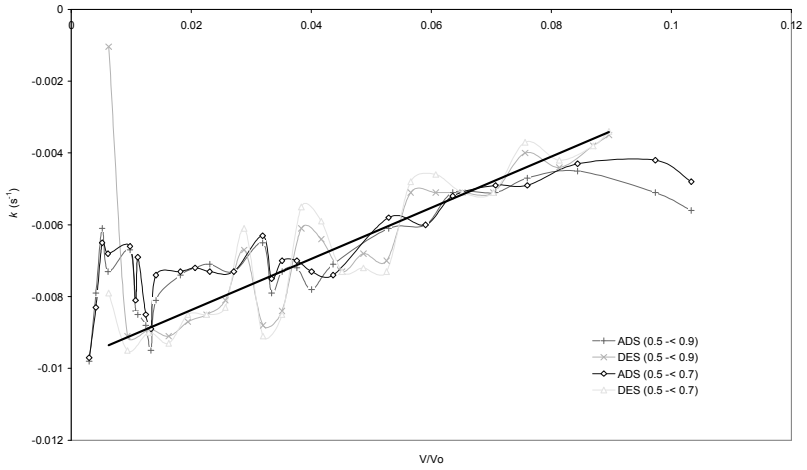

Figure 4.35: C10 Cyclohexane experiment 1 *k* values for adsorption/desorption.

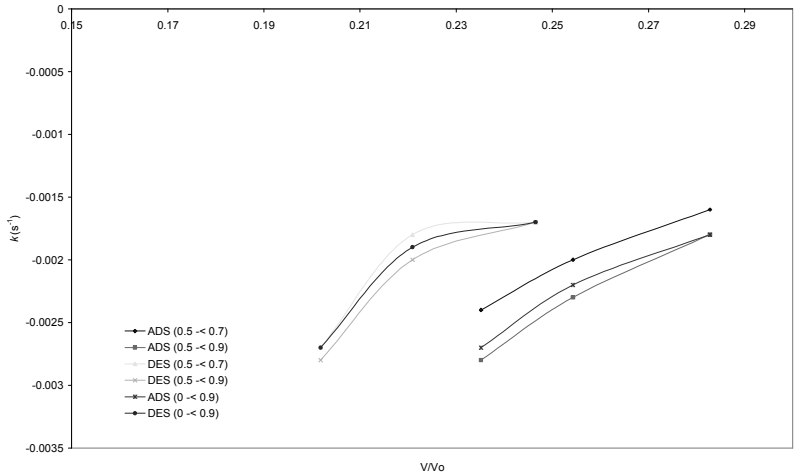

Figure 4.36: C10 Nitrogen experiment 2 *k* values for adsorption/desorption.

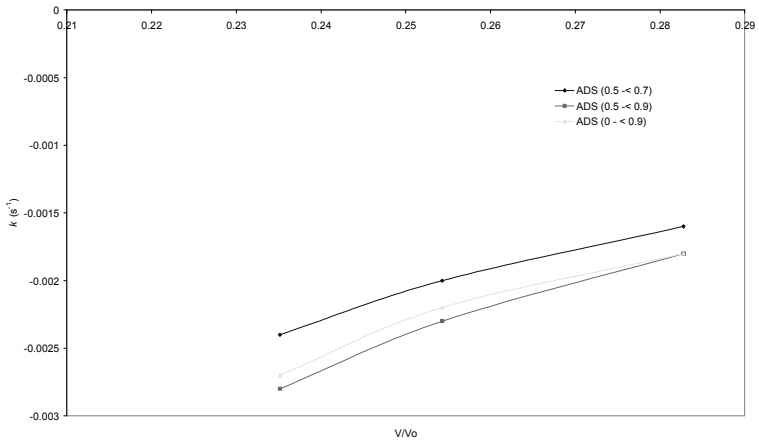

Figure 4.37: C10 Nitrogen experiment 2 *k* values for adsorption.

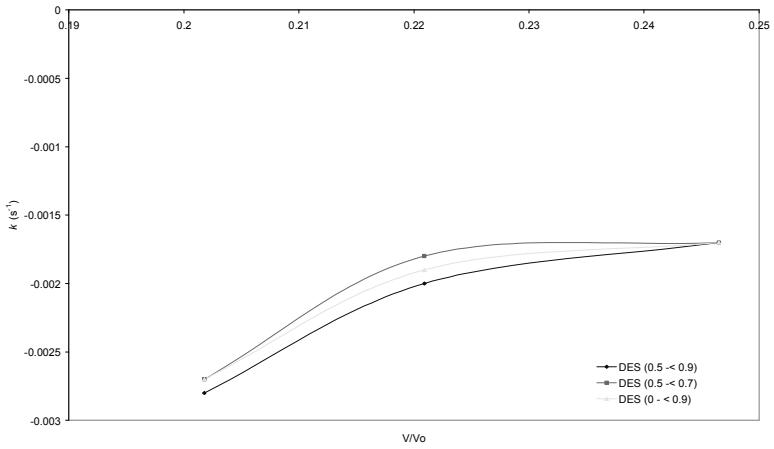

Figure 4.38: C10 Nitrogen Experiment 2 *k* Values For Desorption.

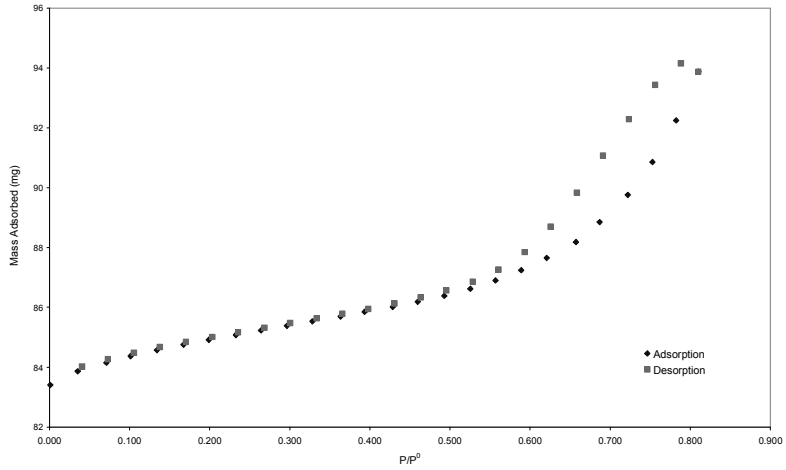

Figure 4.39: Water vapour sorption experiment 5 at 10 ^{o}C on C10 silica pellets.

4.2.10 - Discussions

The molecular mechanisms of adsorption, as well as the effect of the fluid-solid interactions and the placement of active sites, are of major importance in the investigation of the adsorption properties of several porous solids in relation to various adsorbates. For water vapour adsorption, one of two mechanisms could be occurring. The adsorbed vapour phase could form a pervasive monolayer across the whole silica surface, or could be selective and follow a cooperative effect based on the availability of surface active sites (hydroxyl groups). Adsorption isotherms for water on carbons, for

example show a distinctively different behaviour to that of simple adsorbates such as nitrogen, hydrocarbons and organics (Gregg and Sing, 1982).

There is very little work in the literature on water vapour adsorption on silica porous solids, although there is more concerned with porous carbon. This is probably because of the anticipated lower ambiguity in interpreting results for materials with slit shaped pores compared with the more complex pore geometries of amorphous silicas. As a result there is still a debate in the literature concerning the adsorption mechanism. Some authors have proposed that clusters of molecules nucleate around high density sites on the surface, and these adsorbed molecules then act as secondary nucleating surfaces and eventually induce condensation (Dubinin, 1980; Pierce and Smith, 1950). However it is still common to theoretically describe the adsorption mechanism of water in similar ways to that of simple fluids (monolayer is formed at low pressures, and further layers are formed only after essentially full coverage by this primary monolayer (Muller *et al.*, 1996)). The adsorption mechanism for water on the C10 silica pellets is believed to occur by the formation of a peculiar three-dimensional water clusters and networks, whose formation relies on a cooperative effect involving both fluid-fluid interactions and fluid-solid ones on suitable active sites (hydroxyls on silica solids). The arrangement of active sites have a pronounced effect on the exponential growth of the adsorption isotherm, and capillary condensation occurs when most of the active sites have been covered by water clusters and a bridging of clusters have occurred. Muller *et al.* (1996) analysed water adsorption on carbons, which also showed that for graphite carbons for which surface chemical groups have been removed, there is almost no adsorption at low and moderate pressures, and for porous carbons capillary condensation occurs at some higher pressures. The results of Porion *et al.* (1998) show that the two NMR relaxation times and diffusion coefficient for water on silica are strongly dependent on the water content (saturation level), when plotted in normalized coordinates. The T_1 and T_2 vs. relative pressure (P/P^0) curves fit closely with the adsorption and desorption isotherm there by validating the two-population, fast exchange model, and showing that T_1 and T_2 are only dependent on the water content and not on whether this water content was reached on the adsorption or on the desorption branch. In addition, as it was reported that, since at equivalent saturation levels there is no difference between the relaxation times and diffusion coefficients obtained along the adsorption branch and those obtained along the desorption branch,

one is led to the conclusion that despite different equilibrium conditions, the geometry and connectivity of the liquid phase are statistically the same along the two branches. The above study concludes that there are no differences in NMR parameters for adsorption/desorption at equal saturation i.e. the same liquid connectivity exists for both branches. The experiments conducted within this research were performed in an attempt to establish whether this behaviour is universal or restricted to the particular interface morphology of the samples studied by Porion *et al.* (1998). The resulting mass transfer coefficients for the adsorption and desorption branches at high relative pressures (within the region of condensation), overlap and exhibit a similar trend as can be seen by the flat plateau on Figures 4.24, 4.26, and 4.28. These results suggest that there is no difference in the connectivity or the tortuosity factor controlling the pathway of condensed liquid and vapour in the two branches of the isotherm.

It has been reported that MCM-41 adsorbs much greater amounts of organic species than water (Chen *et al.*, 1993), the amount adsorbed exceeded 0.4 g/g for cyclohexane but is less than 0.05 g/g for water at $P/P^0 = 0.4$ which reveals that the internal surface is quite hydrophobic despite the presence of silanol groups. For cyclohexane adsorption experiment 1 (see Figure 4.18 for isotherm), a relative pressure of 0.402 leads to a V/Vo = 0.076 (fraction of C10 pore space occupied) while water vapour adsorption experiment 2 at a relative pressure of 0.404 leads to V/Vo = 0.017. These results are in agreement with the work of Chen *et al.* (1993), and according to Bhatia *et al.* (2001) the trimethylisation renders the materials repellent even to liquid water, which could probably be the explanation for the low uptake. However if trimethylisation renders the silica pellets repellent to most adsorbates, then a possible explanation for the variation in uptake rates for water vapour and cyclohexane is the mechanistic cooperative adsorption of water molecules which to a large extent is dependent on the availability of active sites. The water vapour experiments run here (Figures 4.13 - 4.16); show clearly a different behaviour to that of simple adsorbates such as cyclohexane (Figure 4.17) on C10 silicate materials. In the case of graphite carbons for which surface chemical groups have been removed, the work of Muller *et al.* (1996) showed hardly any adsorption at low and moderate pressures, whereas for these same carbons, nitrogen and hydrocarbons adsorb strongly at much lower pressures. A possible explanation for this behaviour is that, in order to adsorb onto the surface, the water molecules must conform

to the surface geometry, and then form bonds with active sites as well as molecules, and then break into a film.

Pore structure characterisation is very important towards effective porous media applications and as most popular techniques of characterisation are based on adsorption-desorption isotherms of nitrogen molecules at the boiling point of liquid nitrogen it seems worthy to investigate additional probing techniques including the use of other adsorptives such as water vapour, as used within this research. Researchers such as Brunauer *et al.* (1972) emphasised on the importance of using water vapour sorption in pore structure characterisation of porous materials. The water vapour isotherm acts as an independent check on the PSD estimated by nitrogen sorption. In addition as the size of the water molecule (~0.23 nm) is smaller than that of nitrogen (~0.43 nm), the water vapour isotherm can be utilised for materials with narrow pores into which nitrogen cannot penetrate.

It is generally accepted that for nitrogen adsorption the lower closure point of the hysteresis loop is at a relative pressure close to 0.42 but never below (Gregg and Sing, 1982). By using the Kelvin equation and the thickness of the adsorbed layer, it is possible to calculate the minimum pore radius r^p_{min} corresponding to the lower closure limit assuming the values of the surface tension and molar volume are those of the liquid adsorptive in bulk. For nitrogen adsorption in cylindrical pores it was calculated to be 1.7nm (Naono and Hakuman, 1993). The $r^p_{min}(N_2)$ is considered to be the lower limit of pores in which capillary condensation of nitrogen takes place.

Naono and Hakuman (1993) analysed several porous silica gels by means of water vapour adsorption at 25 ^oC with particular emphasis on the region of hysteresis. The lower closure point of the observed hysteresis was found to be situated at a relative pressure close to 0.27 which is lower than that of nitrogen isotherm at 77 K. The pore radius at the closure point was found to be 0.9 -1.1 nm for the water isotherm and 1.7 nm for the nitrogen isotherm. These radii are assumed to be the minimum pore radii determined from the capillary condensation of the adsorptive. The water isotherm at 25 ^oC was reported to have given more information on the porous texture than the nitrogen isotherm at 77 K. They reported on some unique adsorbents in which there was no observed hysteresis in the nitrogen isotherm, but there was apparent hysteresis in the

water isotherm. This result suggested that capillary condensation of water vapour takes place in the smaller pores whose radii are less than 1.7 nm. They went on further to study the lower closure limit of the hysteresis loop of the water isotherm at 25 ^{o}C, which was found to lie at the relative pressure of 0.27 with the corresponding r^{p}_{min} (H_2O) calculated to be 0.9-1.1 nm (the small variation arises from the difference in *t* curve used). The r^{p}_{min} (H_2O) is considered to be the lower limit of pores where capillary condensation of water vapour takes place, therefore when water isotherm is used to analyse pore structure, the resulting PSD curve can be calculated down to 0.9-1.1 nm in pore radius.

The water adsorption isotherms obtained for the commercial mesoporous silica sol gel known as C10 were found to vary in their estimates of the lower closure limit for the region of hysteresis. The five water vapour experiments performed (Expt. 1,2,3,4, and 5) in total can be seen in Figures 4.13 - 4.16 and 4.39 respectively; They all show clearly a different behaviour except for experiment 4 and 5 (Figures 4.16 and 4.39) which gave a lower closure limit at a high relative pressure of (~0.55) and for all the other 3 isotherms (experiment 1, 2, and 3) there was no observed lower closure limit as the desorption isotherm showed a discrepancy in the amount desorbed at Kelvin pressure required for filling at low pressures as with the whole isotherm. The difference between the quoted lower closure limit of ~0.27 (Naono and Hakuman, 1993) for water isotherm in a range of adsorbents including sol gels and that obtained within this research ~0.55 could be attributed to the difference in pore structure of test porous materials, however further studies is required before any conclusions can be made. Again the issues surrounding the operations of the computer controlled automatic adsorption apparatus and the variation in the method of sample preparation could also be contributing factors.

The use of these synthesised silica materials or their carbon replicas as heterogeneous catalyst for use in processes such as water treatment will depend heavily on the selectivity and hence the need for detailed understanding of adsorption mechanisms. Gas adsorption depends upon the applicable mechanism of adsorption, which is greatly controlled by the type and placement of active sites, as in the case of water adsorption. It has been shown that the adsorption of water vapour on C10 silica pellets is different to simple hydrocarbons or non-polar molecules, which form effectively a two-dimensional monolayer, and the low initial uptake and steep increase before the

pressure required for condensation is best explained by the mechanism of cooperative adsorption onto active sites, and hence confirms the theory reported by several researchers including Muller *et al.* (1996), and Iiyama *et al.* (2004). Calculated diffusion rate constants provided evidence of a mechanism of cooperative adsorption, this fluid-fluid effect is unique for water and it explains most of the variations in the adsorption properties of water to cyclohexane (representing hydrocarbons with somewhat low affinity for silanols). When no active sites are present on the surfaces of the pore, or for dehydroxylated surfaces, Muller *et al.* (1996) observed capillary condensation at a certain pressure, as in simpler adsorbate systems. This pressure decreases as the number of active site increases. Experiments 3 and 4 for the dehydroxylated and hydroxylated C10 samples respectively show transitions to capillary condensation, in support of the above observation. For higher pressures this phase transition is no longer observed, as it is replaced by continuous pore filling (Muller *et al.*, 1996).

The small region of low pressure hysteresis observed for some of the water vapour adsorption experiments are negligible when compared to the main hysteresis loop in the pressure range for water vapour condensation to occur and hence is disregarded in the data interpretation. There is also some observable variation in k values within low pressure for both water vapour experiment 1 and 2, and this is probably because the selective adsorption pattern that occurs for water vapour adsorption may not apply to the desorption branch. In the case of water vapour experiment 3. The k values were shown to match within the region of capillary condensation. The deviation seen for the first desorption point is attributed to a mechanism within the water-silica adsorbate-adsorbent system that leads to a further increase in mass uptake, after the pressure has been reduced for desorption. This is probably because this sample had undergone heat treatment that could have condensed all the hydroxyl groups on the silica pellet, and in addition had not been previously hydrated or exposed to water, hence some chemisorption effects might have led to this behaviour. The water vapour experiment 4 has shown that prior exposure to air and soaking in water could prevent the occurrence of low pressure hysteresis. The water vapour experiment 4 isotherm shows that the k values of both the adsorption and desorption branches are exactly the same within the region of capillary condensation. The variation in the k values at low pressures also exits for this system, despite the non existence of low pressure hysteresis, and hence

confirms the hypothesis that the difference in k values is a result of the selective adsorption that occurs for water vapour adsorption that may not necessarily occur for desorption. There is further increase in mass uptake in water vapour experiment 4 when pressure has been reduced for desorption, this is evident in the isotherm and was most probably a result of the systems failure to reach equilibrium for the affected region. The inability of this system to reach equilibrium for the highest pressures within capillary condensation can be overcome by adopting the use of a different equilibration equation within the IGA software, or maybe even by increasing the equilibration time allowed. However if the system had failed to reach equilibrium for the two branches on the affected region, then one can assume that the k for a fraction of the achievable coverage is a fraction of the k obtainable at the maximum coverage possible (equilibrium). The lower points (P/P^0 <0.8) within the region of condensation show that the k for both branches are exactly the same, and these points have been analysed to confirm that equilibration has been achieved. So therefore if the trend is consistent for the lower points, and also for a fraction of high pressure coverage, then one is led to think that this provides additional confirmation that there is no variation in the k value which represents the diffusivity of water vapour, the evaporation of condensate, and hence the tortuosity factor for both branches.

4.2.11 - Conclusions

A comparative study of the mass transfer coefficient of the region of condensation for water vapour experiments, cyclohexane adsorption and nitrogen scanning loop has shown that in the case of nitrogen adsorption the hysteresis is caused by pore blocking effects. There was no hysteresis for cyclohexane sorption and hence the resulting k values have no substantial variation between adsorption and desorption. For the water vapour adsorption experiments, capillary hysteresis loops were observed for all four experiments, however the k values obtained across both the adsorption and desorption branches, show no variation and hence one is led to conclude that the pathway for the evaporation of water vapour is exactly the same as for the condensation of water vapour. Therefore the water vapour adsorption analysis confirms that hysteresis does not occur as a result of a variation in pathways for evaporation, and hence not a result of pore blocking effects. These results are in agreement with the work of Porion *et al.* (1998) on

water adsorption/desorption. For the nitrogen scanning loops, it is further confirmed that even for the least likely possibility of pore blocking effects, capillary condensation hysteresis occurs. The variations in the *k* values confirm that there is a difference in the diffusivity of nitrogen during adsorption, compared to during the evaporation of condensate. Therefore one can conclude that hysteresis occurs for nitrogen adsorption in silica sol gels of type C10 as a result of pore blocking effect arising from a difference in the geometry and connectivity of the liquid phase along the two branches and is thus best described by interconnectivity models.

Chapter 5: The Understanding and Application of Adsorption Models

5.1 – Capillary Condensation Effects

5.1.1 - Introduction

The technological significance of many mesoporous and microporous materials (e.g. the use of catalysts in speeding up reaction rates, or inorganic membranes, porous adsorbents, etc in separation processes) is widely recognised. When performing a sorption characterisation analysis of such materials, the simultaneous incidence of various phenomena such as pore blocking, and avalanche filling etc could lead to an inaccurate assessment of the structural parameters of a porous material. As such, the effective design of heterogeneous processes involving mesoporous and microporous materials, such as catalysis and separations, requires reliability in the methods of characterisation of the chemical composition and physical structure. The accuracy of the determination of pore structure characteristics, in particular pore size distribution measurements resulting from pore filling techniques, is of vital importance to understanding the pore transport of hydrocarbons, and especially in the condensing of hydrocarbon vapours.

The processes involved in the investigations of catalytic phenomena involving macromolecules will benefit from the use of well characterised regular pore structures e.g., MCM-41 and other similarly synthesised mesoporous materials. These materials could be used as models for the observation of catalytic phenomena in uniform pore systems, of a wide range, away from the complexities of irregular materials. The most popular method of determining pore volume and surface area distributions of mesoporous and microporous materials is the nitrogen capillary condensation-evaporation method. The adsorption data at lower relative pressures (usually at P/P^0 between 0 - 0.4) provides the data for the evaluation of the overall specific pore surface

area by applying the BET theory. Capillary condensation/evaporation hysteresis loop constitutes the basis for the deduction of pore volume and surface area distributions.

5.1.2 - Theory

A number of theories have been used to describe the capillary condensation region of nitrogen adsorption and desorption data. In the BJH method, capillary condensation is considered to occur according to the Kelvin equation. The general expression for the Kelvin equation, assuming a contact angle of 0 ^{o}, is:

$$\ln\frac{P}{P^0} = \frac{\gamma V_L}{R_g T}\left[\frac{1}{r_1} - \frac{1}{r_2}\right] \quad \textbf{(5. 1)}$$

The Cohan equation for a cylindrical meniscus gives rise to the best prediction for the relative pressure of capillary condensation in cylindrical pores as shown in Equation 5.2 (Cohan, 1938). The pore filling in the process of condensation follows the formation of a liquid film on the cavity wall and thus is controlled by the radius of curvature of the cavity, r_c. The pressure of condensation is given by the Kelvin –Laplace equation (Equation 2.1). During desorption, evaporation occurs after the formation of a hemispherical meniscus in the pore neck and thus is controlled by the radius of the neck r_n. The pressure for evaporation is also represented in a similar manner to condensation with r_c being replaced by r_n. Therefore, for the filling of a cylindrical and hemispherical meniscus respectively, the following approximation holds:

$$\ln\frac{P}{P_0} = \frac{k\alpha\cos\theta}{r} \quad \textbf{(5. 2)}$$

$$Cylindrical\ \frac{1}{r} + \frac{1}{\infty} \Leftrightarrow \frac{1}{r} \quad \textbf{(5. 3)}$$

$$Hemispherical\ \frac{1}{r} + \frac{1}{r} \Leftrightarrow \frac{2}{r} \quad \textbf{(5. 4)}$$

Where γ is the surface tension of liquid nitrogen, and V_L is the molar volume of liquid nitrogen, R_g is the universal gas constant, T is absolute temperature, and r_1 and r_2 are the liquid interface radii of curvature (defined in two mutually perpendicular planes). By applying the correction for the multilayer, and substituting γ, V_L, R_g, and T in the Kelvin equation with the appropriate values for nitrogen at its normal boiling point, the pore filling pressure can be obtained. For an inkbottle type pore, the pressure required to fill a neck with a cylindrical meniscus exceeds the pressure required to fill a body of hemispherical meniscus, if the neck radius exceeds ½ that of the body. Ideally this should cause the neck and the pore body to be filled by condensed vapours at the same pressure prior to evaporation as by the time the pressure for neck filling (considering cylindrical meniscus) is attained, the exerted pressure is more than sufficient to fill pore body (considering hemispherical meniscus) with condensed vapours.

5.1.3 - Mechanisms of Condensation

Adsorption pore size distribution analysis of mesoporous materials is based on an adopted interpretation of the mechanisms of capillary condensation and evaporation and the associated hysteresis phenomena (Sing *et al.*, 1985). Two main factors determine hysteresis: hysteresis on the level of a single pore of a given shape and cooperative effects reflecting the specifics of connectivity of the pore network. On the pore level, adsorption hysteresis is considered as an intrinsic property of the vapour-liquid phase transition in a finite volume system. A classical scenario of capillary condensation implies that the vapour- liquid transition is delayed because of the existence of metastable adsorption films and hindered nucleation of liquid bridges. In open uniform cylindrical pores, metastabilities occur only on the adsorption branch. Indeed, in an open pore filled by liquid like condensate, the liquid-vapour interface is already present and evaporation occurs without nucleation, via a receding meniscus. The desorption process is therefore associated with the equilibrium vapour-liquid transition, whereas the condensation process involves nucleation of liquid bridges. In sufficiently wide pores, the barrier in the nucleation process is too high and condensation occurs spontaneously near the vapour like spinodal. The mechanism of adsorption hysteresis is

dominant in ordered mesoporous materials with uniform cylindrical pores such as MCM-41 and SBA-15 typically leading to a type H1 hysteresis loop with parallel adsorption and desorption branches. During an adsorption experiment for porous media characterisation, inappropriate assessment of the structural parameters of a porous material could result from the simultaneous occurrence of varied phenomena. Some of these phenomena can be related to the variation of the density of the adsorbed phase along the pore axis (Ravikovitch *et al.*, 1995), as well as the magnitude of the potential field exerted from the pore walls towards the adsorbed molecules. Such factors make it difficult to accurately calculate the conditions for a given pore to be occupied by condensate, especially in the nanopore size interval (Ravikovitch *et al.*, 1997).

Desorption conditions are also hard to evaluate, because of two complications. Firstly, the classical pore blocking effect and the more recently discovered cavitation process (Burgess and Everett, 1970). The concept of pore blocking was put forward in the pioneering work of Kraemer (1931), McBain (1935) and Cohan (1938) to explain some of the characteristics of capillary condensation hysteresis in mesoporous materials. The pore blocking effect implies the evaporation of a condensed liquid from a pore network is a cooperative process. As such, evaporation from a pore, which is connected to the bulk phase by narrower pores, is restricted by, and occurs spontaneously after emptying of one of the adjacent pores. This effect of pore blocking is a conventional explanation of the capillary condensation hysteresis of H2 type by IUPAC classification typically of porous glasses. The structure of these materials is disordered and represents a network of channels with prominent enlargements and constrictions as shown by high resolution microscopy and scattering data (Ravikovitch and Neimark, 2002). The pore blocking effect rests in the inability of a pore to evaporate its condensate if it has no direct access to the vapour phase, thus turning evaporation from pore entities into a percolation process, whereas cavitation implies the possibility that a condensate-filled pore could turn empty by means of bubble nucleation within the condensed liquid. Cavitation studies so far have mainly focused on ink bottle type pores, such as the work of Sarkisov and Monson (2000) which suggested that sometimes the shape of the desorption isotherm is mainly dictated by this phenomenon rather than by the pore blocking effect. Burgess and Everett (1970) associated the lower closure point of adsorption hysteresis loops to the onset of cavitation in the stretched metastable liquid. Cavitation induced desorption is expected to occur in mesopores blocked by micropores.

The cavitation effect was not considered in the classical theories of capillary condensation hysteresis in ink-bottle pores and pore networks. A detailed analysis of cavitation induced desorption is given by Ravikovitch and Neimark (2002). They described a new physical mechanism of adsorption hysteresis in ink-bottle type pores confirmed by gas adsorption experiments of three different gases including N_2 in 3D cage-like structures of nanoporous templated silica such as SBA-16 with narrow pore size distribution. Their analysis revealed three mechanisms of evaporation including evaporation from blocked cavities controlled by the size of connecting pores (ink-bottle; typical pore blocking effect), the spontaneous evaporation caused by the cavitation of a stretched metastable liquid, and, as a new addition, the near equilibrium evaporation in the region of hysteresis from unblocked pore bodies that have access to the vapour phase. Studies of temperature dependence also showed a transition between the cavitation and pore blocking regimes of evaporation. Ravikovitch and Neimark (2002) concluded that the pressure of cavitation depends on the pore geometry and hence questions the conventional assumption (Burgess and Everett, 1970) that the pressure of cavitation which determines the lower closure point of the hysteresis loop is a function of the adsorbate and temperature.

Simulations of adsorption in porous materials has also shown that hysteresis, often exhibited between the adsorption and desorption branches, is usually associated with the occurrence of capillary condensation whereby a low density vapour-like phase of the adsorbate condenses to a liquid-like phase at a chemical potential (or bulk pressure) lower than that which corresponds to the bulk saturation. There is no agreement yet as to the precise relationship between these hysteresis loops and the capillary phase transition. Several researchers, such as Rouquerol *et al.* (1999), and Steele (1973), have explained hysteresis based on the Kelvin equation, suggesting that the occurrence of hysteresis in a single pore is related to differences in geometry of the liquid-vapour meniscus in condensation and evaporation. Some however have argued that hysteresis is caused at the single pore level by the existence of metastable states analogous to the super-cooled liquid and superheated vapour states encountered in bulk systems when nucleation is suppressed, and (Sarkisov and Monson, 2000) carried out further research to investigate the phenomenon. Their results for one model of porous material (silica gel) confirmed hysteresis as having its origin in thermodynamic metastability, although the metastable vapour and liquid phases involved were sample spanning and are not

associated with any concept of a single pore. This study did not eliminate the possibility that pore blocking and networking effects play a significant role in hysteresis although they were evidently not important in the observed system, but reinforced the need to apply their method to other systems such as materials with higher solid volume fractions and other morphologies (e.g. porous glasses).

In more recent years Monte Carlo (MC) and molecular dynamics (MD) simulations have been used to revisit investigations into pore blocking effects in capillary condensation hysteresis with particular emphasis in disordered materials given porous glasses and silica gels which have been considered as case study systems for researching capillary hysteresis and networking effects. MC Simulations work on adsorption-desorption cycles in model porous glasses by Gelb and Gubbins (2002) and Pellenq *et al.* (2000) both did not display any appreciable pore blocking effects. Woo *et al.* (2001) developed lattice DFT models of sorption in disordered media and constructed hysteresis loops resembling the shape of experimental adsorption isotherms on porous glasses, without invoking pore-blocking effects. Similarly, Sarkisov and Monson (2001) performed MC and MD simulations of capillary condensation in a single ink-bottle pore composed by a central rectangular cavity connected with the bulk phase by slit micropores half its size in width. The hysteresis observed in this model was not related to the classical pore blocking effect, as desorption from the central cavity occurred with the connecting pores remaining filled. This behaviour is different from the classical picture of desorption in this geometry which is based on the concept of pore blocking. Therefore, in this particular case, the conditions of evaporation were determined by the onset of cavitation. During the desorption process evaporation occurs from the pore throat into the bulk vapour phase and the molecules removed are then replaced by those coming from the pore body. Hysteresis therefore arises because when the pressure is decreased on desorption there is initially nothing to nucleate a large scale evaporation process in the large cavity until the pore liquid reaches a sufficiently expanded state such that spontaneous local density fluctuations can lead to cavitation.

Molecular dynamics studies by Sarkisov and Monson (2001) also showed that adsorption and desorption in voids of simple geometry like a slit pore, a closed end slit pore, and a wedge pore are related to the evolution of liquid-vapour interfaces in a manner largely consistent with the classical picture of these systems.

Molecular simulation studies by Vishnyakov and Neimark (2003) and experimental studies (Ravikovitch and Neimark, 2002; van der Voort *et al.*, 2002) of adsorption/desorption mechanisms in ink-bottle type pores revealed that, if the neck diameter is smaller than a certain critical size at a given experimental temperature, desorption from the pore body occurs via cavitation (spontaneous nucleation of a bubble). In this case, desorption occurs at a pressure P_{cav} which is higher than the pressure of equilibrium evaporation from the pore neck P_{neck}. The pore body can empty by diffusion, while the pore neck remains filled. Classical pore-blocking effect takes place when the neck size is greater than a certain characteristic value (50 Å for nitrogen at 77 K, assuming that the neck can be considered as a cylindrical pore.

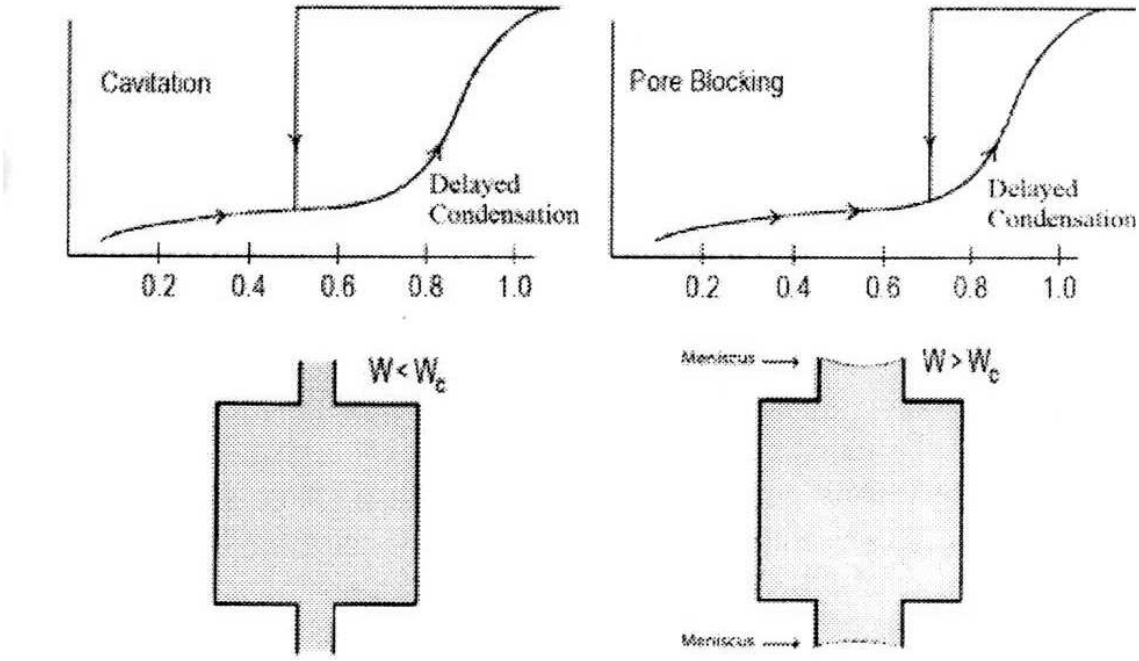

Figure 5.1: Schematic illustration of pore blocking and cavitation phenomena (Thommes *et al.*, 2006).

Thommes *et al.* (2006) studied nitrogen and argon adsorption experiments performed at 77.4 and 87.3K on novel micro/mesoporous silica materials with morphologically different networks of mesopores embedded into microporous matrixes. Test materials included SE3030 silica with wormlike cylindrical channels of modal diameter of ~95 Å, KLE silica with cage like spheroidal pores of 140 Å, KLE/IL silica with spheroidal pores of ~140 Å connected by cylindrical channels of ~26 Å, and also for comparison,

Vycor glass with disordered network of pores of mode diameter of ~70 Å. They showed that the type of hysteresis loop formed by adsorption/desorption isotherms is determined by different mechanism of condensation and evaporation and depends on the shape and sizes of featured pores, as shown in Figure 5.1. Their results confirm that cavitation-controlled evaporation occurs in ink-bottle pores with the neck size smaller than a certain value, and in this case, the pressure of evaporation does not depend upon the neck size. Their result showed clearly that desorption in a structure consisting of large mesopores occurs first by cavitation of the liquid in the large mesopores followed by the desorption in smaller mesopores. In contrast, for pores with larger necks, they confirmed that percolation-controlled evaporation occurs, as observed for nitrogen and argon adsorption on porous Vycor glass. In this case percolation effects contribute to hysteresis and hence information about the size of the pore necks can be obtained from the desorption branch. In conclusion, they demonstrated that adsorption experiments performed with different adsorptives allow for detecting and separating the effects of pore blocking/percolation and cavitation in the course of evaporation.

In addition to the two mechanisms of spontaneous evaporation from the cavity and correspondingly, two types of hysteresis, which depend on the ratios of the sizes of the cavity and the connecting pores reported by Vishnyakov and Neimark (2003), when the necks are sufficiently wide, evaporation from the cavity is determined by the conditions of evaporation from the neck. This is a typical inkbottle scenario or pore blocking effect: desorption from the cavity is controlled by the size of the neck. When necks are narrow, evaporation from the cavity is determined by the conditions of cavitation in the stretched metastable liquid prior to the emptying of the necks and hence does not depend on the size of blocking pores. Despite the recognition of the above phenomena, up until now two additional phenomena termed the advanced and delayed adsorption effect have yet to be incorporated. Advanced adsorption describes the spontaneous liquid-filling observed in a tubular capillary as a result of the eruption of an advancing liquid vapour interface proceeding from an adjacent wider cavity; this irreversible liquid filling occurs ahead of the accomplishment of the limiting condition for a vapour-liquid transition to occur inside the isolated, unconnected tubular pore; this being the reason for the label ‘advanced condensation’ (Vishnyakov and Neimark, 2003). On the other hand, delayed adsorption describes the filling of a wide pore with condensate once the thermodynamic metastability limit of the adsorbed film deposited on the walls of the

void has been surpassed. This was reported to be due to the existence of a discontinuous liquid-vapour interface around a pore cavity, which prevents the movement of a unified liquid vapour meniscus toward the centre of the pore in question; this discontinuity is due to the presence of empty pores surrounding the cavity under analysis (Vishnyakov and Neimark, 2003). The above phenomena are also relevant in catalytic applications, where, in hydrocarbon conversions and in gas production, advanced condensation may sometimes trigger an avalanche of liquid-filling of the pore network and the opposite effect of delayed adsorption may also be rather relevant although there is very little information on it in literature.

5.1.4 - Advanced Adsorption

The work of Neimark (1991) highlights that networking effects are not limited to pore blocking controlled desorption and hence suggested a mechanism of initiated capillary condensation. He argued that condensation in a narrow pore might result in the formation of an unstable vapour-liquid interface in the adjacent wider pore that would cause spontaneous condensation in the latter prior to achievement of the limit of metastability of adsorption films. This effect of initiated capillary condensation or advanced condensation as it is described here, may trigger an avalanche filling of the pore network. Figure 5.2 shows a schematic representation of the cause of advanced condensation for a certain pore criteria. It can be seen from Figure 5.2 that for a cylindrical pore with a narrower neck, capillary condensation could occur by two means. Either by both cylindrical meniscuses filling at the individual P/P^0 determined by the Kelvin equation, or in the case of advanced condensation effects, both body and throat filling at the filling pressure of the throat as this exceeds the pressure required to fill the body with a hemispherical meniscus.

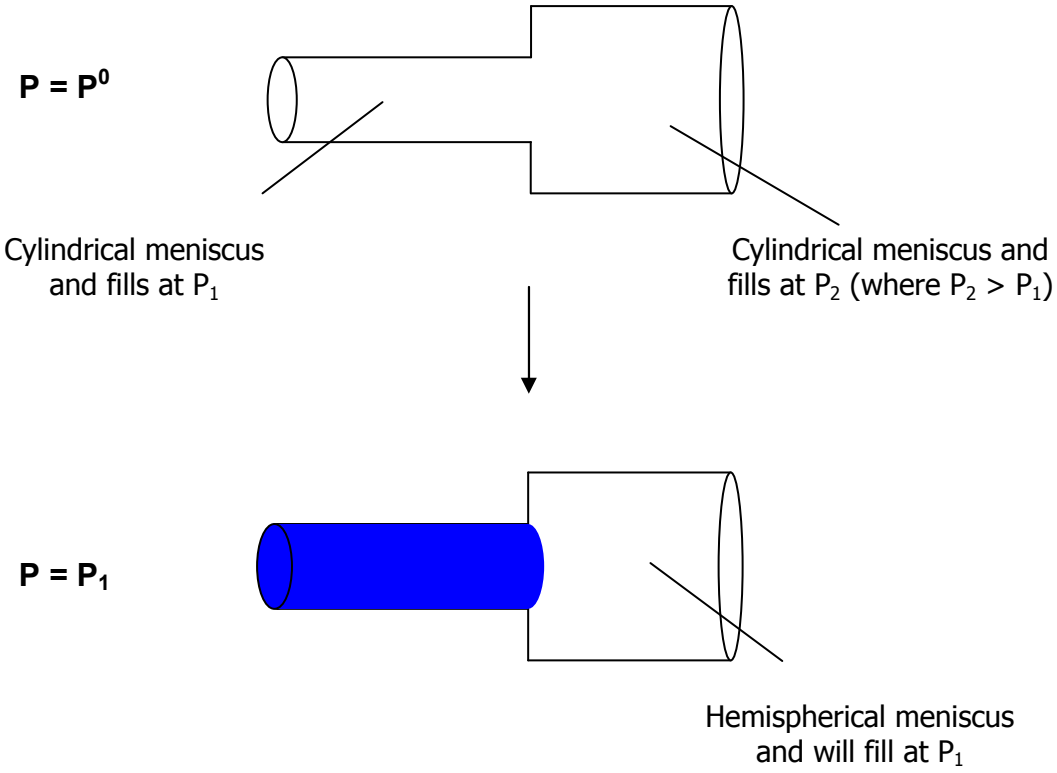

Figure 5.2: Schematic representation depicting the cause of advanced adsorption.

For fluid advancement within a network of pore bodies and throats, two situations can arise. The first one concerns the filling of the central bulge with condensate after an initial condensation at the two surrounding necks. The second situation refers to the filling of a remaining adjacent throat via a liquid-vapour meniscus advancing from the bulge, which is termed advanced condensation. In an ink-bottle type pore, advanced condensation could lead to severe inaccuracy in estimation of PSD e.g. overestimation of available pores of a certain size. Advanced condensation, however, emerges when the sizes of the central cavity and its surrounding necks fulfil certain ratios. For advanced condensation to occur in a cylindrical pore, the diameter of the pore body must be less than twice the size of the neck, or as shown in Figure 5.3, neck diameter > 0.5 × body diameter. The constant of proportionality k in the Kelvin equation (Equation 5.2) for pore size determination turns to; $k = 2$ for hemispherical meniscus and $k = 1$ for a cylindrical meniscus

Rigby and Chigada (2008) carried out MFDFT (mean field density functional theory) simulations to enhance the interpretation of gas adsorption data with emphasis on investigating the effects of the advanced condensation phenomenon on ink-bottle type pores. They looked at two types of cylindrical pores; ink-bottle type one with neck diameter less than 0.5 × body diameter and the other with neck diameter greater than 0.5 × body diameter. They reported that condensation in the neck and body occur independently in the first scenario and in the second scenario, following condensation in neck, at the pressure required for filling a cylindrical meniscus, the pore body automatically fills as the pressure has then exceeded the condensation pressure required for filling a hemispherical meniscus according to the Kelvin equation. Figure 5.3 shows a diagrammatic representation of advanced condensation in cylindrical pores of ink-bottle type (Rigby and Chigada, 2008). The ratio of the pore neck to pore body diameter = ξ and their main conclusions suggests: that as adsorption will not detect pore-mouth blocking for $\xi > 0.9$, for short pore necks, advanced adsorption does not have sharp critical watershed at $\xi=0.5$, as critical ξ depends on adsorbate- adsorbent interaction strength (surface chemistry) and pore neck length significantly affects condensation pressure, therefore great care must be taken whilst interpreting gas sorption data for coked mesoporous catalysts, coated porous materials or in cases of metal deposition.

The work of Rojas *et al.* (2002) also support the above theory that if these ratios exist (neck diameter > 0.5× body diameter) the following sequence can ensue: first, vapour condensation happens at the smaller of the two delimiting necks; next the central cavity fills with condensate (once the vapour pressure attains a critical value); finally the remaining empty neck is trespassed right away by the advancing liquid-vapour meniscus coming from the bulge. During the forming of the ascending boundary isotherm, advanced adsorption causes the liquid filling of tubular pores at pressures smaller than those required for condensation to occur in isolated pores of similar characteristics. If interconnected voids possess comparable sizes, the advancing meniscus can trespass a sequence of adjacent pores thus possibly spreading over the whole network. In a simple pore structure model, composed of a bundle of cylindrical pores, capillary condensation is considered to occur solely through a cylindrical interface. On the other hand, the mechanism of gas condensation within a corrugated pore will involve either a cylindrical or hemispherical interface shape in the context of individual pore segments. Therefore one does not expect any contribution to hysteresis

in the simple geometry during the condensation process directly due to pore structure – gas interactions, however the pore structure characteristics of a corrugated pore will effect on hysteresis during condensation by affecting the condition for liquid interface formation along the corrugated pore and hence influence the mechanism related to the liquid meniscus shape.

Boundary and primary N_2 sorption scanning curves have been experimentally determined for two types of SBA-15 materials (i) substrates made by hexagonal arrays of cylinders of about the same sizes , and (ii) solids including a relatively wide distribution of cylindrical pores of varying diameters arranged in a fairly distorted hexagonal packing by Esparza *et al.* (2004). This made it possible to observe the possible eruption of cooperative processes during the filling and emptying of tubular SBA-15 pores. Pore domain complexion diagrams (i.e. graphs indicating the amount of pore sizes that are occupied by condensate or vapour) were constructed by means of Non-Local Density Functional Theory calculations of the pore size distributions that are incumbent to both boundary and primary scanning curves. Their results inferred that advanced adsorption and single pore-blocking phenomena could take place in reason of the undulating cross-section nature of some SBA-15 tube materials. The extents of the above irreversible processes were shown to depend on the degree of sinuosity of the cross sections of the tubes. From the results of this work, it seemed that both high-quality and low-quality SBA-15 substrates can undergo the phenomena of advanced adsorption and single pore-blocking. The intensity in the latter phenomena was higher in the low-quality substrates because of the increased heterogeneity of these materials in respect to the high-quality SBA-15 solids. They made two important observations with regards to the phenomena of advanced adsorption outlined in their work. Firstly, a more extensive experimental work needs to be analysed to confirm the appearance of this phenomena in capillaries of varying cross section arising in some tubular systems. Secondly, it should also be recalled that the SBA-15 materials studied, contained a certain amount of intrawall pores that can possibly interfere to some extent with the detection of the advanced phenomenon and hence pore structure plays an important role. If these intrawall pores are small enough this interference can turn out to be insufficient to conceal the phenomenon in question during the determination of domain complexion diagrams from scanning sorption curves. In conclusion, they stated that the evidence about the existence of advanced adsorption is based on the accuracy of the results

provided by the NLDFT treatment; although currently one of the best ways of determining PSD of porous solids having pores of definite geometries, may require further confirmation by an equally reliable method.

Androutsopoulos and Salmas (2000) used a random corrugated pore concept to develop a new statistical model called the corrugated pore structure model (CPSM) to simulate capillary condensation-evaporation hysteresis. The pore structure was envisaged to be composed of a statistically large number *N* of independent (non-intersected) corrugated pores. This corrugated pore was assumed to be made of a series of interconnected cylindrical elements (pore segments) of equal length with randomly distributed diameters of mesopore size. For capillary desorption or evaporation of the condensate in a corrugated pore which is fully saturated upon the termination of the condensation process ($P/P^0 \rightarrow 1$), a hemispherical interface is anticipated to be present at either pore necks. When the pressure is decreased gas desorption occurs, resulting in the retreat of the two interfaces in opposite directions and their convergence towards the pore centre. A continual film of liquid interface to the wide pore segments positioned in the interior parts of the corrugated pore is restricted by the intervention of smaller segments or throats where evaporation should occur prior to the interface motion toward the wider sections of the corrugated pore interior. Thus according to the work of Androutsopoulos and Salmas (2000), it is the restricted access of the vapour towards the wider segments that induces hysteresis during capillary desorption-evaporation. CPSM pore networking effects influence mostly the desorption-evaporation process through the variation of the liquid nitrogen meniscus geometry. The CPSM model represents the simplest possible modification of the conventional pore model of a bundle of non-intersected cylindrical pores of distributed size (diameter). CPSM predictions of the intrinsic PSD are based on the simultaneous fitting of both branches of the hysteresis loop and are generally superior compared to those made by conventional methods. Total specific surface area predictions are in satisfactory agreement with the relevant BET values. It is however clear though that the nature of meniscus formation for evaporation after capillary condensation is dependent highly on pore structure restrictions and its influence may speed up or delay the evaporation process. It is therefore necessary to further investigate desorption- evaporation mechanisms in mesoporous materials.

5.1.5 - Delayed Adsorption

Delayed adsorption could occur in a cavity surrounded by vapour-filled necks. This situation is likely to happen in pore networks consisting of a central cavity delimited by necks having sizes not so different from that of the cavity. Imagine for instance, that a set of two cylindrical pores surround a nearly spherical cavity, if the size of this bulge is smaller than twice the size of anyone of its surrounding throats (and assuming that condensation is dictated by the Kelvin equation (Equation 5.2)) then the cavity will only be filled with condensate if a continuous meniscus is formed around this pore. This situation could happen if at least one of the surrounding necks is being filled with condensate (Cordero *et al.*, 2005), i.e. the central cavity will be condensate filled at a pressure larger than that required if this bulge existed isolated from other pores. Cordero *et al*. (2005) used a Monte Carlo procedure to evaluate the extent of delayed and advanced adsorption in porous structures of assorted morphologies. Delayed and advanced condensation was evidenced through the comparison between actual and calculated pore-size distributions proceeding from simulations on two different networks of boundary and primary scanning N_2 sorption isotherms at 77 K.

5.1.6 – Scope of Work

The work of previous researchers ((Neimark, 1995; Ravikovitch *et al.*, 1997; Sarkisov and Monson, 2001) on the studies of adsorption phenomena has shown support for a variety of pore filling mechanisms such as cavitation, ink bottle theory and advanced condensation, which could lead to a misrepresentation of pore characterisation data, and hence highlight the need for direct investigations into the existence and conditions for which they may exist, in order to make more accurate estimates of pore structure information.

Menisci interactions strongly affect the development of adsorption processes in mesoporous materials. Phenomena such as advanced and delayed adsorption are outright manifestations of these interactions, which may result in deceptive determinations of pore size distribution. At present, there are only a few studies

involving real materials where the above processes occur and as such, there is a need to determine the type of mesoporous structures that can experience the incidence of delayed and advanced adsorption. There has so far been little, or no, direct testing of theories of gas sorption within particular pores. It is therefore within the scope of this research to investigate the effect of the advanced adsorption phenomenon through direct testing in mesoporous materials employing gas adsorption techniques. The method of investigations carried out is based on a comparative analysis of a sample of a commercial silica mesoporous solid that has been crushed and powdered down to ~70 – 100 μm to alter the pore structure of the pellet by removing the narrow necks surrounding the bigger pore bodies. Gas adsorption is the most common method of characterising the pore structure of porous materials, which are generally complex and as such may lead to a variety of behaviours, which may occur simultaneously. It is exigent to infer the pore structure of a porous material accurately, for example, a catalyst or adsorbent, as this is fundamental to the effective design of heterogeneous processes. Hence, researchers are continually seeking ways of improving pore structure interpretation and analysis technique and it is for this reason that this work is proposed.

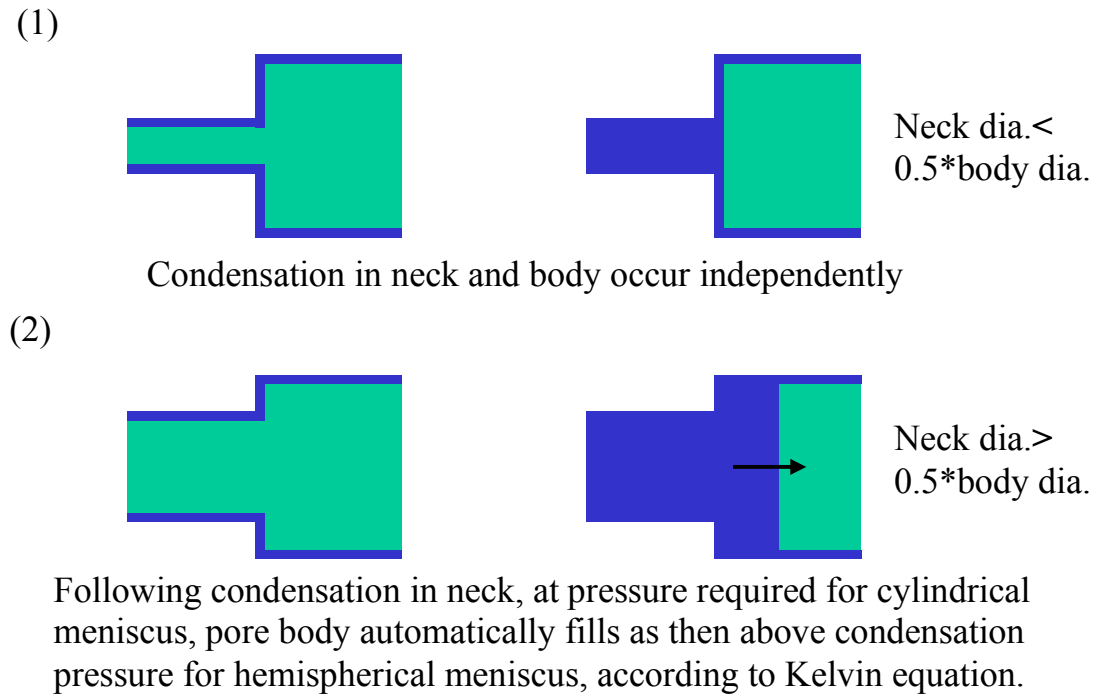

Figure 5.3: shows a diagrammatic representation of advanced condensation in cylindrical pores of ink-bottle type (Rigby and Chigada, 2008).

5.1.7 - Experimental Technique

The nitrogen adsorption isotherms for the test materials, was obtained by the use of the Micrometric ASAP, and the cyclohexane adsorption experiments were performed using the Intelligent Gravimetric Analyser (IGA).This Study was performed on a series of mesoporous silica pellets (S980G), with an estimated BJH average pore diameter of 100 Å, and an average pore volume of ~1.04 ccg^{-1}. The test material is a commercial sol gel silica and the powder samples were obtained by crushing the pellets to powder using a pestle and mortar to the approximate size range of 70 – 100 µm. Nitrogen and cyclohexane adsorption experiments are performed on the same set of silica pellets for accuracy of comparisons. Two sets of cyclohexane experiment were performed at different temperatures on the whole pellets and on the powdered samples, denoted pellets experiment 1 at 10 °C and 2 at 20 °C and powder experiment 1 at 10 °C and 2 at 20 °C. Two sets each of Nitrogen adsorption experiment at 77 K were also ran on the

pellets and powder also denoted as pellet experiment1, pellet experiment 2 and powder experiment 1 and powder experiment 2.

Nitrogen has a high interaction strength with silica walls, and is evident in the resulting type IV isotherm, whereas cyclohexane isotherms have a similar BET region to the water isotherms run in Chapter 4 and as such indicates a lower strength of adsorbate-adsorbent interaction. These two different gases have been chosen for this investigations, in order to cover the high end and low end adsorbate-adsorbent interaction strength.

5.1.8 - Mercury Porosimetry Experiment

Mercury porosimetry experiments were also conducted on both the pellets and powdered S980G samples from cyclohexane and N_2 adsorption experiments. The mercury porosimetry experiments were performed using a Micrometrics Autopore III. The sample was first evacuated to a pressure of 6.7 Pa in order to remove any physisorbed gases from the interior of the sample. The mercury porosimetry data were analysed using the standard Washburn equation, using a value of 0.485 Nm^{-1} for surface tension of mercury, and the corresponding values of the advancing and receding contact angles were both taken as 140 ^{o} to obtain the intrusion and extrusion curves. This is used as a measure to confirm sufficient deshielding effects have been achieved in the powdered samples in comparison to the whole pellets and to ensure that the powdered pellets have been crushed below the ratio of the pore to throat coordination number required to cause advanced condensation. If you compare the powder intrusion curve with the intrusion curve of the whole pellet sample, a shift to larger pore sizes with the powder in relation to the whole pellets indicates a de-shielding process has occurred.

5.1.9 - Nitrogen Adsorption

The nitrogen adsorption experiments were performed using a Micrometric Accelerated Surface area and Porosimeter (ASAP) 2010 apparatus at 77 K. Volumetric gas adsorption (manometry) is based on the measurement of pressure of the adsorptive gas at constant temperature before and after the adsorption by a given mass of adsorbent. In the ASAP, the amount adsorbed is evaluated from the change of pressure. The sample to be analysed is placed in a round bottom tube, and a glass rod is placed gently into the sample tube, to reduce the free space volume and then it is sealed. The weight of the tube and the glass rod is recorded, and hence the sample initial weight is known. The first stage of the analysis is to degas the sample, to drive off any physisorbed water on the sample, without changing the sample morphology. The sample tube is then loaded into the degassing port, and a heating mantle is attached and heated under vacuum at 170 ^{o}C overnight. It is essential to degas the sample, as any liquid present on the sample will hinder the adsorption of nitrogen molecules into the sample, and hence provide inaccurate results. The ASAP 2010 has a facility to ensure that the sample has reached vacuum. Once this check has been completed, the degassed sample is then allowed to cool off. The sample tube and its contents are then reweighed to obtain the sample dry weight, which is then entered into the analysis data, prior to analysis, to calculate the volume adsorbed per gram of sample. The sample tube is placed in liquid nitrogen at 77 K prior to the adsorption measurements. A piece of foam is used to cover the liquid nitrogen tanks to prevent evaporation of the liquid nitrogen. A leak test, and a free space analysis is set up to occur during the analysis, and an equilibration time of 45 s was allowed for each adsorption point to reach equilibrium. The full adsorption/desorption isotherms obtained were analysed using the previously discussed, well-known BJH method to obtain the pore diameter distributions. The film thickness for multiplayer adsorption was accounted for by using the well-known Harkins and Jura equation. In the Kelvin equation, the adsorbate property factor was taken as 9.53×10^{-10} m and it was assumed that the fraction of pores open at both ends was zero for both adsorption and desorption. It was therefore assumed that capillary condensation commenced at the closed end of a pore to form a hemispherical meniscus and the process of evaporation also commenced at a hemispherical meniscus.

5.1.10 - Cyclohexane Adsorption

Cyclohexane adsorption experiments were performed on a Hiden Intelligent Gravimetric Analyser (IGA). The sample was loaded into the IGA and the reactor chamber sealed tightly. The sample was then evacuated to vacuum and heated to 250 °C for 4 hours. Once completed, the reactor chamber was allowed to cool down to room temperature. A bath containing a mixture of ethylene glycol and water jacket was placed around the chamber and the bath was set to the required temperature of 10 °C and 20 °C. Once the temperature was set, the isothermal analysis was performed in the relative pressure region of 0.004 to 1.00 P/P^0. The data acquisition is controlled by computer software along with the adsorption experimental process.

5.1.11 – Results

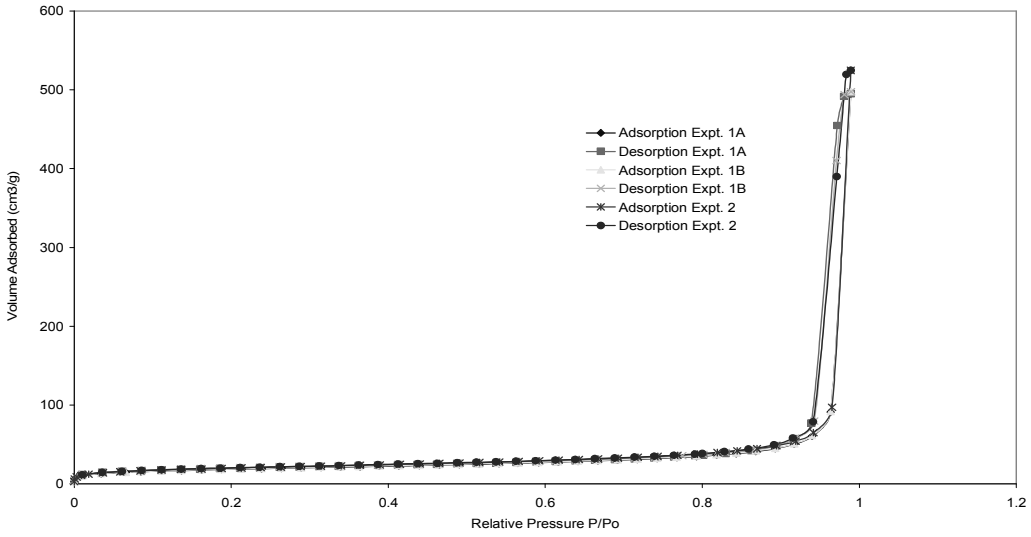

Figure 5.4: S980G Pellet N_2 Sorption at 77 K Isotherm for Expt. 1A, 1B, and 2.

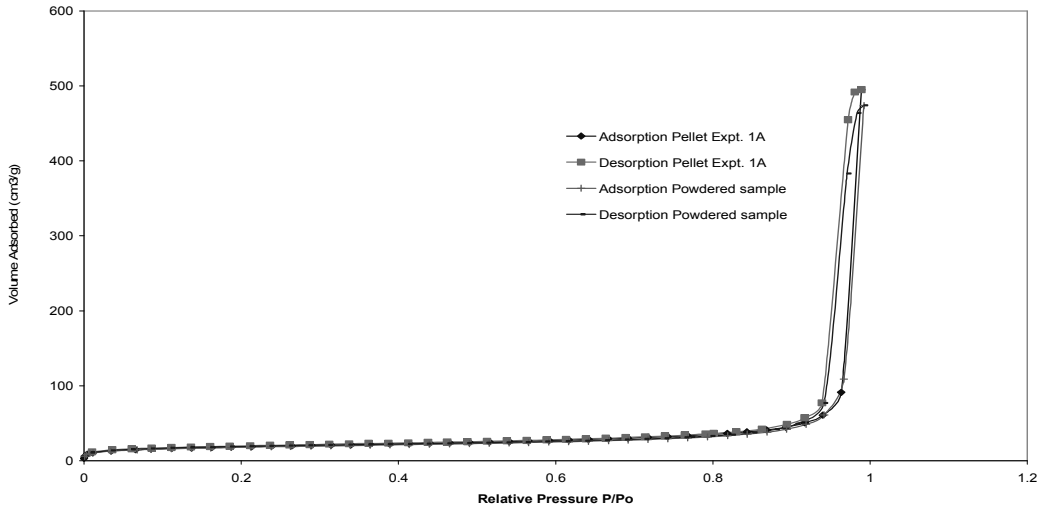

Figure 5.5: S980G Pellets vs. Powder N_2 Sorption at 77 K.

S980G experiment 1 was repeated 3 months after on the same sample (labelled Expt. 1B) for the purpose of verifying result reproducibility. Human/operational errors appear to be minimal also as resulting data for experiment 2 show little or no difference following exposure to air under room temperature for 3 months prior to a further out-gassing and sample preparation at 250 ^{o}C for 4 hours.

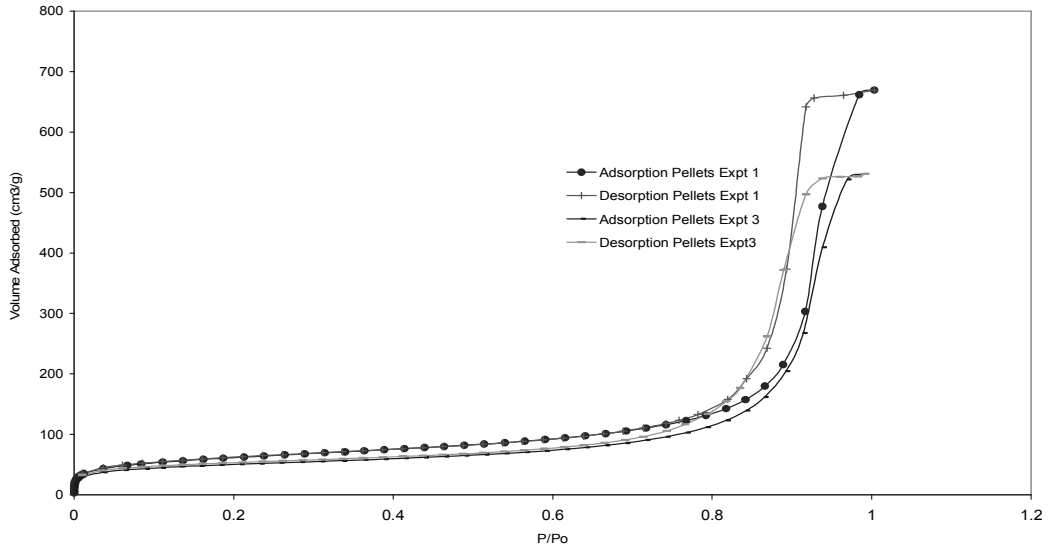

Figure 5.6: Nitrogen sorption at 77 K on S980A Pellets showing two runs (confirms repeatability).

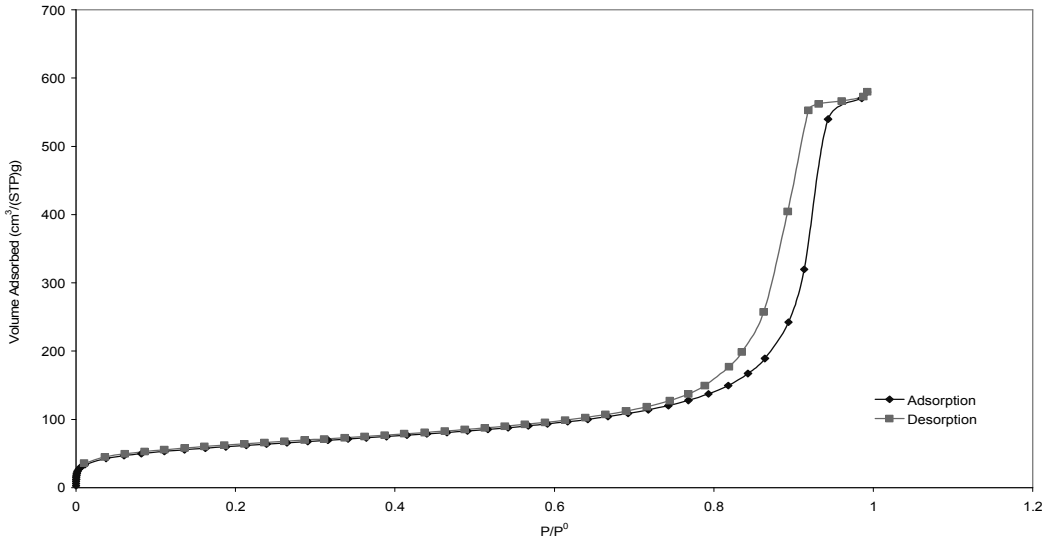

Figure 5.7: Nitrogen sorption at 77 K on S980A Powder.

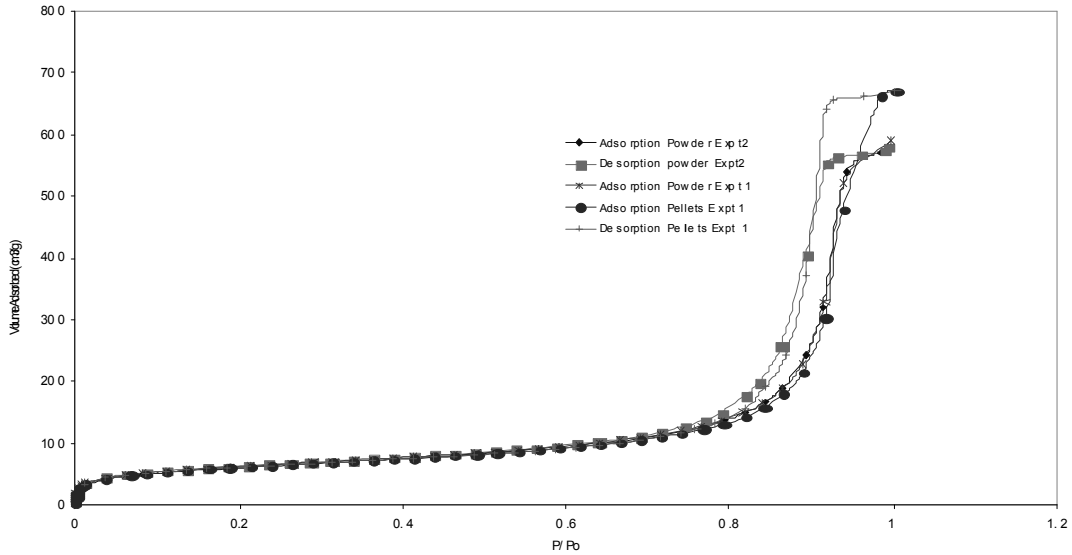

Figure 5.8: Nitrogen Sorption at 77 K on S980A for both Pellets and Powder.

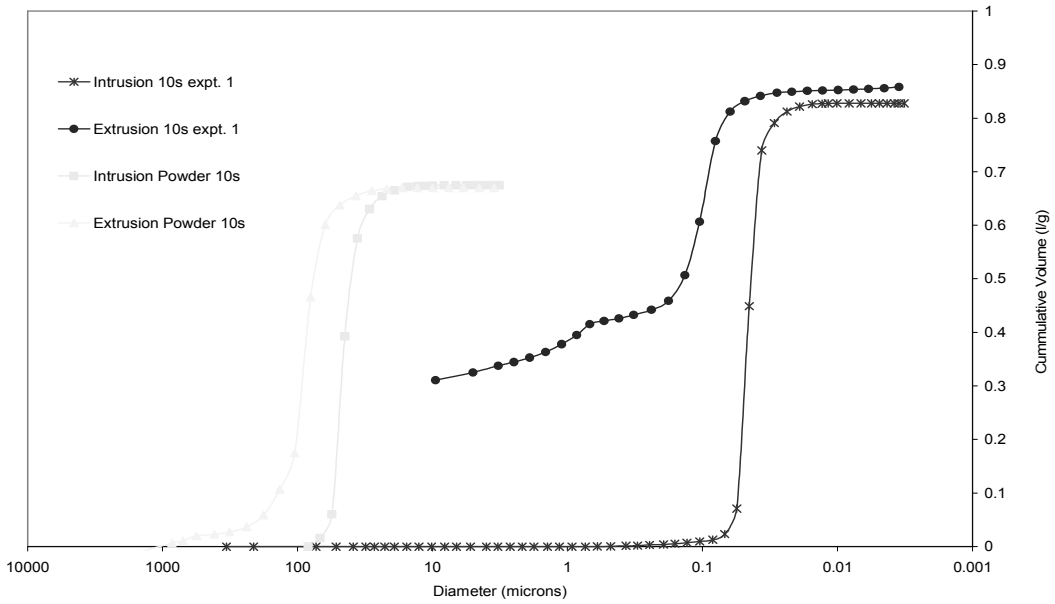

Figure 5.9: S980G Pellets vs. Powder Mercury Intrusion/Extrusion curve.

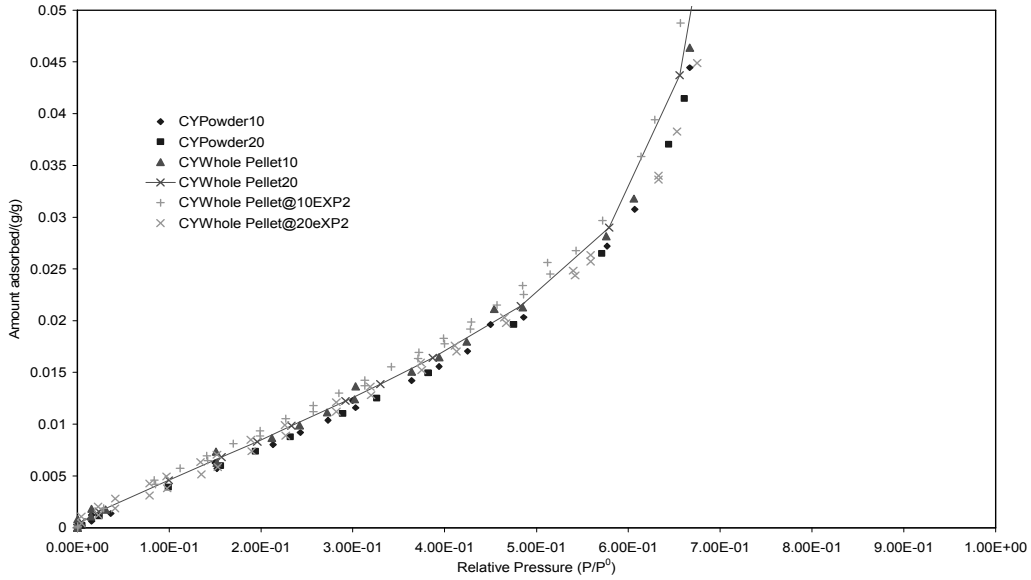

Figure 5.10: S980G cyclohexane adsorption curves (within the region of initial uptake) for Powder vs. Whole Pellet at two different temperatures (10 ^{o}C and 20 ^{o}C).

By comparing the mercury intrusion curve of the powdered sample with the whole pellet sample (see Figure 5.9) it can be seen that the intrusion curve shows a shift to larger pore sizes for the powdered sample, indicating substantial de-shielding has occurred for the fragmented sample. This means that even if a pore throat to body ratio

capable of exhibiting advanced condensation effects existed, it has been successfully altered, by fragmentation to powder, hence some discrepancy in the adsorptive behaviour due to advanced condensation effects should be expected/or made apparent in the pellet vs. powder adsorption isotherms for cyclohexane and N_2 if they existed. The powder intrusion curve also indicates the powder particle size, which is ~10 - 100 microns, within a 20 micron radius. In general, for powder intrusion curves, the second step signifies intra-particle intrusion, and the powder intrusion in Figure 5.9 has been renormalized to adjust for this. The mercury intrusion/extrusion curve for the powdered samples shows a narrower region of hysteresis and a lower value of entrapment, further supporting structural hysteresis through networking effects as a likely cause of hysteresis loops (region of irreversibility).

The results displayed above for both N_2 adsorption and cyclohexane sorption (see Figures 5.4 - 5.8) did not show any advanced condensation effects between the powdered sample and the whole pellets tested. Figure 5.10 shows the cyclohexane adsorption isotherm for S980G powder and pellet at two different temperatures (10 ^{o}C and 20 ^{o}C) superimposed. The adsorption and desorption curves were run at different temperatures to investigate the effect of temperature difference on data and or investigate repeatability. For cyclohexane adsorption, very little or no variation is observed for the different test samples (powdered vs. whole pellets) as well as between the two adsorption temperatures of 10 ^{o}C and 20 ^{o}C employed. There is a small amount of scatter between graphs; however, there is no significant shift in either direction (to larger or smaller pores). If the adsorption curve for powdered samples had shifted to the right, as a result of a delay to higher pressures until larger pores are filled, it would have been an indication of the existence of advanced condensation effects. Therefore, one can suggest that big pores shielded by pore throats in the whole pellet samples filled at the pressures determined by the Kelvin equation for the filling of cylindrical pores of corresponding sizes. Likewise at low pressures, only pores small enough to be filled by condensation at the attained pressure filled, with no extras as a result of the so called avalanche type filling due to having adjoining long pores (necks). As the PSD obtained by the BJH method for both whole pellet and powdered samples are within close match, one can concluded that there is unlikely to be any misconception or over estimation regarding pore size brought about by advanced condensation.

5.1.12 - Discussion

Pellets with non-random heterogeneity (pore bodies of similar sizes surrounded by pore necks of ~ same size) were analysed to identify any effects of advanced condensation; if advanced condensation occurred, it will mean big pores filled at the same time as small pores and if compared to a system incapable of exhibiting advanced condensation, a shift in the latter isotherm to the right suggests an elimination of the above phenomenon through de-shielding. Imagine a pore de-convoluted to constitute a pore structure including a small pore (neck) separate from a big pore (body), small pores will fill up at low pressures and an extended low pressure filling region will be apparent as the build up to higher pressures required for the filling of bigger pores is attained. Powdered pellets adsorption isotherm should result in a shift to the right when compared to whole pellets, as at low pressure fewer pores fill in the powder sample (only those meant to be filled at the pressure determined by the Kelvin equation) whereas due to advanced condensation pore bodies could fill at the same pressure for pore neck filling in the pellets adsorption isotherm. The process of grinding the pellets to powder of 70 – 100 μm is aimed at removing the shielding effect, which is a prerequisite for the advanced condensation phenomenon. To confirm that advanced condensation has occurred, even if there is no visible effect in the adsorption curves of powder vs. pellets, the desorption branches of gas adsorption isotherms should be checked for the effects of pore shielding, because if the pores are crushed below a certain factor sufficient to cause advanced condensation, then a notable difference should be evident in the desorption branches in the powder vs. whole pellets as the effect of pore shielding should be minimised as a result of less blockage. In addition, mercury intrusion and extrusion curves should be used to identify any changes in pore size distribution as well as entrapment levels in other to ascertain whether sufficient change to pore structure has been made to highlight the effects of advanced condensation if any.

Rigby and Chigada (2008) had reported a link in some adsorbate-adsorbent systems between the strength of interaction and the occurrence of advanced condensation. As a result, nitrogen and cyclohexane were both used as adsorbents, as they have different strengths of interaction between gas and surface to investigate the phenomenon of advanced condensation and the likelihood of any links that may exist pertaining to these

systems adsorbate-adsorbent interaction strength. The lack of advanced condensation effects in S980G pellets, is probably an effect of pore geometry in terms of pore neck size and/or pore body-neck ratio sufficient to hinder the formation of a hemispherical meniscus for the pore body and hence the body waits till the pressure required to fill a pore of its size with a cylindrical meniscus is attained. If advanced condensation had occurred in the pellets analysis, it will mean there had been a faster rate of condensation, causing big pores to fill at the same time as small pores. The powdered sample's adsorption isotherm in comparison should shift to the right as at low pressures required for condensation in necks, only necks fill hence less pores filled all together.

The effects of adsorption behaviour such as capillary condensation, prewetting of surfaces as well as the influence of including closed ends on pore bodies, on adsorption mechanisms and subsequent data has been studied extensively by several researchers such as Cohan (1938); Ball and Evans (1989); Neimark *et al.* (1999, 2000) via simulation. Most of this work was done for a few ideal geometries, such as slit or cylindrical pores, and as a result, Malanoski and Swol (2002) carried out studies into the effect of varying pore shape, to see if this variation from ideal geometries results in a theoretical calculation that agrees better with the experimental work. Many studies, including Jaroniec *et al.* (1999) and Smarsly *et al.* (2001), of adsorption in mesoporous materials, employing experimental systems have had one issue, which is the presence of pore connectivity of which the exact nature is often not known. Many of these materials are prepared as powders and the effect of the orientation, packing of the particles on the adsorption is also not known, and as such, these factors present additional complications to modelling these substances. Malanoski and Swol (2002) investigated the effects of varying pore shape from the slits and cylinders that are normally simulated and the adsorption behaviour of pores with very large diameters. They were interested in the more realistic pore structure case, so they obtained results for pores with ends. This introduced a problem as they were also interested in pores where the ratio of the overall pore length to pore diameter is very large (~1000) and little of the length is associated with the openings. Although feasible, modelling such pores would be very time consuming and hence they tracked the adsorption of an interior slice. Their results established that for sufficiently long pores, the adsorption in the centre of the pore length does not depend on the pore length, and the adsorption in this centre slice of the pore measures the total adsorption in pores with very long lengths. It was also shown

that for pores with shapes close to that of a cylinder, the capillary condensation in a cylindrical pore of equivalent pore area will be similar to that of a pore whose shape is not cylindrical, and for very large pores, the details of the shape and even the exact size of the pore is no longer important in determining the hysteresis loop. Therefore, in the absence of advanced condensation one of many processes could be happening, however for a scenario fulfilling the ratios predicted by MFDFT simulations to trigger advanced condensation effects, an absence of the above phenomenon is attributable to the existence of elongated pores (Malanoski and Swol, 2002). There is however, another reason to believe that S980G has long pores, such as through direct testing: Watt-Smith *et al.*, (2006) MRI data suggests that the pore sizes in S980G have a high correlation over macroscopic length scales. The results obtained within this experimental testing of advanced condensation effects show no shift in the powder adsorption isotherm for S980G, indicating there are no advanced condensation effects occurring. The above experimental findings could also be interpreted by the conclusions drawn by Malanoski and Swol (2002). This will mean that for the relatively long necks in S980G the Kelvin pressure for filling a cylindrical meniscus is similar to that of filling a hemispherical meniscus such that there is no difference and pores fill according to their sizes. In a pore structure of ordered correlation (such as in S980G), long pores could seem much more elongated in comparisons to a convoluted pore structure where pores are shortened by changing diameters.

5.1.13 - Conclusion

It is important to note that the features that affect only a small portion of the pore, such as neck constrictions and ratio in relation to pore body in ink-bottle type pores, could have significant impact on the adsorption-desorption curves, and hysteresis of the entire pore. Experimental gas adsorption studies on S980G aimed at investigating the effect of pore neck to throat correlation manifestations in terms of advanced or delayed condensation determined by the cylindrical or hemispherical meniscus show that for very long pores such as the ones observed for S980G there is no difference between the pressure for capillary condensation in a cylindrical meniscus and a hemispherical meniscus. Hence advanced condensation effects cannot impact the adsorptive

behaviours of such materials. A more extensive experimental work needs to be analysed to confirm the appearance of advanced condensation in various capillary systems, and further comparative studies with samples not exhibiting this phenomenon will provide further understanding.

5.2 - Fractal Analysis

5.2.1 - The Theory of Fractality

The internal surfaces of porous media, such as mesoporous alumina or silica supports for heterogeneous catalysts, are highly complex. The pores in these materials are often very different from the idealised, smooth cylinders that they are often assumed to be in models of porous media. Hence, it is important to be able to quantify the degree of heterogeneity in the pore surface of a heterogeneous catalyst. The concept of fractality may offer a method by which complex porous materials may be characterised and modelled. It defines a fractal dimension factor, *d*, for the surface of a porous solid in relation to the variation of surface area measurements and other geometrical parameters with the size of the measuring device. The BET method of determining the surface area is arguably the most popular method of assessing the surface area of adsorbents, among the several methods that have been explored such as empirical methods of isotherm analysis like the standard adsorption isotherm, and the t-method, adsorption from solution and immersion calorimetry. Full details of these methods of assessing the surface area of adsorbents is beyond the scope of this research, however the aim is to identify that there are different techniques with different limitations, and hence as pointed out by Rouquerol *et al.* (1999) the results are expected to differ. The fractal approach provides a way of tackling the problems encountered in evaluating the absolute surface area of a porous solid. Fractal analysis can be used to establish the effective geometry of an adsorbent and hence leads to a better understanding of surface coverage. The fractal dimension is a structural parameter that quantifies the scaling invariance of self-similar systems (Gregg and Sing, 1982). If an object can be decomposed into λ similar parts of size n times smaller than the whole, the fractal

dimension is defined by Equation 5.5 as a scaling exponent in the relation between the fragmentation parameter λ and the contraction ratio, *n*.

$$\lambda = n^d \quad \textbf{(5. 5)}$$

Gas adsorption is a method that is commonly used to determine the surface fractal dimension of porous materials. Several theories have been proposed, for analysing gas adsorption data to obtain surface fractal dimensions. The pioneering work of Avnir *et al.*, (1983,1984) used a power law equation of the form: $A \sim r^2(R/r)^d$ (where *A* is the area obtained for a fractal surface depending on the resolution of the measurement (*r*), d is the fractal dimension and R is the overall linear dimension of the surface. By using different chemical species with different molecular sizes, they varied the resolution of measurement used to obtain the surface area. However, the authors obtained the surface area using the BET theory, which is questionable given that it was derived for planar surfaces and not for structurally heterogeneous surfaces. The range of length scales that could be probed was also limited by the small variation in molecular size over the range of molecules used (Drake *et al.*, 1990). In addition, the effective cross-sectional area of an adsorbed molecule depends on the strength of interaction with the surface (Gregg and Sing, 1982).

Fripiat *et al.* (1986) adapted the BET equation for fractals and used a technique based on the concept of the BET theory to investigate surface fractals by assuming that each layer within a series of adsorbed layers has an apparent fractal dimension of the surface. According to the authors the physical factor that accounts for the effect of fractal character of a surface on multi-layer adsorption, is the filling of the micropores generated by the surface, according to a scaling process, and hence results in a decrease in the fractal dimension of the surface as the thickness of the multi-layer cover increases. On a rough surface, the number of adsorption sites declines with increased multi-layer thickness due to the concavities. Unfortunately, the fractal BET equations still omit the potential effects of chemical heterogeneity and/or adsorbate - adsorbate interactions.

Pfeifer *et al.* (1989, 1997) proposed an alternative theory for obtaining the fractal dimension of surfaces from gas adsorption data, based on the Frenkel-Halsey-Hill (FHH) approach (Halsey, 1948). It only requires one type of adsorptive because it uses the variable thickness of the adsorbed multilayer film as the probe for varying length scale. This method is free from many of the complications in the original molecular tiling method developed by Avnir *et al.* (1983). Any chemical heterogeneity of the surface is discounted because, after completion of the first monolayer the substrate is mostly shielded. In the fractal FHH approach, the relationship between the FHH exponent and the fractal dimension depends on whether the substrate (van der Waals) potential or vapour-liquid surface tension dominates the adsorption. The Frenkel-Halsey-Hill (FHH) equation for the fractal analysis of multi-layer adsorption on surfaces is stated below in Equation 5.6:

$$\ln\frac{V}{V_m} = C + (d-3)\ln\left[\ln\left(\frac{P_0}{P}\right)\right] \qquad \textbf{(5. 6)}$$

Where V is the volume of adsorbed gas at equilibrium pressure P, V_m is the volume of gas in a monolayer, and P_0 is the saturation pressure. The constant C is a pre-exponential factor, and S is a power law exponent dependent on d, the surface fractal dimension, where at higher coverage (represented at coverage above BET monolayer), the interface is controlled by the liquid/gas surface tension, which makes the interface move further away from the surface, to reduce the surface area. d is given by: *(S = d – 3)*.The surface fractal dimension may physically take values in the range 2<= d<= 3, with a value of 2 indicating a perfectly smooth surface, whilst a value of 3 indicates a highly disordered surface. This model is only valid for a multi-layer adsorption and assumes that adsorption on a smooth surface obeys the FHH equation between the equilibrium film thickness and the adsorbate chemical potential. The fractal approach was also adopted by Ehrburger-Dolle *et al.* (1994) as part of a systematic study of the properties of silica aerogels. The value $D_a = 2.1$ was obtained from linear FHH plot for nitrogen on Aerosil 200, whereas values of 2.64 and 2.95 were obtained from the nitrogen multi-layer isotherms on various aerogels. The latter value which is close to 3 appears to be consistent with volume filling by capillary condensation as the

predominant process at high relative pressure. Evidently, the low fractal dimension given by Aerosil is in line with its molecularly smooth surface.

5.2.2 - Small Angle X-Ray Scattering

The SAXS technique is used to determine the particle size distribution and the measurement of the specific surface area. A beam of X-rays are scattered by the electrons in an irradiated material. Porous materials cause the X-ray radiation to scatter, due to the system of the volume-distributed local inhomogeneities of electron density (submicropores and micropores). Pores and shapes exceeding the wavelength of X-ray radiation, condition the angular range of such a scattering and the scattering intensity, *I (q)* is mainly determined by pore concentration and electron density gradient at the pore-matrix border. SAXS can also be used as a technique to determine the fractal roughness of a porous structure, since it probes materials over several orders in length scale, which include both primary particle and fractal aggregates. The surface roughness of a material on a scale in the range of the inverse of q covered in the SAXS measurements can be determined by using the Equation 5.7 (Ramsay *et al.*, 2002):

$$I(g) \propto q^{-\eta} \qquad \textbf{(5. 7)}$$

The intensity of radiation scattered by a fractal surface is proportional to a negative power of the q vector, such that the above equation holds, where $q = 4\pi\lambda^{-1}\sin\left(\frac{\theta}{2}\right)$, λ is the wavelength of the radiation, and θ is the scattering angle (Ma *et al.*, 1999). Usually this dependence is observed only when q satisfies the inequality $q\xi >> 1$, where ξ is the characteristic length of the structure producing the scattering. From the value of η one can determine the fractal nature of the system under investigation. The exponent $1<\eta<3$ describes the mass fractal of dimension $(d_m)_{SAXS} = \eta$, and $3<\eta<4$ describes surface fractals of dimension $(d)_{SAXS} = 6 - \eta$. Where $(d)_{SAXS}$ is the surface fractal dimension, and typical values of $2<d<3$ occur. d = 2 indicates a smooth surface, while d = 3 indicates a highly disordered surface. Reiker *et al.* (2000) used SAXS to

investigate the morphology of carbon black mass fractal aggregates in polymeric composites, and found a surface fractal of 2.3 for the primary particles and a mass fractal dimension of 1.8 for the aggregates. They found that the loading of carbon black in the carbon black/polymer composite could control the arrangements of aggregates. Later, Rigby and Edler (2002) compared pore sizes obtained by SAXS to that obtained from the analysis of mercury porosimetry data, and found the results were in agreement as mercury porosimetry has the ability to perform pore size analysis over a wide range of pore sizes from about 0.003 μm up to about 400 μm.

5.2.3 – Gas Adsorption on Fractal Surfaces

Computer simulation studies have shown that the degree of surface roughness of pores strongly influences the rate of mass transfer in those pores, particularly by surface diffusion (Rigby, 2002, 2003) and Knudsen regime pore diffusion (Coppens and Froment, 1995). Coppens and Froment (1995) applied a theory of fractals to porous catalysts and proposed a method to model the pore morphology and surface accessibility. The catalyst was modelled as a true surface fractal with a finite fractal-scaling regime. A geometrical description of individual pores was determined, and the results obtained allowed the authors to establish one-dimensional equation to be set up for the simulation of diffusion and reaction in the catalyst. The pore morphology was reported to have a considerable influence on diffusion and reaction processes in porous catalysts. An analytical expression for the Knudsen diffusivity in a catalyst with a surface that is fractal in a finite scaling regime was determined and the irregularity of the surface was shown to hinder the Knudsen diffusion especially for small molecules. According to the authors, for a first-order reaction, the amounts reacted in a fractal pore are always higher than in a cylindrical pore of the same length and cross-section, but the differences decrease with increasing diffusional limitations, especially in the Knudsen regime.

Rigby and Gladden (1998) also investigated the influence of structural heterogeneities on selectivity in fractal catalyst structures, by using three-dimensional models to correlate selectivity with model characteristics. The simulations performed suggested

that the voidage fraction and mass fractal dimension are key parameters that influence selectivity, and thus accurately representing a real porous material. The authors also showed that the degree of surface roughness of a heterogeneous catalyst could affect the selectivity between competing diffusion-limited reactions. If the rate constant of diffusion through the pores of a porous pellet is influenced by the degree of surface roughness, it is therefore essential to investigate the existing techniques of determining surface fractal dimensions. In addition to the characteristic information obtained for mesoporous core materials synthesised within this research, a measure of the fractality will be investigated, in view of its contributions to the selectivity and characteristic properties of porous media.

There are so far, very few studies in literature that directly test the validity of fractal adsorption theories by comparing fractal dimensions measured through gas adsorption onto porous materials to those measured independently using alternative techniques such as X-Ray scattering. There is only one study in literature, by Rojanski *et al.* (1986), as reported by Ma *et al.* (1999) that claims that gas adsorption data agrees with scattering data. Ma *et al.* (1999) goes onto further suggest that some authors (Wong and Bray, 1988) have claimed that this agreement is a result of a misrepresentation of the scattering data, although Pfeifer and Schmidt, (1988) have contested that it was a misrepresentation.

Ross *et al.* (1988) compared fractal dimensions of fumed silica materials from gas adsorption using molecular tiling and fractal BET methods with fractal dimensions obtained from Small-angle X-ray (SAX) and small-angle neutron (SANS) scattering. The adsorptives used included nitrogen, argon, n-heptane and n-pentane. The adsorption and scattering methods were found to generally disagree and this was attributed to the neglect of lateral interactions between adsorbed molecules by the adsorption theories. Sahouli *et al.* (1996) also compared the fractal dimensions obtained for carbon blacks from SAXS with those obtained by using the FHH theory to analyse nitrogen adsorption on the materials. Again, the fractal dimensions obtained by gas adsorption were found to disagree with the values obtained from SAXS in most cases. Weidler *et al.* (1998) measured the fractal dimensions of two synthetic geothites using SAXS and the fractal FHH analysis of nitrogen adsorption data and found that they both exhibited the same trend but disagreed about the absolute value of the fractal dimension. Ma *et al.* (1999)

compared the fractal dimensions of three shale samples obtained from the fractal FHH analysis of nitrogen adsorption with those obtained from SANS. They reported that the fractal dimensions obtained from gas adsorption data were significantly lower than those from SANS. Ma and co –workers in subsequent reports (Ma *et al.*, 2001, 2002) attributed this failure of the FHH theory of nitrogen adsorption to the effects on the slope of the FHH plot in the fitted data range arising from the transition from van der Waals-dominated adsorption to the surface tension regime.

More recent work by Watt-Smith *et al.* (2005) tested the validity of the fractal versions of the FHH and BET theories for describing the adsorption of butane and nitrogen on a variety of partially dehydroxylated silica surfaces. The fractal dimensions obtained from adsorption data for both adsorptives were compared to those obtained completely independently using SAXS. It was found that the fractal dimensions obtained from the butane adsorption isotherms, using both the fractal FHH and fractal BET theories, agreed well with the corresponding values obtained from SAXS over overlapping length scales. They also reported a systematic deviation between the fractal dimension obtained from nitrogen adsorption and that obtained from SAXS. The measurements obtained from nitrogen adsorption were consistently larger than those obtained from SAXS, which is the opposite of what was reported by Ma *et al.* (1999). It was suggested that the differences in the suitability of the adsorption theories tested to describe butane and nitrogen adsorption is due to the significant difference between the interaction strengths of these two different molecules with silica surfaces.

The review of previous reports in literature (Ma *et al.*, 1999; Ross *et al.*, 1988; Weidler *et al.*, 1998; Watt-Smith *et al.*, 2005) clearly indicate that the effect of fractals on mass transfer such as in gas adsorption on a fractal surface have not been properly tested. The testing of the FHH theories has predominantly used nitrogen as an adsorptive. It is entirely possible that the FHH theories may not apply to the nitrogen –silica system but may apply for a different adsorptive or range of adsorptives. The work of Watt-Smith *et al.* (2005) has validated the use of the FHH theory to describe butane adsorption on silica, and as butane and cyclohexane have similar affinity for silica this analysis will further test the theory.

It is the purpose of the work described here to compare the surface fractal dimensions obtained from the fractal FHH analysis of butane and cyclohexane adsorption on P123 and F127 templated solids and for C10 silica pellets, with those obtained completely independently using small angle X-ray scattering.

5.2.4 - The Fractal Approach In Relation To the Energy of Interaction

A "compensation effect" also known as the theta rule has been defined by Schwab in 1983, and is evident in the application of the Arrhenius equation, as shown in Equations 5.8 and 5.9.

$$k = k_0 e^{-E/RT} \quad \textbf{(5. 8)}$$

or

$$\ln k = B - \frac{E}{RT} \quad \textbf{(5. 9)}$$

This effect can be used to rate processes especially in the case of heterogeneous catalysis, when a linear relationship is found between the parameters B (= ln k_o) and E of the form

$$B = mE + c \quad \textbf{(5. 10)}$$

Studies by Gwaley (1977), (1983); Conner (1983); and Rooney (1985) have all observed this compensation effect for a range of heterogeneous catalytic reactions. This effect has also been reported for the adsorption of gasses on microporous carbons (Fletcher *et al.*, 2000). The work of Harding *et al.* (1998) relates the observation of this effect on the mechanism of adsorption of water in microporous carbons. However, it has been argued that this effect is a direct consequence of the Arrhenius equation. The work of Rigby (2002), suggests that fractal properties of certain porous media can be used to explain the compensation effect observed in rate studies of the diffusion of benzene

molecules on their internal surfaces. The translational motion of benzene molecules on the surfaces of a number of different types of materials, such as a silica catalyst, was studied using deuteron NMR techniques. When the temperature dependence of the correlation time for this motion was correlated using an Arrhenius type expression, it was found that a compensation effect was observed. This means that there was a linear relationship between the activation energy and the natural logarithm of the pre-exponential factor. The origin of this effect was explained by a theory for the molecular motion based on the fractal nature of the surfaces over which the benzene molecules are moving. The main physical processes taking place during adsorption or heterogeneous catalysis, such as diffusion of adsorbed species, occur close to or directly on the surface of the adsorbent or catalyst hence it is extremely important to be able to characterize the nature of the surface and its effect on the interactions between adsorbed molecules and the adsorbate surface.

A theory that proposes how the surface geometry of a solid influences the heat of adsorption is therefore presented. It assumes that at monolayer coverage the heat of adsorption required for the translational motion of a molecule adsorbed at a particular site consists of a component arising from the adsorbent interactions with the surface beneath the molecule (E_s) and another from its dependency on the number of neighbouring molecules, (n) such that the total heat of adsorption E, is given by the expression:

$$E = E_S + n\varepsilon \qquad \textbf{(5. 11)}$$

Where E_s is the contribution to the activation energy from the surface and n is the contribution to the activation energy from a single neighbouring molecule. As stated above, the number of sites at which molecules may be adsorbed within a particular region of a sample is directly proportional to the local surface area accessible by the specific molecules in question. Hence, on a fractal surface the number of nearest neighbours is given by:

$$n = \left(\frac{R}{r}\right)^d - 1 \quad \textbf{(5. 12)}$$

where R is the distance from the center of one molecule to the outside edge of a neighbouring molecule, hence $\left(\frac{R}{r}\right)^d = (1.5)^d$. Hence, if Equation 5.12 is substituted into Equation 5.11, the following expression (equation 5.13) for the variation of the total activation energy with the surface fractal dimension and hence surface roughness is obtained.

$$E = (Es - \varepsilon) + \varepsilon\left(\frac{R}{r}\right)^d \quad \textbf{(5. 13)}$$

The heat of adsorption should thus be a linear function of $\left(\frac{R}{r}\right)^d$. An estimate of the heat of adsorption can be obtained from the net heat of adsorption in the BET constant, given by the relationship:

$$\left(E = RT \ln C_{(BET)}\right) \quad \textbf{(5. 14)}$$

5.2.5 - Experimental Procedures

Butane adsorption isotherms were obtained for a range of silica solids: the commercial C10, C30, S980G sol gel silica pellets and the P123 and F127 surfactant templated solids, while cyclohexane adsorption was run on the templated solids as well. The SAXS characterisation of the surfactant templated materials $P123_t$, and $F127_t$ were performed by Prof. R. Richardson, of the Dept. of Physics, University of Bristol. They were ran as powder samples in glass X-ray capillaries. Whilst the commercial silica pellets were run by Dr Karen Edler, of the Dept. of Chemistry, University of Bath, at the European Synchrotron radiation facility (ESRF). The SAXS patterns were collected by a technique of suspending the pellets behind a collimating pinhole in the sample position on the DUBBLE beamline on BM26B. The quoted cross-sectional area, σ, of a

butane molecule (0.469 nm^2) and cyclohexane (0.321 nm^2) (Lowell and Shields 1984), and have been used to calculate the BET surface area and appropriate length-scale limits for the fractal dimensions obtained from butane and cyclohexane adsorption. A two-dimensional detector (energy of 15.0 keV) and a sample to detector distance of 3.350 m were used. The pattern was radially averaged over the detector area, and corrected for detector response and the sample transmissi on using a software package called BSL. Several different pellets from the same batch of pellets were run to identify variations in the scattering due to this sampling procedure. The two-dimensional patterns were corrected for detector efficiency, calibrated against silver behenate and pixels at the same radius were averaged to produce one-dimensional patterns. Scattering from an empty capillary was subtracted from the samples run at Bristol to remove background scattering.

5.2.6 - Results

Butane adsorption isotherms were obtained for all test samples and analysed using the BET equation to obtain the BET monolayer coverage, and then applied to the FHH analysis of the fractal dimensions of the range of test materials (C10, $P123_t$, $F127_t$, S980G and C30). Examples of the steps followed and subsequent graphs of the adsorption data and the fit of the FHH equation for the silica materials are shown below in Figures 5.11 – 5.22.

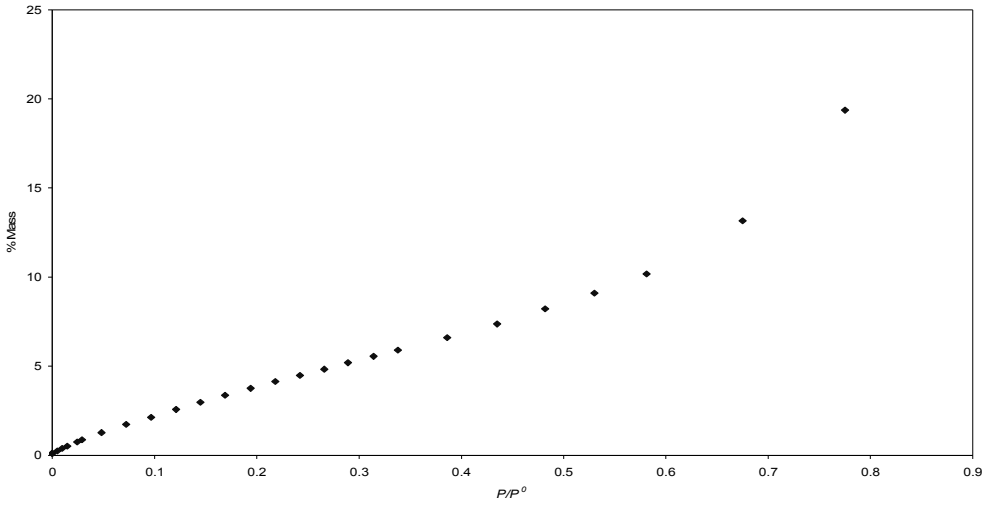

Figure 5.11: C10 Butane Adsorption Plot of Mass % Vs Relative Pressure at 0 °C.

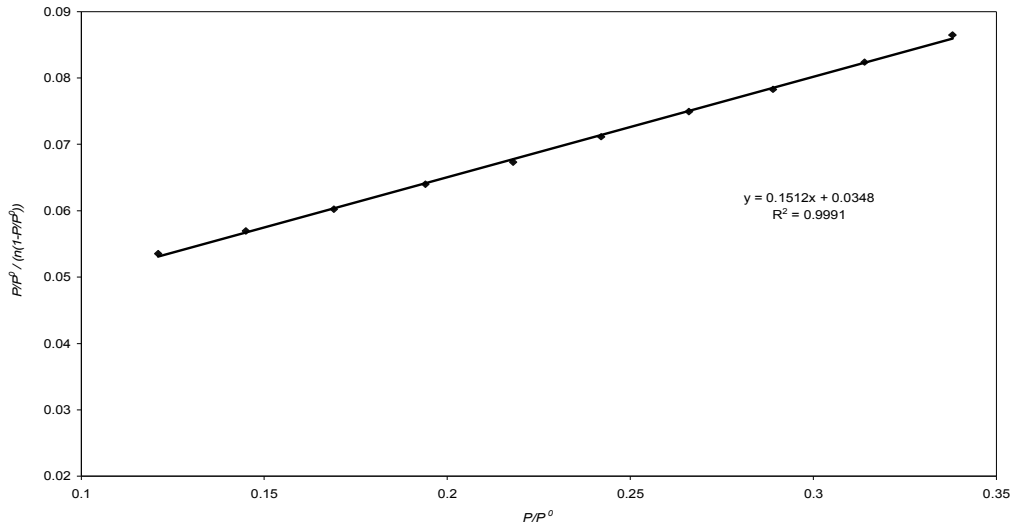

Figure 5.12: BET plot of [(P/P^0)/ ($n\ (1-P/P)$)] Vs. P/Po for C10 Silica Pellets.

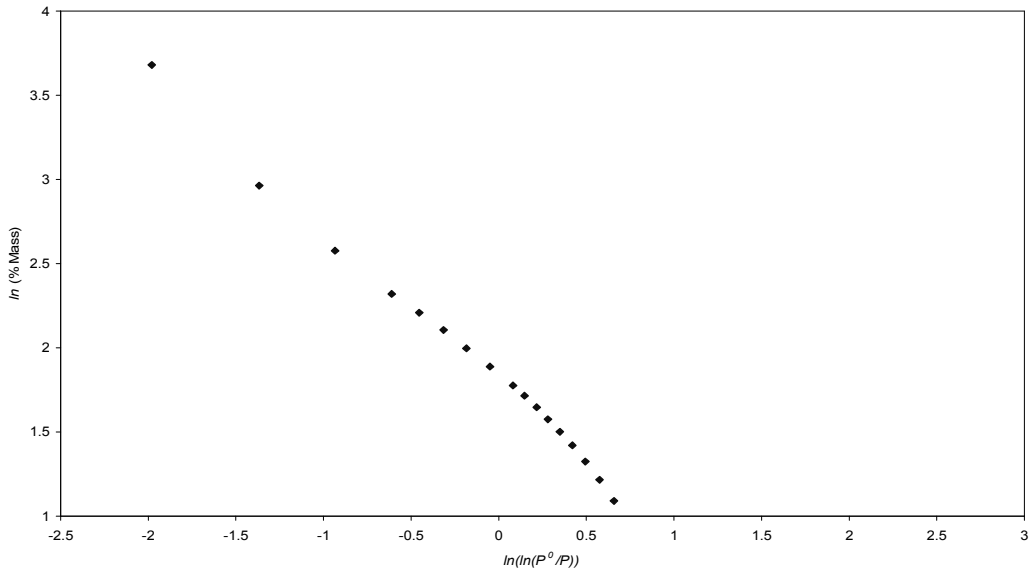

Figure 5.13: The FHH Plot of *ln* (% mass) Vs. $ln\ (ln\ (P^0/P))$ for C10 Silica Pellets.

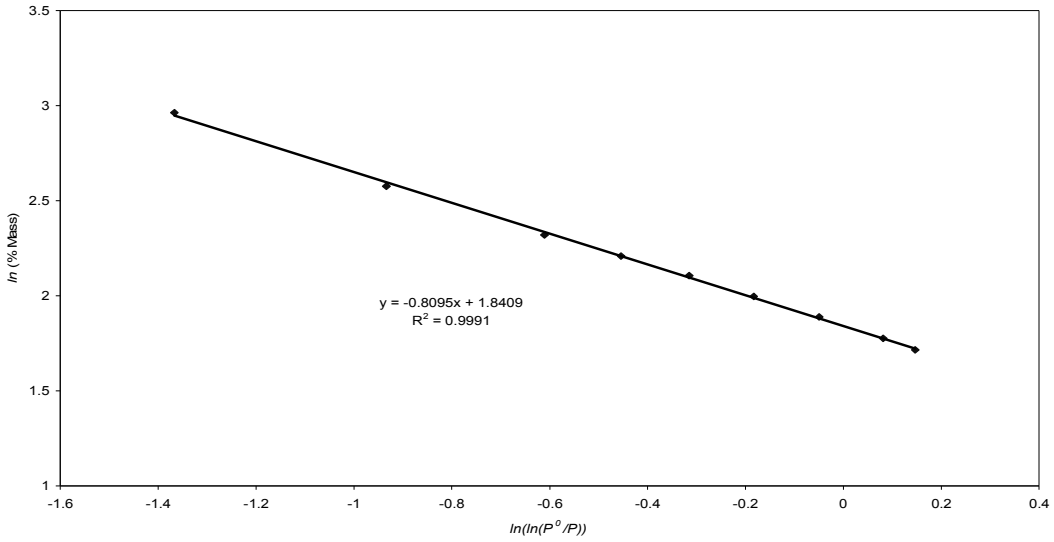

Figure 5.14: The FHH Plot of *ln* (% mass) Vs. *ln (ln (P^0/P))* fitting 5.5, %mass < 19.3 for C10 Silica Pellets.

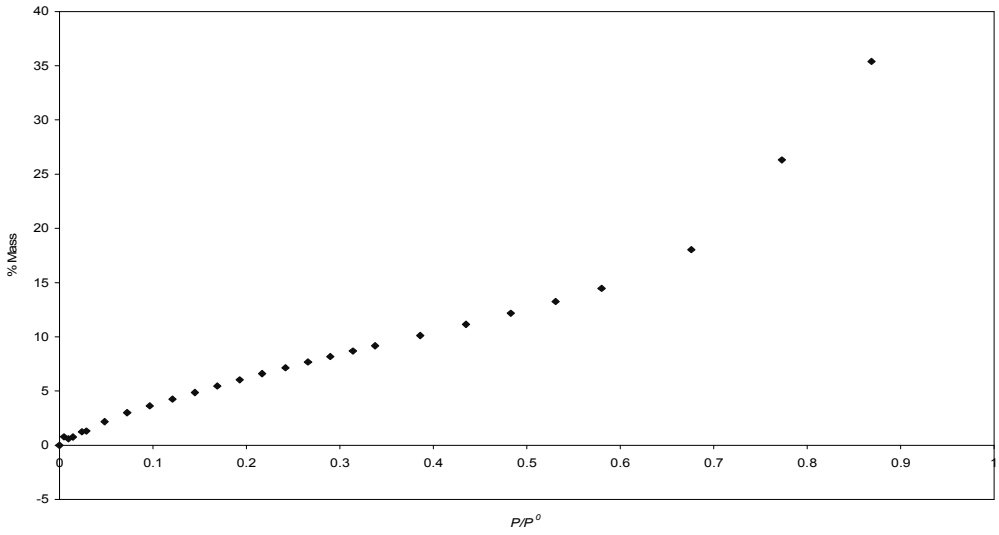

Figure 5.15: P123 Butane Adsorption Plot of Mass % Vs Relative Pressure at 0 ^{o}C.

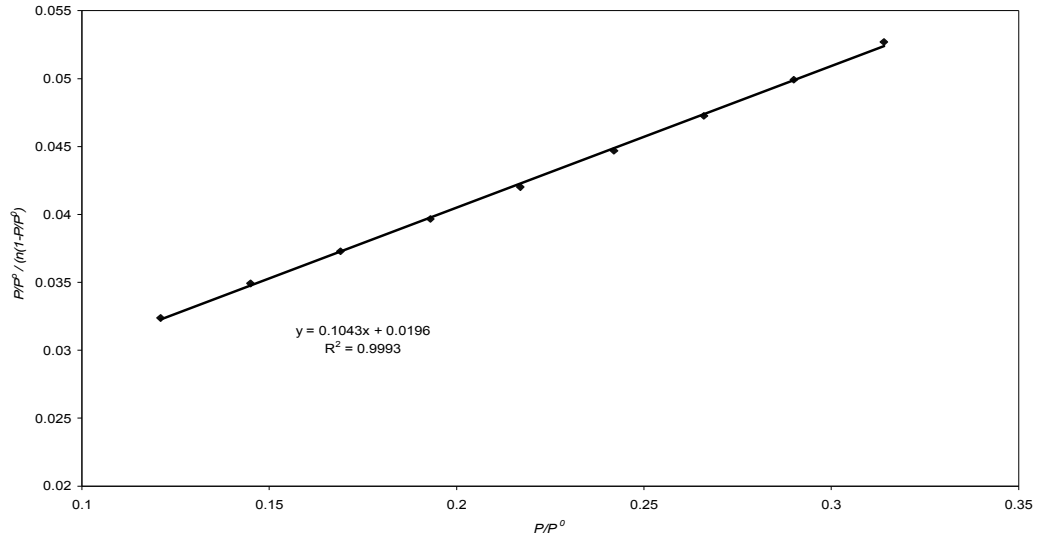

Figure 5.16: BET plot of $[(P/P^0)/ (n (1-P/P^0))]$ Vs. P/P^0 for P123 core.

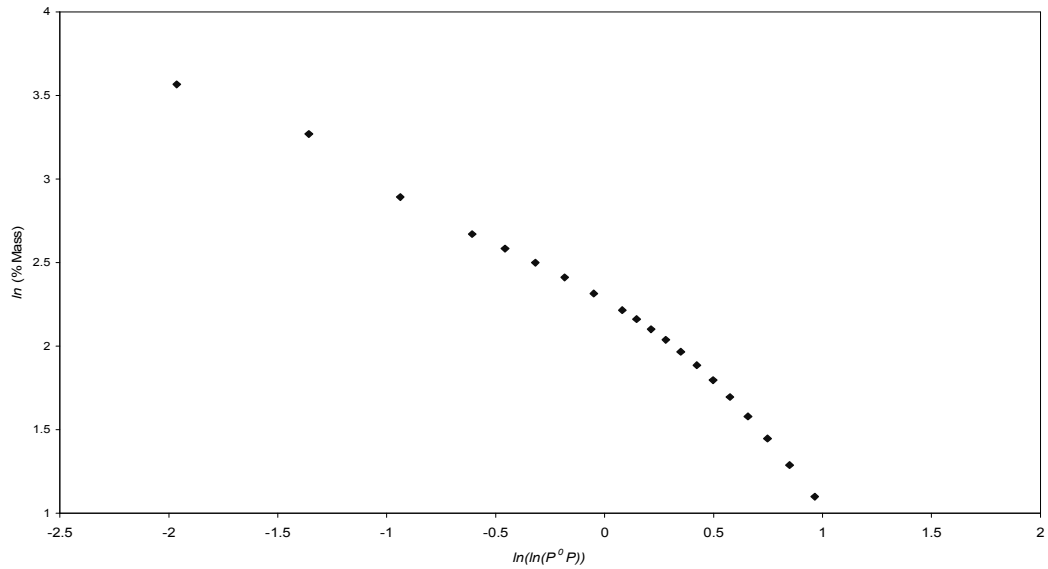

Figure 5.17: The FHH Plot of *ln* (% mass) Vs. *ln (ln* $(P^0/P))$ for $P123_t$ core.

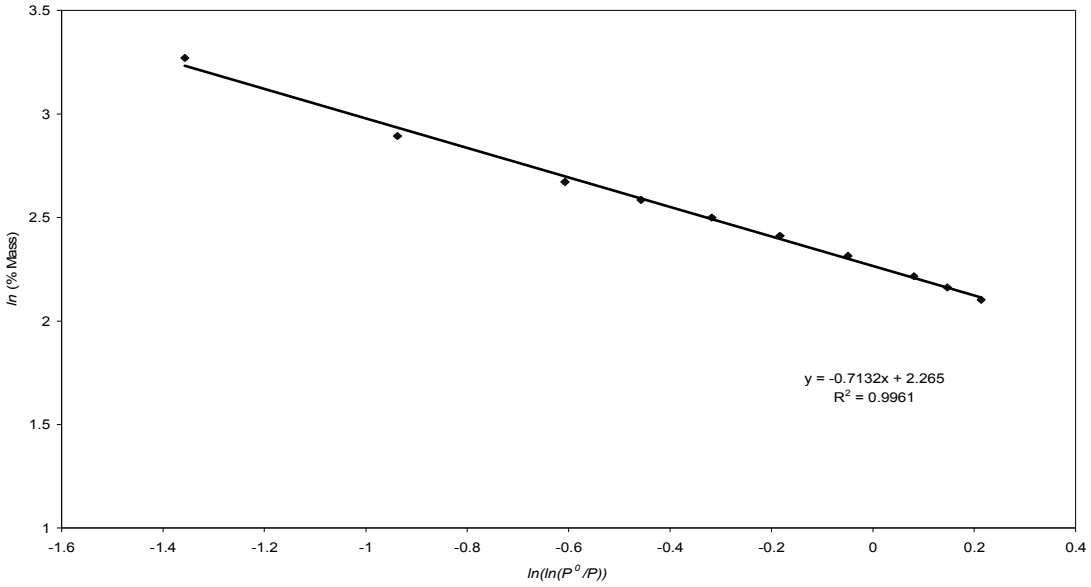

Figure 5.18: The FHH Plot of *ln* (% mass) Vs. *ln (ln (P^0/P))* fitting 8.18, %mass < 26 for $P123_t$ core.

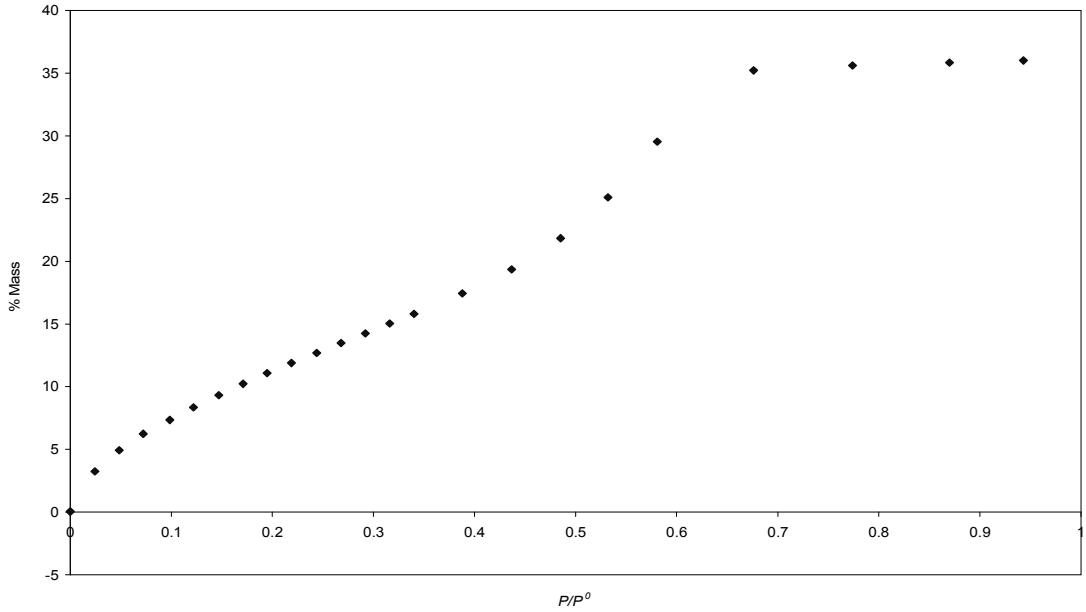

Figure 5.19: $F127_t$ Butane Adsorption Plot of Mass % Vs Relative Pressure at 0 ^oC.

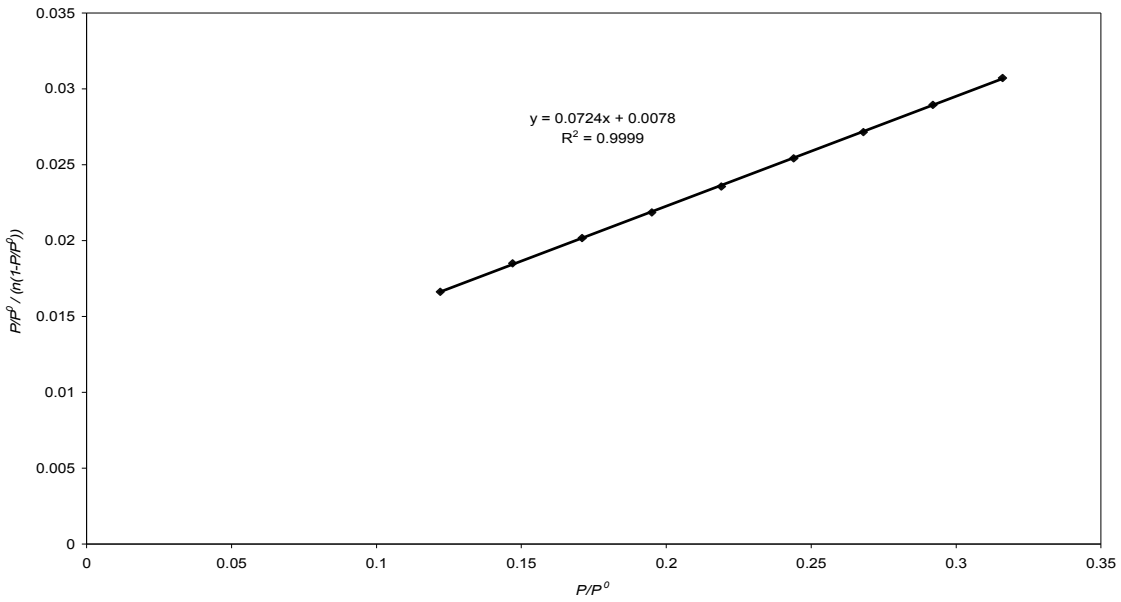

Figure 5.20: BET plot of $[(P/P^0)/ (n (1- P/P^0))]$ Vs. P/P^0 for $F127_t$ core.

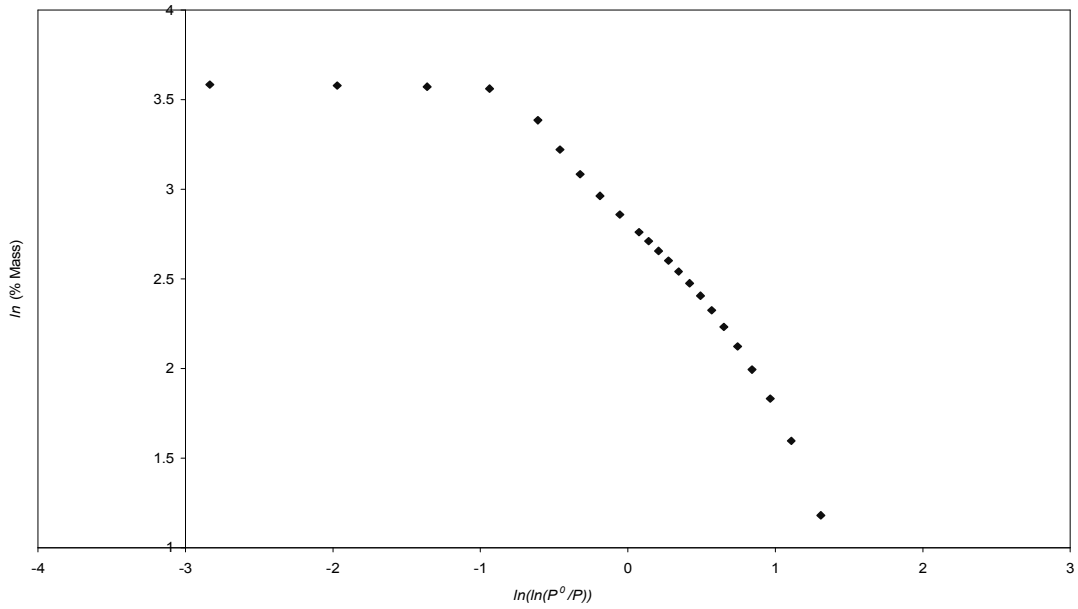

Figure 5.21: The FHH Plot of *ln* (% mass) Vs. *ln (ln* (P^0/P)*)* for $F127_t$ core.

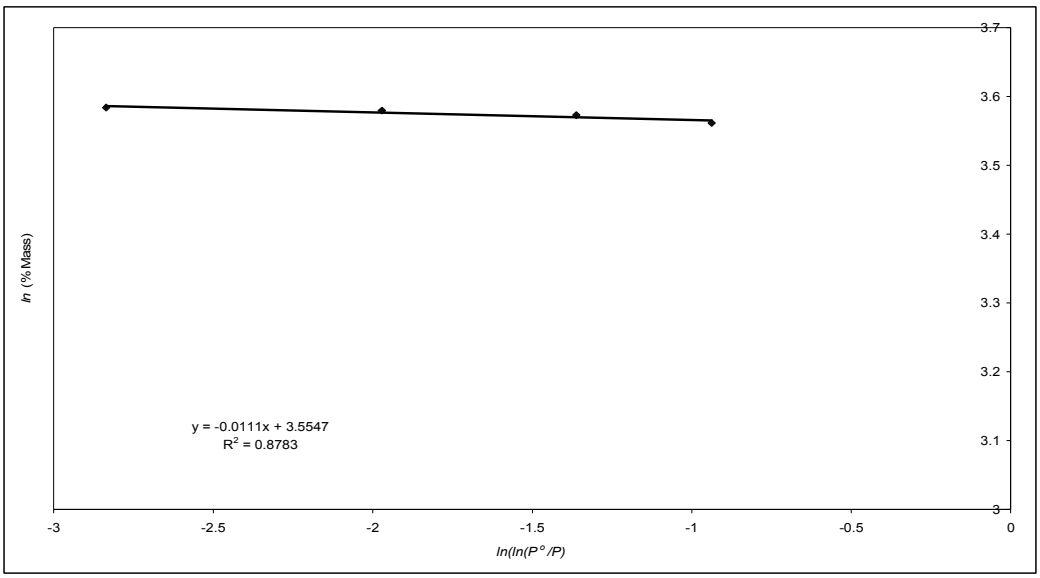

Figure 5.22: The FHH Plot of *ln* (% mass) Vs. *ln (ln (P^0/P))* fitting 35%mass < 36 for $F127_t$ core.

Table 5.1: Showing the results of the steps involved in the application of the FHH theory to Butane adsorption data / Comparison of $d_{(FHH)}$ Butane and $d_{(FHH)}$ Cyclohexane for $P123_t$ and $F127_t$.

Sample	***n_m monolayer coverage (mmol/g)***	***$C_{(BET)}$***	***Fitted P/P^0 range***	***R^2***	***BET surface area (m^2/g)***	***$d_{(FHH)}$ Butane***	***$d_{(FHH)}$ Cyclohexane***
C10	5.375 ± 0.0018	5.343 ± 0.002	0.1 - 0.34	0.9991	261.258 ± 0.113	2.191 ± 0.009	N/A
$P123_t$ Core	8.069 ± 0.0012	6.309 ± 0.0014	0.1 - 0.31	0.9993	392.197 ± 0.175	2.322 ± 0.001	2.262 ± 0.004
$F127_t$ Core	12.468 ± 0.0008	10.312 ± 0.0009	0.1 - 0.31	0.9999	605.961 ± 0.369	2.989 ± 0.002	2.977 ± .0000002
S980G	0.223 ± 0.001	9.032 ± 0.002	0.1- 0.31	0.9997	100.838 ± 0.169	2.580 ± 0.004	N/A
C30	0.321 ±0.005	2.934 ± 0.002	0.1-0.25	0.9979	150.601 ± 0.143	2.408 ± 0.001	N/A

Table 5.2: Showing calculated values of the energy of activation (E), the fractal dimension and $(R/r)^d$ for Butane

Sample	***E (j/mol)***	$d_{(FHH)}$ ***Butane***	$(R/r)^d$
C30	2443.053	2.408	2.986
C10	3803.798	2.191	2.430
$P123_t$ Core	4180.962	2.322	2.564
S980G	4995.145	2.580	2.964
$F127_t$ Core	5296.082	2.988	3.360

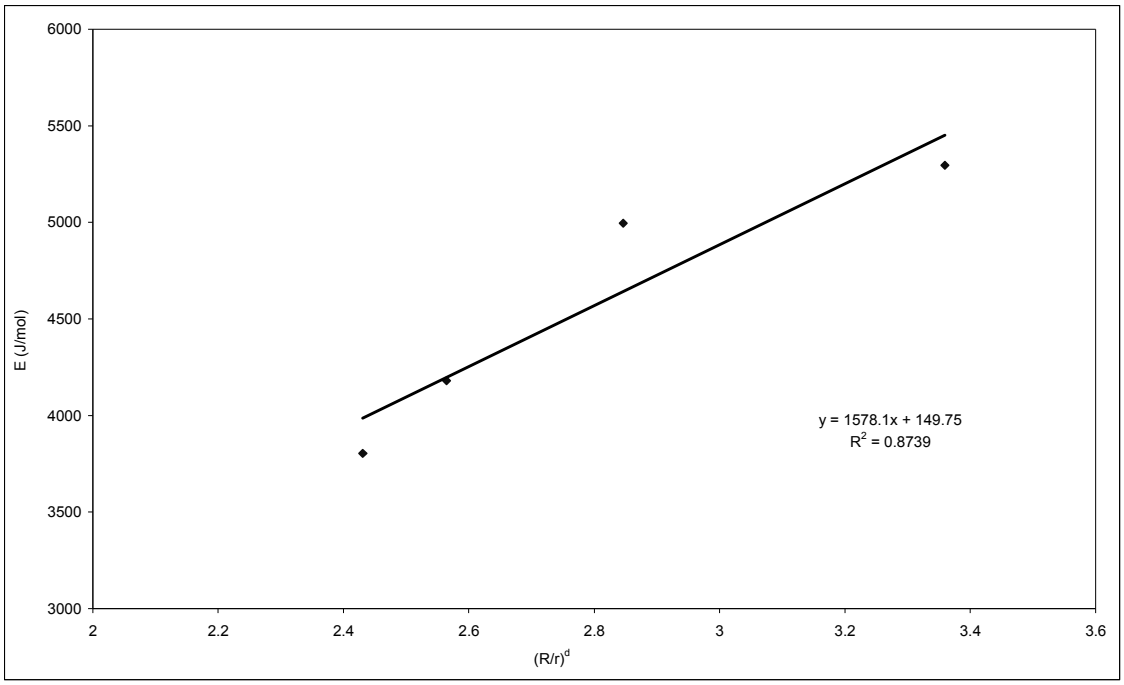

Figure 5.23: A plot of E vs. $(R/r)^d$ for C10, $P123_t$, S980G and $F127_t$, showing a linear relationship.

The isotherms were initially analysed using the BET equation to obtain the BET monolayer coverage, which is shown in Table 5.1 along with the calculated fractal dimensions obtained from the FHH analysis for the silica materials from both butane

and cyclohexane adsorption. The fitted length-scale ranges that the FHH theory of fractals applies to are also shown in Table 5.1.Table 5.2 shows the measured molar net enthalpy of adsorption, for the silica-butane systems tested within this research. The energy of activation was obtained by the use of Equation 5.14, and Figure 5.23 shows a linear relationship between the calculated energy of activation and the FHH fractal dimensions of the sort that a higher fractal dimension results in a higher energy of activation.

Rigby (2005) showed that for SO_2 adsorbed upon a variety of different surfaces, both the characteristic heat of adsorption and the activation energy for surface diffusion are predominately determined, by the surface geometry of the substrate. The author proposed a theory for the surface diffusion of gases adsorbed onto heterogeneous surfaces, which predicts that both the pre-exponential factor and the activation energy from the Arrhenius expression for the surface diffusivity, at monolayer coverage are particular functions of the surface fractal dimension. The fractal dimensions of the C10 and C30 sol gel mesoporous samples ~2.24 and 2.3 respectively, match closely except for that of S980G ~2.5 which has a quoted value of 2.5 (Watt-Smith *et al.*, 2005). As a result, further testing is required to add to the reliability of any theories proposed. An alternative method is therefore proposed within this work for use in future investigations of the link between the heat of adsorption and the fractal dimension, and will be the subject of future work.

5.2.6.1 - SAXS Analysis Results

The fractal analysis of SAXS data obtained for $F127_t$, $P123_t$ run 1 (uncalcined sample) and $P123_t$ run 2 (calcined sample) was used to estimate the surface fractal dimensions of these materials and for the validation of the FHH fractal theories of gas adsorption on fractal surfaces. The graphs of the fit of the SAXS data are shown in Figures 5.24 – 5.29.

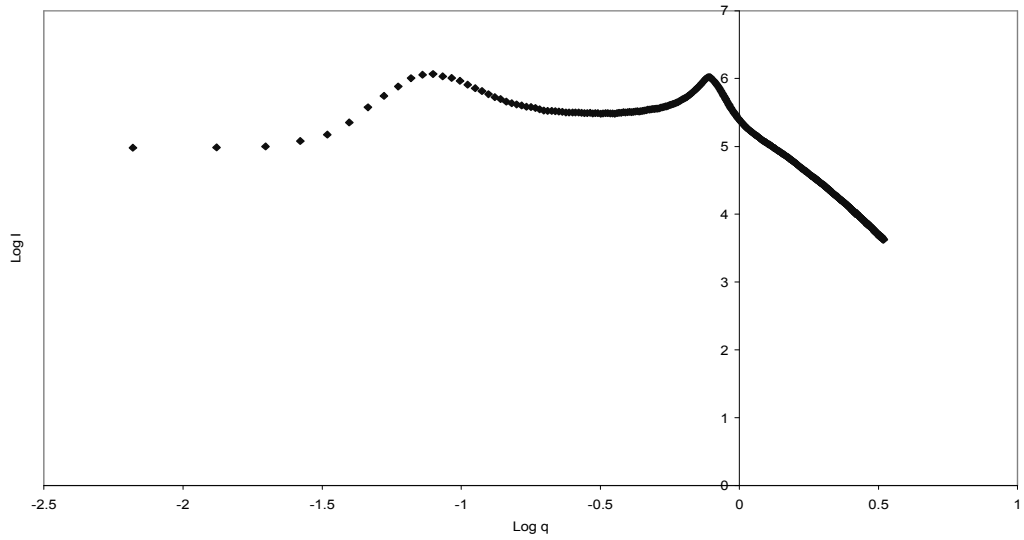

Figure 5.24: F127$_t$ Log I vs. Log q (all inclusive).

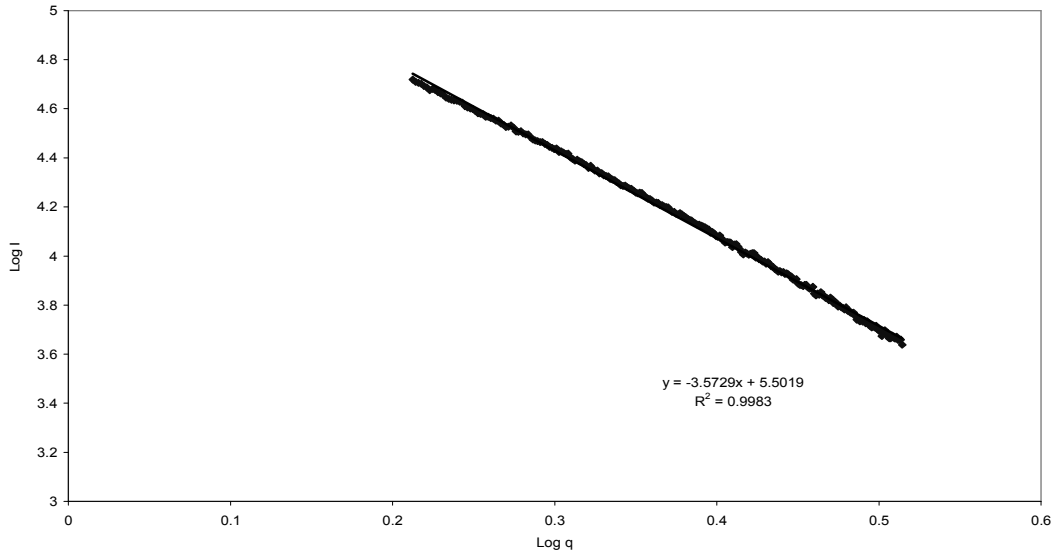

Figure 5.25: F127$_t$ log I vs. Log q for Log I = 3.68-4.92.

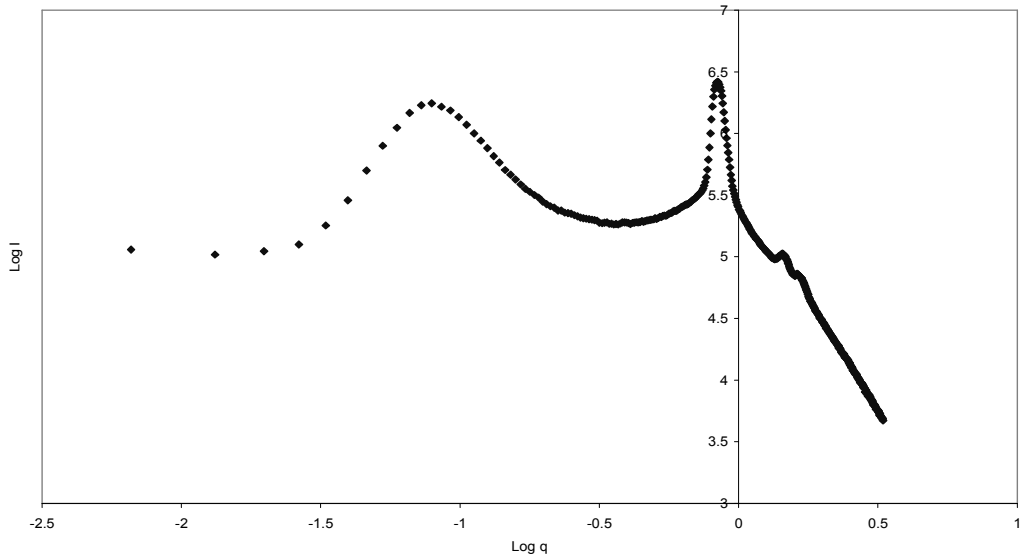

Figure 5.26: P123$_t$ run 1 Log I vs. Log q (all inclusive).

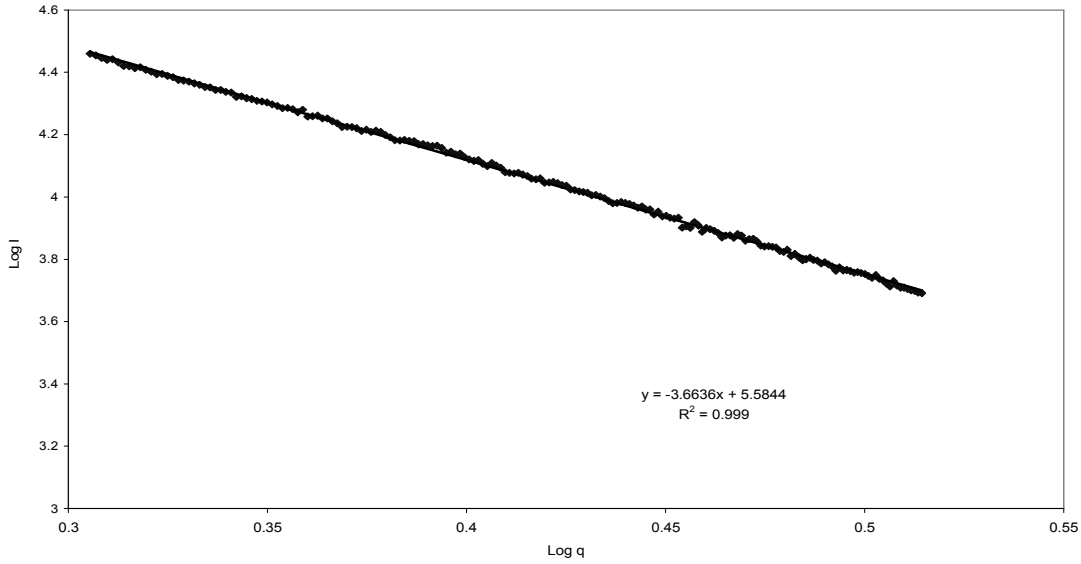

Figure 5.27: P123$_t$ run 1 log I vs. Log q for Log I = 3.69-4.45.

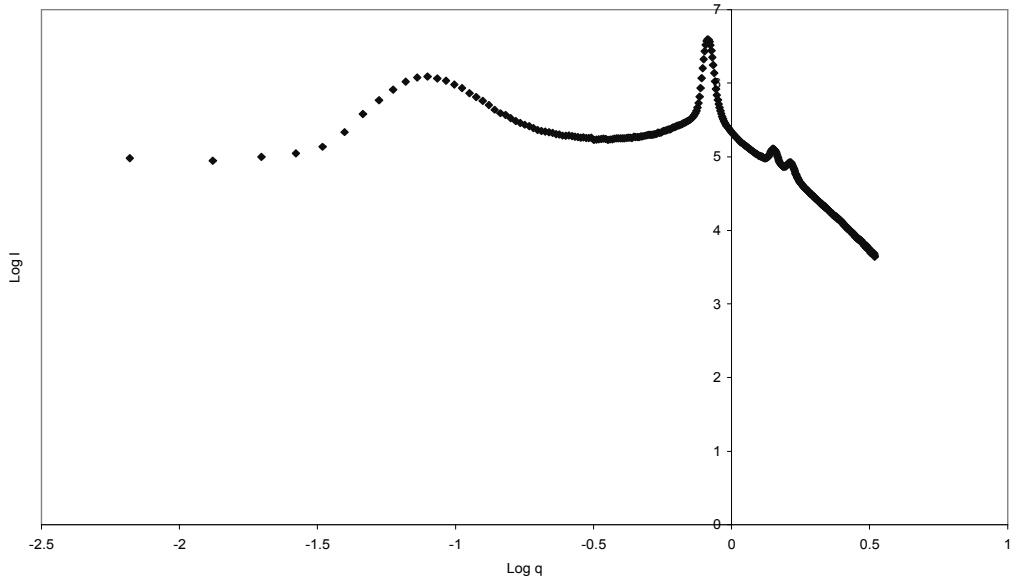

Figure 5.28: P123$_t$ run 2 Log I vs. Log q (all inclusive).

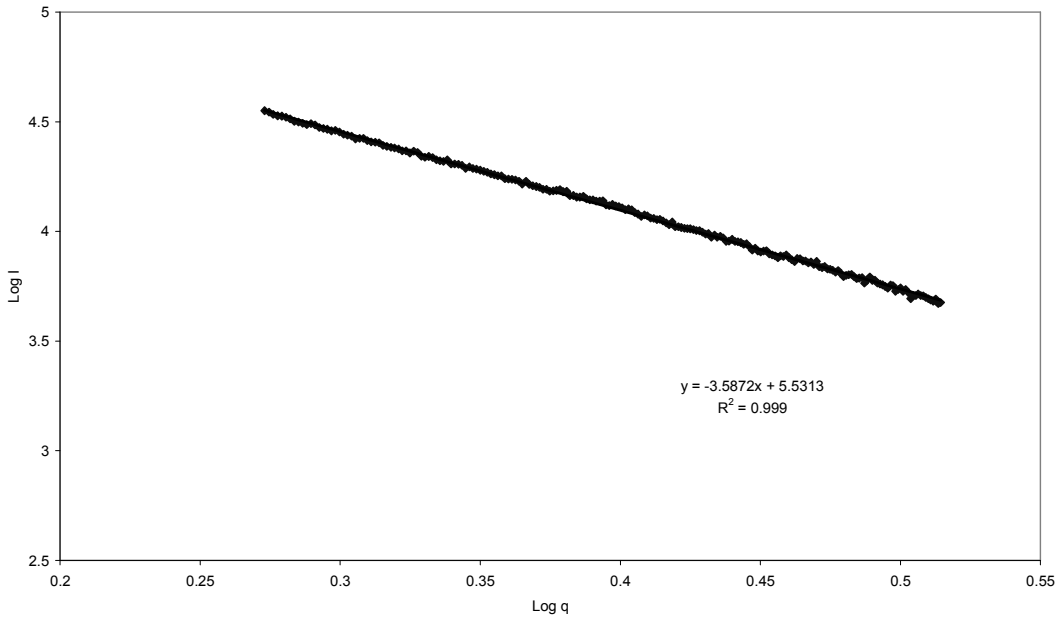

Figure 5.29: P123$_t$ run 2 log I vs. Log q for Log I = 3.69-4.45.

Table 5.3: Showing a comparison for the SAXS and FHH results

(- referenced from Watt-Smith et al., 2005)*

SAMPLE	$d_{(SAXS)}$	$d_{(FHH)}$ ***Butane***	$d_{(FHH)}$ ***Cyclohexane***
C10	*2.24	2.190	N/A
	± 0.11	± 0.009	
$P123_t$ Core run 1	2.336	N/A	N/A
	± 0.008		
$P123_t$ Core run 2	2.405	2.322	2.262
	± 0.009	± 0.001	± 0.004
$F127_t$ Core	2.427	2.989	2.977
	± 0.009	± 0.002	± .0000002
S980G	*2.49	2.580	N/A
	± 0.001	± 0.004	
C30	*2.30	2.408	N/A
	± 0.005	± 0.001	

The resulting fractal dimensions based on the SAXS technique are compared to those obtained using the FHH analysis using cyclohexane and butane adsorption, as shown in Table 5.3. The variation in the SAXS measurements, and the gas adsorption could be linked to the fact that the samples for gas adsorption typically consisted of 3 - 4 individual pellets, whereas the samples for SAXS consisted of only a single pellet. The FHH theory cannot be applied to the uncalcined sample, as the blocked pores will make adsorption impossible.

5.2.7 – Discussion

The similarities between the fractal dimensions obtained from the butane adsorption and those obtained from SAXS suggest that the adsorption of butane on the fractal surfaces of various different silica materials is consistently well described by the fractal FHH. One could have guessed that the SAXS fractal dimension for the uncalcined will be less

than the calcined, as burning out the surfactant will open up pores and may even lead to fractures or roughness, and as a check, this can be confirmed from the results shown in Table 5.3. It is well known, that whereas some adsorptives such as nitrogen may show some specific adsorption on the surface of hydroxylated silicas, butane is unlikely to show any specific adsorption (Gregg and Sing, 1982; Rouquerol *et al.*, 1999), and similarly so for cyclohexane. This is most probably the reason why the fractal dimensions measured by the use of the FHH theory for the synthesised porous materials match closely for butane and cyclohexane adsorption data, indicating that the adsorption of both butane and cyclohexane on rough silica surfaces are similar, and well described by the FHH fractal theory.

There is only a slight variation, in the trends of both FHH and SAXS data, as opposed to the disagreement reported in literature (Ma *et al.*, 1999; Ross *et al.*, 1988;) of scattering data and FHH analysis of nitrogen adsorption data. The results here are in agreement with the work of Watt-Smith *et al.* (2005), where they observed good agreement between the fractal dimensions obtained from SAXS and those from the application of the fractal FHH equation to butane adsorption isotherms. This suggests that the surface tension of hydrocarbons such as butane and cyclohexane may be, relatively, much stronger than nitrogen. This is consistent with the lower strength of interaction (and hence lower values of the BET constant) for butane and cyclohexane compared to nitrogen, on partially dehdroxylated silicas, as shown by the shapes of their respective adsorption isotherms which can be seen in Figures 5.11, 5.15 and 5.19 for butane, and in Appendix B for nitrogen adsorption. Both selective specific adsorption on an active heterogeneous surface and the fractality of the surface can cause a decrease in the number of adsorption sites available in progressively higher levels within the adsorbed multilayer. As butane is not known to exhibit selective specific adsorption, further research is required to ascertain whether the difference observed between the fractal dimensions obtained from butane adsorption and SAXS, is a result of one or both of the above effects giving rise to a decrease in the number of adsorption sites and thus leading to an overestimation of the fractal dimension. Watt-Smith *et al.* (2005), reports an experimental study of gas adsorption on fractal surfaces, where the deviation between the scattering and adsorption data for nitrogen on a range of silica pellets exhibited a trend where the deviation is always such that the fractal dimension obtained from

adsorption is higher than that obtained from SAXS. This sort of deviation was attributed to the above theory.

Since the simulation studies of Ma *et al.* (2001, 2002) suggested that cross-over effects from the van der Waals (substrate potential)-dominated to the capillary condensation-dominated domains is the cause of the deviation between the scattering and adsorption data, such that the fractal dimension from adsorption is lower than that from scattering. Therefore, then, if the observed deviation for butane adsorption occurs in the opposite direction for the test samples analysed within this research, then a different explanation is required to account for the variation. However, as can be seen from Table 3.3, the variations observed are in both directions with $d_{(saxs)}$ for $P123_t$ being higher and that of $F127_t$ being lower than $d_{(FHH)}$. There is no possible explanation in literature for a variation in either of the two paths and since the variation is quite minimal it can be attributed to experimental errors and the differences in the applications of both techniques.

5.2.8 - Conclusion

It can be concluded that the log-log fractal plots are useful for the correlation of adsorption data, and especially on ordered mesoporous materials with well-defined pores. A fractal dimension can also serve as a characteristic empirical parameter for test samples under similar operational conditions. The surface fractal dimensions measured from butane and cyclohexane adsorption are closely related, within experimental error to those obtained from SAXS for silica materials suggesting gas adsorption in these systems is consistently well described by the FHH fractal theory and hence in agreement with the work of Watt-Smith *et al.* (2005). The fractal dimensions have been shown to have a direct relationship with the energy of activation (molar net enthalpy of adsorption), in which a higher fractal dimension leads to a high net molar energy for the samples analysed within this research, and could provide valuable information towards comparative studies of model porous solids under similar conditions.

Chapter 6: Mercury Porosimetry

6.1 - Introduction

Mercury Porosimetry is a method currently used extensively in the petroleum industry, to characterise various aspects of porous materials. It enables the determination of the pore volume, the specific surface area and the pore size distributions (the distributions of pore volume and surface area versus the pore size). The relative performance of different porous solids in several applications is highly dependent on their internal pore structure, and in order to better predict a particular process taking place within a porous medium it is necessary to have a detailed knowledge of the internal geometry and topology of the internal pore network. As early as 1842, Smetana drew attention to the possibility of forcing mercury into wood, to obtain a kind of 'fingerprint' of its porous structure. Washburn (1921) later suggested how a pore size distribution could be obtained from pressure-volume data for mercury penetration into a porous media. The first article to be devoted to the science of mercury porosimetry and showcasing a large quantity of experimental data was later published by Ritter and Drake (1945), and it forms the basis of all subsequent developments. This technique is based on the principle that mercury behaves as a non-wetting liquid towards most substances and consequently does not penetrate into the openings and cracks of these substances unless pressure is applied. If a sample of a porous solid is sealed in a vessel and placed in a capillary tube, evacuated and filled with mercury, a pressure increase will result in mercury penetration into the pores and its level in the capillary will decrease. A plot of the decrease of mercury in the capillary in relation to the pressure produces a retraction curve, which indicates how large a volume penetrated into the pores of the sample at a given time. These curves are useful in interpreting pore geometry and give information which is valuable in assessing multiphase fluid behaviour in oil and gas and, in a strongly water wet system, the trapping of oil or gas is controlled mainly by capillary forces and thus a direct analogy with the air-mercury system is possible. The migration of non-wetting fluids within porous media is also of great interest in areas such as soil remediation.

6.2 - Theory and Background

Mercury porosimetry assessment of porous media favours macroporosity (>50nm diameter) and larger mesoporosity (4 - 50nm), and it has been used extensively as a technique for characterising void spaces. In 1986 Yaun and Swanson pioneered a method for estimating pore sizes by monitoring capillary pressure at a constant injection rate. They reported fluctuations of capillary pressure as responses to pore sizes which could then be estimated. Wardlaw and McKellar (1981) adopted a conventional (pressure controlled) method of measuring capillary pressure curves for polished surfaces of epoxy injected rocks in order to obtain throat and pore size information from mercury intrusion and extrusion curves respectively. Pore sizes derived from the extrusion curves were shown to match those measured independently by a direct method. The volume of mercury V penetrating the pores is measured directly as a function of applied pressure. This P-V information serves as a unique characterisation of pore structure. The smaller the size of the pores, the higher the pressure required to force mercury into the pores of most materials. The Washburn equation relates the pressure to pore size:

$$P = \frac{2\gamma \cos\theta}{r} \qquad \textbf{(6. 1)}$$

Where: P = The Pressure at which mercury enters the pore radius (Pa).

r r = the cylindrical pore radius (m).

γ = The surface tension of mercury (0.485 Nm^{-1})

θ = The contact angle between the mercury meniscus and the solid surface

The quoted surface tension of mercury varies in the range 410-515 mNm^{-1}. For strongly curved surfaces the surface tension is a function of curvature. This equation assumes γ and θ are constants, which is not the case, because,

- They may vary with pore size.
- They may vary with the nature of the surface irregularities.
- θ varies for receding and advancing mercury.

Mercury porosimetry can therefore be used to obtain the pore size distribution and pore volume of a porous medium. Pore size is directly calculated from the corresponding

pressure values using the Washburn equation with the chosen values of surface tension and mercury contact angle (0.485 Nm^{-1}, 148 ^{o} respectively). The surface or interfacial tension of mercury contributes greatly with respect to errors in the determination of the pore size distribution (Schuth *et al.*, 2002). A value of 0.485 Nm^{-1} at 25 ^{o}C is commonly used by most researchers, and temperature has only a minor effect on the surface tension. A temperature coefficient of –0.00021 $Nm^{-1o}C^{-1}$, which means that a temperature change between 25 to 50 ^{o}C would cause only a change of about 1 % for the calculated pore size (Allen, 1997). An accurate estimation of the contact angle between mercury and the corresponding solid sample is very important as the surface roughness of the sample could increase the effective contact angle for advancing/receding mercury in a pore (van Brakel *et al.*, 1981). Pore size distribution data resulting from mercury porosimetry is very useful for interpreting the pore structure of materials, and especially in the comparative study of similar materials. The accuracy of porous media characterisation data obtained from mercury porosimetry has been discussed by several researchers such as Wardlaw and McKellar (1949); Drake (1949); Schuth *et al.* (2002); and Bhatia *et al.* (2001). The general consensus is that it is in agreement with data obtained through other methods and in general pore sizes and volume are repeatable to better than 1 % standard deviation.

Mercury extruding from pores upon reduction of pressure is in general accord with Equation 6.1, but indicated pore diameters are always offset toward larger diameters. This results from equivalent volumes of mercury being extruded at pressures lower than those at which the pores were intruded. It is also commonly observed that actual pores always trap mercury. The first phenomenon is usually attributed to receding contact angles being less than advancing ones. The second is likely due to pore irregularities giving rise to enlarged chambers and “ink well” structures. These phenomena give rise to hysteresis phenomena, i.e., distinct intrusion and extrusion *P-V* curves.

6.3 - Interpretation of the Basic Phenomena Involved in Mercury Porosimetry

A comparative study of gas adsorption and mercury porosimetry will highlight the similarities in the application of the two probing techniques, which could help provide additional support towards the viability of the pore-size characterisation results obtained. Both methods could be considered to depend on the modification of a phase diagram of a pure substance within a confinement, and for each of them the equations and model derived are based either on statistical approaches or thermodynamics. Often the derivation of pore size distribution is obtained based on the assumption that the porous system is made up of non-connected cylindrical pores, whereas the actual complexity of the pore structure is evident in the hysteresis shape. Further to this, a comparison of the varying sample analysis and their corresponding intrusion curves and gas adsorption isotherms, to the typical hysteresis loops of the IUPAC classification shows that the shape of the hysteresis loops obtained from the various methods reveals information on the mechanism of replacement of a phase by another within the porous system. Gas adsorption and mercury porosimetry are both widely accepted techniques used in characterizing porous solids with respect to their pore size, pore size distribution, pore volume and surface area. However, gas adsorption and pore condensation, where the pore fluid wets the pore walls (contact angle $< 90^{o}$ is in contrast to mercury porosimetry where mercury is a non-wetting fluid (contact angle $> 90^{o}$) and (hydraulic) pressure must be applied to force mercury into the pores. Mercury porosimetry is more favourable based on its ability to perform pore size analysis over a wide range of pore sizes from about 0.003 μm up to about 400 μm. In addition, mercury porosimetry data can be interpreted in terms of particle size distributions, tortuosity factors, permeability, and compressibility, as well as to account for pore shapes and network effects in any porous solid. Information about skeletal and bulk density of the material can also be obtained via mercury porosimetry (Lowell *et al.*, 2004). Hence why, for several decades, mercury porosimetry has been used in characterising porous solids, and has proven to be of substantial value to industries dealing with catalysts and oil, ceramics, minerals, coals and soils.

Ritter and Drake (1945) first observed that mercury porosimetry displays hysteresis, and that it occurs when the pressure is reduced after mercury penetration; the pressure-

volume relationship is different for retraction than for penetration. There are two main causes of hysteresis in literature:

1. Structural hysteresis: This type of hysteresis is based on the features that conform to the general structure of the porous medium. Structural hysteresis encompasses the inkbottle theory and the percolation-connectivity. This is not evident in cylindrical homogeneous structures, but almost any three dimensional pore space will display structural hysteresis to an extent.

2. Contact angle hysteresis: This type of hysteresis is caused by the difference in the advancing and receding contact angle, and the resulting retraction curve will be different from the penetration curve. The possible effect of contact angle hysteresis and its importance has been supported by several researchers including (Kloubek, 1981), who gives convincing arguments that it is of importance in particular, because the work of Liasbaster and Orr (1978) showed hysteresis in mercury porosimetry of cylindrical pores.

Several methods exist to determine the contact angle, one of which is to place a drop of mercury on a flat surface of the sample and to visually observe the resulting contact angle. Clearly caution needs to be exercised with regards to contact angle estimation, as a slight variation has been reported to result in substantial differences in results Kloubek (1981), and Seaton *et al.* (1999). Recently Kloubek (1981) and Rigby (2002) obtained empirical correlations for the product $\gamma\cos\theta$ in the Washburn equation (Equation 6.1), from mercury porosimetry experiments on model porous materials with pore sizes already known by other means, such as electron microscopy. These correlations can be inserted into Equation 6.1 to give expressions of the form:

$$r = \frac{-A + \sqrt{(A^2 - 2pB)}}{p} \qquad \textbf{(6.2)}$$

where the values of the constants A and B depend upon the material under test, and whether the mercury meniscus is advancing or retreating. The values of A and B for silica are given in Table 6.1. As described above, the correlations for $\gamma\cos\theta$ are

empirical in origin, and are, therefore, strictly of limited range of applicability, and also contain experimental error (~4-5 % (Kloubek, 1981)). A more accurate solution for the pore radius can be obtained by using the semi-empirical method of analysis proposed by Rigby (2002) as an alternative to the Washburn equation, thereby eliminating the effects of contact angle hysteresis.

Table 6.1: Constants for Semi-empirical Alternatives to the Washburn Equation (Rigby *et al.*, 2004).

Material	$A.10^3$ **/(N.m^{-1})**	$B.10^{12}$**/N**	**Range of known validity /(nm)**
Silica (advancing meniscus)	-302.533	-0.739	6-99.75
Silica (retreating meniscus)	-68.366	-235.561	4-68.5

However, experimental studies have suggested that the primary reason for hysteresis in mercury porosimetry may be unrelated to changes in contact angle as several key observations made, could not be explained by contact angle hysteresis (Porcheron *et al.*, 2006) , such as;

1. The intrusion and extrusion curve should be shifted parallel to each other when using a logarithmic scale for the pressure or pore size axis.
2. When scanning between the hysteresis branches no change in volume should be observed.
3. The contact angle hysteresis fails to explain trapped mercury in the pore system after complete depressurization.

Other types of hysteresis have been reported, for example the hysteresis at high pressure, where mercury atoms get pushed into the crystal lattice. The mercury wetting can be irreversible due to adhesion to the walls at high pressures, and as a result after retraction, part of the imbibed mercury remains distributed as a film on the wall of the large pores (J. Van Brakel *et al.*, 1981). Schuth *et al.* (2002) also explained another form of hysteresis caused by the effects of pore geometry. Pore shape has a strong influence on the extrusion behaviour; the shape of a cylindrical pore closed at one end has no real effect on the intrusion behaviour. However extrusion will occur at a lower pressure in

the above type pore, in comparison to a cylindrical pore, which is open on both ends. Pores are rarely of uniform and well-defined shape, typically the throat is usually smaller than the actual cavity. Mercury will enter the cavity at a pressure determined by the entrance opening and not the actual cavity size. When this theory is taken within moderation, it explains the occurrence of some trapped mercury in the sample. On the extreme this theory will mean nearly 100 % of the intruded mercury will remain in the sample since the network will break at all the throats between pores during the extrusion process. The interconnected network of pores play an important role in mercury porosimetry, as in order for a pore to become filled with mercury it must be equal to or larger than the corresponding "pore size" at the applied pressure, as long as a continuous path of mercury leads to that pore. Large internal voids will not be filled unless the pressure is sufficient to fill the smaller pores. Another theory known as the energy barrier model has also been proposed by Giesche *et al.* (1982) as reported in Giesche (2006) to explain the region of irreversibility. According to this model the liquid/vapour interface has to be newly created during extrusion and thus requires an extra amount of energy. As a result hysteresis is thus a consequence of the distribution of pore sizes and their connectivity in the porous material, and the degree of coalescence of the mercury ganglia.

The occurrence of hysteresis between the intrusion and extrusion branches is a significant feature of mercury porosimetry curves, as well as, an irreducible saturation of mercury (non-wetting fluid) known as entrapment, observed after pressure reduction to ambient (extrusion). Both phenomena are believed to contain important information about the porous material and most be understood in great detail in order to be able to obtain a more accurate mesopore size analysis. These phenomena, i.e., hysteresis and entrapment, are observed in the first mercury intrusion/extrusion cycle of most porous materials. However, entrapment does not usually occur in the second intrusion/extrusion cycle performed on the same material, but the hysteresis loop is still observed (Moscou and Lub, 1981; and Lowell *et al.* 2004). These findings suggest that entrapment and hysteresis have different origins and or are controlled by different factors.

The factors of pore systems that affect the trapping of non-wetting fluids like mercury, or by analogy oil and gas, in porous media include; Pore to throat size ratio, throat to

pore coordination number (also known as aspect rations), random and non-random heterogeneities in pore structures and surface conditions or roughness of pores and throats. These features of pore systems influence the threshold pressure and the contact angle of penetration curves, as well as the gradients and degree of hysteresis displayed in the retraction curve.

Porous systems generally comprise of both pores and throats, where the pores are defined by the larger spaces, and the throats, otherwise known as the necks, are the smaller spaces that link up the pores. The amount of non-wetting phase (nwp) trapped in pores is sensitive to pore to throat size ratio. There is significantly less trapping of mercury in large isolated spaces which have smaller pore to throat size ratios, than in pore systems with large pore to throat size ratios.

Wardlaw and McKellar (1981) performed mercury experiments on glass models to show the amount of residual trapped mercury in samples of varying pore to throat size ratio. Figure 6.1 shows the picture of a glass micromodel which was completely filled with mercury injected under pressure from one end while a vacuum was applied at the other end. The black areas are an indication of mercury filled pores, and when pressure was reduced mercury withdrew partially with trapping of disconnected blobs. There was complete withdrawal in the simple tube where the pore to throat size ratio was small. Pore systems of large isolated pore spaces with large pore to throat size ratios, are common in carbonate reservoirs with vuggy porosity and also in many sandstones with secondary porosity. The authors reported the existence of two key mechanisms of entrapment: entrapment in pore bodies interspersed with pore necks; and entrapment due to larger-scale heterogeneities. In the first scenario, pore-body, pore-neck network models were shown to exhibit ‘pore shielding’ whereby mercury invades ‘shielded’ larger pores only when mercury can penetrate smaller pores. In the second scenario, a pore bond network model with spatial heterogeneities in the distribution of pore sizes, were shown to be simple models where the entire pore space fills at the same pressure step. The resulting entrapment mechanisms in the first scenario is full or partial entrapment occurring within pore bodies due to ‘snap-off’ of menisci at necks whilst in the second scenario entrapment occurs in ‘shielded’, large pore size regions, and has a ‘piston-type’ intrusion and retraction. Their experimental studies of mercury retraction from glass micromodels also suggested that, for heterogeneous, non-random void

spaces consisting of isolated regions of similarly-sized large pores within a more continuous network of smaller pores, snap-off (breakage) of mercury ganglia arises at the boundaries between regions of large and small pore sizes.

The pore to throat coordination number simply represents the number of access ways available from a pore within a porous system. The pore to throat coordination number, which is the average number of throats that connect with each pore, gives an indication of the connectivity of the network of throats, and the higher the connectivity, the higher the chances of achieving complete withdrawal. Wardlaw and McKellar (1981) also investigated the effects of the pore to throat coordination number, and concluded that although it is not solely responsible for the amount of residual mercury trapped following withdrawal, it plays an important role in the processes alongside other factors such as local heterogeneities. By using a simple square network with a coordination number of 4 for mercury analysis, they observed that after injection mercury was withdrawn from all but 12 of the 2240 tubes. A second sample of coordination number 8 and 4 was also analysed and was found to experience more entrapment of the nwp as opposed to the anticipated effect of lower residual mercury. The first sample showed that mercury trapping on withdrawal is not dependent solely on the network coordination number. However the second sample highlights the effect of heterogeneities in relation to the coordination number, because the residual mercury occurred in local clusters of larger tubes, which were imperfections in the model caused by deeper acid etching. A non-random network would have clusters of larger elements together, and clusters of smaller elements in other domains, while a random network will be randomly heterogeneous or evenly spaced out. In a random model, where large elements occur amongst a network of smaller elements, after injection, mercury first withdraws from smaller elements, but by the time the pressure has been reduced below the threshold for emptying the clusters of the larger elements, they would have already reached snap-off and extensive residual mercury is retained.

In a subsequent report Wardlaw (1982) reported multiple displacement experiments in the same pore-throat pair showing the amount of trapped oil to be a function of pore-throat geometry and wettability with little effect from viscosity or interfacial tension. In extending this discovery to a network of multiple pores and throats, Wardlaw (1982) showed that for pore systems with relatively large size differences between larger pores

and smaller adjoining throats, instability and snap-off occurs in the region of the junction of the pore with the exit throat, and is insensitive to the length of the throat which lies beyond. It was noted that trapping by Snap-off (as a result of capillary instability) is only one of several ways trapping can occur, however in the most common cases of strongly water-wet rocks with high aspect ratios, snap-off may be the most important mechanism of trapping. They also showed that the narrow fluid interface in the region of the pore-neck junction would 'neck-down' further prior to snap-off. As a reasonable guide, Matthews *et al.* (1995) suggested that the ratio of the sizes of neighbouring large and small pore elements required to cause snap-off is > ~6.

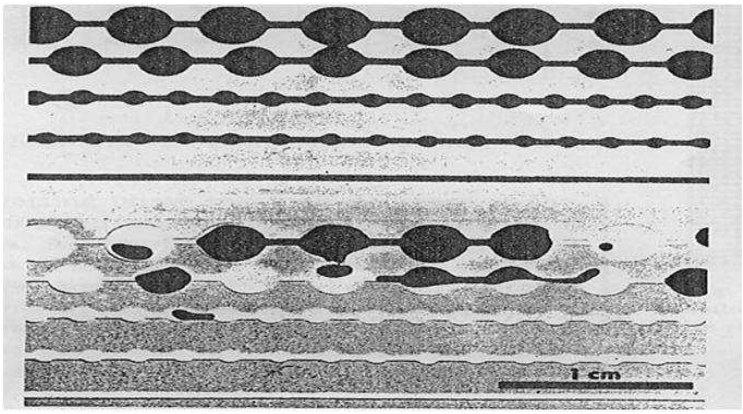

Figure 6.1: Shows trapped mercury in glass micro models (Wardlaw and McKellar, 1981) (With kind permission of Elsevier).

Entrapment is generally believed to be associated with kinetic effects during mercury extrusion, coupled with the tortuosity of the disordered pore network and the surface chemistry of the material (Moscou and Lub, 1981). Porcheron *et al.* (2005) performed dynamic Monte Carlo simulations using both Glauber dynamics and Kawasaki dynamics for a lattice gas model to study the behaviour of a non-wetting fluid within a porous material. They researched into slit and ink-bottle pore geometries in addition to the porous Vycor glass. Their intrusion and extrusion data suggested that mercury entrapment is caused by a decrease in the rate of mass transfer attributed to the fragmentation of liquid during extrusion. Their results were also in agreement with the findings of Lowell *et al.* (2004), where they reported that often at the completion of the intrusion and extrusion cycle, mercury would slowly continue to extrude for hours. This finding suggests that extrusion under such conditions involves an intrinsically low flux

vapour phase transport indicating a slowing down of the dynamics in the "transport" regime.

More recent studies (Porcheron *et al.*, 2007) investigated the relationship between entrapment and hysteresis by performing re- intrusion and extrusion cycles immediately after the first cycle of experiments, so that the second cycle begins with mercury entrapped in the system. They observed that in both test cases a hysteresis loop is present in the second cycle but that there is no additional entrapment, suggesting that hysteresis and entrapment have different origins. In the case of the first test sample, a controlled pore glass, the second intrusion and extrusion curves follow closely the first intrusion and extrusion curves, i.e. the width and shape, and position of the hysteresis loop remains unchanged. However for the Vycor glass (random heterogeneity), the shape and width of hysteresis loop changes because the second intrusion curve is shifted significantly to lower pressures and appears to be less steep as compared to the first intrusion/extrusion cycle, whilst the position and shape of the extrusion branch remains unaffected. One could expect that the extrusion curves for the first and second intrusion and extrusion cycles would be identical given that in each case the extrusion starts from the same state (i.e. the material mostly filled with mercury) however this is not the case. One possible explanation given for the differences in the intrusion and extrusion cycles between CPG and Vycor was that the entrapment of mercury in CPG does not change the overall character of the pore network. The is because pores filled with entrapped mercury represent only about 10 % of the complete pore volume and the pore size is relatively uniform in comparison with that of Vycor. For Vycor the fraction of the pore space with entrapped mercury after the first cycle is significantly larger, approaching 25 % in the experiments with the longest sample times and much greater for shorter sample times. Also the distribution of pore size is more non-uniform so that at the beginning of the second cycle the available void space can be expected to have a different topology. The shift of the intrusion branch for the Vycor to lower pressures in the second cycle is consistent with the assumption that mercury entrapment occurs in the smaller pores. However, the volume of entrapped mercury was rather large, and GCMC simulations of mercury extrusion within a model of Vycor indicated that large pores can remain filled after fragmentation of the mercury during extrusion. The kinetics of extrusion of this entrapped mercury was extremely slow, because it could only occur via a process of vapour transfer from isolated droplets of entrapped mercury. Such an interpretation is

somewhat similar to a point of view presented by Moscou and Lub (1981). They argued that pore shape determines the mercury retraction because mercury that has been penetrated into ink-bottle shape pores will not leave these pores through smaller pore entrances during extrusion. As a result Porcheron *et al.* (2007) concluded, based on their experimental findings that differences in the reintrusion and extrusion behaviour between Vycor and CPG are due to the fact that Vycor exhibits a much more pronounced textural heterogeneity (with wider PSD) as compared to CPG.

6.4 - Modelling of Mercury Porosimetry Data

The simplest derivation of the Washburn equation generally only involves a consideration of the mechanical equilibrium of the pressure and capillary forces within a pore. However for smaller pores, the dispersion forces between the mercury and the solid, and the change in chemical potential of mercury corresponding to the change of its structure in the force field in pores just being filled must be considered also (Kadlec, 1985). As mercury porosimetry is used to characterise materials of a wide range of pore sizes from large macropores down to ~3 nm, it is therefore important to understand in detail the effects of extreme geometric confinement of mercury on the interpretation of mercury porosimetry data.

Most common applications of mercury porosimetry analysis assumes that the porous material has a void space structure analogous to a parallel bundle of pores, and then the intrusion curve can be converted directly using the Washburn Equation to a volume-weighted pore diameter distribution (PDD). On the contrary most materials are complex in nature and hence pore 'shielding' or 'shadowing' effect may occur because large pores may only be accessed after surrounding small pores have filled. Hence, the pressure must rise sufficiently to enter the surrounding small pores before filling the shielded large pores. Many structural models have been suggested to account for the pore 'shielding' effects and thereby render a more accurate PSD. Generally these models are based on random pore networks (Fatt, 1956; Androutsopoulos and Mann, 1979).

In general the mercury retraction curve is rarely used, however it should, as it constitutes half the data of a standard experiment and is also potentially a useful source for obtaining information concerning the pore structure. The retraction curve has been used in simulation work to validate pore-bond network structural models obtained using the intrusion curve (Mann and Golshan, 1981; Mata *et al.*, 2001). It has also been used to test models for the pore-scale mechanisms of meniscus retraction and snap-off (Tsakiroglou *et al.*, 1997; Tsakiroglou and Payatakes, 1998), as well as to obtain information about pore connectivity (Portsmouth and Gladden, 1991, 1992), and the spatial arrangement of pore sizes (Rigby, 2000). However, unless the method to obtain pore space descriptors from mercury retraction is based on an accurate model of the underlying physical process, the pore space descriptors will have little validity.

Androutsopoulos and Mann (1979) developed a two-dimensional network model to explain hysteresis and mercury entrapment by allowing the retraction curve and the extent of entrapment to contribute to the determination of the pore structure of a porous material. Their model consisted of cylindrical pore segments assembled into square grids and thus it incorporated the element of interconnectivity which is vital in determining the accessibility of the interior of porous materials, and likewise important in a range of catalysts selectivity and deactivation problems as well as being relevant to fluid flow problems pertaining to the recovery of oil trapped in porous media in reservoir rocks. Their theory and simulation showed that pore interconnectedness alone can lead to mercury entrapment and thus an important alternative to the ink-bottle type pore mechanism. Better understanding of the mercury intrusion and extrusion process would lead to an improved structural pore model for interpreting diffusion, reaction and deactivation phenomena in catalysts. At the completion of the penetration process, they assumed that a single pair of interfaces remains separated from the rest within the finest segment in the pore network, and they predicted that it is from these two interfaces that the retraction of mercury begins upon sufficient lowering of the pressure. Although some coalescence of interfaces occurred during pressure increase, it was assumed that since a complete evacuation of the sample will not be possible, the residual amount of gas ultimately contained within the smallest pore at the highest pressures will prevent a final coalescence taking place. The site from which retraction commences is therefore the same as the smallest segment in the network. Their conclusions suggested that mercury retraction may involve a slower relaxation process as well as the more rapid,

capillary flow process described by Washburn (1921). The slow retraction process is attributed to the formation of ganglia of entrapped mercury that, under a non-zero net force prior to equilibration, tend to move around slowly and may coalesce with the bulk. It may be inaccurate therefore to interpret mercury retraction solely on the basis of a piston-like withdrawal. In earlier work of porosimetry simulations and data interpretation of mercury retraction, this relaxation process was presumed so slow, it was regarded negligible (Androutsopolous and Mann, 1979).

Most of the mercury porosimetry simulation work carried out previously has used network models for void space structure and percolation processes to model the pore scale mercury displacement. Recent simulation work on mercury porosimetry includes the use of lattice-Boltzmann (Hyvaluoma *et al.*, 2007), and statistical mechanics (Porcheron *et al.*, 2007) methods to simulate porosimetry on structural models obtained directly from full 3D X-ray tomographic reconstructions of void spaces (Hyvaluoma *et al.*, 2007), or statistical reconstructions based on scattering data (Porcheron *et al.*, 2007). The main drawback with these simulation techniques is that only a potentially unrepresentative microscopic fraction of the void space of a potentially macroscopically heterogeneous mesoporous solid can be represented on computer. However, the lattice-Boltzmann simulations conducted in the X-ray tomographic reconstructions by Hyvaluoma *et al.* 2007 validated the invasion percolation model for mercury intrusion into disordered materials. In addition, the statistical mechanical modelling (Porcheron *et al.*, 2007) of porosimetry indicated that mercury retraction involves two different dynamical regimes; the first regime is known as the transport regime, which is associated with mass transfer to the external surface, whilst the second regime is known as the quasi-equilibrium régime, which relates to the re-distribution of the fluid inside the material. The experimental time-scale generally exceeds the typical time-scale of the transport regime but not necessarily the quasi-equilibrium regime. In the statistical mechanical simulations, the mass transport in the transport regime was considered to be diffusional relaxation. Many researchers (Wardlaw and McKellar, 1981; Tsakiroglou *et al.*, 1997; Tsakiroglou and Payatakes, 1998) have considered mass transport to occur by viscous flow processes. As yet, there has been very little or no experimental studies of the actual rates of relaxation or quasi-equilibrium, process involved in mercury retraction.

A comparison of the shapes of mercury retraction curves simulated using statistical mechanics (Porcheron *et al.*, 2007) with experimental data suggests that the simulations do not accurately re-create the shape of the initial knee in the high pressure region of the experimental retraction curves. This research aims to study the transport regime in detail, and, in particular the region of the onset of mercury retraction not accurately described by statistical mechanical models. In addition, the test materials will also be examined over even longer time-scales after the initial porosimetry experiment to study the quasi-equilibrium regime. These data will be used to infer the initial spatial arrangement of entrapped mercury for heterogeneous, nanoporous materials, and thereby improve the understanding of the mechanism of entrapment.

6.5 - Experimental

The materials studied in this work include a selected range of structured mesoporous and bi-modal silica materials synthesised within this research ($P123_t$ core, $F127_t$ core, and $P123_t$ coated in $F127_t$ previously characterised in Chapter 3) as well as five different batches of commercial sol-gel silica spheres, one is denoted C30, having a typical pellet diameter of ~3 mm and a nitrogen BET surface area of ~99 $m^2.g^{-1}$, and another one denoted S980G with a pellet diameter of ~3mm and a BET surface area of ~171 $m^2.g^{-1}$ as well as Q176, with a typical pellet diameter of ~3 mm and a nitrogen BET surface area of ~192 $m^2.g^{-1}$, and C10 with a pellet diameter of ~3 mm and a BET surface area of ~274 $m^2.g^{-1}$and finally P7129 with a pellet diameter of ~3 mm and BET surface area of 322 $m^2.g^{-1}$. This mercury porosimetry study aims to explore means of increasing the accuracy of data interpretation in terms of pore structure parameters, for sol gel type materials. It will also investigate causes of volume hysteresis and the entrapment of the non-wetting fluid in relation to surface roughness, interconnectivity and relaxation time effects.

An understanding of the mechanisms of entrapment and distribution of the irreducible non-wetting phase within porous media is of fundamental interest in a number of fields, including enhanced oil recovery and the internal structural characterisation of porous media using liquid penetration methods. The presence of mercury entrapped in a sample can be seen by microscopic observation, and the residual quantity can be weighed.

Alternatively residual mercury can be analysed using nitrogen sorption to assess the resulting pore size reduction in comparison to the previously obtained PSD, as a check for the level of mercury entrapment and comportment. This leads to the application of the newly introduced integrated nitrogen sorption and mercury porosimetry technique to study the mechanisms of entrapment of the non-wetting fluid in ordered mesopores (synthesised materials) and in complex, irregular, nanoporous solids. Comparative studies of gas adsorption and mercury porosimetry is potentially very useful, for example since both gas desorption and mercury intrusion are both considered to be invasion percolation processes, an effect known as 'pore shadowing' or 'pore shielding' arises in mercury intrusion porosimetry, which has some similarity to the pore blocking effect in gas adsorption (Androustsopoulos and Mann, 1979), and hence could be used to investigate the effect of hysteresis. Comparisons of the pore size distribution from gas desorption and mercury porosimetry can therefore be used to investigate pore blocking effects. A match of PSD obtained from both mechanisms, will confirm the existence of pore-blocking effects.

Mercury porosimetry has been used extensively in pore structural characterisation but, the interpretation is most often only based on the intrusion data and the data obtained during the extrusion process known as the retraction curve is simply not used. This may be because mercury retraction is significantly less well understood than intrusion, and hence it is more difficult to reliably extract pore structure information. The retraction curve amounts to half the data in any given experiment and thus possesses substantial valuable information in terms of pore space descriptors. It is also therefore within the scope of this study, to obtain fundamental knowledge that could form the basis of methods to reliably extract accurate information from the retraction curve. A detailed study of the process of mercury retraction may reveal valuable information about the nature of the pore structure and could lead to better understanding of the retraction process. In addition, it could improve the interpretation of integrated gas sorption data and hence the study of fundamentals of adsorption processes. The theory and interpretation of data for integrated gas sorption experiments is based on the amount of mercury entrapped within the particular pores suggested by the mercury retraction curve prior to nitrogen sorption and thus it is important to understand any mercury mass transport processes that may occur during retraction and before the mercury is frozen in place. Once the mechanisms of mercury retraction and entrapment have been identified

the retraction curve will be better understood and its interpretation would become more reliable.

While the penetration, retraction and entrapment of non-wetting fluids within macroporous media such as reservoir rocks and glass micromodels have been studied directly, using techniques such as microscopy, prior to this research there has been very little study of these processes in nanoporous media where they could be quite different due to the restricted length scale. This research therefore aims to investigate the insights of the molecular mechanisms and the effects of extreme geometric confinement (small pores) on mercury occurring during mercury porosimetry experiments in nanoporous silica based materials. By experimental observations of mercury porosimetry at varying relaxation times the link between hysteresis, the equilibration time and the varying amount of mercury entrapped can be explored, and thereby improving the reliability of pore structure analysis. This study also aims to present a comparison of the theoretical predictions with new experimental results for intrusion and extrusion dynamics of mercury in mesoporous silica pellets.

The result section will detail experimental studies of the materials synthesised within this research and then followed by that of the commercial mesoporous silica sol gels.

6.6 - Mercury Porosimetry Methodology and Analysis

The mercury porosimetry experiments were performed using a Micrometrics Autopore III. The Autopore III analyser is a 60,000 psi (414 MPa) mercury porosimeter covering the pore diameter range from approximately 360 to 0.003 μm. This model has four built-in low pressure ports and two high pressure chambers. All aspects of low pressure and high pressure analyses, as well as data collection, reduction and display are processed by the interface controller and the control module.

Prior to analysing a sample, a sample information file is created, that describes the sample, the analysis conditions and other parameters. This file also includes a pressure table, which lists the pressure points at which data are collected during analysis. To

begin the analysis, you load the sample into a penetrometer, and then install the loaded penetrometer in a low pressure port. After the sample has been evacuated to a pressure of 6.7 Pa in order to remove any physisorbed gases from the interior of the sample, the penetrometer is then backfilled automatically with mercury. After the sample has been evacuated, it is then put into the penetrometer and inserted into the low pressure analysis port. The sample is then surrounded with mercury as the entire system is still under reduced pressure. Air is then sucked into the system to increase the applied pressure on the mercury entering the pore system of the sample. As the air pressure is increased, the fall in level between the air-mercury interfaces (in the capillary stem) is monitored to determine the amount of mercury penetrating into the sample. The first reading is usually taken at pressures within the range 3000 - 4000 Pa (the exact pressure reading for the analysis carried out within this research is 0.54 psi), although lower pressure readings are possible. When the low pressure analysis is completed, the weight of the penetrometer is determined, from which the bulk density of the sample may be calculated. The penetrometer is then transferred to the high pressure system where it is surrounded by hydraulic oil for continuation of the analysis. The high pressure analysis collects data at pressures indicated in the high pressure portion of the pressure table (up to 60000 psi), after which the extrusion process follows. Using a hydraulic pump and a pressure intensifier, the pressure is further increased up to values of 414 MPa if required and then reduced in steps whilst recording the volume of mercury extruded. The intrusion and extrusion data for the mercury porosimetry analysis were acquired in both the so-called continuous scanning (zero equilibration time) and stepwise modes (ranging from 10 s to 150 s), in order to evaluate the effect of experimental sample time on the nature of the retraction hysteresis and entrapment. In the scanning mode the rate of pressurization is controlled by the motor speed of the pressure generator system, for the selected pressure sets. This scanning mode allows high-resolution intrusion and extrusion curves to be obtained. In the step-wise data acquisition mode with equilibration time greater than zero, the pressure can be incremented by programmed amounts between each measurement after a fixed equilibration (relaxation) time for all pressure data sets.

6.7 - Correction Methods

Correction methods exist to counteract certain characteristic artefacts such as the compressibility effect of the sample and thermal effects. Due to compressibility effects on the sample, the measured pore volume of a porous material usually appears larger than its true pore volume. Compressibility, β, is defined as the fractional change in volume per unit pressure. The corresponding Young's modulus is the linear equivalent. For most solids the compressibility lies in the range 10^{-3} to 10^{-4} $(Pa)^{-1}$. Thus 1 cm^3 of sample will compress by about 0.006-0.06 cm^3 at the final pressure of 400 MPa. For liquids such as mercury the compressibility is much larger. Schuth *et al.* (2002) suggests a well-balanced combination of the compressibility of the glass sample cell and the mercury and the changes of dielectric properties, especially of the high pressure fluid, to minimize the "blank effects". The estimated error is approximately 1 % without any further "blank-run" corrections, but can be reduced to 0.1 % by the use of proper correction procedures. A larger sample and pore volume of the sample in comparison to the amount of mercury in the penetrometer will minimize errors due to compressibility according to Schuth *et al.* (2002). In order to calculate the true volume intrusion of mercury into the pores of a sample, a correction must be made to account for the compression of mercury, sample cell (penetrometer) and sample (Allen, 1999). According to Giesche (2006), Compressibility makes a major impact on the accuracy of mercury analysis data and ideally this problem can be corrected for by running a corresponding blank run using an empty penetrometer.

6.8 - The Link between Equilibration Time and Mercury Entrapment

As shown in the Washburn equation, in order to transform mercury capillary pressure to the size of the throat being invaded, the shape of the space being invaded must be known in addition to contact angle and surface tension for mercury. Also as important in obtaining the pressure-volume relationship for a sample is to ensure equilibrium has been achieved at each pressure increment and that the form of the injection curve is not time-dependent because of insufficient time being allowed for equilibrium (i.e. each pressure step is held constant allowing sufficient time for uptake to reach steady state).

Through the use of both computer and experimental verification, Wardlaw and McKellar (1981) showed that for a horizontal cylindrical capillary mercury will enter the capillary at a certain pressure "threshold pressure" given by the Washburn Equation (Equation 6.1), but will not continue to advance until an excess pressure above the threshold pressure is attained. A finite rate of advance exists, and is dependent on the excess pressure (ΔP) above the threshold pressure and the distance to time relationship for the advancing mercury front is given by:

$$t = \frac{4l^2\eta}{\Delta P r^2} \tag{6.3}$$

Where t = time, l = distance, η= viscosity (1.536 centipoises), r = radius, and ΔP = pressure applied in excess of the injection pressure. The distance-to-time relationship for mercury may have such limitations; however in practice those limitations may only apply to very large samples or for extremely small pore sizes. According to Schuth *et al.* (2002), an equilibration time of up to a maximum of 5 minutes should be sufficient in all samples to achieve apparent equilibrium. Other side effects such as the heating or cooling effects of the mercury and the sample cell for data points at high pressures, may require much longer equilibration times.

Giesche (2006) carried out an investigation into the effects of intrusion rates on pore size and volume. They analysed five samples of an alumina extrudate using the scanning mode (equilibration time for 0 seconds), equilibration – interval settings of 2, 10, and 30 seconds and an equilibration rate of 0.001 $\mu lg^{-1}sec^{-1}$. The cumulative intrusion volume and the log-differential curves of the five experiments both showed an increasing trend in the value of pore volume and diameter in the order of experiment. The data obtained for the scanning mode run yielded the smallest pore volume and smallest pore diameter. The data for the equilibration by rate experiment yielded the highest total pore volume and the largest pore diameter, whereas equilibration by time gave intermediate results. A difference of close to 10 % in pore volume and 40 to 50 % in pore size was reported between the fastest and the slowest analysis condition. Their observations of the intrusion/extrusion volume as a function of time by varying the equilibration time showed that reaching equilibrium during intrusion was achieved much faster than during extrusion for the same sample. Considering that the extrusion

tests covered data points at higher as well as lower pressure values (pore size) compared to the intrusion tests, their findings suggested that other factors besides the flow of mercury through the pore-network or temperature effects are responsible for the delay in reaching equilibrium.

6.9 - The Concept of Integrated Nitrogen Sorption and Mercury Porosimetry

A new technique has been introduced known as the integrated nitrogen sorption and mercury porosimetry by Rigby *et al.* (2004). The two different techniques of nitrogen sorption and mercury porosimetry, which are generally utilised completely separately, have been integrated into the same experiment to improve upon the information obtained from both methods separately and hence improve the knowledge of the internal geometry and topology of the internal pore network of mesoporous materials. Mercury entrapment results in pore blockages in areas due to snap-off of connecting menisci of mercury, and therefore these pores are inaccessible to other pore probes. It is on this basis, that the integrated gas sorption and Hg porosimetry technique is applied. By comparing the nitrogen adsorption PSDs obtained before and after mercury entrapment, it is hoped that any notable changes in the shape of the hysteresis loop and shift in PSD, may provide useful information towards better understanding the entrapment mechanism. Integrated nitrogen sorption and mercury porosimetry is poised to provide structural characterisations that are more statistically representative of a sample as a whole than electron microscopy. In addition, this novel technique acts as a means of testing some of the theoretical predictions of the behaviour of non-wetting fluids in relation to the structural heterogeneities of the templated materials.

6.10 - Integrated Nitrogen Sorption and Mercury Porosimetry Methodology

The finished core-only and core-coat composite materials were analysed using the integrated nitrogen sorption and mercury porosimetry technique which consists of the application of nitrogen sorption to the same sample both prior to, and after, a mercury porosimetry experiment, facilitated by freezing the entrapped mercury in place. The integrated nitrogen sorption and mercury porosimetry experiment were conducted at

Johnson Matthey. These kinds of experiments carry a serious risk of contamination of the nitrogen porosimeter with mercury, and as there was only one ASAP available in the department, Johnson Matthey kindly agreed to run the experiments. The initial nitrogen sorption experiment was carried out at 77 K using a Micromeritics ASAP 2400 apparatus, and the sample was allowed to reach room temperature (298.9 K), and then transferred to the mercury porosimeter still under nitrogen. Mercury porosimetry experiments were performed, using a Micromeritics Autopore III. The sample was first evacuated to a pressure of 6.7 Pa in order to remove physisorbed gases from the interior of the sample. Following mercury porosimetry the sample was transferred back to the nitrogen sorption apparatus.

6.11 - Results and Discussion

This section details the results of the mercury porosimetry and the integrated nitrogen sorption and mercury porosimetry analysis of the mesoporous silica pellets synthesised within this research namely: $P123_t$ core and its bimodal version $P123_t$ coated in $F127_t$ as well the $F127_t$ core.

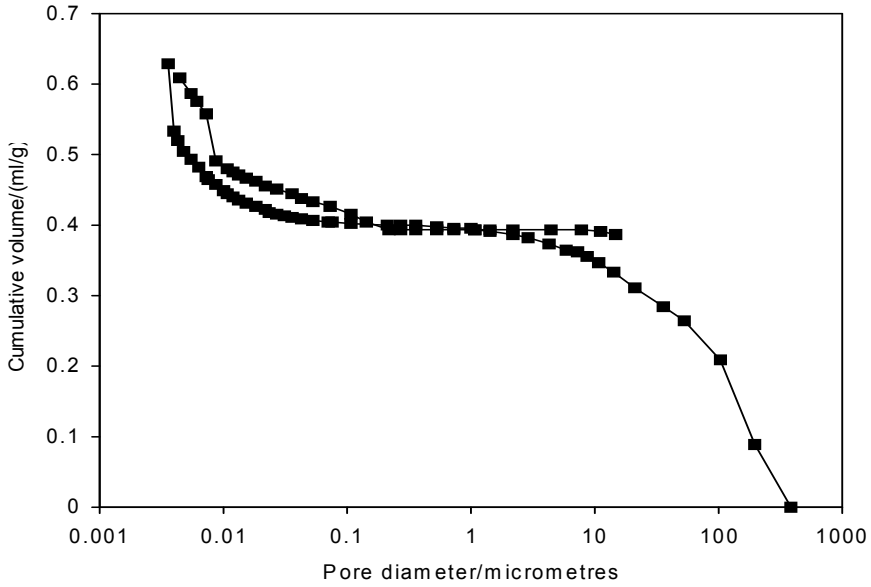

Figure 6.2: Mercury porosimetry data obtained at Johnson Matthey, analysed using the standard Washburn for $P123_t$ core.

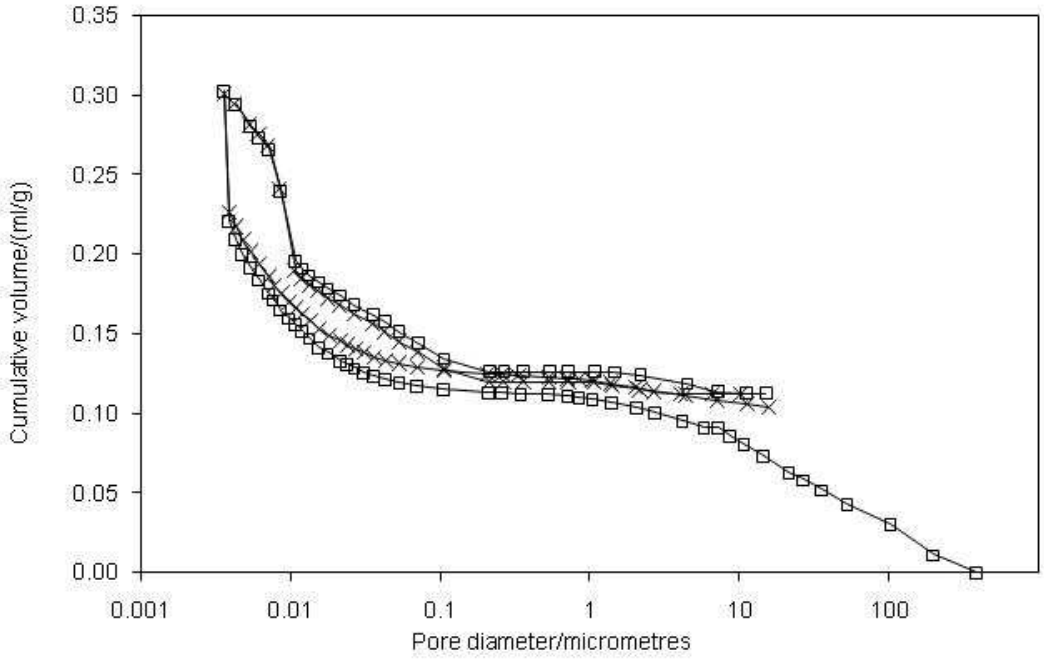

Figure 6.3: Primary (□) and Secondary (x) Mercury porosimetry intrusion and retraction cycles run by Johnson Matthey, analysed using equation 6.1 for $P123_t$ coated in $F127_t$.

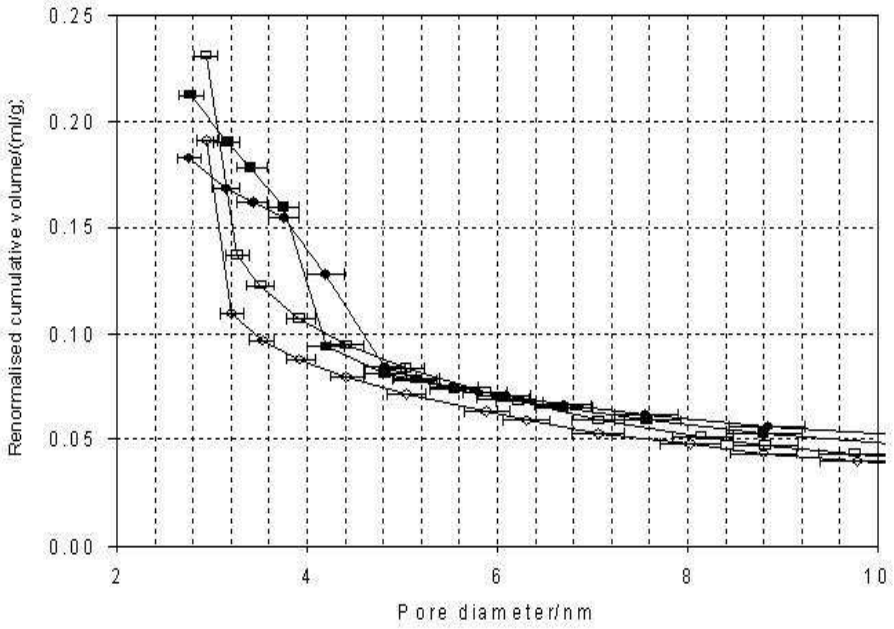

Figure 6.4: Mercury intrusion (open symbols) and extrusion (solid symbols) curves, analysed using Equation 6.6, for $P123_t$ core (squares), and $P123_t$ coated in $F127_t$ (diamonds).

Figure 6.2 shows the mercury porosimetry data for a sample of $P123_t$ core material analysed using the standard Washburn equation (Equation 6.1). The test sample was a single roughly cubic particle with a side length of 3 mm. The sample appears to be a

bimodal structure with a macroporous peak at ~100 μm, followed by a long flat plateau, and a mesoporous peak at 3 - 4 nm. Since the test sample was a single particle of $P123_t$ core, the macroporous peak is unlikely a result of intra-particle intrusion effects. A more likely explanation for this behaviour will be to assume that the large pores of ~100 μm are probably a result of cracks formed during the drying process as the materials were synthesied materials were formed through a gelation process, and such gels may crack during drying.

Figure 6.3 shows the mercury porosimetry data for $P123_t$ core coated in $F127_t$ analysed also using Equation 6.1. In this porosimetry experiment, a primary intrusion up to 412 MPa was followed by a retraction back to atmospheric pressure, which is followed by a re-intrusion (secondary intrusion) back up to ~412 MPa and then a retraction back to ambient. It can be seen from Figure 6.3 that at the highest pressures (correlates to the smallest pore diameters), the paths of the secondary intrusion and retraction curves closely matches the original paths in the primary cycle, within experimental error. This observation suggests that even the highest pressures (~412 MPa) experienced by the sample during the course of porosimetry, does not result in pore structure collapse. Hence, therefore in contrast to the report of Groen *et al.* (2002), silicas templated with triblock copolymers can maintain structural integrity during mercury porosimetry experiments.

The mercury porosimetry data in Figures 6.2 and 6.3 for $P123_t$ and $P123_t$ coated in $F127_t$ respectively were also analysed using Equation 6.2 and the parameters appropriate to silica from Table 6.1 (Rigby *et al.*, 2002). Figure 6.4, shows a superposition of the mercury porosimetry data and the horizontal error bars have been included to represent the errors arising in the pore sizes from Equation 6.2. For both data sets the value of the intruded volume at the long flat plateau, occurring in the intrusion curves between the macroporosity and mesoporosity regions, was subtracted from the original cumulative volume. This renormalization brought the two intrusion curves for the $P123_t$ and $P123_t$ coated in $F127_t$ samples into a close match for the low intrusion region with pore diameters greater than 10nm. However, significant differences between the coated and core materials were evident for pore diameters less than 10 nm. It can be seen that there is a significant shift in the intrusion curve (down to ~3 nm) of ~1 nm towards smaller pore diameters for the coated sample, when compared

to the uncoated material. The difference between the ultimate intruded volumes (at maximum pressure (~412 MPa)) for the $P123_t$ core and the $P123_t$ coated in $F127_t$ samples is commensurate with the difference in the cumulative specific volumes of mesopores with diameters up to 2.94 nm obtained from the BJH PSD derived from the respective nitrogen adsorption isotherms. However, at pore diameters close to the knees in the two intrusion curves for example at 3.5 nm, the difference between the two intrusion curves is significantly more (by a factor of ~2) than can be accounted for simply from the drop in the cumulative specific mesopore volume (for pore diameters up to the diameter in question) for the composite material compared to the core sample alone. The additional pore shielding effect in the coated sample is probably due to the effect of the smaller pore necks present in the $F127_t$ surrounding the larger pore necks in $P123_t$. These smaller pore necks are probably those which were previously observed, by nitrogen desorption isotherms in Chapter 3. Equation 6.2 has been shown to account for contact angle hysteresis (Rigby *et al.*, 2005) and the resulting irreversibility is from the contributions made by structural hysteresis. The remaining hysteresis between the intrusion and extrusion curves in Figure 6.4 is due to structural hysteresis. The mercury extrusion and intrusion curves in Figure 6.4 suggests that the modal pore body size for $P123_t$ is ~4 nm, and the modal pore neck size is ~3.2 nm. When the $F127_t$ coat is added the modal pore body size is then increased to ~4.4 nm, whereas the modal pore neck size is reduced to ~3 nm. The shift in the extrusion curve for the coated material suggests the $F127_t$ shell is intruded with mercury, and that pore bodies within $F127_t$ are slightly larger than they are in $P123_t$.

6.11.1 – Studies of the Transport Mechanisms of $P123_t$

Figure 6.5 shows the nitrogen sorption isotherms obtained both before and after mercury porosimetry for the $P123_t$ core. Both isotherms have been superimposed to make apparent any changes in pore structure. The isotherms were analysed using the standard BJH algorithm, and the resulting pore diameter distributions are presented in Figure 6.6. For the $P123_t$ core sample, prior to porosimetry, the modal pore diameter from a BJH analysis of the adsorption isotherm is ~4 nm. The use of the BJH analysis has received support from the work of Kruk *et al.* (1997). They proposed that the Kelvin

equation for a hemispherical meniscus with a *t*-layer correction (used in the BJH analysis) applied to the adsorption isotherm gives pore diameters within ~0.3 nm of the true value, for MCM-materials. In addition, Ravikovitch and Neimark (2001) showed that pore diameters obtained from BJH analysis of adsorption isotherms for P123 templated materials agreed with the values obtained using a NLDFT method. For $P123_{t,}$ the modal pore body size obtained from nitrogen adsorption BJH is similar to the value obtained from mercury extrusion, (see Figure 6.4), as would be expected if nitrogen adsorption and mercury extrusion are both controlled by the pore body diameter. In contrast, the work of Hartman and Vinu (2002) reported a match in the modal pore size obtained from nitrogen adsorption to that obtained from mercury intrusion for silica solid templated with $P123_t$. However, these workers did not state the value of the $\gamma\cos\theta$ parameter they used and how it was obtained. The modal pore diameter obtained from the $P123_t$ desorption isotherm prior to porosimetry is ~3.5 nm. This is a close match to the value obtained from mercury intrusion in Figure 6.4. One can expect such a match if nitrogen desorption and mercury intrusions were both controlled by the "pore-blocking" or "pore-shielding" effects of smaller pore necks, respectively.

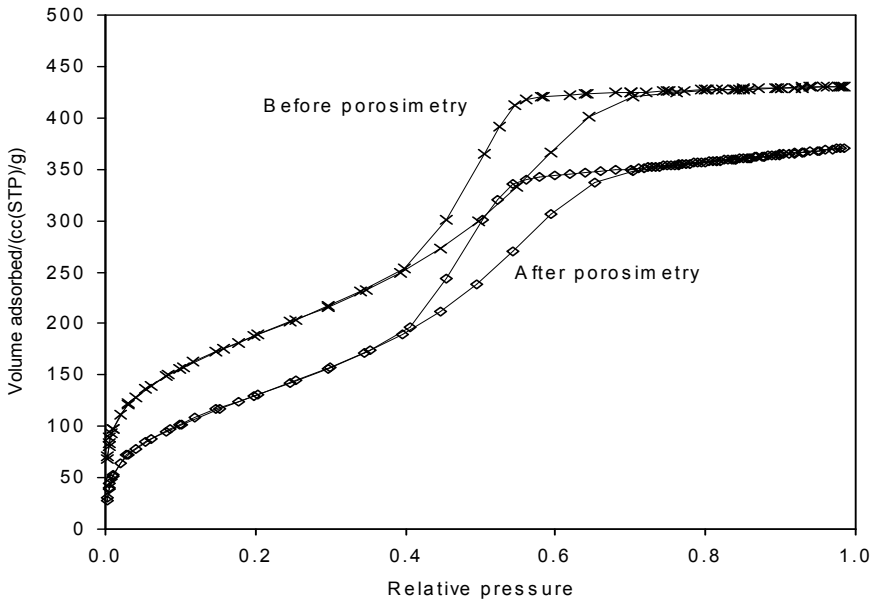

Figure 6.5: Nitrogen sorption isotherms obtained before and after a Mercury Porosimetry Experiment on the same sample of $P123_t$ core.

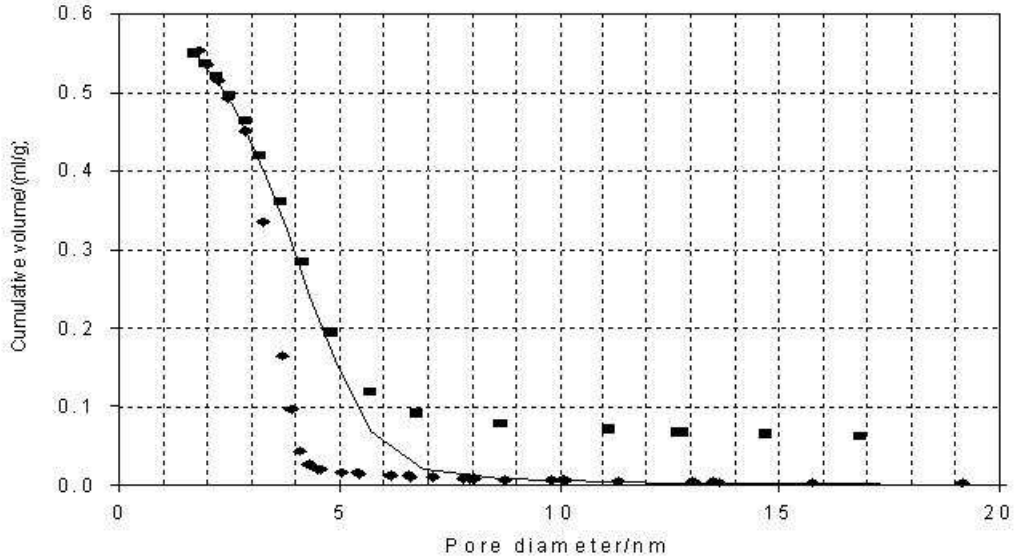

Figure 6.6: Pore diameter derived using the BJH algorithm, from the adsorption isotherms obtained before (solid line) and after (■) porosimetry, and from the desorption isotherm before porosimetry (♦) shown in Fig. 6.5. The ultimate cumulative volume for the PSD obtained after porosimetry has been renormalized to that obtained before porosimetry.

6.11.2 – Studies of the Transport properties of $F127_t$

The $F127_t$ nitrogen adsorption isotherm for before and after mercury porosimetry can be seen in Figure 6.7. The maximum volume of nitrogen adsorbed for prior and post mercury porosimetry shows a decrease in pore volume of (~80 ccg^{-1}). The manner of gas desorption from $F127_t$ pores is most likely a result of spontaneous cavitation as discussed in Chapter 3 and thus insensitive to pore size. This means its desorption BJH pore diameter distribution will not match the mercury intrusion curve for the coated sample, however the porosimetry data suggests the critical neck size for cavitation is ~3 nm. The mercury porosimeter used to analyse the $F127_t$ core is raised to its maximum attainable pressure of ~60000 psi, which corresponds to ~3 nm and just about then, some of the pores appear to be filling with mercury as the pore filling pressure determined by the size of the apparently small necks might have been attained.

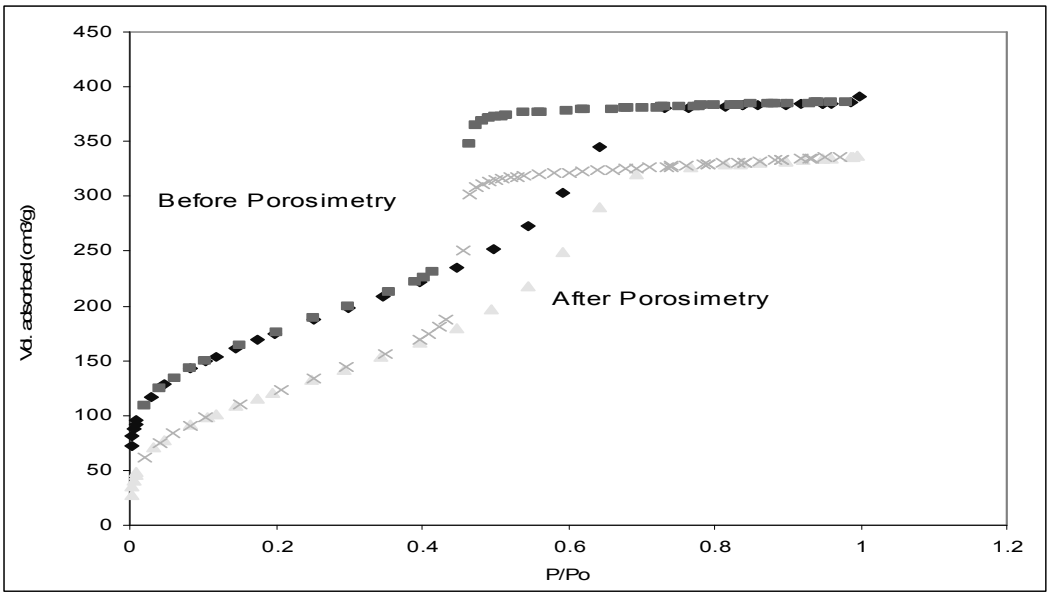

Figure 6.7: Nitrogen sorption Isotherm at 77 K obtained before and after mercury porosimetry on the same sample of $F127_t$ core.

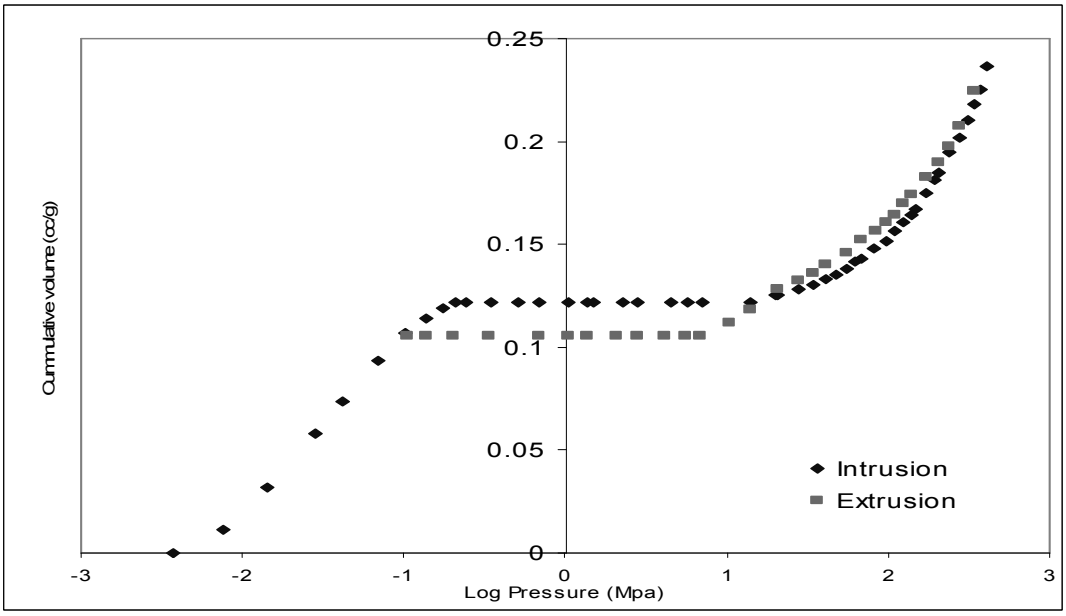

Figure 6.8: Mercury porosimetry curve of cumulative volume vs. log pressure for F127.

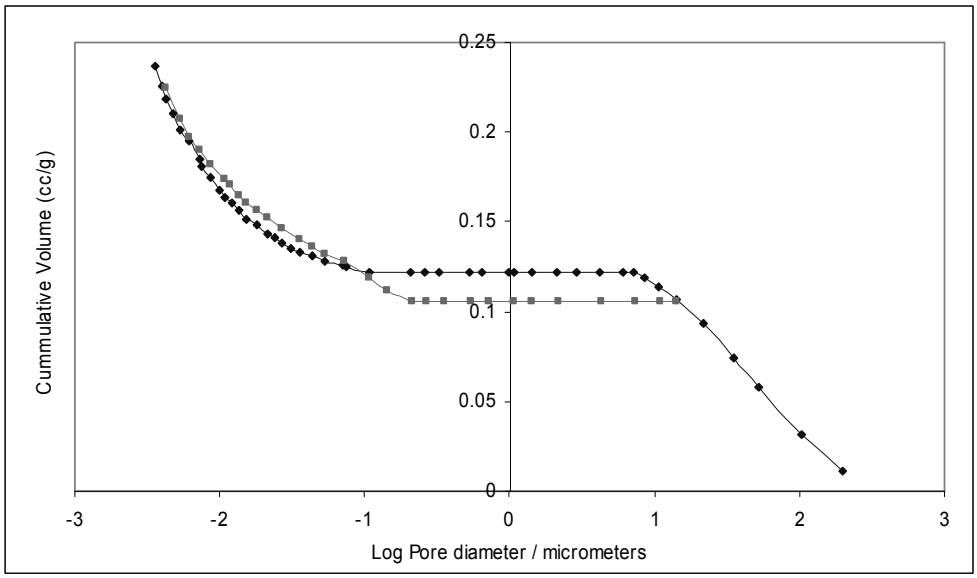

Figure 6.9: Mercury porosimetry intrusion and retraction cycles, analysed using Equation 6.1 for F127.

The Mercury porosimetry data is interpreted using the standard Washburn equation (Equation 6.1), and the resulting porosimetry curve (see Figure 6.9) shows no hysteresis and a lack of entrapment of the non-wetting phase. The results of the integrated mercury porosimetry and nitrogen adsorption on the F127 templated material shows a decline in pore volume after the second nitrogen adsorption experiment, which would usually be attributed to the loss of pore space following the entrapment of the non wetting phase, however their mercury porosimetry curve (Figure 6.7) and the plot of pore radius vs. cumulative pore volume (Figure 6.8) shows no sign of entrapped mercury, since there are no observed hysteresis, despite the fact that no corrections have been made for contact angle hysteresis by adopting the semi-empirical alternative to the Washburn equation which accounts for these effects (Rigby *et al.*, 2004). Hence one is led to think that the loss of pore volume is an effect due to the crushing of pores in the sample caused by the applied pressure. The pores of the F127 templated silica material are small and will require high pressures for intrusion, and hence, before the pressure for the smallest pores is attained the large ones would have lost mechanical stability. This proposition is supported by the work of Pirard *et al.* (1997); they performed mercury porosimetry experiments on low-density xerogels, which showed no trace of entrapped mercury and it was been observed that even at the relatively lowest pressures employed in mercury porosimetry, irreversible crushing of pores within silica solids can result. It was found that, in mercury porosimetry experiments of relatively low pressures, the

mercury intrusion and retraction curves seem to show that substantial mercury entrapment was occurring within the sample. A close inspection of the sample following porosimetry, using light microscopy, revealed that in fact no mercury had become entrapped at all and the overall sample size has decreased. These findings suggested that the initial rise in mercury caused the collapse of the larger pores in the material, which was then followed by the intrusion of smaller pores. One would expect the sample pore size distribution to reflect pores of the same size prior to and after mercury porosimetry to confirm the absence of entrapped mercury. However, as they noticed the mercury volume variation was very small, or non-existence during the course of retraction, it was certain that the actual mechanism is an irreversible mechanical shrinking of the pore walls under isostatic mercury pressure. These xerogels are silica gels synthesized in the sol gel fashion by hydrolysis and condensation of Tetraethylorthosilicate (TEOS) in alcohol. The gel is dried by solvent evaporation at room temperature and atmospheric pressure. Synthesized materials were templated from several surfactants, as can been seen in method section, and the resulting porous solids share certain similarities in their method of synthesis with the xerogels. According to Pirard *et al.* (1997) this behaviour could be a result of the buckling of the brittle filaments constituting the solid skeleton of the material. The crushing of the larger size pores, results in a decrease in volume, however the small size pores remain intact during the compression at low pressure. After the transition period, which varies according to the material composition and microstructure, the mercury can intrude into the network of small pores, which require a higher intrusion pressure. Pirard *et al.* (1997) also performed a control experiment, where samples were sheathed in a membrane that was impermeable to mercury, and the porosimetry data for this sample was found to be the kind that will normally be interpreted as meaning that intrusion and substantial entrapment was occurring. Groen *et al.* (2002) later proposed that silicas templated with triblock copolymers cannot be structurally stable during mercury porosimetry experiments. However the results of mercury porosimetry run on the silica materials synthesised from triblock copolymers show that this is true in the case of $F127_t$ and not so in the case of $P123_t$ core, and even in the $P123_t$ coated in $F127_t$ bimodal sample. It can be concluded, that penetration is impossible, if the mechanical stability of the pore walls of silica materials is affected by the isostatic pressure of mercury, resulting in a reduction of pore sizes. These results indicate that apparent mercury entrapment in porosimetry data may actually be indicating pore collapse instead, and hence care

should be given to the mechanical stability of model porous materials under test conditions.

Most porous solids have complex geometries, which are not cylindrical pores, The effect of the assumption of cylindrical pores in the Washburn equation is still not very clear, although it has been suggested, that the Washburn equation can still be used to obtain an equivalent or effective pore radius (Brakel *et al.*, 1981). It is also known that the roughness of a surface, will increase the effective contact angle (for non wetting fluids), and hence a limitation may arise in the application of the same value of surface tension for the coated samples, with two distinctive regions as well as the core samples. However in most systems, hysteresis will depend on the ratio of the curvature of the menisci that fit into the pore bodies and pore throats (structural hysteresis). The semi-empirical alternatives suggested, by Rigby *et al.* (2002), was applied to the comparative study of $P123_t$ core and the bimodal $P123_t$ coated in $F127_t$ (see Figure 6.4) which de-convolved the effect of contact angle hysteresis and allowed for increased accuracy in pore structure analysis. In addition, the property of the sample could cause difficulties in interpreting the results, as due to the high pressure involved in mercury porosimetry, the structural stability can be altered. As this research has been alerted to limitations such as mechanical damage, all samples of reported tests were also visually observed using the (naked eye, and or x-ray scattering) to ensure that due to high pressure involved in mercury porosimetry, elastic or permanent structural changes had not occurred. All test materials retained stability except for the $F127_t$ core.

Figures 6.10 - 6.14 show the mercury intrusion/extrusion curves obtained on the commercial test mesoporous materials. The intruded and extruded cumulative volume of mercury is shown as a function of pore diameter calculated by the use of the standard Washburn equation. The mercury porosimetry curves all show a well defined hysteresis loop, with significant entrapment, yet exhibiting different variations in samples with equilibration time. C30 and S980G display a flat plateau at the top of their intrusion curves signifying complete pore filling was achieved, however in P7129, Q716, and C10 (see Figures 6.10 - 6.14) this plateau is not apparent and although some inconsistencies could be attributed to issues surrounding appropriate blank corrections, the test materials could also contain some very small pores that require pressures higher than that attainable by the Autopore III (60000 psi). A well defined terminal plateau in

the intrusion curve is reported to indicate the penetration of mercury into an identifiable total pore volume and on the other hand, an extensive extrusion plateau is generally associated with a complex pore structure (Rouquerol *et al.*, 1994).

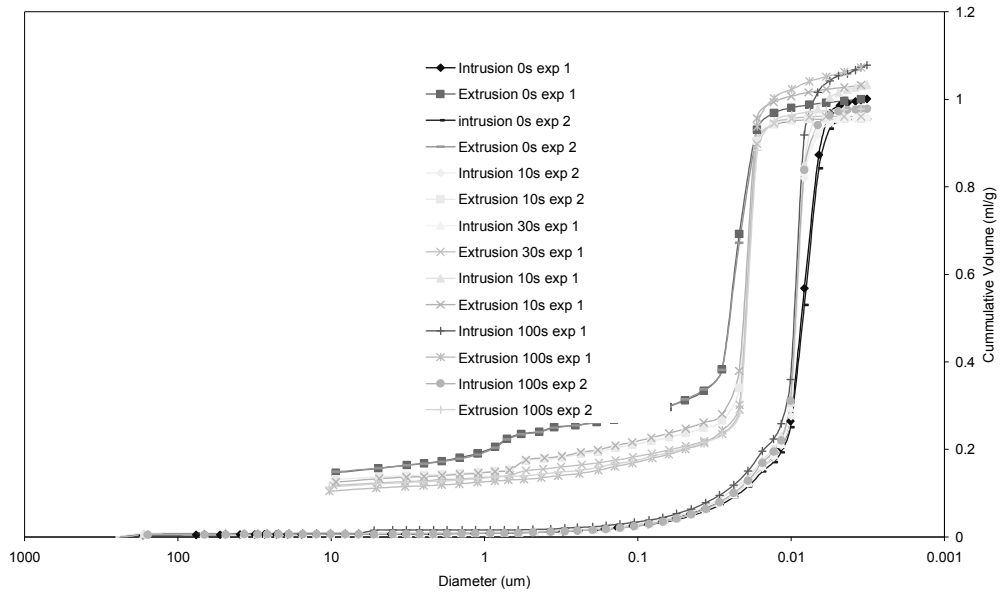

Figure 6.10: Mercury intrusion/extrusion curves for C10 silica pellets.

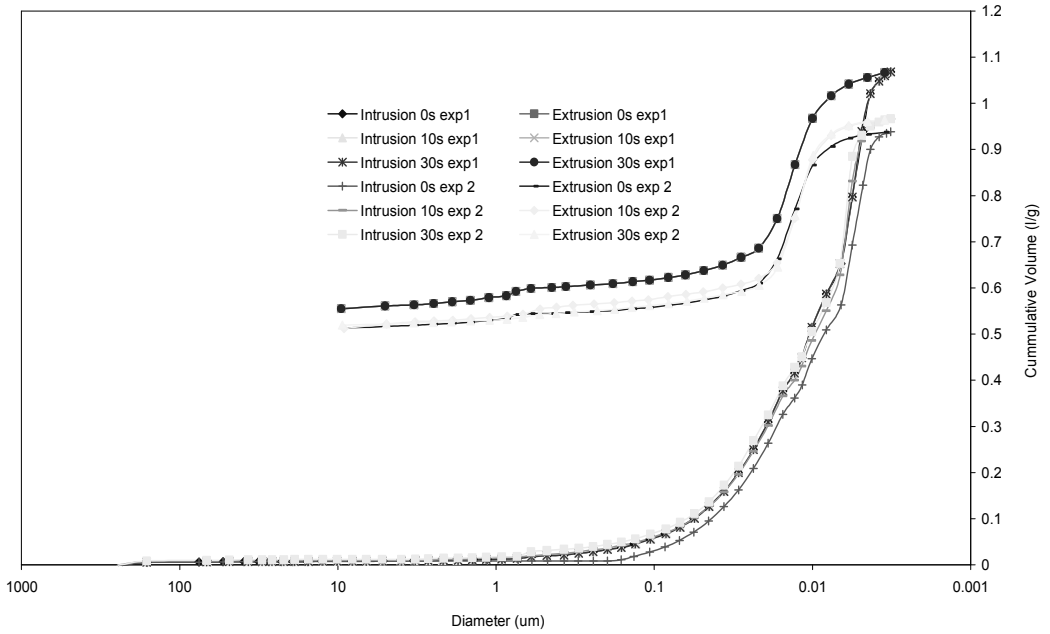

Figure 6.11: Mercury intrusion/extrusion curves for P7129.

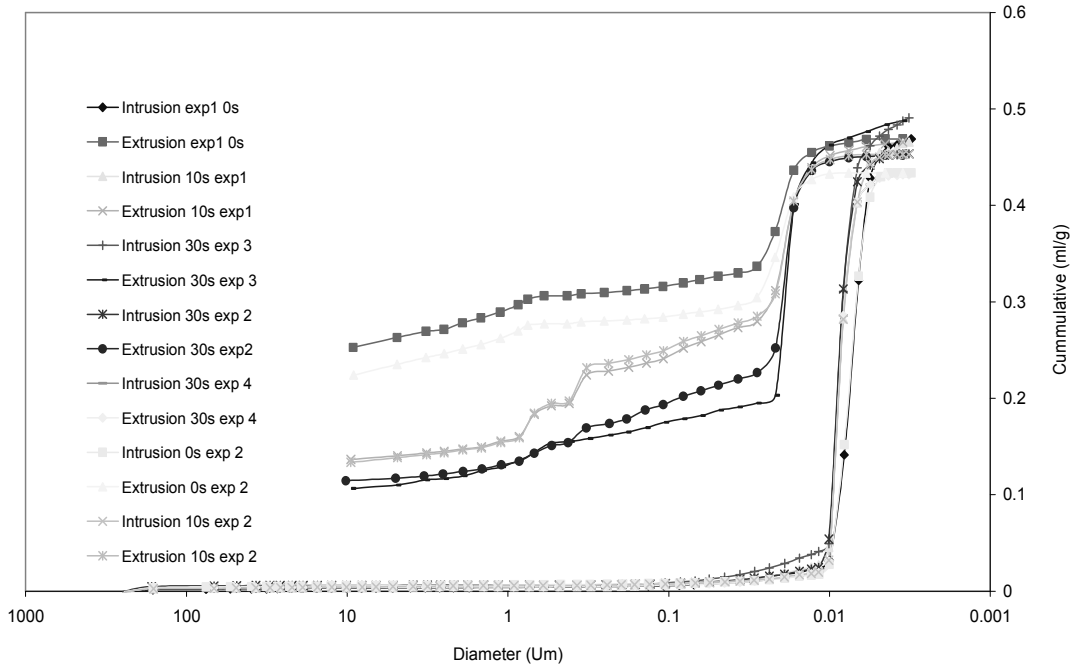

Figure 6.12: Mercury intrusion/extrusion curves for Q176.

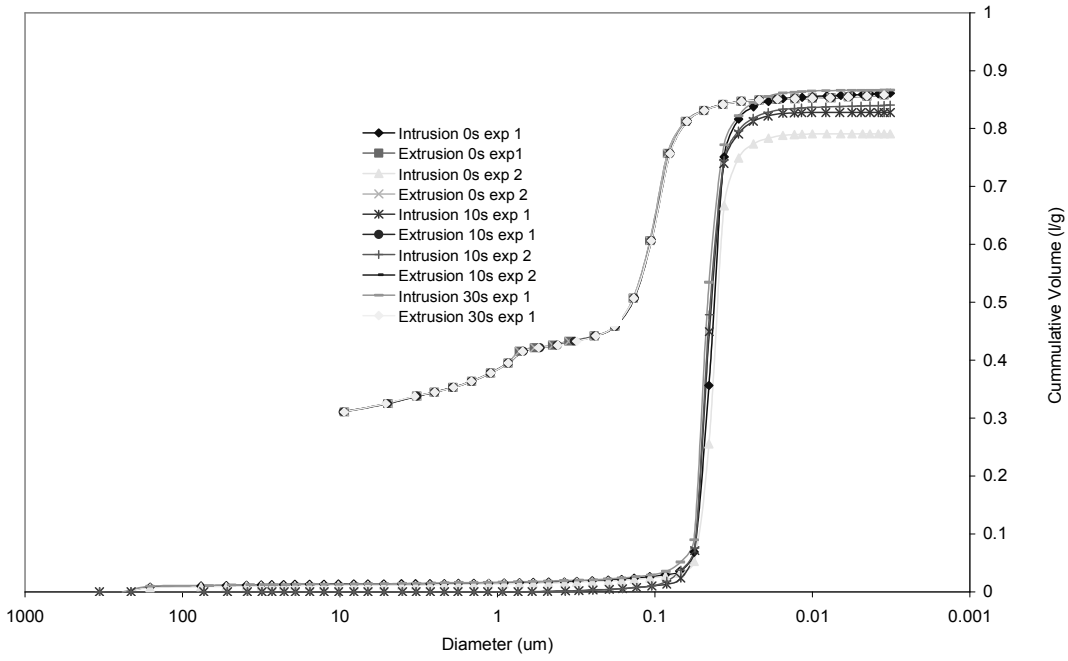

Figure 6.13: Mercury intrusion/extrusion curves for S980G pellets.

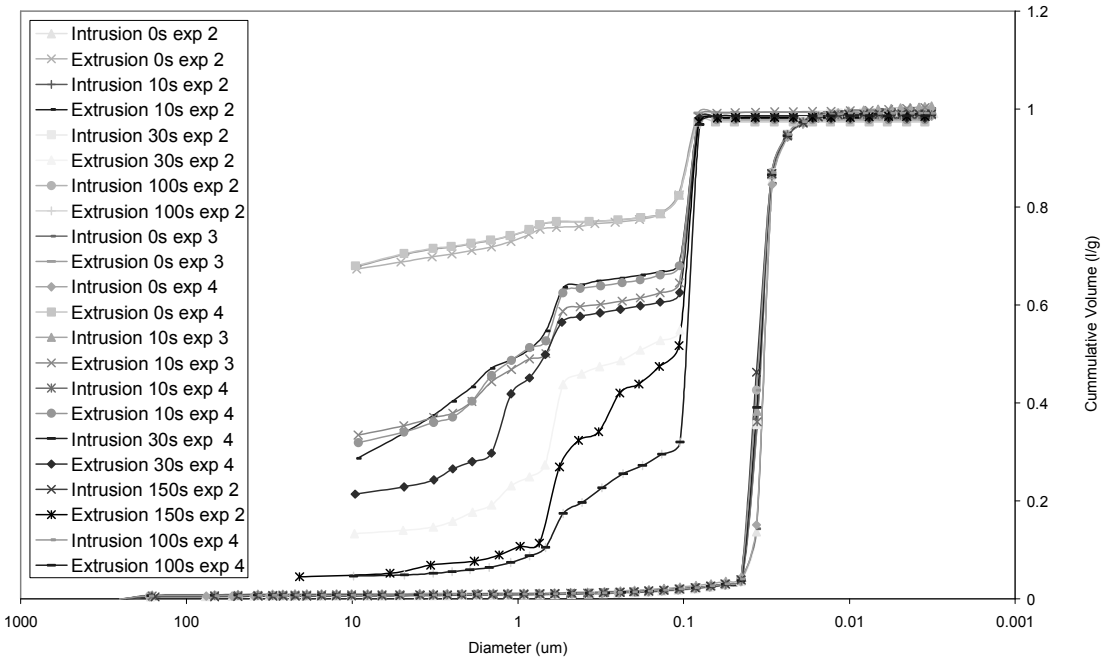

Figure 6.14: Mercury porosimetry intrusion/extrusion curves for C30.

6.11.3 - Studies of the Transport Regime for C30

Figure 6.15 an adaptation of Figure 6.14 showing typical examples of the mercury retraction curves obtained from porosimetry experiments on C30 samples at different equilibration times in the range 0 - 150 s, with only a single intrusion curve shown as there was little or no measured difference. It can be seen that the initial part of the mercury retraction curves all exhibit a similar, almost horizontal plateau. Hence the onset of retraction is independent of the experimental time-scale, as it appeared to be governed by the rapid equilibration of the narrowing of mercury necks, to form a connecting meniscus. There is virtually no change in mercury volume until a Washburn pore size of ~800 Å. then there is a steep decrease in mercury volume. Although the shapes of the subsequent mercury retraction curves are very similar, it is apparent that for several downward pressure steps the amount of mercury lost is also a function of equilibration time. Figures 6.15 also show both hysteresis and entrapment to be sensitive to the variation in sample time at different degrees. It can also be concluded that the shape of the extrusion branch is less sensitive to the sample time except at lower pressures, indicating a difference in mechanism between intrusion and extrusion. At

lower pressures we see that the amount of entrapped mercury increases substantially as the sample equilibration time is decreased.

Figure 6.16 shows the variation of the volume of mercury lost (expressed as a ratio of the amount lost in one step to the maximum volume for a reference 150 s equilibration data-set) with the square root of equilibration time for some of the pressure steps identified in Figure 6.15. From Figure 6.16, it can be seen that step 2 shows no significant, systematic variation of volume with equilibration time for all retraction curves with equilibration times higher than 0 s. The data for equilibration times of 0 s showed appear to be anomalous, and this could be attributed to the finite time period of the pressure step itself (which may vary with the absolute size of the pressure step), and/or the difficulty in achieving exactly zero equilibration time with porosimeter used. This suggests that an equilibration time of 10 s or close is enough to reach (pseudo-) equilibrium of the mercury menisci for this step. However, equilibrium is only reached for the very longest equilibration times for steps 1 and 3.

Figure 6.17 shows that the variation of the volume of mercury leaving the sample during step 1 for shorter equilibration times with the square root of the equilibration time, which results in a good straight line fit. The data for 0s equilibration in Figure 6.16 appear anomalous and is probably due to the finite time period of pressure equilibration (which may vary with the absolute size of the pressure step), and or the difficulties associated with obtaining exactly zero equilibration in the apparatus used. This possibility has been explored accordingly by re-plotting the data for the variation of mercury volume with equilibration time for step 1 with a correction factor δ added to the original apparent equilibration time before the square-root is obtained, such that the independent variable, $(t')^{0.5}$, is equal to $(t+\delta)^{0.5}$. Both graphs of the variation of the volume of mercury lost for step 1 with the square root of the programmed experimental equilibration and with the renormalized time described above can be seen on Figure 6.17. δ was adjusted such that the data fitted the mathematical form of Equation 6.3, *i.e.* the line fitted to the variation of mercury volume with $(t')^{0.5}$ passed through the origin. The corrected data was found to give rise to a good fit to a straight line through the origin with δ=25 s. A similar correction was not necessary for step 3, but this may be because, in absolute pressure terms, step 3 is a smaller size than step 1, and thus may

happen faster. For longer equilibration times ~50 s and above, the volume of mercury leaving the sample in step 1, V, is constant, within intra-batch variability, and is denoted V_{max}.

Figure 6.18 shows the variation of the total fractional mercury entrapment, left behind when the pressure is reduced to ambient conditions versus the fraction of V_{max} left behind in step 1 which is ($1-V/V_{max}$). For equilibration times greater than ~50 s the value of $1-V/V_{max}$ is ~ 0 and it can be seen that for values of $1-V/V_{max}$ greater than zero the final mercury entrapment increases approximately linearly with $1-V/V_{max}$. The equation for the fitted line suggests that approximately 38 % of the mercury left behind in step 1 remains entrapped when the pressure is reduced to ambient. These findings suggest that entrapment is dependent on equilibration time to a limit, so far as sufficient time is allowed for stages in the retraction process comprising of the necking down process of mercury in the onset of retraction and the subsequent stages based on the availability of a connecting pathway of mercury menisci to the surface of the sample before snap-off occurs within the structure.

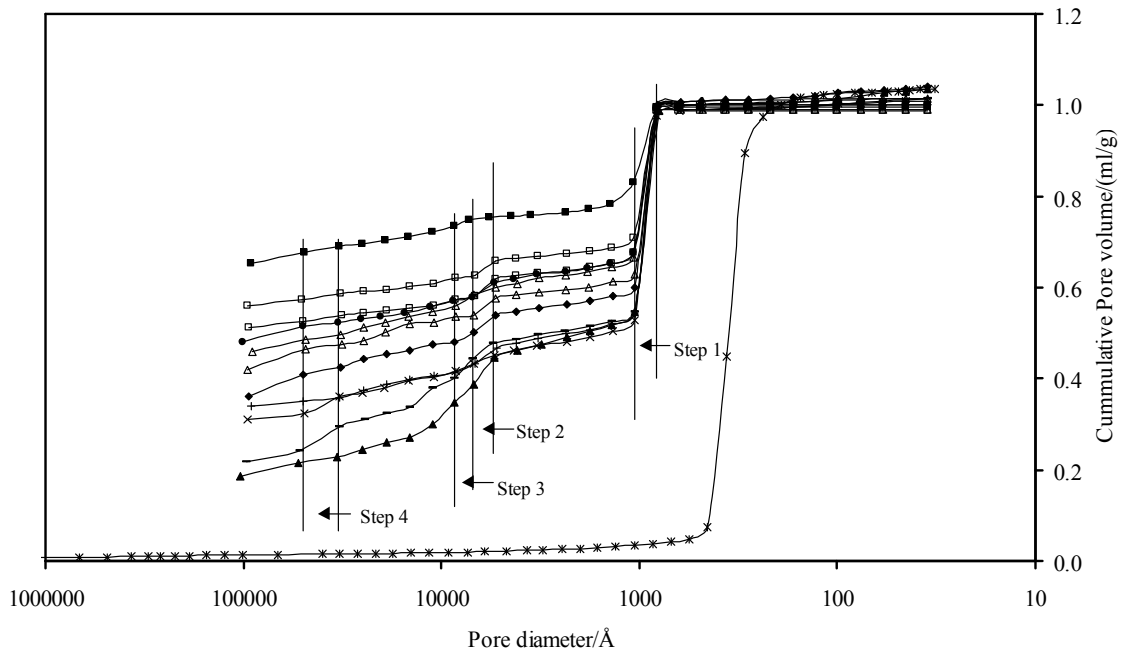

Figure 6.15: Representative mercury intrusion curve (*), and a set of different extrusion curves, obtained with various equilibration times (■, 0 s; □, 10 s; ●, 15 s; △ 20 s; ◆, 30 s; +, 50 s; ×, 80 s; -, 100 s; ▲, 150 s), for C30. The vertical lines demarcate the pressure steps featured in Figures 6.16 and 6.1 7.

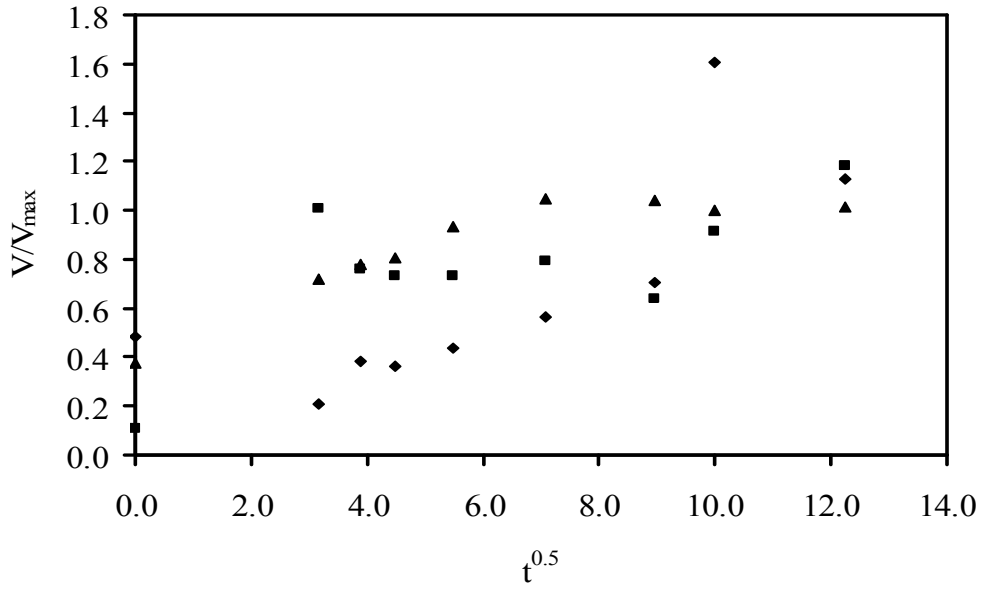

Figure 6.16: Variation of the volume of mercury lost (expressed as a fraction of the amount lost for a reference 150 s equilibration time curve, V_{max}) with the square root of the experimental equilibration time, t, for steps 1 (▲), 2 (■) and 3 (◆) in the C30 mercury retraction curves shown in Figure 6.15.

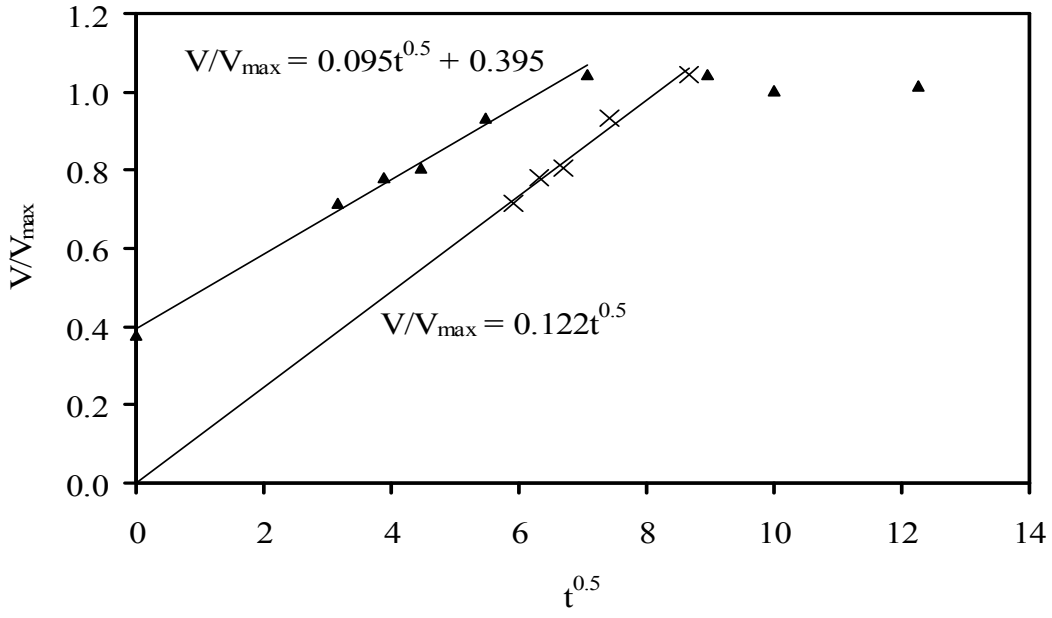

Figure 6.17: Best fit straight lines (and equations) for the variation of the volume of mercury lost for step 1 in Figure 6.15 (expressed as a fraction of the maximum amount lost, V_{max}), with the square root of the programmed experimental equilibration time, t (▲), and with the square root of the renormalized time, t' (×), as defined in the text.

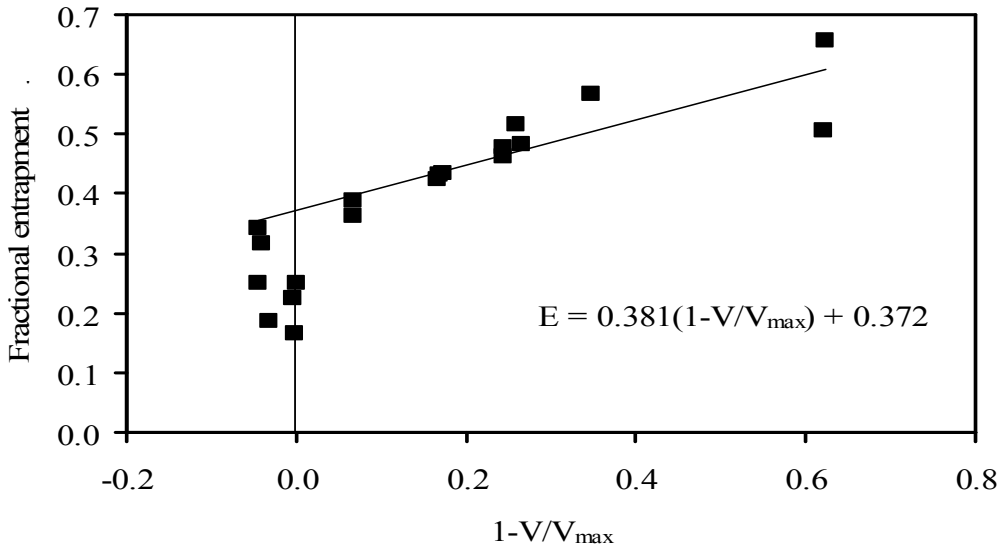

Figure 6.18: Variation of the ultimate, total fractional mercury entrapment with the fraction of the maximum amount of mercury leaving the sample in Step 1 (shown in Figure 6.15) ($1-V/V_{max}$) as equilibration time is varied.

The experimental analysis performed for a range of mesoporous sol- gel silicas within this research has shown a variation in the mercury retraction process of different samples. The initial part of mercury retraction, particularly the first sharp knee, in the extrusion curve of C30 is independent of the experimental time-scale determined by the equilibration time. Hence, it seems likely that the process governing the initiation of retraction in C30 rapidly reaches equilibrium, as it is independent of equilibration time. This suggests that the initiation of retraction is caused by the thinning of the mercury connection at the intersection of large and small pore size regions as the pressure is progressively reduced, as observed in glass micromodels (Wardlaw and McKellar, 1981; Wardlaw 1982). The very small volume decrease in the initial retraction curve plateau is probably thus due to the narrowing of mercury connections at pore intersections. The small volume change before the first knee suggests that the narrowing of the mercury ganglia at intersections is only occurring at a limited number of places. Previous work (Rigby *et al.*, 2006) has shown that mercury entrapment is very sensitive to the numbers of free menisci generated, and thus the above result is a severe test of the model. Analysis of the intermediate part of the retraction curve for C30, between the initial retraction knee and the ultimate final entrapment, suggests that, since the volume leaving the pellets in a given pressure step varies with the square root of equilibration

time, retraction is a flow-rate controlled process, even for nanoporous media. In this study of the effects of varying equilibration time during mercury retraction from C30 it was found that, while step 2 reached equilibrium rapidly, step 3 did not. However, these pressure steps were of similar size and occurred when the total residual amounts of mercury remaining within the sample were very similar, thus it might be expected that similar pathways remained to access the sample surface. Hence, this finding suggests that the pathways for mercury flow from the pores that emptied during step 3 are likely to be longer, fewer in number and/or more tortuous than those for the pores that emptied in step 2. Therefore, the differences in required equilibration time for pores that empty at different pressures suggests the retraction curves obtained at different equilibration times contain information on pore accessibility and connectivity, and can be explored further in future work.

6.11.4 - Investigative Studies of The Mechanisms of Entrapment in (P7129) Silica Pellets Using Integrated Sorption And Mercury Porosimetry.

The nitrogen adsorption isotherm for before and after porosimetry for P7129 can be seen in Figure 6.19, while Figure 6.20 shows the mercury intrusion and extrusion curve. By comparing the BJH PSD before and after Hg, Figure 6.21 shows a shift in the PSD to the left, towards smaller pores suggesting that entrapment causes loss of volume and larger pores. Partial pore filling with entrapped mercury following retraction leads to apparent ‘creation’ of small pores.The ultimate pore volume in the cumulative PSD obtained after porosimetry has been renormalized such that it is the same as the corresponding value obtained before porosimetry. The inset in Figure 6.21 shows schematically how mercury entrapment causes loss of accessible pore volume and larger pores, and partial pore filling leads to the apparent creation of smaller pores. The results obtained suggest that one of the two principle mechanisms reported from experiments on more regular and well-defined, macroscopic glass micromodels by Wardlaw and McKellar (1981) are also observed for complex, irregular, nanoporous solids.

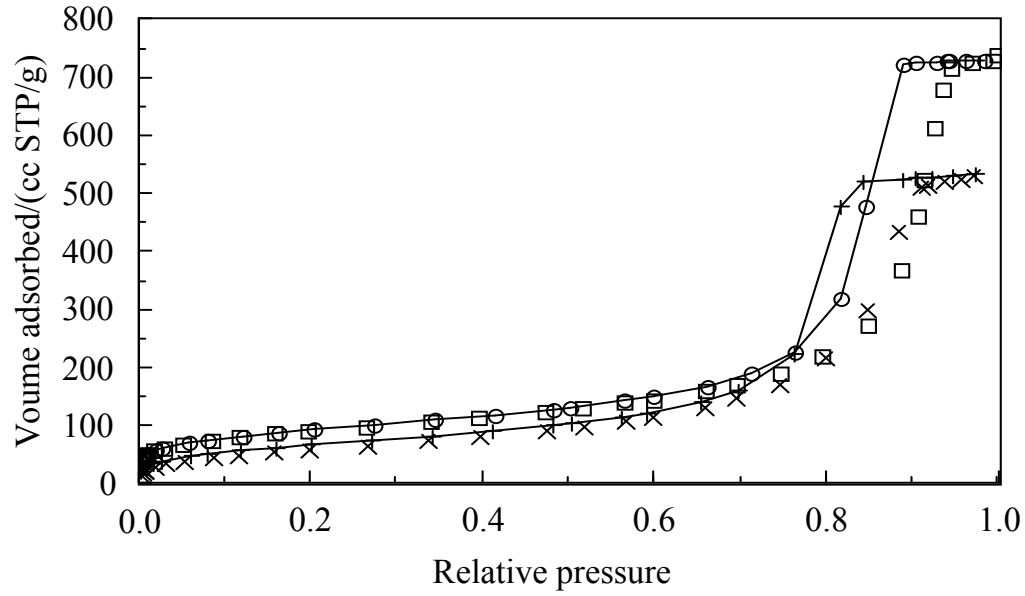

Figure 6.19: Nitrogen sorption Isotherm at 77 K obtained before and after mercury porosimetry on P7129.

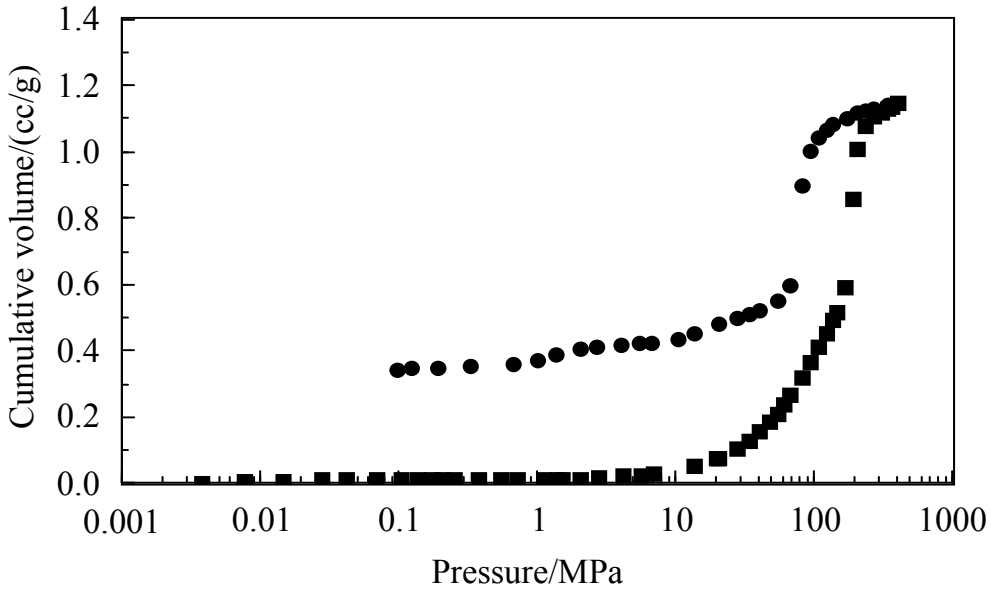

Figure 6.20: P7129 Mercury Porosimetry curve.

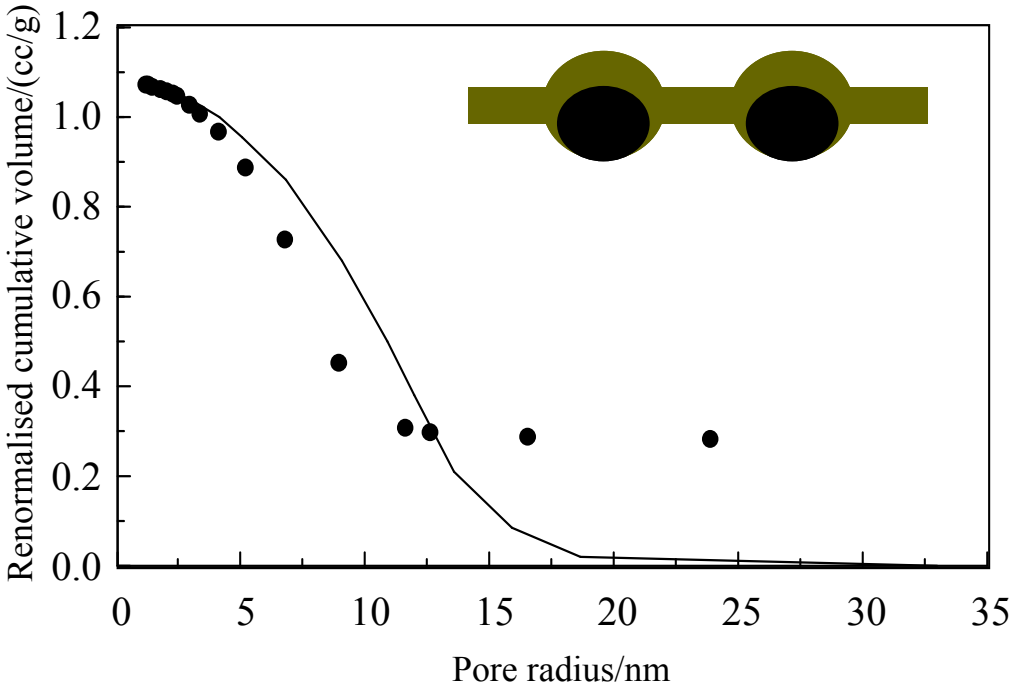

Figure 6.21: BJH cumulative PSDs derived from nitrogen adsorption isotherms obtained before (solid line) and after (●) mercury porosimetry to 414 MPa on P127.

6.11.5 - Studies of the Transport and Quasi-Equilibrium Regime for Q176 - By Use of Integrated Gas Sorption and Mercury Porosimetry

Figure 6.22 shows the raw mercury porosimetry data obtained for Q716 with an equilibration time of 100 s, following an initial nitrogen sorption experiment on the same sample. The nitrogen sorption isotherms obtained prior to and immediately after mercury porosimetry as well as that obtained 7 days following the mercury porosimetry experiment are shown in Figure 6.23. There is a shift in the shape of the isotherms obtained immediately following porosimetry and that of 7 days later; the total pore volume accessible to nitrogen appears to decrease with time. As there has been no additional mercury added to the sample, this suggests that mercury may have moved around during the intervening period altering the accessible void space, but not long enough to make it to the surface and leave the sample.

Electron microscopy of a cross-section of Q176 through a crack in the surface of a sample was reported to reveal its nanoscopic pore structure with apparent cylindrical

type pores (Rigby *et al.*, 2008). Subsequently the nitrogen adsorption isotherms from the integrated experiments of Q176 were analysed using the method of Broeckhoff and de Boer (1968) by Peter Chigada of the Department of Chemical Engineering, University of Bath (Rigby *et al.*, 2008). The Broeckhoff and de Boer method was adopted in order to obtain a better estimation of spherical pores and hence to yield a more accurate pore size distribution. Typical examples of the cumulative distribution curves obtained are shown in Figure 6.24. The nitrogen desorption isotherms were analysed using the BJH method with the Kelvin equation for a hemispherical meniscus. From Figure 6.24, it can be seen that the entrapment of mercury leads to a decrease in accessible pore volume, and loss of larger pores. There is also some apparent growth in the numbers of smaller pores in the adsorption isotherm differential pore body size distribution just like P7129 discussed above. The loss of larger pores, and apparent formation of smaller pores, is again probably due to the partial filling of larger pores with entrapped mercury, as has been seen for glass micro-models with larger pore bodies interspersed with narrower pore necks (Wardlaw and McKellar, 1981; Wardlaw 1982).

The Q176 mercury porosimetry experiments performed at varying equilibration times (see Figure 6.12) show that while the shape of the intrusion curve is independent of equilibration time over the range studied, the shape of the extrusion curve varies with equilibration time. Figure 6.25 shows the mercury intrusion and extrusion data for 15 s and 100 s, comparing short and long equilibration times. At short equilibration time, the extrusion curve is shifted to lower pressures and more entrapment occurs. Q176 intrusion/extrusion data does not exhibit a flat plateau followed by a sharp knee at the onset of retraction like C30, hence the transport regime is different. To further investigate this feature, the pellets from Q176 were fragmented to form a powder (with particle sizes ~10 - 100 m), and mercury porosimetry was performed on the powder with 15 s equilibration time. Figure 6.26 shows a comparison of the porosimetry results for a whole pellet sample run with an equilibration time of 100 s, and a powder sample with an equilibration time of 15 s. For ease of comparison, the intrusion volumes have been divided through by the total specific intra-particle pore volume for each sample and it can be seen that the shape of the mercury extrusion curve (including the final level of entrapment) of the powder data for 15 s is more similar in shape to that of the whole pellet data for 100 s than for 15 s. Hence, the difference in shapes between the

two sets of whole pellet data can be attributed to the longer path for mercury to leave the sample in the whole pellet, thus requiring more time to occur. Based on the above analysis it is therefore proposed that the retraction in Q176 is also controlled by a flow process.

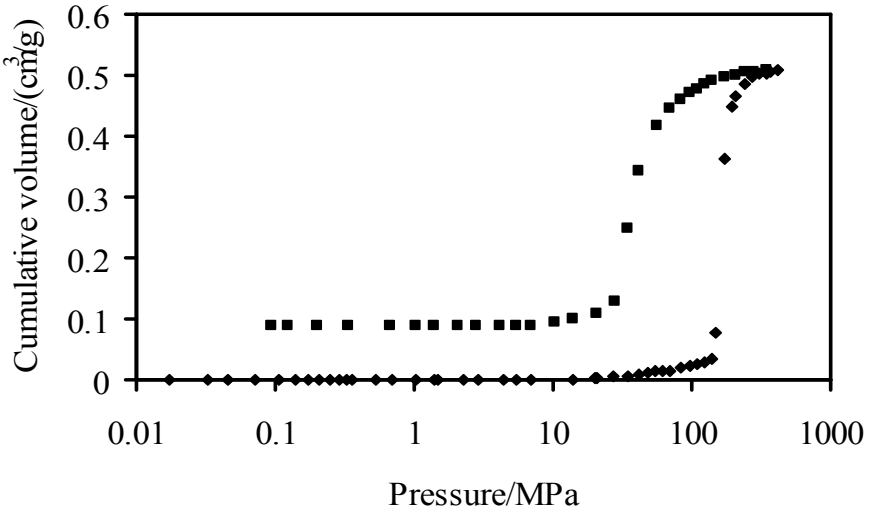

Figure 6.22: Mercury intrusion (◆) and extrusion (■) curves for the same sample of Q176 as was used to obtain the gas sorption data shown in Figure 12.

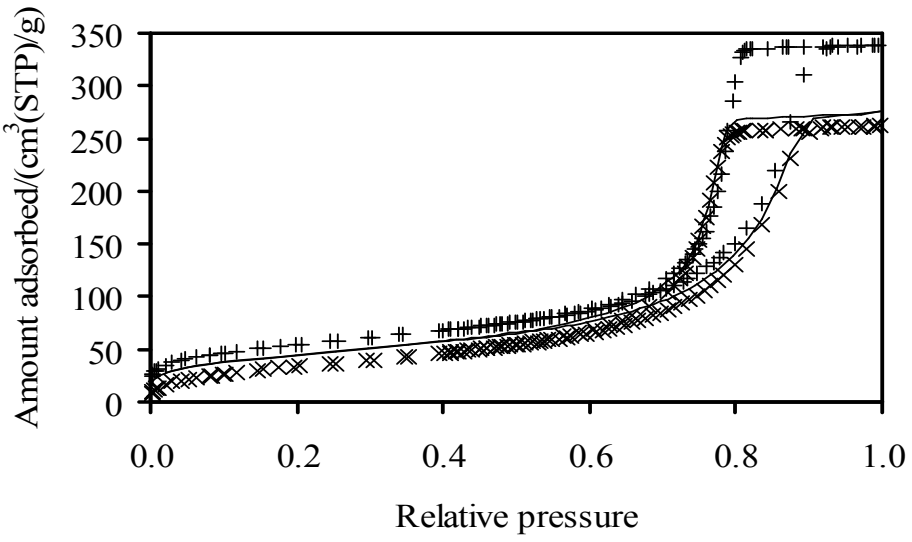

Figure 6.23: Nitrogen sorption isotherms for a single sample of Q176 obtained before mercury porosimetry (+), immediately after porosimetry (line), and 7 days following porosimetry (×).

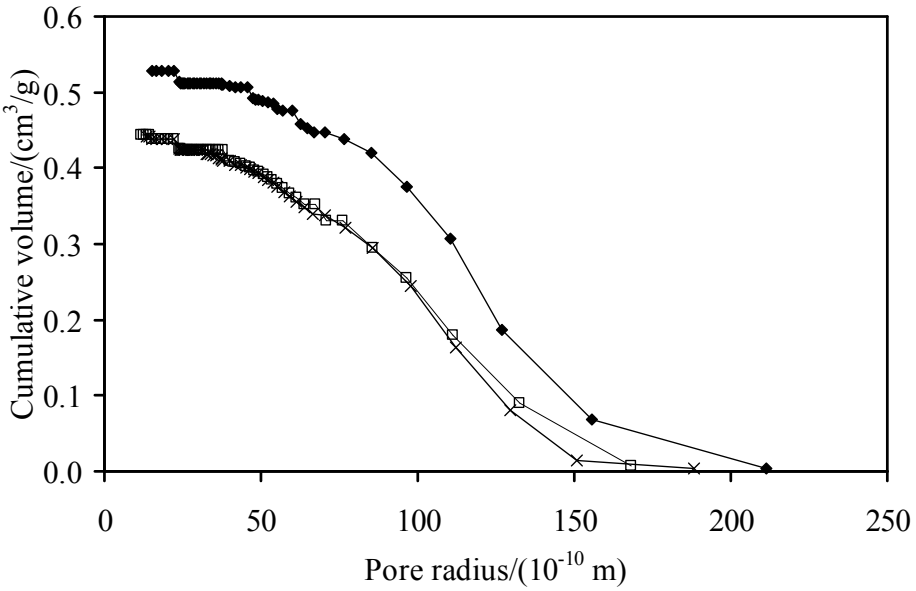

Figure 6.24: (a) Cumulative pore body size distributions, obtained using a Broeckhoff and de Boer (1968) analysis of nitrogen adsorption isotherms, for a sample of Q176 before porosimetry (◆), immediately after porosimetry (□), and 7 days after porosimetry (×). (b) The corresponding differential pore body size distributions, obtained from a Broeckhoff and de Boer (1968) analysis of nitrogen adsorption isotherms, for a sample from Q176 before porosimetry (◆), and immediately after porosimetry (■).

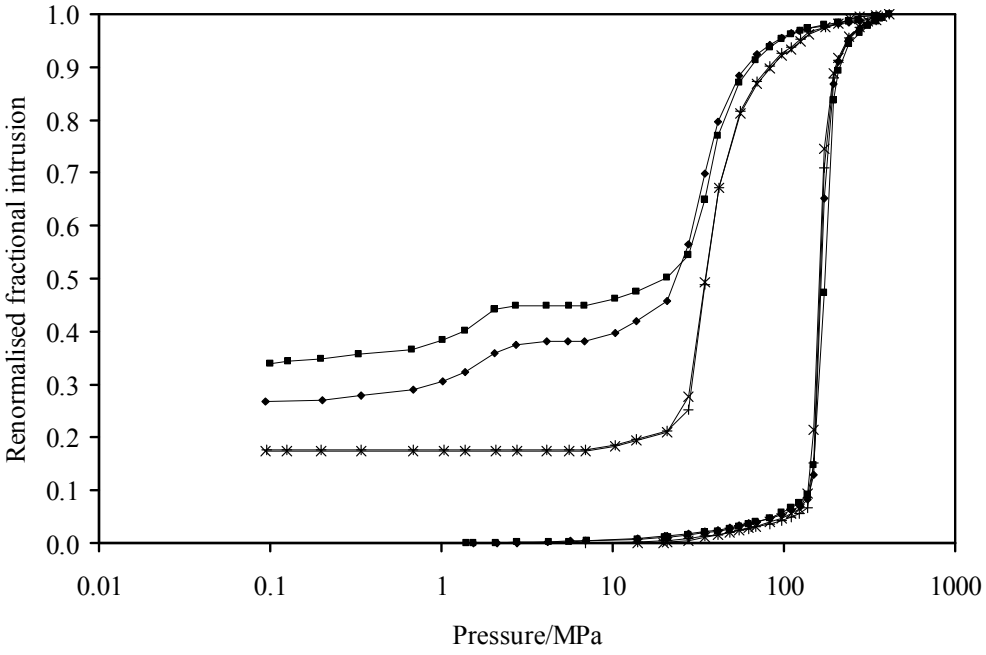

Figure 6.25: Mercury intrusion and extrusion curves for porosimetry experiments conducted on four separate samples from batch Q1 with equilibration times of 15 s(◆ and ■) 100 s (+ and ×). In each case, the cumulative volume has been renormalized by dividing through by the ultimate intruded volume.

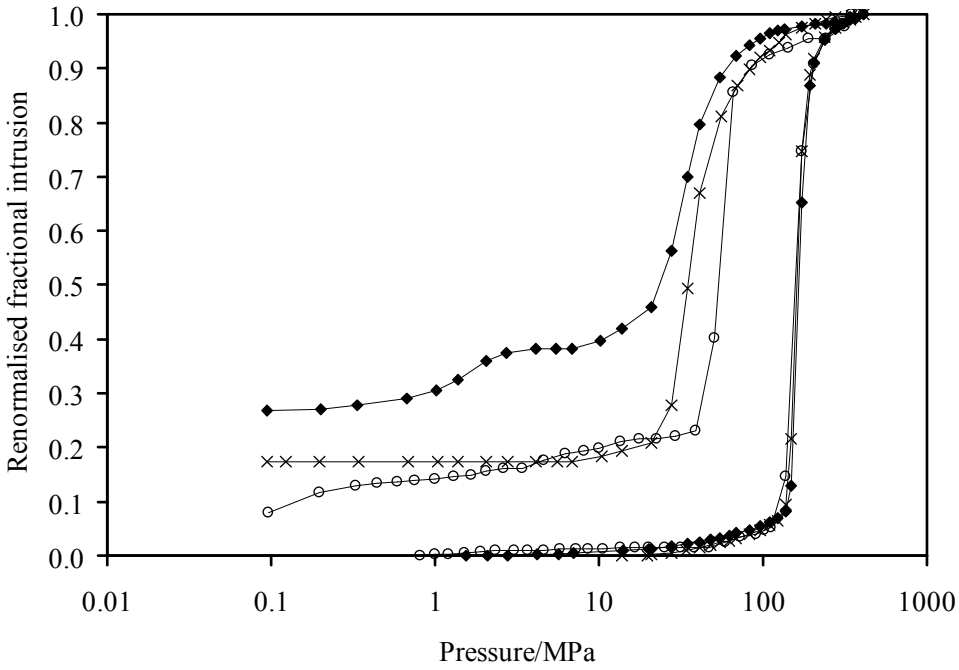

Figure 6.26: Mercury intrusion and extrusion curves for porosimetry experiments conducted on whole pellets samples from batch Q1 with equilibration times of 15 s (◆) and 100 s (×), and for a powder sample with an equilibration time of 15 s (○). The intra-particle, cumulative intrusion volumes have been renormalized by dividing through by the total, intra-particle, specific pore volume obtained from porosimetry.

6.11.6 - Micro-CT Imaging of Q176 pellets

Micro CT (Computed Tomography) is a completely non-destructive technique for providing igh resolution assessments of geometry in the interior of opaque solid objects, and for obtaining digital information on their 3-D geometries and properties. It is useful for a wide range of materials, including rocks, bone, ceramic, metal and soft tissue. Resolutions are typically less than 40 microns. It has the ability to resolve details as small as a few tens of microns in size, even when imaging objects are made of high density materials.

Following porosimetry on Q176, the pellets were imaged using micro-CT whilst containing entrapped mercury. Figure 6.27 shows an example of a 2D slice image and as mercury has a high electron density compared to the surrounding silica, the dark

areas correspond to the void space regions containing entrapped mercury, while the lighter areas correspond to the silica. The spatial distribution of entrapped mercury is seen to be highly heterogeneous. As mercury entrapment has been found to be generally associated with larger pores, the mercury also makes apparent the heterogeneous spatial distribution of larger pores, since entrapped mercury is not distributed throughout the pellet cross-section.

X-ray Images of pellets containing entrapped mercury was run by Taghi Miri, of the Centre for Formulation Engineering, Department of Chemical Engineering, University of Birmingham, U.K.

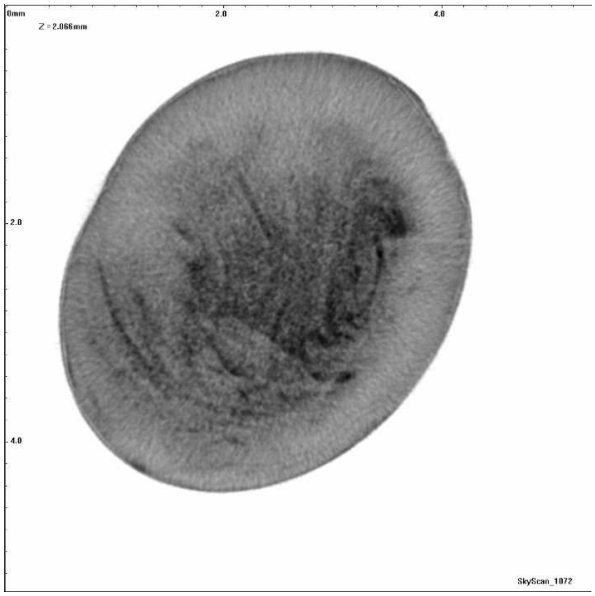

Figure 6.27: CXT images of slice through a pellet of Q176 following porosimetry. The black areas are entrapped mercury, while the grey is the silica matrix.

The initial stages of retraction were independent of equilibration time in Q176 in contrast to C30. This difference may be because of differences in the numbers of free mercury menisci left at the top of the intrusion curve. The mercury intrusion curve for C30 ended in an extended flat plateau indicating that all of the void space had been filled with mercury and there were no free menisci. In contrast, the mercury intrusion curves for Q176 ended before the curve flattens out to a plateau. In addition, there was ~2 % increase in the specific pore volume determined from nitrogen adsorption compared to that determined by mercury intrusion. This suggests that some void space

is probably left unfilled with mercury at the top of the Q176 intrusion curve, thus leading to an underestimation as some mercury-containing pores have free menisci at the junctions with residual empty pores. The results of the integrated gas sorption experiments here also suggest that the form of spatial arrangement of entrapped mercury in Q176 is similar to that observed in glass micromodels of similar pore geometry by Wardlaw and McKellar (1981). The results for glass micromodels with wider pore bodies connected by narrow pore necks are therefore relevant for interpreting mercury retraction in materials exhibiting the above entrapment mechanism like Q176 and P7129.

The study of the relaxation of mercury after porosimetry is useful in investigative studies of the likely flow effects of mercury also present during the porosimetry experiment. The study of the relaxation of mercury following porosimetry makes it possible to assess its rate relative to flow effects when they both occur during the porosimetry retraction experiment. Hence, the relative importance of the effects described above, in the interpretation of mercury retraction curves can be assessed. The above studies show that the relaxation process within the materials studied is so slow that it can probably be neglected when interpreting mercury retraction curves. A better understanding of the relaxation of mercury in nanopores of amorphous materials allows a study to be made of the complex interaction between capillary forces and dispersion forces within a convoluted and confined geometry. Monte-Carlo simulation results have suggested that in some pore models, the strong pore potential arising from close confinement of mercury ganglia may either accelerate the relaxation process or suppress it in others (Rigby *et al.*, 2008).

The CXT images obtained for Q176 (Figure 6.27) and for C30 (Rigby *et al.*, 2006), demonstrate that the spatial distribution of entrapped mercury is highly heterogeneous, on the contrary to findings in literature. Previous work conducted by Androutsopoulos and Mann (1979), had reported that, in almost every case, where a sample is broken to reveal the internal distribution of entrapped mercury it is found to be uniformly distributed. This difference may be due to the fact that the materials studied may have been more macroscopically homogeneous than the materials studied here.

For improved accuracy of the simulation of mercury retraction, the correct pore structural model and appropriate mercury retraction mechanism for a given disordered material can be established, potentially using the methods described above, and then statistical information on the entrapment process from the relevant glass micro-model could be used.

6.12 - Drawbacks in Mercury Analysis

Typical mercury intrusion and extrusion curves exhibit a flat plateau at the region of maximum filling (high pressures). This is an indication that complete filling has been attained and suggests that all pores have been completely filled with mercury. However, for the samples analysed within this research some of the blank run corrections appeared to be insufficient correction for compressibility factors, as some of the experiments that were run at a later stage of the research did not exhibit any of such flat plateaus at the top of the intrusion curve. Also a range of experiments yielded anomalous results (such as 1 % entrapment) on closer examination; it appeared the samples were not penetrated with any mercury at all. This was obviously a result of a machinery malfunction. However for the former a series of exercises were run to identify the cause of the discrepancy. Several adjustments were made to correct this, including running a blank run at varying equilibration times to match the range of equilibration times run during the test analysis. If the discrepancy was a result of the difference in the length of time of exposure to high pressures then this would have accounted for it, however it did not.

The use of both the continuous or incremental mode of analysis has also shown little or no variation in the intrusion curve of test samples and as such one can conclude that the possibility of any discrepancies as a result of temperature differences has also been eliminated. According to Giesche (2006), the continuous mode of mercury porosimetry analysis offers the possibility to run analysis in a very short time and useful in recording a large number of points and consequently allows small differences between samples to be revealed. And in contrast the incremental technique offers better assurance for true equilibrium to be reached for each data point as long as the time interval is sufficiently long enough that temperature effects can be

avoided. Sufficiently long equilibration times (20, 30, 50 and up to 100 s), longer than the general industry standard of 15 s, were allowed for some of the experiments that did not exhibit the flat plateau.

In addition, the resulting mercury intrusion and extrusion curves for the tested porous materials could have been obtained under false estimations of the free space analysis of the penetrometer which could have changed over time as a result of wear due to exposure to excessive high pressures. Under visual examination there was no apparent wear or tear or cracks. Microscopic examination also did not show any cracks liable of causing such discrepancies. The issue of inaccurate empty penetrometer adjustments were eliminated as subsequent repeat experiments showed further discrepancies at such close time scales that could not have amounted to relevant wear. Further work is required before conclusions can be made about the discrepancies noted in some experiments around the region of the top of the intrusion curve and the onset of retraction, pertaining to the suitability of the compressibility correction factor and free space analysis in these experiments. So far within this research, the reason for this discrepancy has been narrowed down to a combination of the effect of poor performance of the porosimeter, limitation of the highest pressure obtainable (~414 MPa) and/or difficulties relating to the existence of small pores in samples requiring much higher pressures (>60000 psi) to achieve complete pore filling. An engineer from the manufacturer of the machine identified some worn out banana plugs and a need for more frequent servicing which might have affected the mercury capacitance readings and hence could have led to inaccurate measurements.

After carefully reviewing the mercury porosimetry data, it can be concluded, that the drawback to the mercury analysis leading to the lack of flat plateau is probably an effect of machinery related failures or sample structure dependent alone or a contribution of both. Although there is reason to believe incomplete filling and free menisci exists in the test samples. Therefore further work would be required to clarify/eliminate these issues.

6.13 - Conclusion

The newly introduced integrated nitrogen sorption and mercury porosimetry has been shown to be a useful quality-control method for assessing the homogeneity of the surfactant templated silica materials and also their mechanical stability. Volume hysteresis in mercury porosimetry has been interpreted up to now by the presence of inkbottle pores. The smallest radius of the pore is considered as the limiting factor for the pressure needed for the intrusion of mercury. Equation 6.6, which accounts for contact angle hysteresis has been used to confirm the existence of structural hysteresis, in support of pore blocking effects. The effect of the contact angle hysteresis in the case of $P123_t$ coated in $F127_t$ is evident, though minimal. This is contrary to the significant difference predicted by Kloubek (1981). This suggests that the assumed contact angle (140^o) for mercury on the silica templated porous materials such as those in question ($P123_t$ and $P123_t$ coated in $F127_t$) is a reasonable assumption. Mercury porosimetry studies have demonstrated that the initiation of mercury retraction from one type of sol-gel silica material is independent of equilibration time, and thus probably results from a rapidly equilibrating necking-down process, and subsequent breaking, of the mercury ganglia (intersections) at the boundaries of the region of smallest pores within the material.

It has been shown that integrated gas sorption and mercury porosimetry experiments on mesoporous silica sol gels can be used to study the relaxation of entrapped mercury, and reveal information on the morphology of the remaining void space. In Q176 and P7129, it was also found that one of the two principle mechanisms of entrapment reported from experiments on more regular and well-defined, macroscopic glass micromodels by Wardlaw and McKellar (1981) are also observed for complex, irregular, nanoporous solids. It has been shown that the relaxation process is so slow that it can be neglected in the interpretation of mercury retraction over typical experimental timescales.

The development of a good pore model requires the choosing of a combination of structural parameters and philosophies which make the model sufficiently realistic. This work would help the development of a simple, but more realist model of a porous solid which can be used to simulate mercury porosimetry and to show how to infer the pore connectivity of the model from the final porosimetry curves.

Chapter 7: Conclusions/Future Work and Recommendations

7.1 - Conclusions

The work carried out in this project has shown the importance of using multiple techniques and models to characterise complex heterogeneous catalysts. The work has clearly shown how determining the structural properties of complicated materials can enhance future catalyst and catalyst supports design and for the overall improvement on catalytic performance. The following paragraphs summarise and illustrate the main findings of the work.

The development of mesoporous materials from nanosynthesis techniques has received a great deal of advancement in recent years due to its promising applications in the majority of chemical industries. This thesis has reported on a variety of synthesis methods and explored the ability of creating such materials to particular specifications with regard to the formation of specific structures and pore sizes. The nature and relative amounts of various ingredients required for the synthesis of MCM-type materials can be varied greatly, hence offering a high degree of flexibility for the design of new materials. The issue of the stability of these materials, especially the hydrothermal and mechanical stability, does not meet the requirements for industrial applications, and there is a strong need for extremely stable structures. Notwithstanding, these materials will still, even in the absence of improved stability, offer significant supplementary advantages such as an improved diffusion rates for transport in catalytic processes resulting in faster reactions (Karlsson *et al.*, 1999). Finally, the importance of their use in modelling porous solids for gas adsorption theories as well as for investigating fluid transport properties cannot be emphasized enough.

Substantial amount of evidence has been produced through experimental gas adsorption studies in support of the proposal to create a bimodal structure with two distinctive pore size regions. Completely formed coats on the surface of previously synthesized and uncalcined core particles of an alternative pore size has highlighted the effects of pore blocking, and supporting phenomena such as the inkbottle theory for the explanation of

the reduced rate of adsorption or hindered desorption. The structural characterization and analysis of these synthesised materials has improved the understanding of the behaviour of several porous media.

A number of surfactant micelles including Brij 56, Brij 76, and the tri-block copolymers P123, and F127 have been used to synthesize bimodal porous solids. The core materials with pore sizes in the range 4 - 10 nm were encased in a silica material templated with CTAB, a surfactant generating significantly smaller pore sizes. All experiments performed on these bimodal samples having a mesoporous internal with a microporous coat were in agreement in providing supporting evidence for pore blocking effects in composite materials with a microporous outer shell and a mesoporous core. The BET surface area of the coated samples also showed an increase in comparison to the average surface area of the core material, suggesting the existence of a completely formed coat around the core material. The reverse combination of the above bi-modal structure were also synthesized, and the outer regions comprised of mesoporous coats of P123, F127, Brij 56, Brij 76, which offered no restriction to the desorption rate indicating a lack of shielding effect of the kind attributable to blockages caused by small pores. There was also an observed increase in the maximum volume adsorbed compared to the core alone confirming the existence of an outer shell of a mesoporous nature. It has also been shown, that a range of size modification experiments can be performed to produce materials independent of the standard surfactant chain lengths. The microscopy results of the method of silica templating with PS beads shown in Section 3.8.1 confirms that heterogeneous solids with pore sizes of ~100 nm have been successfully synthesized. These materials could be used to model reservoir rocks with a variety of pore to throat size ratios. Also for invasion processes where the pore body to neck ratio played a very important role, this is an essential progression.

The occurrence of the two-step hysteresis loop and reduced diffusion rate constants observed in the isotherms of the bimodal materials suggests that catalyst supports, or speciality materials, that possess engineered diffusion barriers have been successfully synthesized. The kinetics of gas uptake in the synthesised core and bimodal porous materials have also been shown to follow the linear driving force (LDF) model, and it has been used to obtain values of the mass transfer coefficient of butane and cyclohexane in the synthesised materials and hence their diffusivities. Adding a

microporous coat (CTAB) to a mesoporous core (such as P123, F127 and Brij 76) brings down the diffusion coefficient in line with the decrease in modal pore diameter.

A comparative study of the mass transfer coefficients (k) of adsorbate within the region of capillary condensation for water vapour sorption, cyclohexane sorption and nitrogen scanning loop in one type of sol gel silica has shown that in the case of nitrogen adsorption, hysteresis is caused by pore blocking effects. There was no apparent hysteresis in the case of cyclohexane sorption and hence the resulting k values showed no substantial variation between adsorption and desorption. For the water vapour adsorption experiments, capillary hysteresis loops were observed for all four experiments, however the k values obtained across both the adsorption and desorption branches, show no variation and hence one is led to conclude that the pathway for the evaporation of water vapour is exactly the same as for the condensation of water vapour. Therefore the water vapour adsorption analysis confirms that hysteresis does not occur as a result of a variation in pathways for evaporation, and hence not a result of pore blocking effects. For the nitrogen scanning loops, it is further confirmed that even for the least likely possibility of pore blocking effects, capillary condensation hysteresis occurs. The variations in the k values confirm that there is a difference in the diffusivity of nitrogen during adsorption, compared to during the evaporation of condensate. Therefore one can conclude that hysteresis occurs for nitrogen sorption in silica sol gels of type C10 as a result of pore blocking effect arising from a difference in the geometry and connectivity of the liquid phase along the two branches and is thus best described by interconnectivity models.

The comparison of the diffusion rate constants of two adsorbates with similarly low affinity for silica solids, (cyclohexane and water vapour) on one type of sol gel silica pellet have shown that their adsorption kinetics follow the LDF model, and are consistent with diffusion through a barrier being the rate determining step. For the same sample adsorptive, the kinetics of water vapour was shown to produce a peculiar trend in the rate constant across the two branches of the isotherm which is significantly different to that displayed by cyclohexane vapour adsorption. Pore blocking effects in the former is believed to have occurred as a result of the formation of water clusters on active sites which lead to a ‘piggy back’ effect developing a barrier to diffusion and hence a decrease in the rate constants. The observation of a steep decline in the water

adsorption kinetics on the C10 silica pellets at low relative pressures (low surface coverage) can therefore be explained by the percolation theory, where the percolation threshold is reached and at least 70 - 75 % of the passage through the pore space for the vapour phase is blocked. The rate constant for cyclohexane diffusion in C10 silica pellets is gradually increasing for adsorption and vice versa for desorption as one will expect under a very small degree of variation in an exponential fit. The decrease in the entire range of cyclohexane adsorption is less steep than that evident in only 10 % of pore coverage in water vapour adsorption. As a result one is led to conclude that the adsorption mechanism for water adsorption is markedly different from that of simple non-associating molecules such as cyclohexane and other hydrocarbons on silica pellets and in general a mesopore blocking mechanism exists for water adsorption into a silicate mesoporous adsorbent of this type.

The effect of varying pore shapes, and features that affect only a small portion of the pore, such as neck constrictions, as well as the effect of pore size ratio on the adsorption and desorption behaviour of mesoporous materials, can not be underestimated. Experimental gas adsorption studies have been performed on a regular ordered mesoporous material aimed at identifying the effect of pore neck to throat correlation manifestations in terms of advanced or delayed condensation determined by the cylindrical or hemispherical meniscus. Experimental studies of one type of sol gel silica showed that for very long pores (such as the ones observed for S980G), there is no difference between the pressure for capillary condensation in a cylindrical meniscus and a hemispherical meniscus. Hence advanced condensation effects can not have an impact on the adsorptive behaviours of such materials.

The fractal approach was used to analyse the effect of surface roughness on the interaction energy between the adsorbate and adsorptive, and a fractal dimension was shown to be a characteristic empirical parameter for test samples under similar operational conditions, and hence can be used to provide additional information towards core characterisation. In conjunction with published data, the fractal dimension of C10, C30, S980G silica pellets and F127 and P123 surfactant templated material have been shown to have a direct relationship with the energy of activation (molar net enthalpy of adsorption), in which a higher fractal dimension results in a higher net molar energy for the comparisons carried out within this research, and could provide valuable

information towards comparative studies of model porous solids under similar conditions. In the petroleum industry, the fractal analysis of model porous materials or reservoir rocks could be an added advantage during the conversion and application of laboratory results to avoid underestimating the effect of surface irregularities.

The surface fractal dimensions measured from butane and cyclohexane adsorption are closely related, within experimental error, to those obtained from SAXS for silica materials suggesting gas adsorption in these systems are consistently well described by the FHH fractal theory and hence in agreement with the work of Watt-Smith *et al.* (2005). The adsorption of butane on the surface of rough mesoporous silica samples investigated within this research were shown to be well-described by both the fractal FHH and BET theories, and is in agreement with the experimental studies of such systems reported by Watt-Smith *et al.* (2005), but in contrast with the corresponding results observed for nitrogen by several researchers (Ross *et al.*, 1988; Ma *et al.*, 1999; Watt-smith *et al.*, 2005) which were more mixed. The results suggest that nitrogen behaves differently to butane adsorption on a rough silica surface as it shows specific adsorption on the surface of the hydroxylated pellets, whereas both butane and cyclohexane do not. It is postulated that nitrogen only adsorbs on a fraction of the silica surface area potentially accessible to it, whereas hydrocarbons such as butane and cyclohexane probably adsorbs across the whole surface. This hypothesis can be validated by the fact that the BET areas from nitrogen adsorption are consistently lower than those obtained for butane and cyclohexane. This concept is in accordance with what would be expected if nitrogen tends to adsorb upon specific surface patches on partially dehydroxylated silicas. It is suggested that these patches may be associated with regions of higher concentrations of hydroxyl groups on the surface. The experimental studies of the theory of fractility have shown the importance of characterising porous catalysts using a variety of gases, and by employing different models.

Mercury porosimetry has also been shown to be a very useful method for analysing the structure of mesoporous media. The newly introduced integrated nitrogen sorption and mercury porosimetry has been shown to be a useful quality-control method for assessing the homogeneity of the surfactant templated silica materials and also their mechanical stability. All test materials retained structural integrity, except for the F127

core material, which appeared to be crushed by the high pressures employed in mercury porosimetry. It was suspected to be a hyperporous type material. Volume hysteresis in mercury porosimetry has been interpreted up to now by the presence of inkbottle pores. The smallest radius of the pore is considered as the limiting factor for the pressure needed for the intrusion of mercury. Equation 6.6, which accounts for contact angle hysteresis by the use of semi-empirical alternatives, has been used to confirm the existence of structural hysteresis, in support of pore blocking effects. The effect of the contact angle hysteresis in the case of P123 coated in F127 is evident, though minimal. This is contrary to the significant difference predicted by Kloubek (1981). This suggests that the assumed contact angle (140^{o}) for mercury on the silica templated porous materials such as those in question (P123 and P123 coated in F127) is a reasonable assumption.

Mercury porosimetry studies carried out within this research has revealed that the initiation of mercury retraction from one type of mesoporous sol-gel silica is independent of equilibration time. It is thus probably a result of rapid equilibration of the necking-down process and subsequent breaking, of the mercury ganglia at the boundaries of the region of smallest pores within the material. This theory has been confirmed by step-wise experiments ran within this research and also by modelling studies using structural models obtained from MRI by Rigby *et al.* (2008). The use of nitrogen sorption experiments as an integrated part of mercury porosimetry can also be used to study the mechanisms of entrapment of the non-wetting phase in porous materials down to the nanometre scale. It was also shown, for two different sol gel silicas investigated within this research, that the newly introduced integrated gas sorption experiments can be used to distinguish different mechanisms for mercury entrapment within nanopores. Studies on Q17/6 and P7129 sol gel silicas revealed that one of the two principle mechanisms of entrapment previously reported from experiments on more regular and well-defined macroscopic glass micromodels, by Wardlaw and Mckellar (1981) are also observed for such complex, irregular, nanoporous solids. Also micro-CT imaging of pellets following mercury retraction over a period of several days has shown that the relaxation process is so slow that it can be reasonably neglected in the interpretation of mercury retraction over typical experimental timescales (Rigby *et al.*, 2008). The development of a good pore model requires the choosing of a combination of structural parameters and philosophies which

make the model sufficiently realistic. This work would help the development of a simple, but more realist model of a porous solid which can be used to simulate mercury porosimetry and to show how to infer the pore connectivity of the model from the final porosimetry curves.

7.2 - Problems Encountered With Weak Structured Particles

Difficulties were encountered in the production of the core materials and in the coating of bimodal materials. The first few attempts were weaker in structure having visible cracks. It was difficult to pick them up, and trying to immense them in coats was hardly possible, and if it was possible, the samples disintegrated. After mastering the act of synthesis resulting samples were stronger and glassier. When the evacuation procedure for methanol was carried out for longer, which resulted in the pre-oven solution being extremely viscous, the resulting particles were stronger. One is led to believe that a significant amount of methanol was left in the previous set of solutions, and that was the reason why it was very fragile even after solidification. When coating samples, it was found that it's essential that particles were coated at the right stage in the synthesis process, as the most stable bimodal structures were achieved after the cores had formed in the oven at the set temperature and have been allowed to dry off gradually over several days. A combination of this process and the preparation of a viscous coat ensured the successful production of bimodal particles.

7.3 - Future Work and Recommendation

The work contained within this thesis has shown the importance of, and benefits of the methods and techniques used to successfully characterise mesoporous nanomaterials used as catalysts or support materials in chemical industries. Possible suggestions for extensions to the work contained in this thesis are:

7.3.1 - Computer simulations

Computer simulations could be used to simulate the steady state and transient diffusion coefficients in a range of adsorbents with various engineered pore structures. Future work could look at a compilation of the gas adsorption data, by a Monte Carlo type simulation, to simulate the motion of adsorptives diffusing into a pore. Molecular dynamics studies can be carried out for cyclohexane and water vapour adsorption by solving the Newton's law of motion for the adsorbed phase, to envisage the adsorption mechanism for these two adsorbates that have showed a difference in the trends of mass transfer coefficient obtained from gas adsorption despite their similarities in the gas adsorption isotherm.

In line with the work of Muller *et al.* (1996), where they modelled water adsorption in carbonate slit shaped type pores, computer simulations could be employed to interpret water adsorption in cylindrical pores, as is the case with the synthesised mesoporous silica solids, for further understanding.

7.3.2 - Synthesis of More Complex Heterogeneous Materials

The present study has considered the adsorption properties of the synthesised materials, including the homogeneous porous silica solids, and the non-random heterogeneous bimodal solids. The synthesis of bi-modal solids could be extended to create a material with a thicker outer coat, presumably by subsequent coating, which may lead to a more pronounced shielding effect than can be achieved by one layer of coating. Further studies should also investigate the effects of a more random heterogeneity, which could be achieved by synthesising a material with distinctive regions embedded within the porous structure. A hierarchical structure, combining the use of synthetic latex spheres to produce 3D interconnected macroporosity, and block copolymer to produce mesoporosity, in addition to individual polymer templating to produce microporosity, has recently been synthesised by Sen *et al.* (2003). There has also been a report on a process of making porous silica materials by inducing phase separation with a chemical trigger. Nakanishi *et al.* (1991) report on a method where water-soluble polymers are used to induce phase separation in a sol-gel silica system. This can be classified into

two groups. Firstly, polymers having comparatively weak interaction with silica are mainly partitioned into a different phase from silica when phase separation occurs, and the polymer rich phase forms pores. Secondly, surfactants and polymers that include polyoxyethylene units are partitioned into the same phase as silica owing to the formation of hydrogen bonds with silanol radicals; therefore it is mainly the phase comprising the solvent phase that becomes pores. The above developments suggest that more complicated materials could be synthesised to achieve desired outcomes.

Since the wettability of a porous media will strongly affect its relative permeability, and control the location, flow and distribution of fluids in a porous media, further work should consider using a pre-wetted sample either to achieve an oil-wet system or a water-wet system. The second method of synthesis within this research could also be explored further by investigating the affinity of the synthesised materials based on their surface chemistries to different adsorbates.

7.3.3 - Scanning Electron Microscopy and Transmission Electron Microscopy

Further work should include the use of techniques such as small angle scattering, and SEM, and TEM to confirm the highly uniform and ordered structures of the synthesised materials. This will also be useful in confirming that the materials synthesised from the same surfactants but with different silica sources are truly of the same size and structure, but yet still lead to different adsorption properties as a result of the difference in surface chemistries alone.

7.3.4 – Modification to the LDF Model

The LDF model has been used to analyse the mass transfer coefficients of various adsorbates within this research, and although the model was followed for most parts of the isotherm, a model could be developed to account for the drawbacks highlighted within this research. Further work could include performing diffusion experiments and modelling of diffusion patterns for controlled rates, and then comparing the results with mathematical models in which data on factors that influence the D values described in

the thesis have been utilised, such as the temperature and the effects of surface chemistries and fractals. Future work could also include an investigation into why values of mass transfer coefficient *k* varies at low pressure, and matches closely at high pressures for both branches of water vapour sorption.

7.3.5 - Magnetic Resonance Imaging

It would be beneficial to use magnetic resonance imaging to investigate the structure of a wider range of samples of porous catalyst pellets, and thus build-up a greater library of structural data for a large number of samples. Future experiments could include employing MRI to investigate the adsorption of water within the pellets. This would be done by performing imaging experiments of water at different vapour pressures, and hence would allow the imaging of an adsorption isotherm. This would give additional information into the uptake properties of the materials, and could be compared to data obtained using the IGA.

7.3.6 - Gas Adsorption and Kinetics

The gas adsorption data obtained throughout the work has shown the validity of the models used, and has given a better understanding of the pellets examined. It would therefore be beneficial to investigate the structural properties and behaviour of more pellets and gases to fully explore this area of research. This would allow for a wider representation of these types of catalyst support pellets, and would provide vital information that could be beneficial to industry. It would be useful to pair-up samples that have been examined by adsorption with MRI images to fully characterise the materials investigated. The resultant MR images and adsorption data for a wider extent of materials could then be used to predict the adsorption kinetics for a wider selection of materials and gases. This would allow for a greater understanding and description of the physical processes taking place within the pellets.

7.3.7 - Mercury Retraction Curve

In the studies of the effects of varying equilibration time on mercury retraction in C30, retraction step 2 was found to reach equilibrium rapidly while step 3 did not, even though these pressure steps were of similar size and had very similar total residual mercury (amount contained in sample). One would expect that similar pathways remained to access the sample surface at these stages; hence, this finding suggests that the pathways for mercury flow from the pores that emptied during step 3 are different from that in step 2. They may either be longer, less in number and/or more tortuous than those pores that emptied during step 2. Further work could be carried out to investigate the depth of information obtainable through exploring the link between the retraction curves obtained at different equilibration times and the information they contain on pore accessibility and connectivity.

7.4 - Preliminary Work - Closure Point of Hysteresis Loops and Variation with Temperature Changes

Investigative studies of the pore hysteresis critical point has been carried out by running cyclohexane adsorption experiments on C10, a sol gel ordered mesoporous material at 10 ^{o}C, 15 ^{o}C, 40 ^{o}C and 60 ^{o}C. The range of sorption isotherms obtained can be seen in Figures 7.1-7.4. The point where the hysteresis loop closes which is so far not well understood has been estimated by extrapolating the point of inflection obtained for cyclohexane adsorption and desorption data at 3 different temperatures (10 ^{o}C, 40 ^{o}C and 60 ^{o}C) as shown in Figure 7.5. The point where the adsorption and desorption data intersect was calculated to be at an approximate temperature reading of 132 ^{o}C and could be considered a valid prediction of when the hysteresis loop will shut down. It is worthy to note that the critical temperature of cyclohexane is 280 ^{o}C. The hysteresis critical point (i.e T when the hysteresis disappears) will be less than the critical temperature of cyclohexane. Anomalous behaviour is expected at temperatures close to the critical point.

Figure 7.5 shows the points obtained and they seem to be arranged in a curve like manner before the desorption and adsorption line meet, as a result only the first two data

were fitted in obtaining the estimate of the hysteresis critical temperature in Figure 7.6. The temperatures ran within this preliminary work was within the range of 10 ^{o}C - 60 ^{o}C, the shrinking of the hysteresis loop was apparent and the prediction of complete shutting of the loop at about 132 ^{o}C seems about right. Due to operational constraints of obtaining reliable isotherms at temperatures higher than 60 ^{o}C this could not be confirmed experimentally, however the widths of the hysteresis loop have been confirmed to shrink with increase in temperature.

Future work would look at estimating the critical temperature at which the region of irreversibility disappears by obtaining the pore hysteresis critical point for a range of adsorptives using different adsorbents, and hence obtain useful information towards the understanding of the contributors to hysteresis and differentiating between the effects attributable to adsorbate - adsorbant interactions, multiphase interactions as well as temperature to pressure and van der Waals forces.

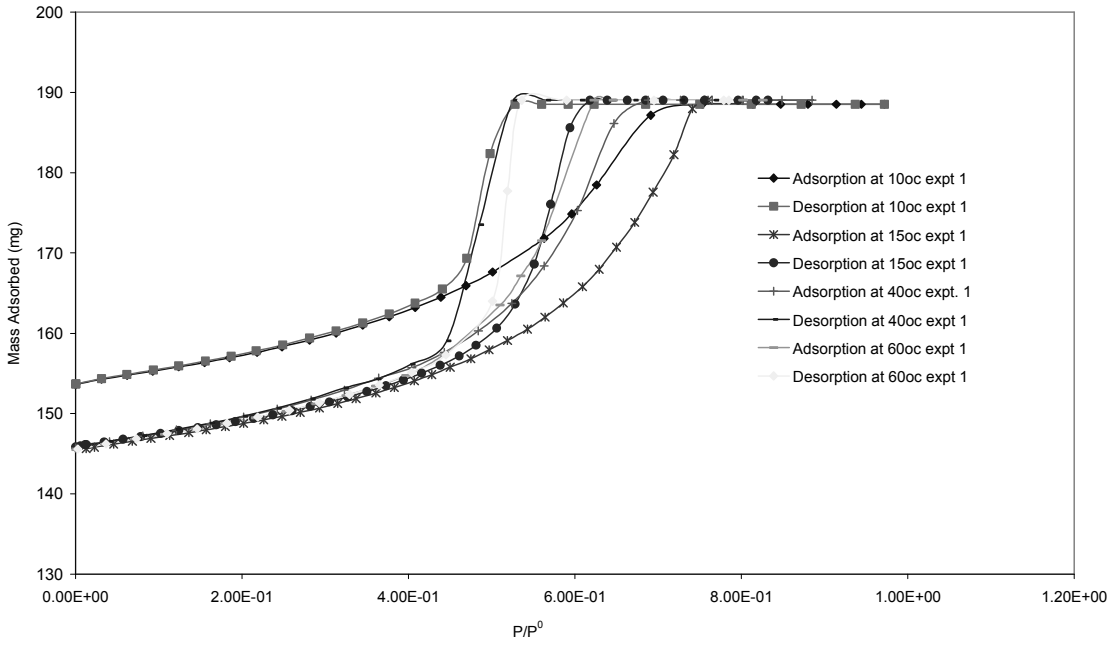

Figure 7.1: Cyclohexane sorption isotherms on C10 pellets at various temperatures.

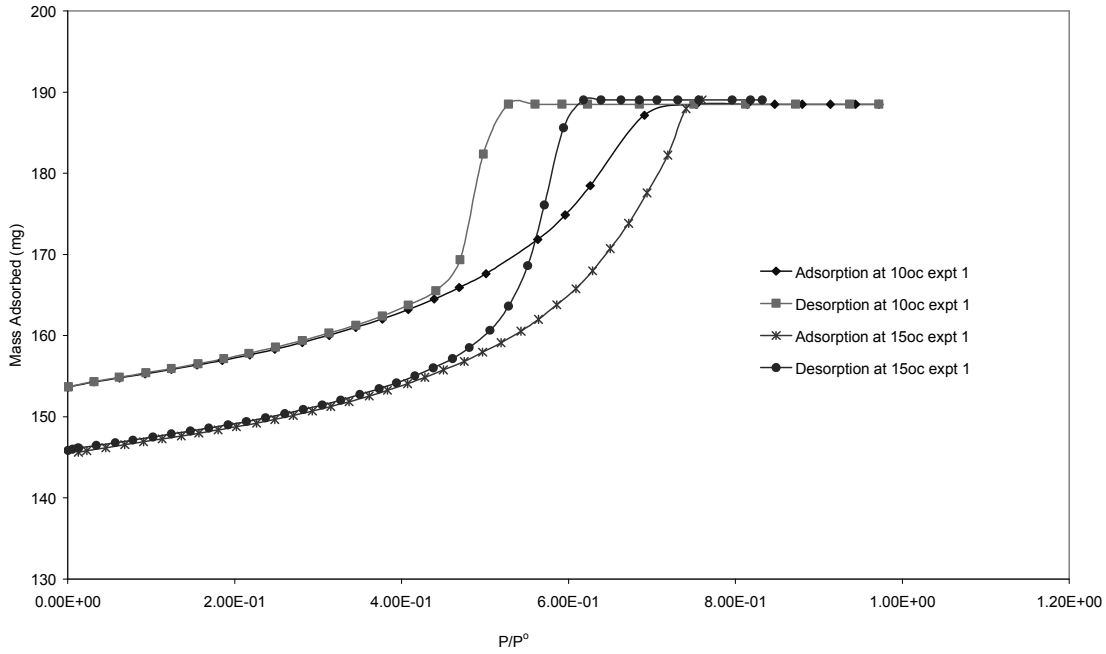

Figure 7.2: Cyclohexane sorption isotherms at 10 °C and 15 °C on C10 pellets.

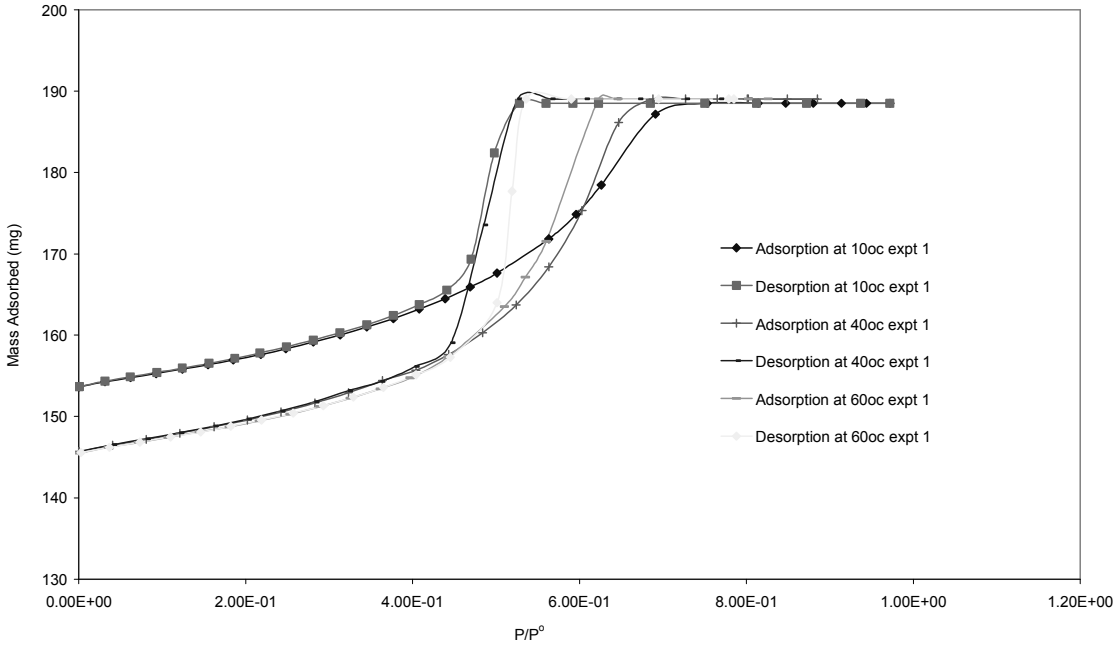

Figure 7.3: Cyclohexane sorption isotherms at 10 °C, 40 °C and 60 °C on C10 pellets.

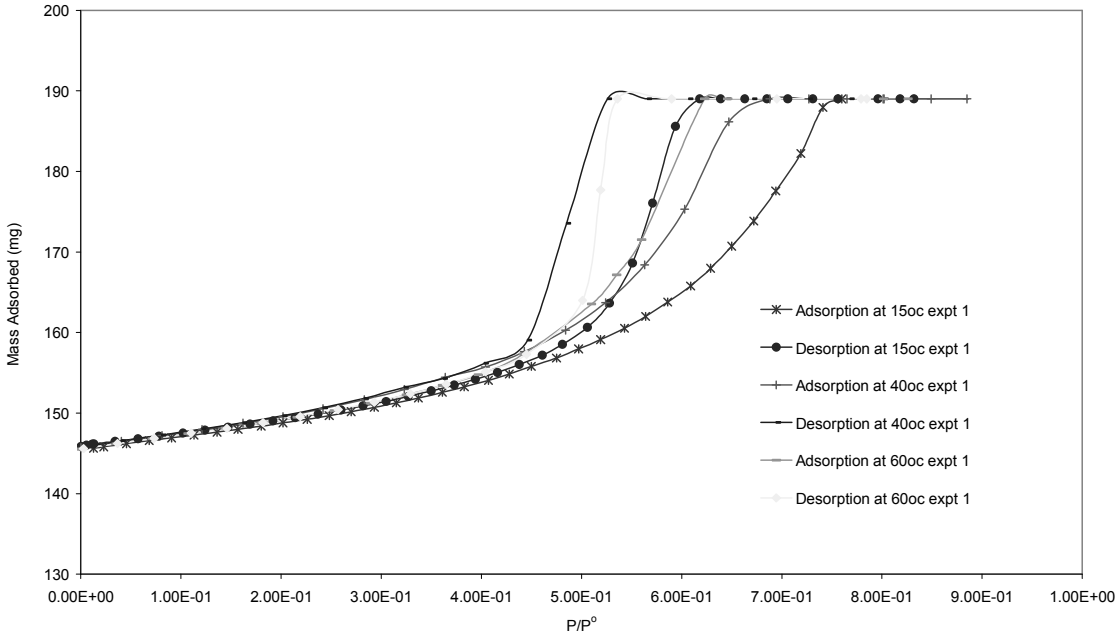

Figure 7.4: Cyclohexane sorption isotherms at 15 °C, 40 °C and 60 °C on C10 pellets.

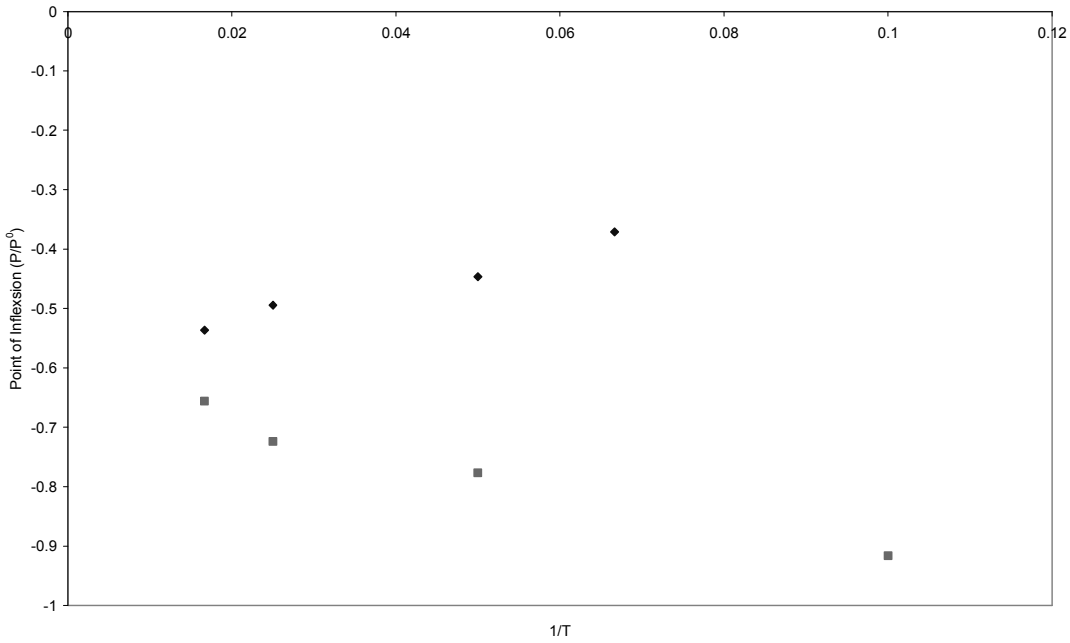

Figure 7.5: Inflexion point vs. 1/T for C10 cyclohexane isotherms at 15 °C, 20 °C, 40 °C and 60 °C.

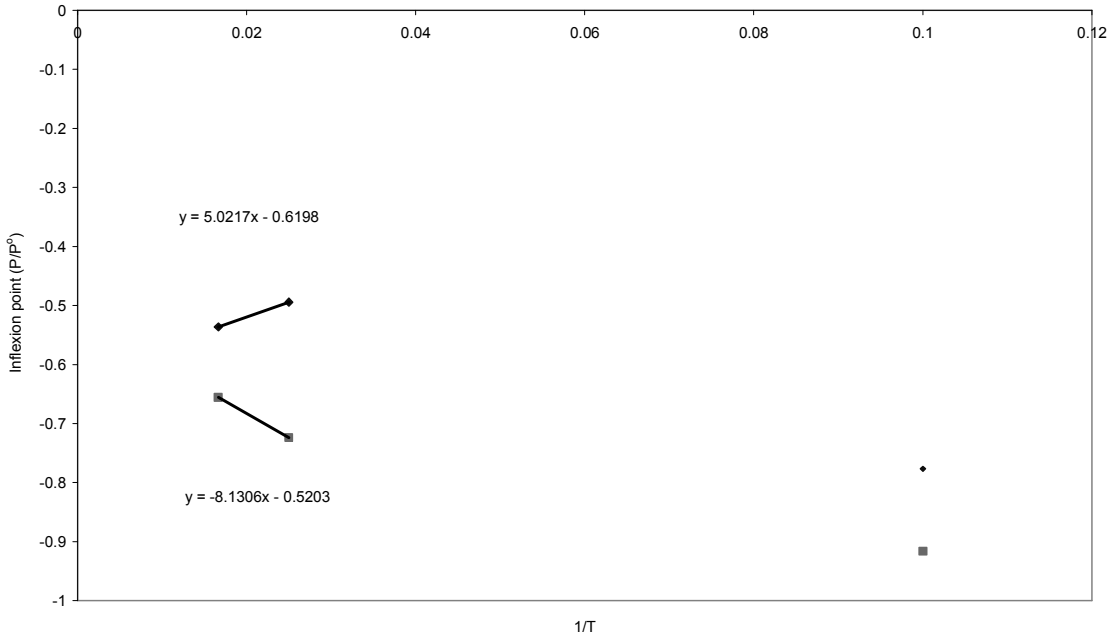

Figure 7.6: Extrapolation of the inflexion points vs. 1/T for C10 cyclohexane sorption isotherms on C10.

References

1. Allen, T., Particle size measurement. Fifth edition. Dordrecht, The Netherlands: Kluwer Academic publishers. 1997. **2**: p. 251.

2. Anderson, W.G., In Wettability literature survey - Part 6: The effects of wettability on waterflooding, J. Pet. Technol.; (United States), 1987. **39**: p. 12.

3. Androutsopoulos, G.P. and Mann, R. Chem. Eng. Sci., 1979. **34(10)**: p. 1203-1212.

4. Androutsopoulos, G.P., Papakonstantopoulos, G.D., Philippopoulos, C.J., Chem. Eng. Sci., 2001. **56**(18): p. 5413-5417. C

5. Androutsopoulos, G.P. and Constantinos, E.S., Ind. Eng. Chem, 2000. **39**: p. 3747 – 3763.

6. Attard, G.S., Glyde, J.C. and Goltner, C.G., Nature, 1995. **378**: p. 366-378.

7. Aydin, A., Marine and Petroleum Geology, 2000. **17**: p. 797-814.

8. Bagshaw, S.A., Prouzet, E. and Pinnavaia, T.J., Science, 1995. **269**: p. 1242-1244.

9. Barrer, R.M., Barrer, F.R.S. and Gabor, T., Proceedings of the Royal Society of London. Series A, Mathematical and Physical Sciences, 1959. **251**: No. 1266, p. 353-368

10. Barrett, E.P., L.G. Joyner, and P.P. Halenda., J. Am. Chem. Soc, 1951. **73**: p. 373.

11. Bashforth, F. and Adams, C., An Attempt to Test The Theory of Capillary Action. 1883. Cambridge University Press, Cambridge.

12. Beck, J.S., et al., A New Family of Mesoporous Molecular Sieves Prepared with Liquid Crystal Templates. J. Am. Chem. Soc, 1992. **114**: p. 10835.

13. Beck, J.S., Method for Synthesizing Mesoporous Material. 1991. US Patent 5,057,296.

14. Beck, J.S. and Vartuli, J.C., Curr. Opin. Solid State Mater. Sci, 1996. **1**: p. 76.

15. Berenguer-Murcia, A., et al., J. Phys. Chem. B, 2003. **107**: p. 1012-1020.

16. Bloch, F., W. Hansen, and M. Packard, Phys. Rev., 1946. **69**: p. 127.

17. Bloch, F., Hansen, W. and Packard, M., Phys. Rev., 1946. **70**: p. 474.

18. Branton, P.J., Hall, P.G. and Sing, S.W., Adsorption, 1995. **1**: p. 77-82.

19. Braymer, T.A., Coe, C.G., Farris, T.S., Gaffney, T.R., Schork J.M. and Armor, J.N., Carbon, 1994. **32**(3): p. 445-452.

20. Broekhoff, J.C.P., and de Boer, J.H., Journal of Catalysis, 1968. **10**: p. 153-165.

21. Broekhoff J.C.P. and van Dongen R.H. In: Physical and Chemical aspects of adsorbents and catalysts (ed. B.G. Linsen), 1970. Academic Press; London, p. 63.

22. Brunauer, S., Emmett, P.H. and Teller, E., J. Am. Chem. Soc. 1938. **60**: p. 309–319.

23. Broadbent, S.R. and Hammersley, J.M., Proc. Cambridge Philos. Soc., 1957. **53**: p. 629.645.

24. Burgess, C. G. V. and Everett, D. H., J. Colloid Interface Sci., 1970. **33**: p. 611–614.

25. Chagger, H.K., Ndaji, F.E., Sykes, M.L., and Thomas, K.E., Carbon, 1995. **33** (10) (1995), p. 1405–1411.

26. Chen, C.Y., et al., Microporous Mater., 1993. **2**: p. 27.

27. Chen, C.Y., T. Tsuchiya, and J.D. Mckenzi. J. Non-Cryst. Solids, 1988. **100**: p. 162.

28. Chen, S., Qin, F., Kim, K.H.and Watson, A.T., AIChE J., 1993. **39**: p. 925.

29. Chilingar, G.V., I.B. Harold, and W.F. Rhodes, Carbonate Rocks Origin, Occurrence and Classification. 1967: Elsevier.

30. Cohan, L.H., J. Am. Chem. Soc, 1938. **60**: p. 433.

31. Coppens, M.O. and Froment, G.F., Chem. Eng. Sci., 1995. **50**: p. 1013–1026.

32. Cordero, S., et al., Adsorption, 2005. **11**: p. 91 – 96.

33. Cuiec, L.E., Evaluation of reservoir wettability and its effects on reservoir recovery, in Interfacial Phenomena in Oil Recovery, N.R. 1990, Marcell Dekker: New York.

34. Davies, G.M., et al., Characterisation of Porous Solids IV; Rouquerol, F., Rodrigues-Reinoso, F., Sing, K. S. W., Unger, K. K. Eds. Royal Society of Chemistry, 1997: p. 504.

35. Dandekar, A.Y., Petroleum reservoir rock and fluid properties, CRC/Taylor & Francis, 2006. ISBN: 9780849330438.

36. Davies, G.M. and N.A. Seaton. A.I.Ch.E, 2000. **46**: p. 1753.

37. Davis, M.E. and S.L. Burkett, Zeolites, 1995. **12**: p. 33.

38. De Boer J.H. (1968) The Dynamical Character of Adsorption, Oxford University Press, London, p. 179.

39. Drake, L.C. and Ritter, H.L., Industrial and Engineering Chemistry, Analytical Edition, 1945. **17**(12): p. 782.

40. Drake, J. M.; Levitz, P.; Klafter, J., New J. Chem., 1990. **14**: p.77.

41. Dubinin, M.M., The Potential Theory of Adsorption of Gases and Vapors for Adsorbents with Energetically Nonuniform Surfaces, Chem. Rev., 1960, **60** (2): p. 235–241.

42. Dubinin, M.M., Carbon, 1980. **18**: p. 335.

43. Ehrburger-Dolle, F., Langmuir, 1999. **15**: p. 6004.

44. Ehrburger-Dolle, F., Langmuir, 1994. **10** (7), p. 2052–2055.

45. Esparza, J.M., et al., Journal of Colloids and Interface Science, 2004. **241**: p. 35-45.

46. Evans, R., Marconi, U.M.B. and Tarazona, P., J. Chem. Soc., Faraday Trans. 2. 1986. **82**: p. 1763.

47. Everett, D.H., Adsorption Hysteresis in"The Solid Gas Interface", ed. E.A. Ltd. Vol. 2. 1967. 1055.

48. Everett, D.H and Haynes, J.M., Journal of Colloids and Interface Science, 1972. **38**: p. 125 – 137.

49. Fassifihri, O., Robin, M. and Rosenberg, E., Revue De L'Institut Francais Du Petrole, 1992. **47**(5): p. 686.

50. Feng, P., Bu, X. and Pine, D.J., Langmuir, 2000. **16**: p. 5304-5310.

51. Feng, P., et al., J. Am. Chem. Soc, 2000. **122**: p. 994.

52. Fletcher, A.J., et al., J. Am. Chem. Soc, 2001. **123**(41): p. 10001-10011.

53. Fletcher, A.J. and K.M. Thomas, Langmuir, 2000. **16**: p. 6253.

54. Foster, A.R. G., Trans. Faraday Soc. 1932. 28, p. 645.

55. Friedman, S.P. and N.A. Seaton, Chem. Eng. Sci., 1995. **50**: p. 897-900.

56. Fripiat, J.J., L. Gatineau, and Van Damme, H., Langmuir, 1986. 2: p. 562.

57. Gelb, L.D. and K.E. Gubbins, Langmuir, 1998. **14**: p. 2097-2111.

58. Gelb, L.D.et.al., Mol. Phys, 1996. **88**(6): p. 1541-1561.

59. Gelb L. D,and Gubbins K. E Fundamental of adsorption 7. Kanek, K., Kanoh, H., Hanzawa, Y., Eds IK International Chiba city (2002) p. 333.

60. Gelb, L.D. and Gubbins, K.E., Fundamentals of Adsorption, 2002. **7**: p. 333–340.

61. Godshalk, K.M. and Hallock, B.B., Phys. Rev. B, 1987. **36**: p. 8294-8301.

62. Greaves, M. and Turta, A.T., Oil field in situ combustion process. 1997. US Patent No. 5,626,191.

63. Gregg, S.J. and Sing, K.S.W., Adsorption, Surface Area and Porosity. 2nd edition ed. 1982.

64. Groen, J.C., L.A.A. Peffer, and Perez-Rairez., Stud. Surf. Sci. Catal., 2002. **144**: p. 91-98.

65. Gunther, H., NMR Spectroscopy: Basic Principles, Concepts, and Applications in Chemistry. Second Edition ed. 1995, Chichester, New York: John Wiley and Sons.

66. Giesche, H., Part. Part. Syst. Charact., 2006. 23, 9–19.

67. Giuliano, F.A., Introduction to Oil and Gas Technology (second ed.), 1981. International Human Resources Development Corporation, Boston, MA.

68. Hahn, E.L., Spin Echoes. Physical Review, 1950. **80**: p. 580-594.

69. Harding, A.W., et al., Langmuir, 1998. **14**(14): p. 3858-3864.

70. Hartmann, M. and A. Vinu, Langmuir, 2002. **18**: p. 8010-8016.

71. Horvath G.; Kawazoe, K., Journal of Chemical Engineering of Japan ISSN 0021-9592 CODEN JCEJAQ, 1983. **16**, n°6, p. 470-475.

72. Hiromi, M., et al., The Journal of Physical Chemistry, 2001. **105**(40): p.9669 – 9671.

73. Hiromitu, N and Hakuman, M., Journal of Colloid and Interface, 1993. **158**, p.19-26.

74. Halsey, G., J. Chem. Phys., 1948. **16**, p. 931-937.

75. Holland, B.T., et al., Chemical Materials, 1999. **11**: p. 795-805.

76. Holland, B.T., C.F. Blanford, and A. Stein, Science, 1998. **281**: p. 538-540.

77. Hollewand, M.P. and L.F. Gladden, Chem. Eng. Sci., 1995. **50**(2): p. 309.

78. Hollewand, M.P. and L.F. Gladden, Chem. Eng. Sci., 1992a. **47**, p. 1761–1770.

79. Hollewand, M.P. and L.F. Gladden, Chem. Eng. Sci., 1992b. **47,** p. 2757–2762.

80. Hollewand, M.P. and L.F. Gladden, Chem. Eng. Sci., 1995. **50**(2): p. 327-344.

81. Hollewand, M.P., and Gladden, L.F., Journal of Catalysis. 1993. **144**: p. 254-272.

82. Hore, P.J., Nuclear Magnetic Resonance. 1995: Oxford University Press.

83. Huo, Q., et al., Nature, 1994. **368**: p. 317.

84. Huo, Q., et al., Chem. Mater., 1994. **6**: p. 1176.

85. Hyvaluoma, J.; Turpeinen, T.; Raiskinmaki, P.; Jasberg, A.; Koponen, A.; Kataja, M.; Timonen, J. and Ramaswamy, S., Physical Review E, 2007. **75**: p. 036301.

86. Inagaki, S., Fukushima, Y. & Kuroda, K., J. Chem. Soc. Chem. Commun., 1993. p. 680–682.

87. Iiyama, T., et al., Colloids and Surfaces A-Physicochemical and Engineering Aspects, 2004. **241 (1-3)**: p. 207-213.

88. Ishikawa, T., et al., J. Chem. Soc., Faraday Trans., 1996. **92**: p. 1985.

89. Jarzebski, A.B. and J. Lorenc, J. Chem. Eng. Sci., 1995. **2**: p. 357.

90. Joo, S.H., et al., J. Phys. Chem. B, 2002. **106**: p. 4640-4646.

91. Jun, S., et al., J. Am. Chem. Soc, 2000. **122**: p. 10712-10713.

92. Katz, B.J., Petroleum Source Rocks, Springer-Verlag. In Tyson, R.V., 1995 Sedimentary Organic Matter, Chapman and Hall, London.

93. Kadlec, O., Collection of Czechoslovak Chemical Communications, 1985. **50**: p. 2788-2803.

94. Kainourgiakis, M.E., Stubos, A.K., Kostantinou, N.D., Kanellopoulos, N.K., and Milisic, V., Journal of Membrane Science, 1996. **114**: p. 215 – 225.

95. Kainourgiakis, M. E., Kikkinides E. S., Stubos, A.K., Kanellopoulos, N. K., J. Chem. Phys., 1999. **111**, 2735 ; DOI:10.1063/1.479550.

96. Karger, J., S. Frey, and J. Walther, J. Magn. Reson., 1988. **79**: p. 336.

97. Karger, J., Mol. Phys., 1981. **43**, 1189–1191.

98. Karlson, A., M. Stocker, and R. Schmidt, Microporous and Mesoporous Mater., 1999. **27**: p. 181.

99. Kayser, H., Wiedermann's Ann. Phys. Chem., 1881. 14: p. 451.

100. Kirkpatrick, S., In Balian, R., Mayward, R., Toulouse, G. (Eds), III-condensed Matter, North-Holland Amsterdam. 1979(321).

101. Kloubek, J., Powder Technology, 1981. **29**: p. 63-73.

102. Koster, A.J., et al., J. Phy. Chem. B., 2000. **104**: p. 9368.

103. Kowalczyk, P., et al., Langmuir, 2005. **21**: p. 10530 – 10536.

104. Krause, C., et al., Adsorption, 2003. **9**: p. 235-241.

105. Kresge, C.T., et al., Nature, 1992. **359**: p. 710-712.

106. Kruk, M. and M. Jaroniec, Langmuir, 1997. **13**: p. 6267-6273.

107. Kuther, J., et al., J. Mater. Chem, 1998. **8**(3): p. 641-650.

108. Langmuir, I., Phys. Rev. 1916. **8**, p. 149.

109. Lastoskie, C., K.E. Gubbins, and N. Quirke, Langmuir, 1993. **9**: p. 2693.

110. Lastoskie, C., K.E. Gubbins, and N. Quirke, J. Phys. Chem., 1993. **7**: p. 4786.

111. Lowell S., Shields J.E., Thomas, M. A., Thommes, M. Characterisation of Porous Solids and Powders; Surface Area, Pore size and Density, 2004. Edition: 4, Published by Springer, ISBN 1402023022, 9781402023026.

112. Lowell S. & Shields J.E., Powder Surface Area and Porosity. 1984 London: Chapman & Hall, 2nd ed. ISBN: 0412252406.

113. Liu, H., L. Zhang, and N.A. Seaton, Journal of Colloid and Interface Science, 1993. **156**: p. 285-293.

114. Lui, H., L. Zhang, and N.A. Seaton, Chem. Eng. Sci., 1992. **47**: p. 4393.

115. Lui, H. and N.A. Seaton, Chem. Eng. Sci., 1994. **49**: p. 1869.

116. Mackenzie, J.D., J. Non-Cryst. Solids, 1988. **100**: p. 162-168.

117. Magee, J. S. and Dolbear, G. E., Petroleum Catalysis in Non-technical Language, Hydrotreating Catalysts, 1998. PennWell Books, US.

118. Makri, P.K., Stefanopoulos, K.L., Mitropoulos, A.Ch., Kanellopoulos, N.K., Treimer, W. Physica B, 2000. **276-278**: p. 479-480.

119. Malanoski, A.P. and Swol, F., Physical Review, 2002. E **66**: 041602.

120. Mann, R. and Golshan, H. (1981). Chemical Engineering Communications, 1981. **12**: p. 377-391.

121. Masel, R. I, Principles of adsorption and reaction on solid surfaces. 1996. Published by Wiley-IEEE, ISBN 0471303925, 97804713039.

122. Mason, G., Proc. R. Soc., A. 1988. **415**: p. 453-486

123. Mason, G., J. Colloid Interface Science, 1983. **95**: p. 277.

124. Mata, V.G., Lopes, J.C.B. and Dias, M.M., Industrial and Engineering Chemical Research, 2001. **40**: p. 3511 – 3522.

125. Mata, V.G., Lopes, J.C.B., and Dias, M.M. Industrial and Engineering Chemistry Research**,** 2001**. 40**: p. 4836-4843.

126. Matthews, P.G. and Spearing, M.C., Marine and Petroleum Geology, 1991. **9**: p. 146 - 154. Journal of Colloid and Interface Science, 1995. **171**: p. 8-27.

127. McCaslin, J.C., International Petroleum Encyclopedia. 1989: PennWell.

128. Megens, M., van Kats, C.M., Bösecke, P. and Vos, W.L., J. Appl. Cryst., 1997. **30**, p. 637-641 doi: 10.1107/S002188989700191X.

129. Mengens, M., et al., Xray Diffraction on Photonic Colloidal Single Crystals, ed. E.Y.P.e. al. 1997. 60-61.

130. Miller, M.N., et al. Spin Echo Magnetic Resonance Logging: Porosity and free Fluid Index Determination. 1990. SPE Annual Technical Conference and Exhibition, 23-26 September 1990, New Orleans, Louisiana

131. Moller, K. and Bein, T., Chem. Mater., 1998. **10**: p. 2950.

132. Moro, F., and Böhni, H., Journal of Colloid and Interface Science, 2002. **246**: p. 135-149.

133. Morrow, N. R. and Harris, C. C., Soc. Pet. Eng. Jour. March 1965. p.15.

134. Moscou, L. and Lub, S., Powder Technology, 1981. **29**: p. 45-52.

135. Muller, E.A., Rull, L. F., Vega, L. F. and Gubbins, K. E., J. Phys. Chem., 1996. **100**: p. 1189-1196.

136. Murray, K.L., Seaton, N.A. and Day, M.A., Langmuir, 1998. **14**: p. 4953-4954.

137. Naono, H. and Hakuman, M., Journal of Colloid and Interface Science, 1993. **158:** p. 19-26.

138. Neimark, A.V., Stud. Surf. Sci. Catal., 1991. **62**: p. 67.

139. Ozin, G.A., Adv. Mater., 1992. **10**: p. 612.

140. Page, K.S. and Monson, P.A., Phys. Rev. E, 1996.

141. Pellenq, R.J. –M, Rodts, S., Pasquier, V., Delville, A., and Levitz, D.P., Adsorption, 2000. **6,** p. 241–249.

142. Pfeifer, P. and D. Avnir, J. Chem. Phys., 1983. **79**: p. 3558.

143. Pfeifer, P.; Wu, Y. J.; Cole, M. W.; Krim, J. Phys. Rev. Lett., 1989. **62**, p.1997-2000.

144. Pfeifer, P.; Schmidt, P. W. Phys. Rev. Lett., 1988, **60**, p. 1345.

145. Pfeifer, P.; Lui, K. –Y. Stud Surf. Sci. Catal., 1997. 104, p. 625-677.

146. Pierce, C. and Smith, N.R., J. Phys. Chem., 1950. **54**(6): p. 795-803.

147. Pirard, R., Alie, C. and Pirard, J.P., Powder Technology, 2002. **128**: p. 242-247.

148. Pirard, R. and J.P. Heinrichs, Mercury Porosimetry applied to Low Density Xerogels, in B. McEnaney, T.J. Mays, J. Rouquerol, F. Rodriguez-Reinoso, K.S.W. Sing, K.K. Unger (Eds), Characterisation of Porous Solids IV. 1997: p. 470.

149. Porcheron, F., Monson, P.A, and Thommes, A., Langmuir, 2004. **20**: p. 6482.

150. Porcheron, F., Monson, P.A, and Thommes, A., Adsorption, 2005. **11**: p. 325-329.

151. Porcheron, F., Thommes, M., Ahmad, R., and Monson, P.A., Langmuir, 2007. **23**: p. 3372-3380.

152. Porion, P., et al., Magnetic Resonance Imaging, 1998. **16**(Nos. 5/6): p. 679-682.

153. Portsmouth, R.L., and Gladden, L.F., Chemical Engineering Science**, 1991. 46**: p. 3023-3036.

154. Price, W.S., Concepts in Magnetic Resonance, 1997. **9**: p. 299.

155. Ma, J., Qi, H. and Qong, P., Colloids and Surfaces a-Physicochemical and Engineering Aspects, 2002. **206**: p. 401-407.

156. Ma, J., Qi, H. and Wong, P., Phys. Rev. E, 2001. **64**(041601): p. 1-4.

157. Ma, J., Qi, H. and Qong, P., Phys. Rev. E, 1999. **59**: p. 2049-2059.

158. Ramsay, K.S., Handbook of Porous Solids, ed. F. Schuth, Sing, K. Vol. 1, 145. 2002.

159. Rao, M.B., Jenkins, R.G. and Steele, W.A., Langmuir, 1985. **1**(1): p. 137-141.

160. Ravikovitch, P.I. and Neimark, A.V., Langmuir, 2002. **18**: p. 9830-9837.

161. Ravikovitch, P.I. and Neimark, A.V., J. Phys. Chem. B, 2001. **105**: p. 6817-6823.

162. Ravikovitch, P.I., et al., J. Phys. Chem. B., 1997. **101**: p. 3671 – 3679.

163. Ravikovitch, P.I. Domhnaill, S.C.O., Schueth, F., Unger, K. K.and Neimark, A.V., Langmuir, 1995, 11 (12) p. 4765.

164. Reiker, T.P., F. Hindermann-Bischoff, and Ehrburger-Dolle, Langmuir, 2000. **16**: p. 5588.

165. Rigby, S.P., Chigada, P.I., Evbuomwan, I.O., Chudek, J.A., Miri, T., Wood, J., and Bakalis, S. Chem. Eng. Sci., 2008. **63**: p. 5771 – 5788.

166. Rigby, S. P., Chigada, P. I., Adsorption, 2008. DOI 10.1007/s10450-008-9147-4.

167. Rigby, S.P., Fletcher, R.S., and Riley, S.N., Journal of Colloid and Interface Science, 2001. **240**: p. 190-210.

168. Rigby, S.P. and Edler, K.J., Journal of Colloid and Interface Science, 2002. **250**: p. 175-190.

169. Rigby, S.P., Evbuomwan, I.O., Watt-Smith, M.J., Edler, K.J., and Fletcher, R, S., Part. Part. Syst. Charct, 2006. **23**: p. 82 – 93.

170. Rigby, S.P., Fletcher, R.S., and Riley, S.N., Chem. Eng. Sci., 2004. **59**: p. 41-51.

171. Rigby, S.P., Langmuir, 2002. **18**: p. 1613-1618.

172. Rigby, S.P. and Fletcher, R.S., J. Phys. Chem. B, 2004. **108**: p. 4690-4695.

173. Rigby, S.P., Fletcher, R.S., and Riley, S.N., Applied Catalysis A, 2003. General 8526: p. 1-13.

174. Rigby, S.P., Journal of Colloid and Interface Science, 2000. **224**: p. 382-396.

175. Rigby, S.P., Journal of Colloid and Interface Science, 2005. **262**: p. 139 – 149.

176. Rigby, S.P., Chigada, P.I., Perkins, E.L., Lowe, J., Edler, K.J., Adsorption, 2008. DOI 10.1007/s10450-007-9091-8.

177. Rigby, S.P., Watt-Smith, M.J., Chigada, P., Chudek, J.A., Fletcher, R.S., Wood, J., Bakalis, S., Miri, T., Chem. Eng. Sci., 2006.. **61**: p. 7579-7592.

178. Rigby, S.P., Watt-Smith, M.J., Fletcher, R.S., J. Catal, 2004b. **227**: p.68-76.

179. Rojas, F., et al., Phys. Chem. Chem. Phys., 2002. **4**: p. 2346 – 2355.

180. Ross, S. B.; Smith, D. M.; Hurd, A. J.; Schaefer, D. W., Langmuir, 1988, **4,** p. 977-982.

181. Rouquerol, F., J. Rouquerol, and K. Sing, Adsorption by Powders and Porous Solids: Principles, methodology and Applications. 1999: Academic press.

182. Rouquerol, F., et al., Pure Appli. Chem, 1994. **66**: p. 1739.

183. Rouquerol, J., F. Gomez, and R. Denoyel, Langmuir, 2000. **16**: p. 4374.

184. Ruthven, D.M., Principles of Adsorption and Adsorption Processes. March 1984. Wiley, New York.

185. Ryoo, R., Ko, C.H. and Park, I.S., Chem. Commun., 1999: p. 1413.

186. Ryoo, R. and Ko, C.H., Chem. Commun., 1996: p. 2467.

187. Sahouli, B.; Blacher, S.; Brouers, S.; Sobry, R.; Van den Bossche, G.; Diez, B.; Darmstadt, H.; Roy, C.; Kaliaguine, S., Carbon, 1996, **34**, p.633-637.

188. Sarkisov, L. and Monson, P.A., Langmuir, 2000. **16**: p. 9857 – 9860.

189. Saito, A., Foley, H.C., AIChE Journal, 1991. **37** (3), p. 429 – 436.

190. Saam, F.W. and Cole, M.W., Phys. Rev. B, 1975. **11**, p. 1086-1105.

191. Schuth, F. and K. Sing, Eds. F. Schuth, K.S.W. Sing, J. Handbook of Porous Solids. Vol. 1, 84. 2002, Germany.

192. Seaton, N.A., et al., Chem. Eng. Sci., 1991. **46**(8): p. 1895-1909.

193. Selvam, P., Bhatia, S.K. and Sonwane, C.G., Ind. Eng. Chem. Res, 2001. **40**: p. 3237-3261.

194. Sen, T., et al., Angewandte Chemie, 2003. **42**: p. 4649-4653.

195. Sing, S.W.K., The Journal of Collide and Interface Science, 1989. **38**: p. 113 – 124.

196. Sing, K.S.W., Everett, D.H., Haul, R.A.W., Moscou, L., Pierotti, R.A., Rouquerol, J., and Siemieniewska, T., Pure Appl. Chem., 1985. **57**(4), p. 603–619.

197. Sircar, e.a., Adsorption, 2000. **6**: p. 137-147.

198. Slasli, A.M., et al., Carbon, 2003. **41**: p. 479-486.

199. Smarsly, B., et al., J. Phys. Chem. B., 2001. **105**: p. 831.

200. Smithwick, R.W.I., Powder Technology, 1986. **48**: p. 233-238.

201. Stejskal, E.O. and Tanner, J.E., J. Chem. Phys., 1965. **42**: p. 288.

202. Straley, C., et al., NMR in partially Saturated Rocks: Labouratory insight on Free Fluid Index and Comparison to Borehole Logs. Paper CC in Transaction of the SPWLA 32nd Logging Symposium Society of Professional Well Log Analysts, 1991.

203. Stucky, G.D., et al., Stud. Surf. Sci. Catal., 1998. **117**: p. 1.

204. Sun, J. Shan, T. Maschmeyer and M.O. Coppens,., Langmuir, 2003. **19**: p. 8395.

205. Tanev, P.T. and Pinnavaia, T.J., Sciences, 1995. **267**: p. 865.

206. Tanev, P.T. and T.J. Pinnavaia, The Royal Society of Chemistry/Chem. Mater., 1996. **8**: p. 2068.

207. Thomas, K.M. Ndaji, F.E. Chagger, H.K., Sykes, M.L., Carbon, 1995. **33**: p. 1405.

208. Thommes, M. Smarsly, B. Groenewolt, M., Ravikovitch, P.I., Neimark, A.V., Langmuir, 2006. **22**(2): p. 756-764.

209. Thommes, M. Kohn, R. and Froba, M., Applied Surface Science, 2002. **196**: p. 239-249.

210. Tsakiroglou, C.D., et al., Journal of Colliod and Interface Science, 1997. **193**: p. 259-272.

211. Tsakiroglou, C.D. and Payatakes, A.C., Journal of Colloid and Interface Science, 1990. **137**: p. 315-339.

212. Tsakiroglou, C.D. and Payatakes, A.C., Advances in Colloid and Interface Science, 1998. **75**: p. 215 -253.

213. Tzevelekos, K.P. Romanos, G.E. Kikkinides, E.S. Kanellopoulos and Kaselouri, V., Microporous and Mesoporous Materials 1999. **31**: p. 151 – 162.

214. Tzevelekos, K.P., Kikkinides, E.S., Stubos, A.K., Kainourgiakis, M.E., and Kanellopoulos, N.K., Advances in Colloid and Interface Science, 1998. **76-77**: p. 373 – 388.

215. Van Brakel, J., Modry, S. and Svata, M., Powder Technology, 1981. **29**: p. 1-12.

216. Van der Voort, P., et al., J. Phys. Chem. B, 2002. **106**: p. 5873-5877.

217. Van der Voort, p., et al, The Royal Society of Chemistry/Chem. Comm., 2002. p. 1010 – 1011.

218. Vandreuil, S., et al., Advanced Materials, 2001. **13**(No 17).

219. Vartuli, J.C., et al., Chem. Mater., 1994. **6**: p. 2070.

220. Vavra, C., Kaldi, J. G. and Sneider, R. M., The American Association of Petroleum Geologists Bulletin, 1992. **76**(6): p. 840-850.

221. Velev, O.D., et al., Nature, 1997. **389**: p. 447-448.

222. Vishnyakov, A. and Neimark, A. V., Langmuir, 2003. **19**: p. 3240-3247.

223. Wallacher, D. et al., Physical Review Letters, 2004. **92**(19): p. 195704-1-195704-4.

224. Walsh, D. and Mann, S., Nature, 1995. **377**: p. 320.

225. Walsh, D., Hopwood, J.D. and Mann, S., Science, 1994. **264**: p. 1576-1578.

226. Wang, Y. et al., Review of Scientific Instruments. 2001. **72**: p. 2062.

227. Wanka, G., Hoffmann, H. and Ulbricht, W., Macromolecules, 1994. **27**: p. 4145-4159.

228. Wardlaw, N.C. and Mckellar M., Powder Technology, 1981. **29**: p. 127-143.

229. Wardlaw, N.C., Journal of Canadian Petroleum Technology, 1982. **21**: p 21-27.

230. Washburn, E.W., The Physical Review, 1921. **17** (3): p. 273-283.

231. Watt-Smith, M.J., et al., AIChE Journal, 2006. **52** (9): p. 3278-3289.

232. Watt-Smith, M.J., et al., Langmuir, 2005. **21**: p. 2281 – 2292.

233. Watt-Smith, M.J., Rigby, S.P., Chudek, J.A., and Fletcher, R.S. Langmuir, 2006. **22**: p. 5180-5188.

234. Watzke, H.J, Dieschbourg, C., Adv. Colloid Interface Sci., 1994. **50**: p.1-14.

235. Weckhuysen, B.M., et al., Chem. Eur J., 2000. **6**(16): p. 2960-2970.

236. Weidler, P. G.; Degovics, G.; Laggner, P. J., Colloid Interface Sci., 1998, **197**, p. 1-8.

237. Wijnhoven, J.E.G.J. and W.L. Vos, Science, 1998. **281**: p. 802-804.

238. Wood, J., and Gladden, L.F. Chem. Eng. Sci., 2002. **57**: p. 3033 – 3045.

239. Wood, J., Gladden, L.F., and Keil, F.J., Chem. Eng. Sci., 2002. **57**: p. 3047 – 3059.

240. Woo, H-J., Sarkisov, L. and Monson. P.A., Langmuir, 2001. **17** (24), p. 7472–7475.

241. World Oil Journal 2005.

242. World Oil Journal 2006.

243. Xia, T.X., and Greaves, M., Chem. Eng. Research and Design, 2006. **84**(A9): p. 856 – 864.

244. Yanagisawa, T., et al., Bull. Chem. Soc. Jpn., 1990. **63**: p. 988.

245. Zhao, D., et al., J. Am. Chem. Soc, 1998. **120**: p. 6024-6036.

246. Zhao, D., et al., Chem. Mater., 1999. **11**: p. 2668.

247. Zsigmondy, A., Anorg. Chem., 1911. **71**, p. 356.

Appendix A

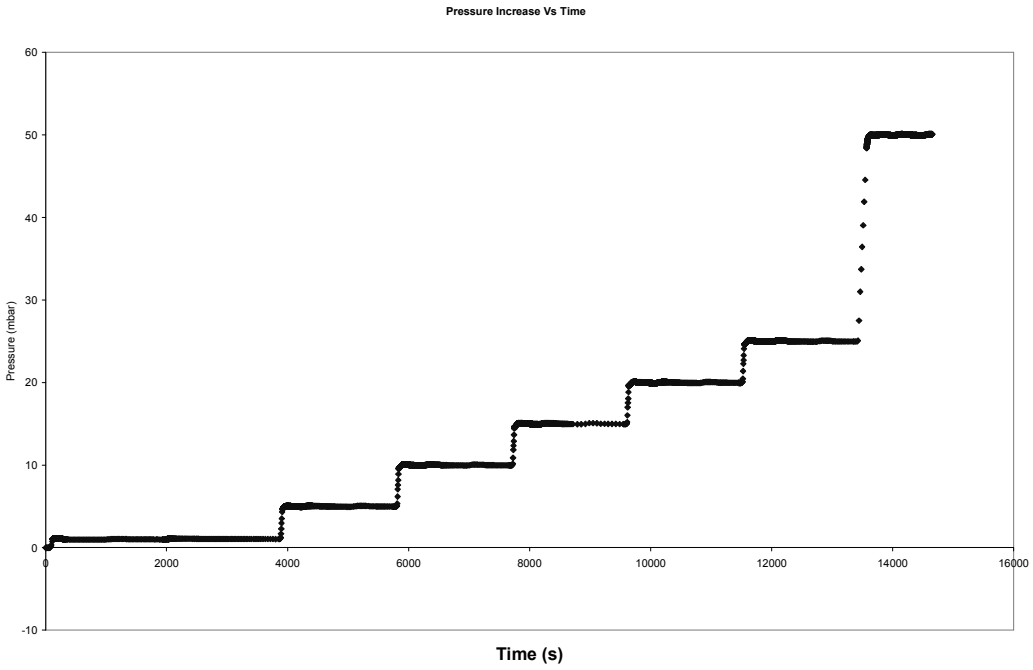

Graph A1

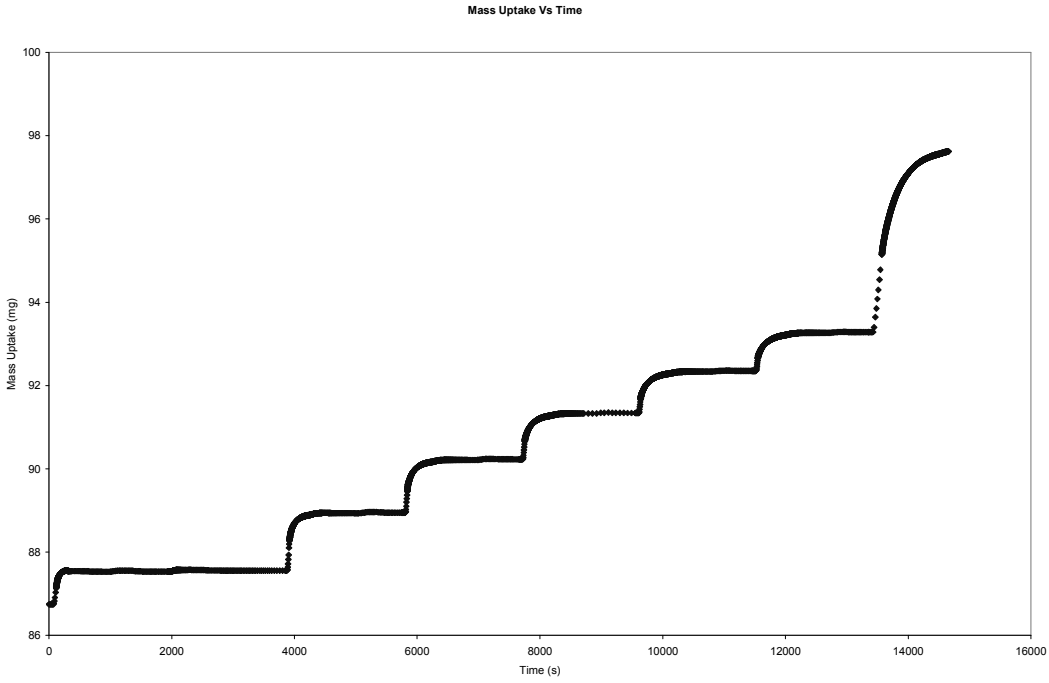

Graph A 2

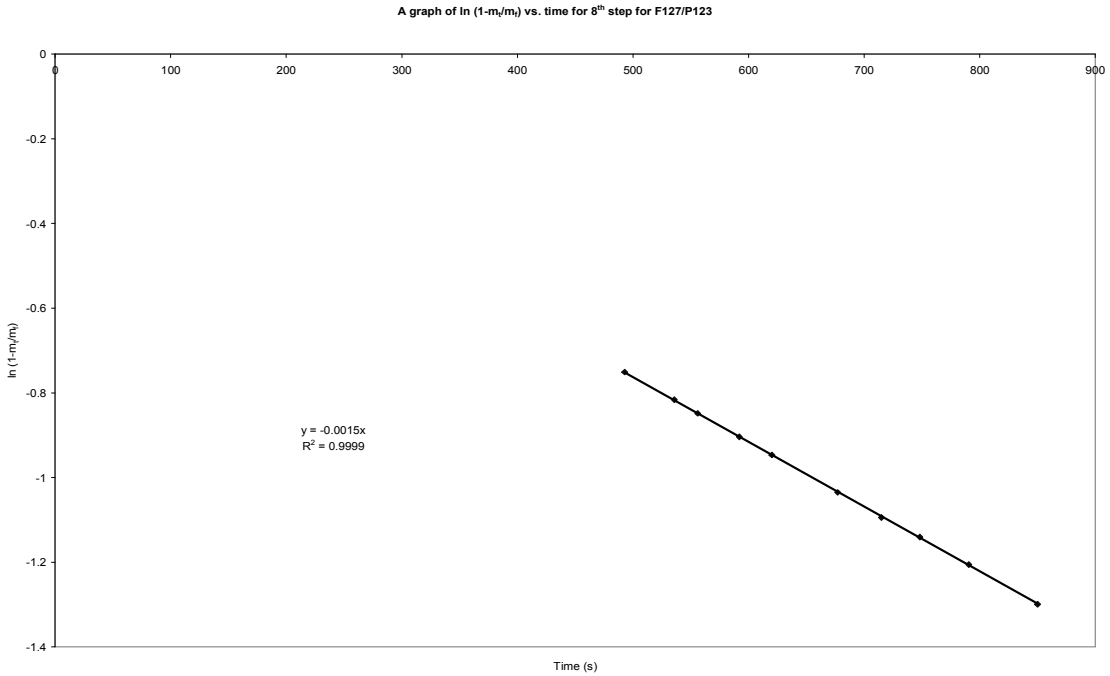

Graph A 3

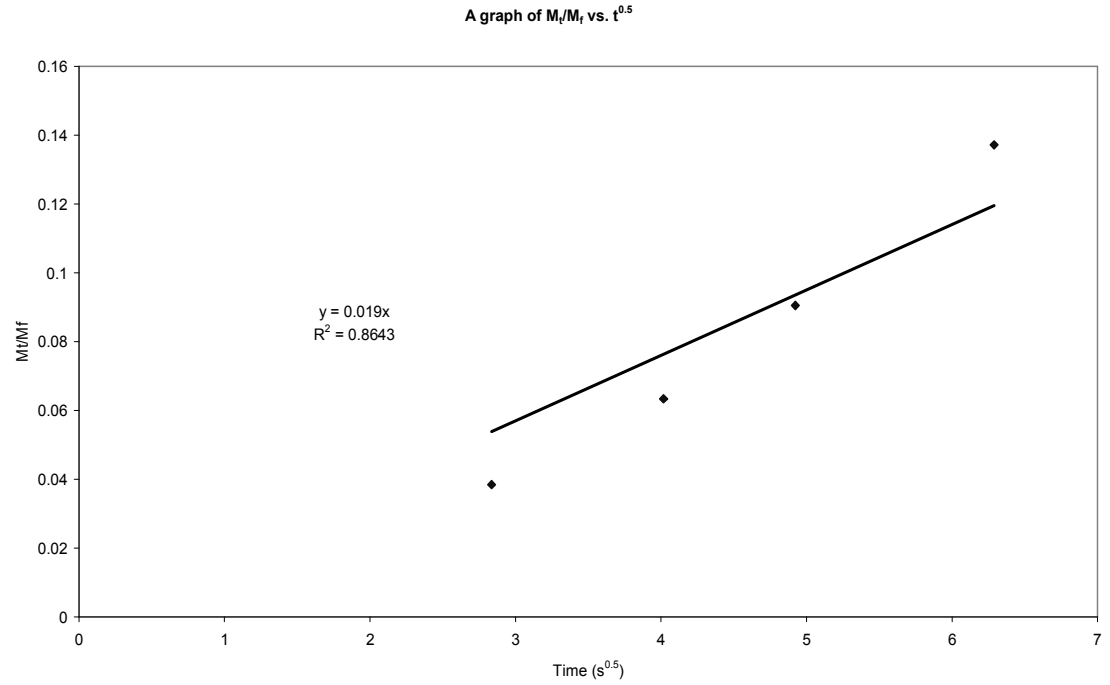

Graph A 4

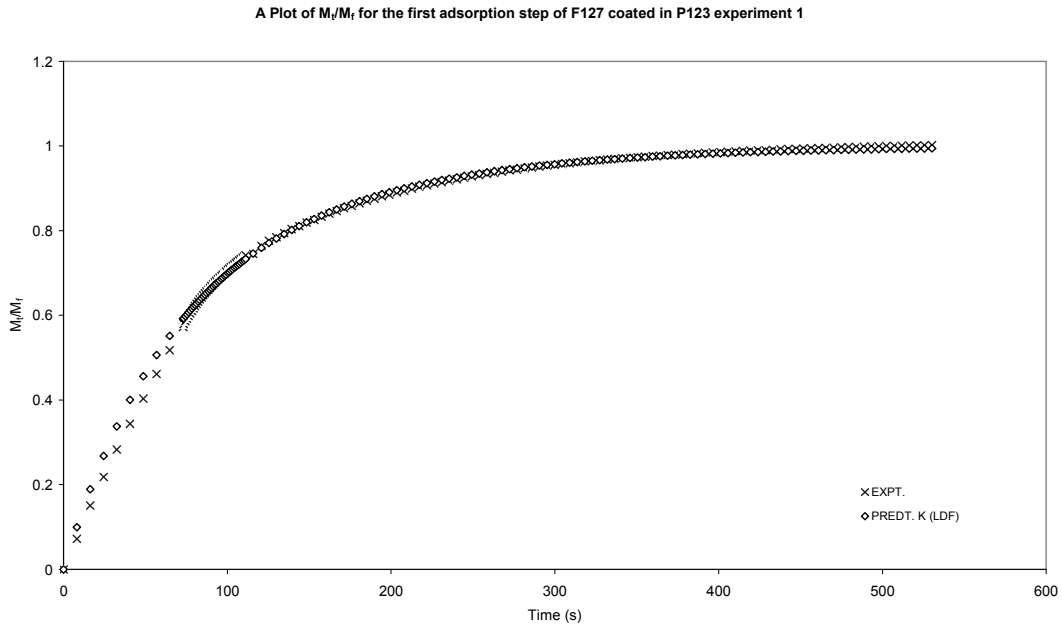
A Plot of M_t/M_f for the first adsorption step of F127 coated in P123 experiment 1
1.2
1
0.8
0.6
0.4
0.2
0
M_t/M_f
0
100
200
300
400
500
600
Time (s)
EXPT.
PREDT. K (LDF)

Graph A 5

Appendix B

Showing example data sets collected from pore characterisation techniques for all materials synthesised within this research.

B 1: P123 CORE EXPERIMENT 1

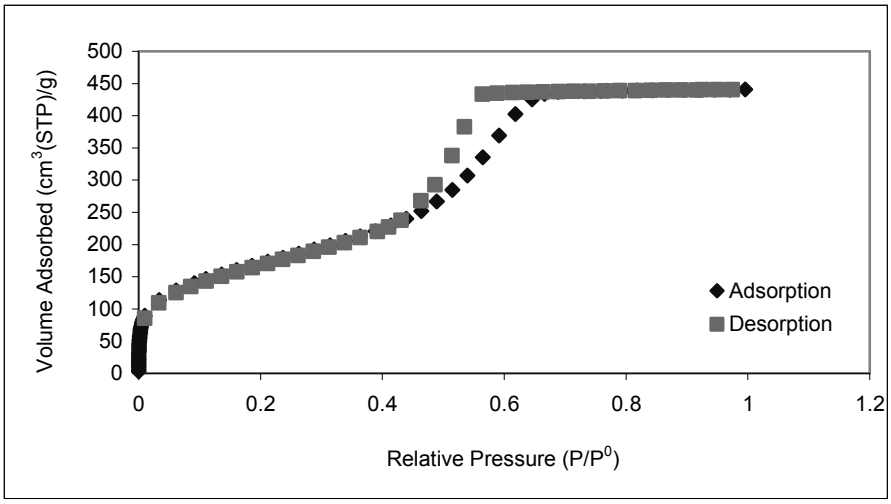

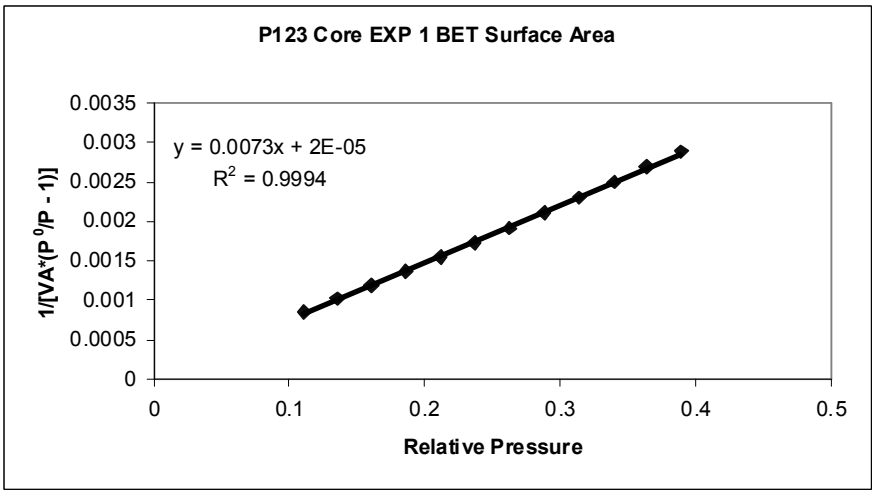

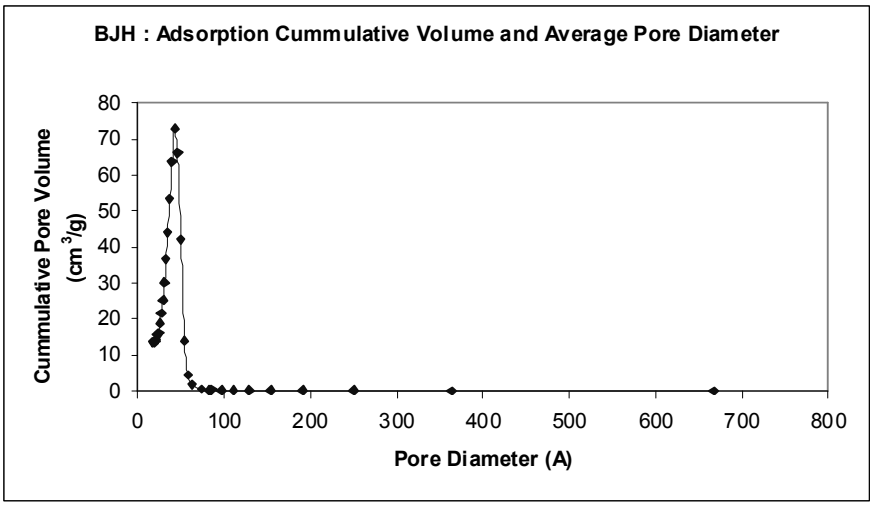
BJH : Adsorption Cummulative Volume and Average Pore Diameter
Cummulative Pore Volume (cm3/g)
0
10
20
30
40
50
60
70
80
0
100
200
300
400
500
600
700
800
Pore Diameter (A)

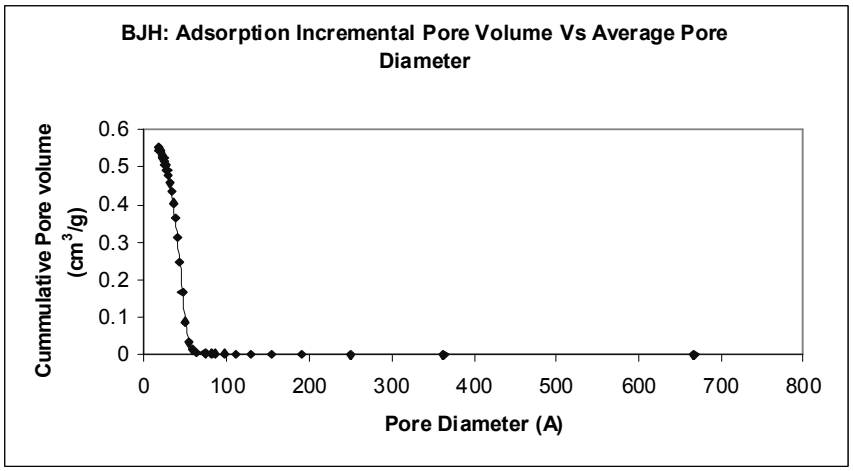
BJH: Adsorption Incremental Pore Volume Vs Average Pore Diameter
Cummulative Pore volume (cm3/g)
0
0.1
0.2
0.3
0.4
0.5
0.6
0
100
200
300
400
500
600
700
800
Pore Diameter (A)

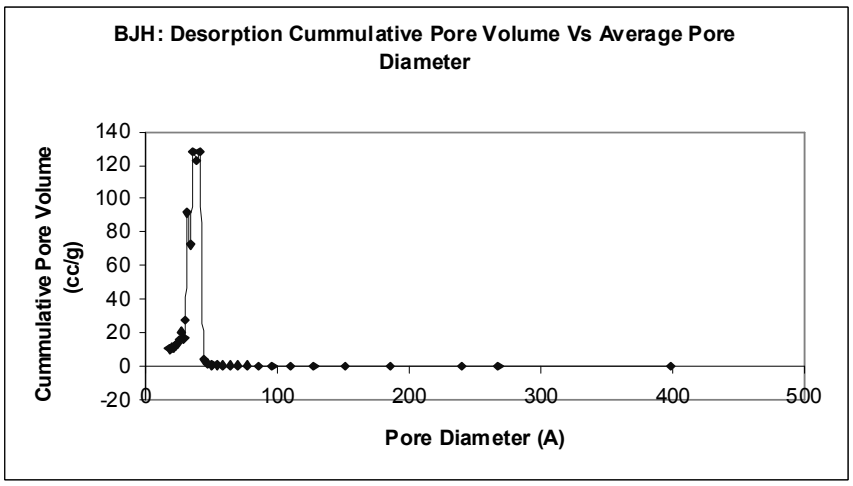
BJH: Desorption Cummulative Pore Volume Vs Average Pore Diameter
Cummulative Pore Volume (cc/g)
-20
0
20
40
60
80
100
120
140
0
100
200
300
400
500
Pore Diameter (A)

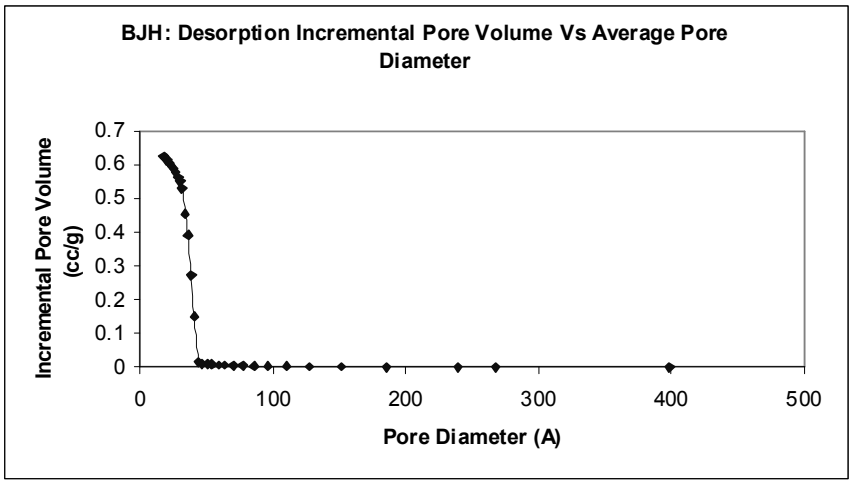
BJH: Desorption Incremental Pore Volume Vs Average Pore Diameter
Incremental Pore Volume (cc/g)
0.7
0.6
0.5
0.4
0.3
0.2
0.1
0
0
100
200
300
400
500
Pore Diameter (A)

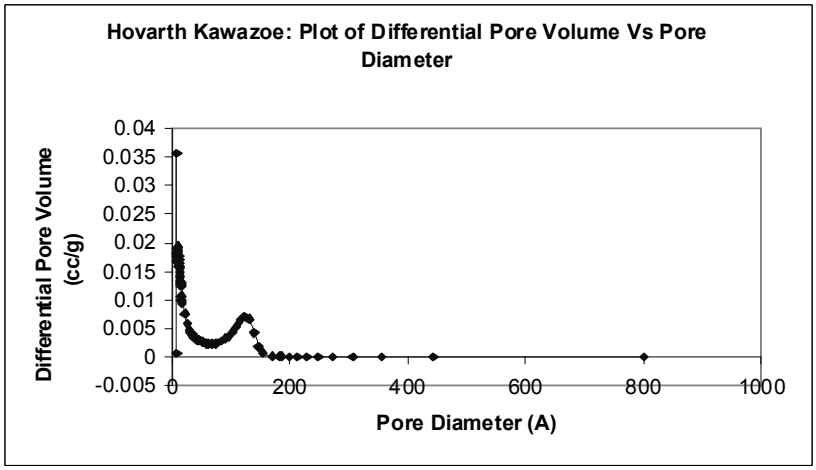
Hovarth Kawazoe: Plot of Differential Pore Volume Vs Pore Diameter
Differential Pore Volume (cc/g)
0.04
0.035
0.03
0.025
0.02
0.015
0.01
0.005
0
-0.005
0
200
400
600
800
1000
Pore Diameter (A)

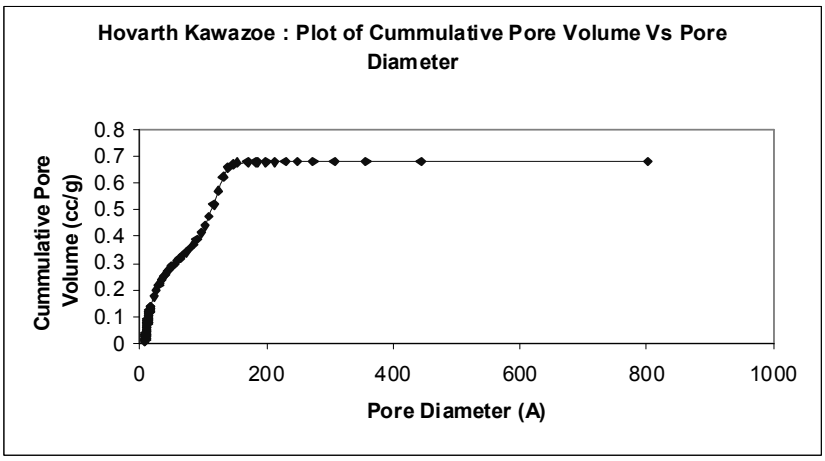
Hovarth Kawazoe : Plot of Cummulative Pore Volume Vs Pore Diameter
Cummulative Pore Volume (cc/g)
0.8
0.7
0.6
0.5
0.4
0.3
0.2
0.1
0
0
200
400
600
800
1000
Pore Diameter (A)

Summary Report

Area		
Single Point Surface Area at P/Po 0.28836763 :	595.1877	m^2/g
BET Surface Area:	594.0336	m^2/g
BJH Adsorption Cumulative Surface Area of pores between 17.000000 and 3000.000000 Å Diameter:	582.9906	m^2/g
BJH Desorption Cumulative Surface Area of pores between 17.000000 and 3000.000000 Å Diameter:	703.4655	m^2/g
Volume		
Single Point Adsorption Total Pore Volume of pores less than 4471.6568 A Diameter at P/Po 0.99567517:	0.681858	cm^3/g
BJH Adsorption Cumulative Pore Volume of pores between 17.000000 and 3000.000000 Å Diameter:	0.551602	cm^3/g
BJH Desorption Cumulative Pore Volume of pores between 17.000000 and 3000.000000 Å Diameter:	0.622961	cm^3/g
Pore Size		
Adsorption Average Pore Diameter (4V/Å by BET):	45.9138	Å
BJH Adsorption Average Pore Diameter (4V/Å):	37.8464	Å
JH Desorption Average Pore Diameter (4V/	35.4224	Å
Horvath-Kawazoe		
Maximum Pore Volume at Relative Pressure 0.995675174:	0.681858	cm^3/g
Median Pore Diameter:	73.3187	Å

Appendix C

Mercury Porosimeter (Autopore III) Operations

The Penetrometer and the Sample Cell

The sample cell is in the shape of a cup usually made of glass, which can be opened to accommodate the sample. The sample cup is then connected to a capillary tube of uniform inner bore, which is the part used to measure the intruded volume of mercury into pores of the sample. An attempt is made to ensure the penetrometer bulb is nearly filled to ensure that less mercury waste is created, the density measurement (which is also performed simultaneously to the pore size characterisation) is more accurate and compressibility effects are reduced, thus making the entire analysis more accurate

Measurement of Pore Volume

The volume of mercury intruded/extruded is measured by the use of precision capacitance bridges to note changes in the capacitance between the column of mercury in the dilatometer stem and a coaxial metal sheet surrounding the column. The pore volume data is then calculated by determining the volume of mercury remaining in the penetrometer stem. As pressure increases, mercury moves into the sample's pores, vacating the stem (Intrusion). Intrusion of different size pores occurs at different pressures. Greater amount of pressure is required to force mercury into the smaller pore diameter. Since mercury has a high surface tension and is non-wetting to most materials, its angle of contact and radius of curvature can be used to calculate the pore diameter into which it intrudes at a given pressure. The volume of mercury in the penetrometer's stem is measured by determining the penetrometer's electrical capacitance. Capacitance is the amount of electrical charge stored per volt of electricity applied. The penetrometer's capacitance varies with the length of penetrometer stem that is filled with mercury. When the penetrometer is initially backfilled with mercury, the mercury extends the entire length of the penetrometer. As increasing pressure causes the mercury

to intrude into the sample's pores, the volume of mercury in the penetrometer stems decreases by an amount equal to the volume of the pores filled. This decrease in the length of the penetrometer stem that is filled with mercury causes a reduction in the penetrometer's capacitance. The Autopore III software converts measurements of the penetrometer's capacitance into data points showing the volume of mercury intruding into the sample's pores.

Table 1

Characteristics	**Specification**
Low Pressure:	
Measurement:	0 to 50psia (345 kpa)
Resolution:	0.01 psi (69 Pa)
Pore Diameter:	360 to 3.6μm
High Pressure:	
Measurement:	Atmospheric pressure to 60,000 psi (414 MPa)
Resolution:	0.3 psi (2070 Pa) [from 5000 psi (34 MPa) to 60,000 psi (414 MPa)], and 0.03 psi (207 Pa) [from atmospheric pressure to 3000 psi (34 MPa)]
Pore Diameter:	6 to 0.003μm
Equlibration Techniques:	
By Time:	0 to 10,000 seconds
By Rate:	0 to 1000.000μL/g per second

Sample Preparation

It is important to select the right choice of penetrometer for each sample, and to fill the penetrometer volume as much as possible to reduce the total amount of mercury. This is given as a guide towards a higher precision of the density determination and it also reduces the blank effect due to the compressibility effects of the mercury (Sing and Weitkamp 2002). The test samples were in the form of a pellet, and the pelletization serves two purposes. Firstly the material is easier to handle and the regular sample bulbs can be used. Secondly the interparticle porosity is reduced.

Handling of Mercury

Mercury poses a health hazard, and as it is slightly volatile at room temperature, experiments were run in a properly ventilated room to avoid accumulation of mercury vapour. The appropriate protective clothing was worn whenever handling mercury, and all spillages were cleaned up immediately by both mechanical and chemical means.

Appendix D

D 1: Schematic for the use of Latex Particles in Porous Media Synthesis

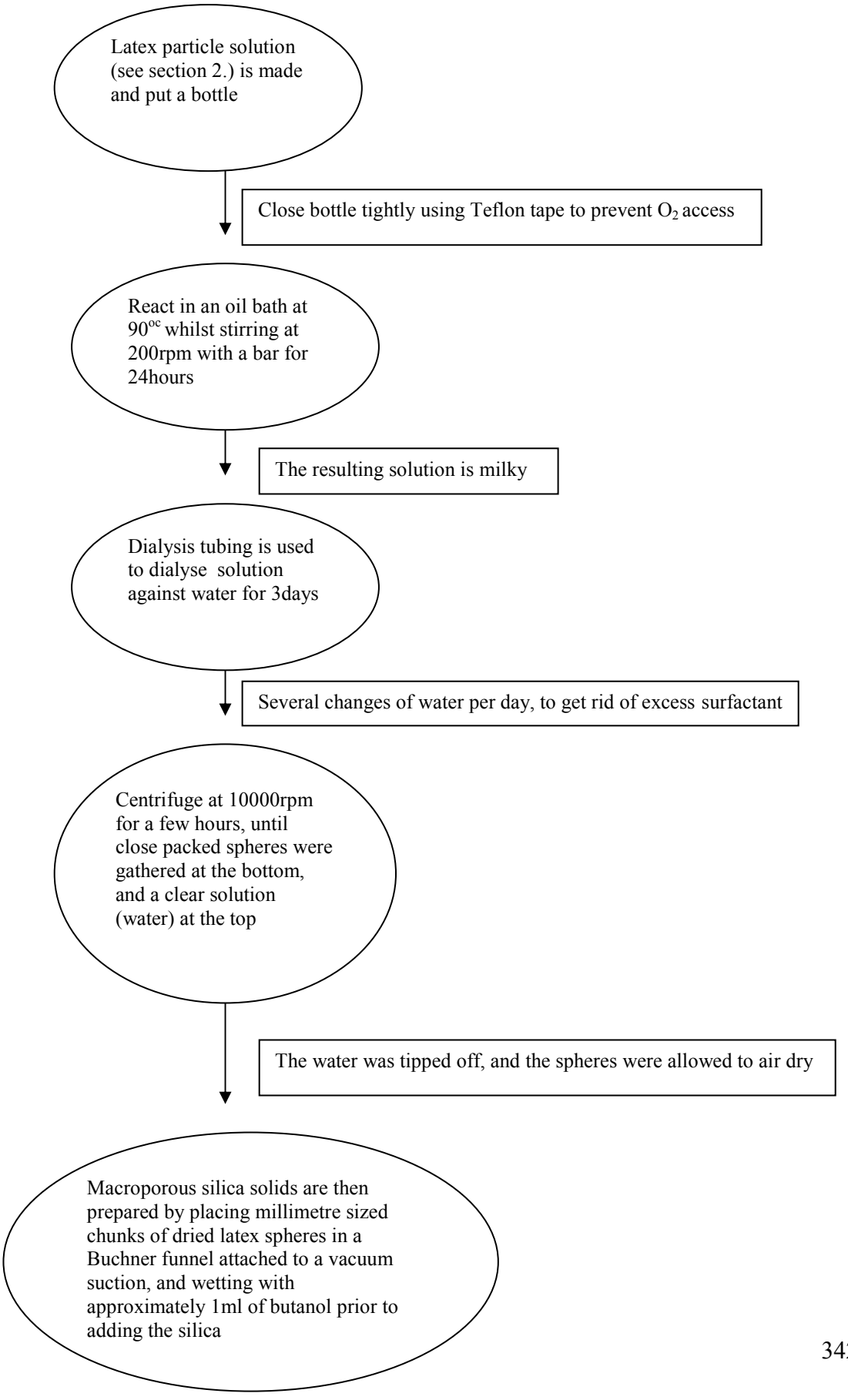

D 2: Diagram for Surfactant Synthesised Porous Materials

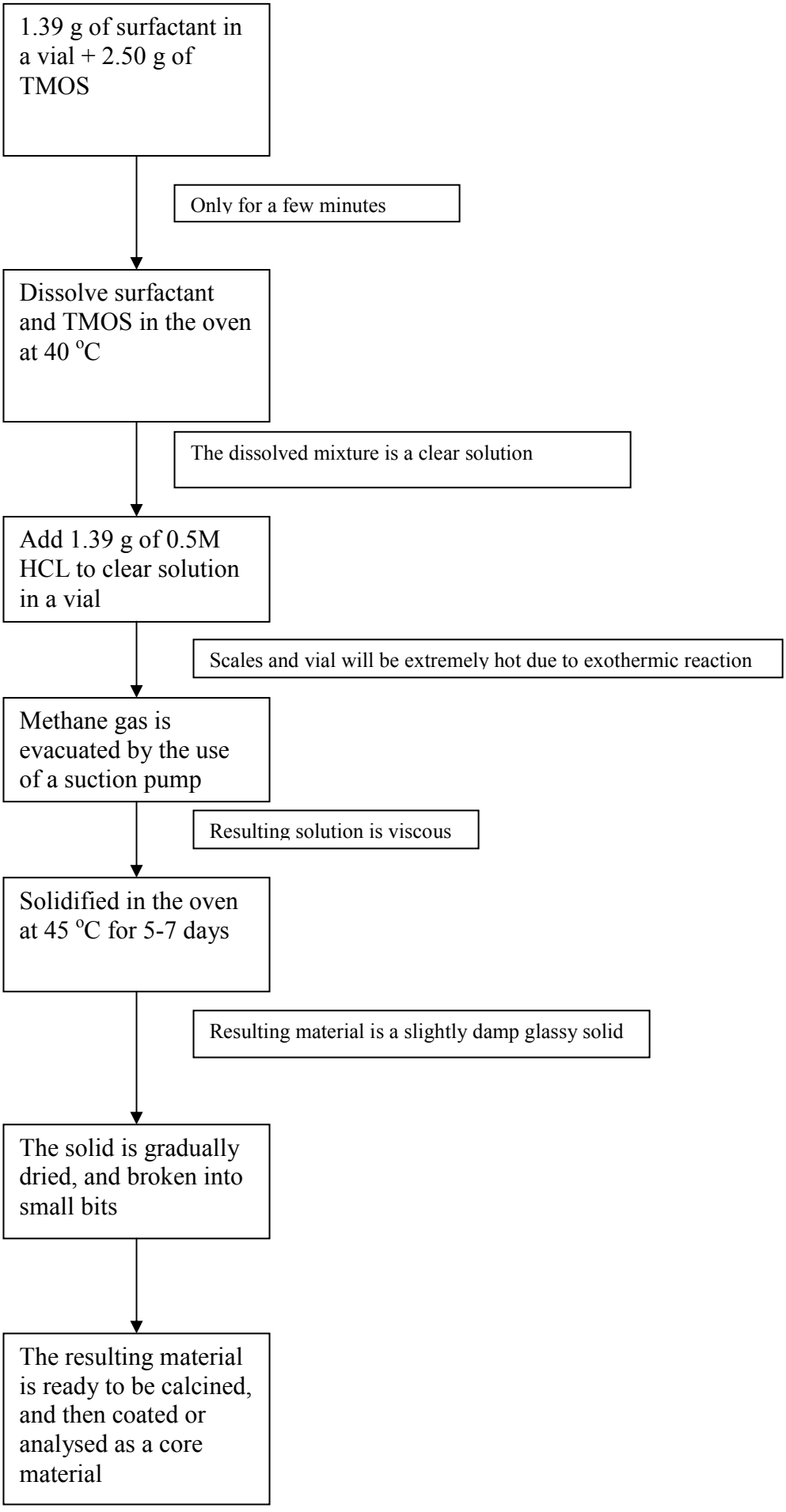

D 3: Schematic Representation of the Fourth Synthesis Method- (Latex Sphere Templating)

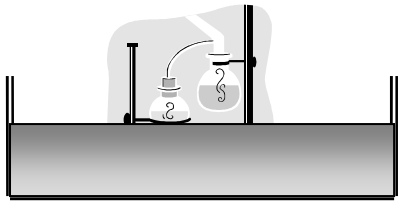

Latex particle is sealed tightly in a bottle using Teflon tape to prevent O_2 access solution is reacted in an oil bath at 90^{oc} whilst stirring at 200rpm with a bar for 24hours

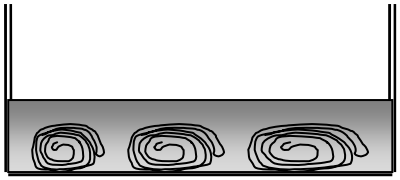

The resulting solution is milky. Dialysis tubing is then used to dialyse solution against water for 3days several changes of water per day, to get rid of excess surfactant

Centrifuge at 10000rpm for a few hours, until close packed spheres were gathered at the bottom, and a clear solution (water) at the top

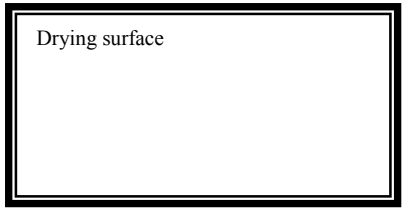

The water is tipped off, and the spheres were allowed to air dry gradually over several days. In the centrifuge vial first, and then on a flat open container

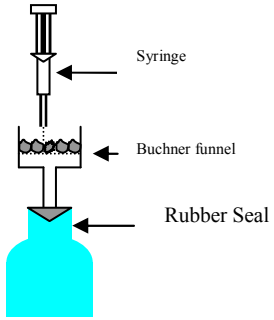

Macroporous silica solids are then prepared by placing millimetre sized chunks of dried latex spheres in a Buchner funnel attached to a vacuum suction, and wetting with approximately 1mL of butanol prior